Bridging Innovations of Phase Change Heat Transfer to Electrochemical

2	Gas Evolution Reactions
3	Manuscript for Chemical Reviews
4 5	Lenan Zhang ^{1,2,*} , Ryuichi Iwata ³ , Zhengmao Lu ⁴ , Xuanjie Wang ² , Carlos D. Díaz-Marín ² , Yang Zhong ²
6	
7 8	¹ Sibley School of Mechanical and Aerospace Engineering, Cornell University, Ithaca, New York 14853, United States
9 10	² Department of Mechanical Engineering, Massachusetts Institute of Technology, Cambridge, MA 02139, USA
11	³ Toyota Central R&D Labs., Inc, Nagakute City, 480-1192, Japan
12	⁴ Institute of Mechanical Engineering, EPFL, 1015 Lausanne, Switzerland
13	
14	*Corresponding author: <u>lzhang@cornell.edu</u> , <u>lzhang2@mit.edu</u> (L. Zhang)
15	
16	
17	
18	
19	
20	
21	
22	
23	
24	
25	
26	
27	
28	
	* Corresponding author E-mail address: <u>lzhang@cornell.edu</u> , <u>lzhang2@mit.edu</u> (L. Zhang)

ABSTRACT

1

2

3

4

5

6

7

8

9

10

11

12

13

14

15

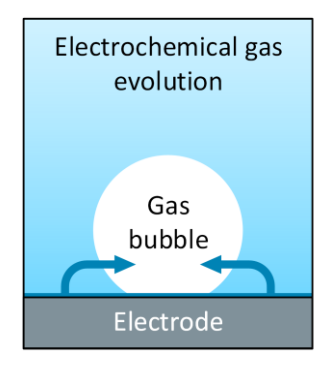
16

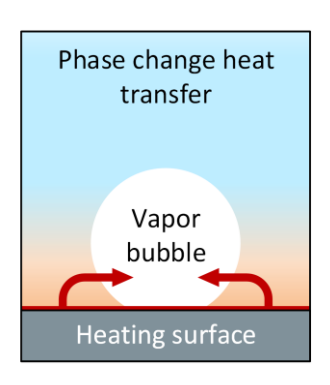
17

18

Bubbles play a ubiquitous role in electrochemical gas evolution reactions. However, a mechanistic understanding of how bubbles affect the energy efficiency of electrochemical processes remains limited to date, impeding effective approaches to further boost the performance of gas evolution systems. From a perspective of the analogy between heat and mass transfer, bubbles in electrochemical gas evolution reactions exhibit highly similar dynamic behaviors to them in liquid-vapor phase change. Recent developments of liquid-vapor phase change systems have substantially advanced the fundamental knowledge of bubbles, leading to unprecedented enhancement of heat transfer performance. In this Review, we aim to elucidate a promising opportunity of understanding bubble dynamics in electrochemical gas evolution reactions through a lens of phase change heat transfer. We first provide a background about key parallels between electrochemical gas evolution reactions and phase change heat transfer. Then, we discuss bubble dynamics in gas evolution systems across multiple length scales, with an emphasis on exciting research problems inspired by new insights gained from liquid-vapor phase change systems. Lastly, we review advances in engineered surfaces for manipulating bubbles to enhance heat and mass transfer, providing an outlook on the design of high-performance gas evolving electrodes.

TOC graphic (3.25 in \times 1.75 in)





20

19

21

CONTENTS 1 2 1. Introduction 3 2. Fundamentals 2.1. Bubbles in Electrochemical Gas Evolution Reactions 4 5 2.2. Connections between Electrochemical Gas Evolution Reactions and Phase Change Heat Transfer 6 2.3. Physical Origin of Electrochemical Overpotentials 7 3. Bubble Dynamics: Multiscale Understanding and Insights from Phase Change Heat Transfer 8 3.1. Bubble Nucleation 9 3.1.1. Nucleation from a Single Site 10 11 3.1.2. Distribution of Nucleation Sites: Statistical Description and Impacts on Bubble **Dynamics** 12 3.1.3. Advances in Metrology Tools for the Probe of Nucleation Sites 13 3.2. Bubble Growth 14 3.2.1. Regimes of Single Bubble Growth 15 3.2.2. Interfacial Transport Associated with Bubble Growth: Opportunities of 16 17 **Knowledge Translation** 3.2.3. Bubbles in Phase Change Heat Transfer and Electrochemical Gas Evolution 18 **Reactions: Distinctions** 19 3.2.4. Impact of Bubble Growth on Electrochemical Overpotentials 20 3.3. Bubble Interaction and Departure

3.3.2. Statistical Description of Bubble Interaction

3.3.1. Regimes of Bubble Departure

21

22

1	5.5.5. Impact of Bubble Interaction on Electrochemical Overpotentials
2	3.4. Bridging the Microscopic Bubble Dynamics to the Macroscopic Transport Properties
3	3.4.1. Multiscale Understanding of Phase Change Heat Transfer through a Statistical
4	Description
5	3.4.2. Full-field Analysis of Phase Change Heat Transfer with High-fidelity
6	Simulations
7	3.4.3. Opportunities and Challenges for High-fidelity Simulations of Electrochemical
8	Gas Evolution Reactions
9	4. Pathway toward a Better Design of Gas Evolution Systems by Manipulating Bubbles
10	4.1. Role of Surface Structures in Manipulating Bubbles: Insights from Phase Change Heat
11	Transfer
12	4.2. Design Trade-off by Engineering Surface Structures
13	4.3. Approaching the Fundamental Limits by Manipulating Transport across Multiple
14	Length Scales
15	5. Conclusions and Outlook
16	Author Information
17	Corresponding Author
18	Authors
19	Author Contributions
20	Notes
21	Biographies
22	Acknowledgements
23	References

1. INTRODUCTION

1

2

3

4

5

6

7

8

9

10

11

12

13

14

15

16

17

18

19

20

21

22

23

24

25

26

27

28

29

Electrochemical gas evolution reactions play a ubiquitous role in numerous industrial applications and exert a significant impact on sustainability. In chemical manufacturing, the large-scale industrial production of multiple essential chemicals, such as aluminum (the Hall-Héroult process),² sodium chlorate,³ as well as chlorine and sodium hydroxide (the chloralkaline process),⁴ relies on electrochemical gas evolution reactions. In addition, electrochemical gas evolution reactions have found immense utility in energy conversion and storage. These reactions include hydrogen (H2) and oxygen (O2) evolution during water splitting, 5 hydrazine oxidation reaction, 6 carbon dioxide reduction reaction for the regeneration of fuels, and direct methanol fuel cells. More importantly, owing to the unique capability of directly converting electricity into useful chemicals without emissions, several electrochemical gas evolution reactions have been recognized as one of the major techniques to achieve energy sustainability. For example, green hydrogen, produced by splitting water with renewable sources (e.g., wind and solar) of electricity, is a clean alternative of fossil fuels and a leading option for energy storage, which is expected to fundamentally alter the fossil fuels-centered global energy landscape and promises our ambitious goal of net zero emissions by 2050.9-12 The rapid expansion of various electrochemical gas evolution reactions-based technologies highlights the necessity of attaining optimal performance by further improving energy efficiency. Inefficiencies in an electrochemical process are primarily described by overpotential, which is defined as the additional voltage required on top of the thermodynamic voltage (e.g., 1.23 V for water splitting at standard temperature and pressure) to trigger the reaction.⁵ Due to the limited solubility of electrolytes, the continuous generation of gaseous products can lead to the formation of bubbles on the electrode, which makes the gas evolution reactions distinct from the rest of electrochemical processes (e.g., electroplating and lithium ion batteries). The evolution of bubbles can fundamentally change the characteristics of an electrochemical reaction through multiple complex interactions with gas evolving electrodes and liquid electrolytes. On the one hand, the presence of gas phase can be detrimental, because it reduces the active electrode area and the effective ionic conductivity of electrolytes, inducing

undesirable overpotentials for the electrochemical system.^{13–18} On the other hand, the periodic bubble growth and departure create strong convection to enhance the transport of ions and dissolved gases, which can contribute positively to the electrolytic cell.^{19,20} In particular, taking hydrogen evolution as an example, it has been suggested that the energy efficiency of commercial water electrolyzers (< 74%) can be increased to over 98% by mitigating the adverse effects induced by bubbles,²¹ reaching the 2050 cell energy consumption target (> 94% energy efficiency) set by the International Renewable Energy Agency.²² The critical role of bubbles manifests a significant engineering space to improve the performance of electrochemical gas evolution systems by manipulating bubble dynamics.

Despite tremendous progress over the past four decades, rationale design of high-performance electrolytic cells through the control of bubble behaviors is still elusive due to two fundamental challenges. First, it is unclear what the optimal bubble dynamics are to achieve the highest energy efficiency of an electrochemical gas evolution system, because there lacks fundamental understanding of how bubbles ultimately affect the overpotential. Bubbles in an electrolytic cell experience a multiscale process (from \sim nm to \sim cm), which couples multiple physical phenomena including the electric field, chemical kinetics, ion transport, gas transport, and liquid electrolyte flow through the electrode-electrolyte, electrolyte-gas, and electrode-gas interfaces. $^{13-15}$ It is hence essential to identify the key coupling mechanisms associated with bubbles at each individual length scale and project their ultimate impacts to the change of overpotential. Second, there is a significant knowledge gap of how to precisely manipulate bubbles toward the ideal dynamic behaviors. Innovative solutions to the next-generation high-performance gas evolving electrodes and electrolytic cells require combining the in-depth understanding of bubbles with the development of effective manipulation approaches.

Recent advances in phase change heat transfer could potentially provide viable solutions to address existing challenges in electrochemical gas evolution reactions. Liquid-vapor phase change heat transfer (*i.e.*, boiling, evaporation, and condensation) is a fundamental thermophysical process associated with the evolution of bubbles (boiling) or droplets (condensation).²³ Owing to the analogy between heat and mass transfer, bubbles in phase change heat transfer and electrochemical gas evolution reactions have a similar physical

origin.^{24–26} Driven by the rapid development of steam cycles and the growing demand of electricity generation over the past century, however, bubbles in the boiling process have been extensively investigated and are more comprehensively understood compared with them in the electrochemical process.^{23,27} Therefore, translating the knowledge from phase change heat transfer holds significant promise for addressing the bubble induced challenges in electrolytic cells. In fact, there have been a few valuable discussions about the connections between phase change heat transfer and electrochemical gas evolution reactions since 1980s. 24-26,28-30 After the 2000s, tremendous progress in phase change heat transfer, including fundamental understanding, computational tools, and bubble manipulation approaches, sheds light on even more exciting opportunities for the knowledge translation. In particular, the theoretical breakthroughs in recent five years have established a unified framework with a focus on the multiscale nature of bubbles in phase change processes, which is capable of quantifying how bubble dynamics dictate the overall heat transfer.^{31–33} Meanwhile, the rapid development of numerical methods and the boost of computational power have facilitated a full-field, firstprinciples capability for the high-fidelity simulations of phase change heat transfer.^{34–36} More notably, with the increased accessibility to micro-and-nanofabrication technologies since 2000s, there have been a number of successful implementations that manipulate the behaviors of bubbles and droplets in phase change systems by introducing micro-and-nanoscale features to the boiling and condensation surfaces. ^{27,37,38} These efforts have enabled a systematic design strategy to enhance the phase change heat transfer performance through surface engineering. It is thus worth exploring how the knowledge developed in phase change heat transfer can bring meaningful impacts to advance our understanding of bubbles in electrochemical gas evolution reactions. This review aims to discuss potential opportunities to address the bubble associated challenges

1

2

3

4

5

6

7

8

9

10

11

12

13

14

15

16

17

18

19

20

21

22

23

24

25

26

27

28

29

in electrochemical gas evolution systems by delivering transformable and interdisciplinary messages from the perspective of phase change heat transfer. Owing to the rapid growth and increasing demand of hydrogen energy, 9–11 the rest of our discussion will mainly focus on hydrogen evolution, while the key concepts shown in this review are generally applied to other electrochemical gas evolution processes. We structure the review as follows. In Section 2, we

introduce several fundamental concepts in electrochemical gas evolution reactions and phase change heat transfer. In addition to elucidating the connections between electrochemical gas evolution reactions and phase change heat transfer (Section 2.2), we clarify some common misunderstandings in electrochemistry, which are critical to an accurate description to the physical origin of overpotentials (Section 2.3). In Section 3, bubble dynamics are systematically discussed. We aim to demonstrate the governing physics of bubbles at each length scale (Section 3.1 to 3.3) and how the microscopic bubble dynamics can be related to the macroscopic transport properties (e.g., overall mass transfer and overpotentials) through a multiscale perspective (Section 3.4). We not only comment on potential research opportunities inspired by advances in phase change heat transfer, but carefully identify the key differences of bubbles on boiling surfaces and gas evolving electrodes. In Section 4, we discuss how to control the bubble behaviors, with an emphasis of surface engineering approaches. With knowledge developed by the phase change heat transfer community, we demonstrate the connections between bubble dynamics and micro-and-nanoscale features on surfaces, which might inspire innovative solutions to the design of gas evolving electrodes. With a convergent understanding of bubbles, we envision that our discussion in this Review will promote increasing interactions between the electrochemical gas evolution reactions and phase change heat transfer communities. We believe there will be promising opportunities at the intersection of two communities and hence encourage researchers from both sides to exchange their critical thoughts and catalyze synergetic solutions to the next-generation high-performance electrochemical gas evolution systems.

22

23

24

25

26

27

28

1

2

3

4

5

6

7

8

9

10

11

12

13

14

15

16

17

18

19

20

21

2. FUNDAMENTALS

2.1. Bubbles in Electrochemical Gas Evolution Reactions

Properties of an electrochemical system are typically characterized by the polarization curve which describes the potential (ϕ , unit in V) as a function of current density (i, unit in A/cm²) applied to the electrolytic cell (Fig. 1a).³⁹ i is proportional to the reaction rate and the mass flux of the products. It is thus practically feasible to operate the electrolytic cell in a high-current

density regime. To initiate an electrochemical reaction, the potential acting on the electrodes should be above the thermodynamic limit of the reaction ($\phi_{th} = 1.23 \text{ V}$ for water splitting at standard temperature and pressure), which is fundamentally dictated by the Gibbs free energies of products and reactants.⁵ The thermodynamic limit represents an "ideal potential" of the electrochemical system with zero losses. If an electrochemical system can be operated at the thermodynamic limit, all the input electricity is converted to the chemical energy of products. However, for a realistic system, the potential applied to the electrolytic cell is always above the thermodynamic limit due to various sources of irreversibility, leading to an overpotential (η , unit in V).^{39,40} Therefore, the overpotential is an important measure for various losses of an electrochemical system. The energy efficiency ε of an electrolytic cell, which is defined as the ratio of the energy of produced hydrogen E_{H2} to the total input electricity E_{tot} , can be expressed as,^{41,42}

$$\varepsilon = \frac{E_{\rm H2}}{E_{\rm tot}} = \frac{\phi_{\rm th}}{\phi_{\rm th} + \eta}.\tag{1}$$

A higher overpotential indicates larger losses and hence lower energy efficiency. These losses are induced by the activation energy required for the electrochemical reaction, ohmic loss due to electrical and ionic resistance, and transport loss of ions and dissolved gases, which are reflected from the polarization curve (Figure 1a). In the low-current density regime, activation loss is the governing loss mechanism, resulting in a nonlinear dependence of overpotential with current density ("activation region" in Figure 1a). The induced overpotential corresponding to the activation loss is known as the activation overpotential (η_{act}). With the increase of current density, ohmic loss becomes more significant and the polarization curve in this regime is more linear ("ohmic region" in Figure 1a), which is represented by the ohmic overpotential (η_{ohm}). In the high-current density regime, however, inefficient transport of ions and gases becomes the major bottleneck to the electrolytic cell efficiency, leading to a rapid increase of overpotential ("mass transport region" in Figure 1a). The overpotential associated with mass transport is typically known as the concentration overpotential (η_{con}) or the mass transport overpotential. In general, the total overpotential is hence given by, η_{act}

$$\eta = \eta_{\rm act} + \eta_{\rm ohm} + \eta_{\rm con}. \tag{2}$$

- 1 More details related to the physical origin of each loss mechanism and several common
- 2 misunderstandings will be discussed in Section 2.3.

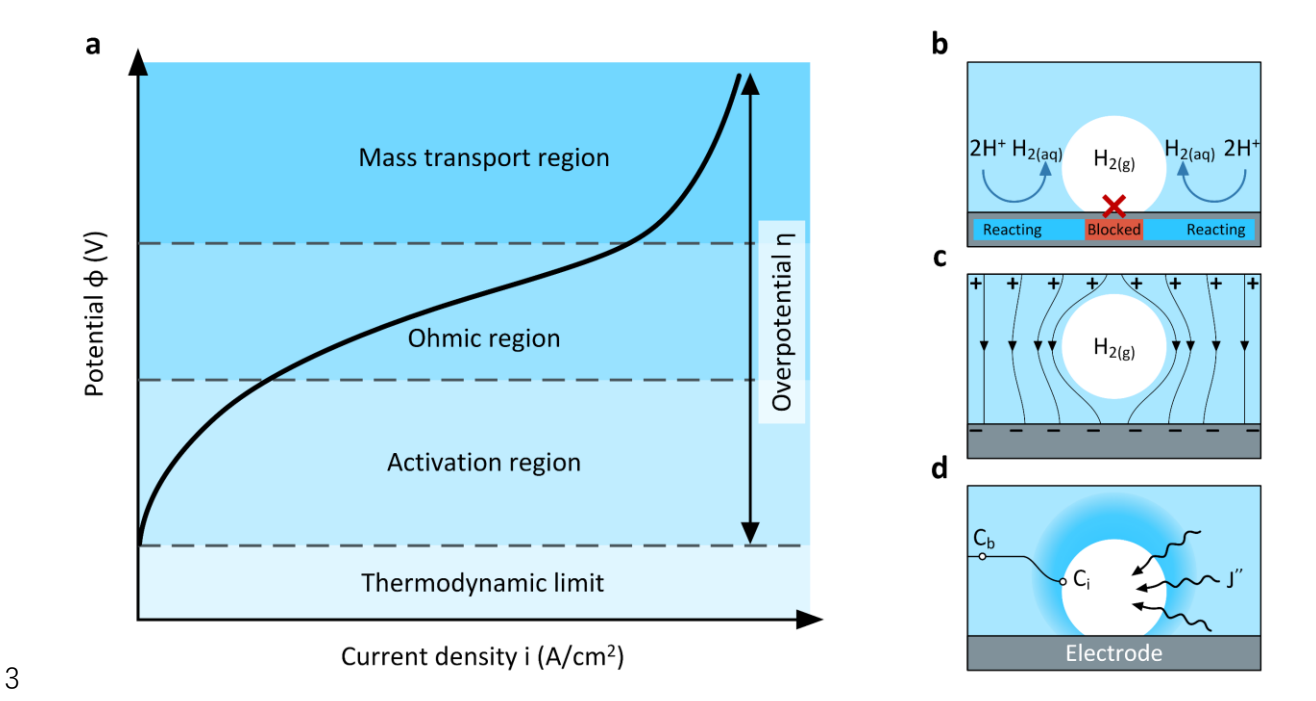


Figure 1. Overview of impact of bubbles on electrochemical performance. (a) Schematic illustration of polarization curve describing the applied potential as a function of current density through the electrolytic cell. Overpotential (η) is the additional voltage required to drive the electrochemical process over the thermodynamic limit (ϕ_{th} = 1.23 V). The total overpotential typically can be decomposed into activation overpotential (η_{act}), ohmic overpotential (η_{ohm}), and concentration overpotential (η_{con}). (b) Impact of bubbles on activation overpotential. Reaction area (blue region) can be blocked by bubble bases (red region), which reduces the area-projected effective current density. (c) Impact of bubbles on ohmic overpotential. Gas bubbles are electrically insulating, which create additional resistance for ion transport across the electrolyte. (d) Impact of bubbles on concentration overpotential. The presence of electrolyte-gas interface can induce undesirable concentration profiles of gas and ion, leading to the increase in concentration overpotential. Meanwhile, convection flows induced by bubble dynamics can potentially reduce the concentration overpotential.

In an electrochemical gas evolution process, behaviors of bubbles can significantly impact all major loss mechanisms. 13-17 Electrochemical reactions mainly occur at the electrodeelectrolyte interface. Bubbles cover the active sites on electrodes and block the reaction area, which increases the total overpotential of the electrolytic cell due to the reduction of the areaprojected effective current density (Figure 1b). Bubbles on electrodes and liquid electrolytes impede the ion migration, i.e., ion transport driven by the electric field, and result in the decrease of effective ionic conductivity (Figure 1c). In addition to migration, ion transport also relies on diffusion. Meanwhile, diffusion is also the major driving force for the transport of dissolved gases. The presence of bubbles changes the concentration profiles of both ions and dissolved gases and hence impacts the concentration overpotential (Figure 1d). Effects of bubbles on the concentration overpotential can be complex. On the one hand, bubbles block ion diffusion toward or away from the electrode-electrolyte interface, which could potentially increase the concentration overpotential. 43-45 There is also a gas diffusion layer on the electrolyte-gas interface, which dictates the supersaturation of dissolved gases on the electrodeelectrolyte interface (Figure 1d).⁴⁶ It is commonly believed that the increase of gas supersaturation can lead to the increase of concentration overpotential, 46,47 however, the underlying mechanisms could deviate from the conventional understanding, which will be discussed in detail in Sections 2.3 and 3.2.4. On the other hand, the dynamic behaviors of bubbles, e.g., growth, coalescence, and departure, can induce strong convection to enhance mass transfer in the liquid electrolyte, which can be a desirable mechanism to reduce the concentration overpotential. 14,19,20 Although it is generally believed that the presence of bubbles is undesirable due to the above conceptual understanding, the specific role of bubbles in electrochemical gas evolution reactions is still in debate and requires further investigations. This is because precisely quantifying the variations of each overpotential term as a function of bubble dynamics is fundamentally challenging. In Sections 2.2 and 2.3, we will discuss the origins of these bubble induced challenges and potential solutions from the angle of phase change heat transfer.

2.2. Connections between Electrochemical Gas Evolution Reactions and Phase Change

Heat Transfer

1

2

3

4

5

6

7

8

9

10

11

12

13

14

15

16

17

18

19

20

21

22

23

24

25

26

27

28

Analogy between heat and mass transfer leads to a couple of similarities between electrochemical gas evolution reactions and phase change heat transfer in terms of both device configurations and transport characteristics. Figure 2 shows three representative device configurations used for water electrolysis (Figure 2a - 2c) and liquid-vapor phase change systems (Figure 2d - 2f). For each type of electrolytic cell, interestingly, there is an analogous device in phase change heat transfer exhibiting a similar configuration. The pool-type electrolytic cell (Figure 2a), also known as the conventional/batch electrolytic cell, is associated with the first discovery of water electrolysis in 1789 and has become one of the most mature and widely commercialized technologies for hydrogen production.⁴⁸ The pool-type electrolytic cell is typically operated in a liquid alkaline electrolyte solution of potassium hydroxide (KOH) or sodium hydroxide (NaOH). Two electrodes are immersed in the liquid electrolyte with a separator, known as the diaphragm, ^{49,50} between them (Figure 2a). The diaphragm separates the produced hydrogen and oxygen while allowing the transport of hydroxide ions (OH⁻) from cathode to anode. With electricity through the external circuit, hydrogen and oxygen bubbles evolve from the cathode and anode, respectively. In alkaline water electrolysis, the anode and cathode reactions are given by,

1

2

3

4

5

6

7

8

9

10

11

12

13

14

15

Anode:
$$20H^- \rightarrow H_2O + 1/2O_2 + 2e^-$$
 (3)

Cathode:
$$2H_2O + 2e^- \rightarrow H_2 + 2OH^-$$
. (4)

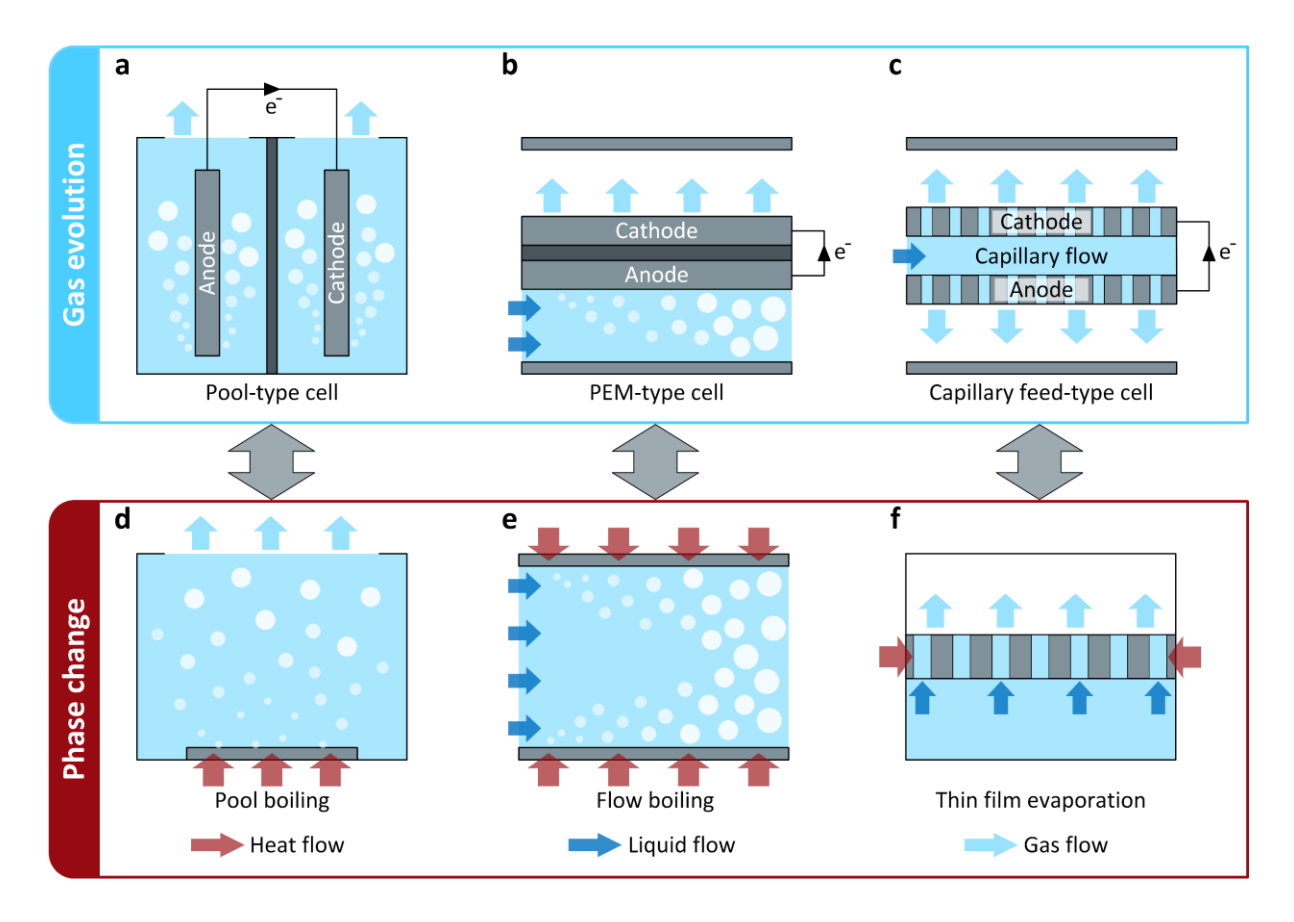


Figure 2. Similar device configurations of electrochemical gas evolution and liquid-vapor phase change systems. (a) Pool-type electrolytic cell. Anode and cathode are immersed into a pool of electrolyte and separated by a diaphragm. (b) Polymer electrolyte membrane (PEM)-type electrolytic cell. Anode and cathode are separated by a gas impermeable but proton conductive PEM. Liquid containing oxygen bubbles flows through the channel adjacent to the anode. (c) Capillary feed-type electrolytic cell. Anode and cathode are separated by a hydrophilic porous structure containing electrolyte, which enables a fully passive supply of electrolyte and a nearly bubble-free electrolysis. (d) Pool boiling process. A heating surface is immersed into the liquid pool. When the liquid temperature is above the boiling point, boiling occurs with continuous bubble generation on the heating surface. (e) Flow boiling process. Liquid flows through a channel with heat supplied from the sidewall. Bubbles are carried by the flow with vapor void fraction (ξ) increasing along the channel. (f) Thin film evaporation process. A hydrophilic porous structure with micro/nanopores is placed on a reservoir and used as the evaporator. Liquid flows into the evaporator due to capillary pressure, creating meniscus

1 liquid-vapor interfaces pinned by micro/nanopores. When heat is applied, most of evaporation

2 occurs near the thin film region of the meniscus liquid-vapor interface.

3

4

5

6

7

8

9

10

11

12

13

14

15

16

17

18

19

20

21

22

23

24

25

26

27

28

The counterpart of the pool-type electrolytic cell in phase change heat transfer is the pool boiling (Figure 2d). Industrial applications of pool boiling originated from the invention of the first boiler and the first steam engine.⁵¹ At the present time, pool boiling is still one of the most widely used phase change processes, from utility-scale power plants to cooking at home.⁵² In a pool boiling device, a solid surface, i.e., the analogous component to electrodes, is immersed into the liquid pool, where vapor bubbles are generated on the surface with heat supply (Figure 2d). We discuss three key similarities between the pool-type electrolytic cell and pool boiling device. First, bubble formation occurs at the solid-liquid interface in both devices due to heterogeneous nucleation, which is fundamentally dictated by the supersaturation. For electrochemical gas evolution reactions, the supersaturation indicates that the gas concentration exceeds the solubility of electrolytes. For the boiling process, on the other hand, supersaturation is described by the wall superheat, referring to the liquid temperature above the saturation temperature (i.e., boiling point). Second, both devices are operated in a quiescent liquid pool. This indicates that the major fluidic forces in such systems are induced by bubbles (e.g., capillarity and buoyancy). Third, transport mechanisms associated with the growth of bubbles in both devices are similar. In the gas evolution process, mass (i.e., the produced gases) diffuses from the solid-liquid (i.e., electrode-electrolyte) interface to the gas bubble through the liquidgas (i.e., electrolyte-gas) interface. In the boiling process, heat, the counterpart of mass, diffuses along the same path to vapor bubbles. Since heat and mass diffusions have the same mathematical formulation, it is expected that the resulting transport properties and bubble dynamics in both devices exhibit similar behaviors. In addition to the pool-type cell, another major type of water electrolysis relies on the polymer electrolyte membrane (PEM) (Figure 2b). PEM, also known as the proton exchange membrane, is capable of conducting proton (H⁺) while remaining impermeable to gaseous products.^{53–57} Owing to these unique properties, PEM can effectively separate the cathode and anode reactions, making it an ideal replacement of the liquid electrolyte and diaphragm. the PEM-

- type cell is operated in an acidic environment, resulting in the following anode and cathode
- 2 reactions,

Anode:
$$H_2O \rightarrow 2H^+ + 1/2O_2 + 2e^-$$
 (5)

Cathode:
$$2H^+ + 2e^- \rightarrow H_2$$
. (6)

The PEM-type electrolytic cell has attracted increasing attention since 2010s. 54-57 Compared with the pool-type electrolytic cell, the implementation of PEM facilitates a more compact design and reduces the ohmic loss, enabling a high-current density (> 2 A/cm²) operation with a relatively high energy efficiency ($\approx 70\%$). ^{54,56} The cathode reaction of PEM-type cell (eq. 6) indicates that the cathode is exposed to a gaseous environment containing hydrogen whereas the anode reaction (eq. 5) requires a continues water supply with oxygen bubble generation (Figure 2b). During the PEM-type cell operation, water is pumped into a liquid channel in contact with the anode, creating a forced convection flow. This forced convection flow accelerates the bubble departure from the anode and carries bubbles out of the electrolytic cell (Figure 2b), leading to an increase of gas phase void fraction ξ along the flow direction (Figure 2b). 15,58-63

The transport mechanisms and bubble behaviors in the PEM-type electrolytic cell exhibit similar features to the flow boiling process in phase change heat transfer (Figure 2e). In a flow boiling device, liquid is pumped into a channel and heat is supplied from the sidewall (Figure 2e). When the liquid temperature is higher than the boiling point, vapor bubbles nucleate from the sidewall and evolve along the flow. The similarities discussed in the pool-type devices, including the bubble nucleation, bubble induced forces, and diffusion processes, are also valid when comparing the PEM-type electrolytic cell with the flow boiling device. In addition, performance of both devices is largely dictated by the coupling between forced convection flow and bubble dynamics, which makes their behaviors considerably more complicated than those of the pool-type devices. Heat transfer characteristics and design principles of flow pooling devices have been comprehensively investigated since 1960s. For example, the coupling of hydrodynamics and heat transfer dominates the change of flow patterns along the forced convection flow, resulting in different local heat transfer performance. With the increase

1 of vapor void fraction ξ , it has been shown that the two-phase flow in the channel gradually transitions from a "bubbly flow regime" (i.e., $\xi \approx 0$) to a "mist regime" (i.e., liquid dry-out with 2 $\xi \approx 1$), passing through a "slug flow regime" and an "annular flow regime" (i.e., $0 < \xi < 1$), 3 which leads to a monotonic decrease of local heat transfer coefficient (HTC).⁶⁶ The position of 4 each two-phase flow regime depends on both the forced convection flow rate and applied heat 5 flux. 64-66 To ensure an efficient heat transfer, it is essential to avoid liquid dry-out, which 6 constrains the dimensions and operation of the flow channel. It has been shown that similar 7 flow patterns and transition mechanisms occur in the PEM-type electrolytic cell, 60-63 which 8 further confirmed its close connections with the flow boiling device. It is thus worth 9 considering how to take advantage of the established knowledge in flow boiling to further 10 improve the water management of PEM-type electrolytic cells. 11 In addition to the pool-type and PEM-type electrolytic cells, the capillary feed-type electrolytic 12 cell is an emerging configuration of the water splitting device that was first reported by Hodges 13 et al. in 2022 (Figure 2c).²¹ In this configuration, a hydrophilic porous separator is sandwiched 14 by the porous gas diffusion electrodes (Figure 2c). The end of the separator is inserted into an 15 electrolyte reservoir. Due to the capillary pressure created by the micropores of the separator, 16 liquid electrolyte can flow through the separator without the requirement of additional pumping 17 power. When the electrolyte contacts the electrodes, electrochemical reactions occur at the 18 19 electrode-electrolyte interface. Two significant features of the capillary feed-type electrolytic 20 cell make it highly attractive for practical applications. First, the capillary feed-type electrolytic cell enables a completely passive electrolyte supply, because the consumed water during 21 22 electrolysis can be continuously re-supplied by the capillary flow through the separator (Figure 2c). Second, the design by avoiding the direct contact of electrolyte reservoir and electrodes, 23 i.e., keeping electrodes "dry", can effectively eliminate the detrimental impacts induced by 24 bubbles. Since the electrode-electrolyte interface is close to the electrolyte-gas interface, the 25 supersaturation of gases at the electrode-electrolyte interface can be maintained at a low level. 26 As a result, the produced gases can directly diffuse to the electrolyte-gas interface without 27 bubble nucleation. It has been shown that state-of-the-art capillary feed-type electrolytic cell 28 can remain bubble-free under a moderate current density up to 0.2 A/cm². By reducing bubble 29

- 1 formation, both bubble induced overpotentials and instabilities of current density can be
- 2 mitigated, resulting in superior energy efficiencies of 98% and 93% under 0.5 A/cm² and 1
- 3 A/cm², respectively. Despite the highly promising performance, there is still a significant
- 4 engineering space to further optimize the porous structures of the separator and extend the
- 5 bubble-free electrolysis to the high current density conditions (> 1 A/cm²).
- 6 The phase change process that shows a similar transport nature to the capillary feed-type
- 7 electrolytic process is the thin film evaporation. Figure 2f shows a thin film evaporator with
- 8 micro/nanopores. The small pore size, typically from \sim 10 nm to \sim 100 μ m, $^{67-71}$ induces a strong
- 9 capillary effect, leading to a meniscus liquid-vapor interface in each micro/nanopore. A region
- with liquid thin film (typically with ~ 10 nm to ~ 1 µm thickness depending on the pore size and
- contact angle) is created along the three-phase contact line. 67,68,72 Since the thin film region has
- 12 a low thermal resistance, most of evaporation occurs near the three-phase contact line, ⁷³
- 13 resulting in a highly desirable HTC (up to 40 W/cm²/K) for heat dissipation.⁷¹ Meanwhile,
- there is a large capillary pressure across the meniscus liquid-vapor interface ΔP_{cap} , which is
- described by the Young-Laplace equation,

$$\Delta P_{\rm cap} = \frac{2\gamma \cos\theta}{r} \tag{7}$$

- where γ is the liquid-vapor surface tension, θ is the contact angle of the liquid-vapor interface,
- and r is the pore radius. The capillary pressure drives the liquid flowing from the reservoir to
- the evaporating interface by overcoming the viscous loss induced by the porous structures of
- the evaporator, enabling a passive and continuous liquid supply during evaporation (Figure 2f).
- The pressure drop ΔP_{vis} due to viscous loss is described by the Darcy's law in the low-Reynold
- 21 number regime,⁶⁸

$$\Delta P_{\text{vis}} = \frac{\mu_1 L}{K} u \tag{8}$$

- where μ_l is the dynamic viscosity of liquid. K is the permeability of the porous evaporator. u is
- 23 liquid flow velocity. L is the wicking length of liquid. Depending on the operating condition of
- 24 the evaporator, L can be approximately equal to the thickness of the evaporator if liquid is

- supplied from the bottom (Figure. 2f) or the width of the evaporator if liquid is supplied from
- 2 the sides.

11

12

13

14

15

16

17

18

19

20

21

22

- 3 The maximum heat flux through the thin film evaporator is limited by capillarity. The capillary
- 4 pressure reaches its maximum value $\Delta P_{\text{cap,max}}$ when θ becomes the receding contact angle θ_{rec} .
- $\Delta P_{\text{cap,max}}$ dictates the maximum capability of passive liquid supply. When the heat flux applied
- 6 to the evaporator is sufficiently high, capillary pressure cannot overcome the viscous loss,
- 7 leading to the de-pinning of meniscus interface and dry-out of evaporator. Equating $\Delta P_{\text{cap,max}}$
- and ΔP_{vis} , the maximum heat flux that can be dissipated through thin film evaporation, known
- 9 as the capillary limited heat flux or dry-out heat flux $q''_{dry-out}$, can be derived as,⁶⁸

$$q_{\text{dry-out}}^{"} = \left(\frac{\rho_{l} h_{lv} \gamma}{\mu_{l}}\right) \left(\frac{2 \cos \theta_{\text{rec}}}{r}\right) \left(\frac{K t_{\text{w}}}{L^{2}}\right) \tag{9}$$

where ρ_1 and h_{1v} are the density and vaporization enthalpy of liquid. t_w is the thickness of the evaporator. Compared with the capillary feed-type electrolysis, the role of micro/nanopores in the heat transfer enhancement during thin film evaporation has been extensively investigated over the past decade. Therefore, it is highly desirable to explore whether insights gained from the thin film evaporation can contribute to further pushing the performance limit of the capillary feed-type electrolytic cell. Although we mainly discussed the pool-type, PEM-type, and capillary feed-type electrolytic cells above, we note that anion exchange membrane and solid oxide are the other two predominant types of electrolytic cells for water electrolysis. In addition, membrane-less electrolytic cells based on microfluidic devices hold promise to enable high-efficiency water electrolysis with simple architecture, increased lifetime, and reduced cost. Recent development of membrane-less electrolytic cells has been systematically reviewed by Esposito, for Ibrahim et al., Swiegers et al., and Manzotti et al.

- 23 In addition to the close connection at the device level as described above, electrochemical gas
- evolution reactions and phase change heat transfer have similar overall transport characteristics.
- 25 Figure 3a and 3b show the schematics of polarization curve by plotting current density i as a
- function of overpotential η and boiling curve describing heat flux (q", unit in W/cm²) as a

function of wall superheat (ΔT , unit in °C), respectively. Interestingly, the key features of polarization curve and boiling curve exhibit a one-to-one correspondence (Figure 3a and 3b). In the boiling curve, there is a peak value of heat flux, known as the critical heat flux (CHF) point, which represents the maximum amount of heat to be carried by the nucleate boiling process (Figure. 3b) and corresponds to a huge temperature rise.²³ After the CHF point, the boiling process transitions from the nucleate boiling regime to the film boiling regime, resulting in a decrease of heat flux due to bubble interaction. Therefore, the CHF point is not only a descriptor of the heat transfer performance, but more importantly, an indicator for the safe operation of boiling based systems, such as the power plant. Meanwhile, the mechanism of CHF is one of the most elusive fundamental problems in thermal-fluid science. Although mechanistic understanding of CHF is still highly required, tremendous efforts in theory, ^{32,89–91} numerical simulation, ^{34,35,92,93} experimental characterization, ^{94–97} and surface engineering ^{98–101} over the past several decades have already enabled theoretical predictions of the CHF with a reasonably high accuracy and demonstrated multiple reliable approaches to enhance the CHF. 27,37,38 Similarly, the peak value of current density, *i.e.*, the critical current density (CCD) point, was observed in gas evolution reaction (Figure 3b). ^{26,102} Through an *in operando* neutron imaging, the CCD point was attributed to an extreme gas saturation on the electrode. ¹⁰² Despite the important role of CCD as a performance indicator of the electrochemical process, it is unclear how to accurately predict and further enhance the CCD in gas evolution reactions.

1

2

3

4

5

6

7

8

9

10

11

12

13

14

15

16

17

18

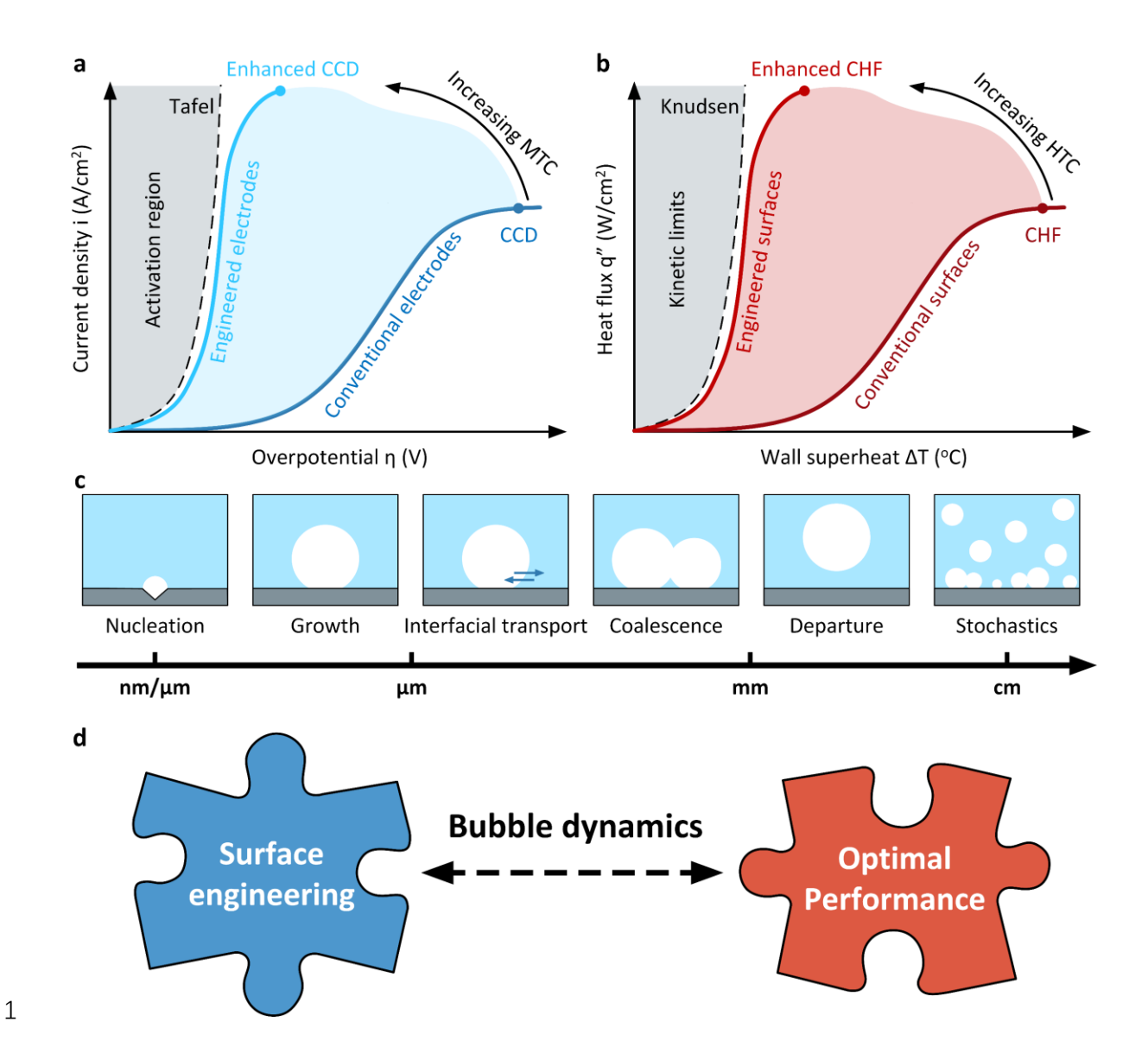


Figure 3. Similar transport characteristics of electrochemical gas evolution and liquid-vapor phase change systems dictated by bubbles. (a) Transport properties of the gas evolution process described by the polarization curve. Critical current density (CCD) is the maximum current density that can be achieved in an electrolytical cell. The larger slope of the polarization indicates the higher mass transfer coefficient (MTC) of the electrochemical system. The electrochemical kinetic limits (grey shadow) are given by the activation overpotential, which can be described by the Butler–Volmer equation or Tafel equation. It is possible to enhance both CCD and MTC of the gas evolution process, *i.e.*, left-shift the polarization curve, using engineered electrodes with surface structures. (b) Transport properties of the boiling process described by the boiling curve. The boiling curve exhibits similar features to the polarization

curve, from an analogous perspective of heat and mass transfer. The maximum amount of heat dissipated through the nucleate boiling process is known as the critical heat flux (CHF). The slope of the boiling curve is an indicator of heat transfer coefficient (HTC). The kinetic limits of liquid-vapor phase change describe the transport resistance induced by liquid-vapor interface, which originate from the Knudsen layer on liquid-vapor interface. Numerous studies have shown enhanced CHF and HTC through engineered surfaces, shifting the boiling curve toward the kinetic limits. (c) Similar dynamic behaviors of bubbles during the gas evolution and boiling processes at different length scales. (d) Toward the optimal performance of electrochemical gas evolution reactions by manipulating bubble dynamics through surface engineering. Two critical knowledge gaps are associated with bubbles, *i.e.*, how to gain a fully quantitative understanding of the impact of bubble dynamics on electrochemical performance and how to well control bubble dynamics through surface engineering. Insights gained in phase change heat transfer can be translated to bridge critical knowledge gaps in electrochemical gas evolution reactions.

On the other hand, the slopes of both polarization curve and boiling curve represent the efficiency of transport. Although it is always desirable to increase mass transfer coefficient (MTC) for electrochemical gas evolution reactions and HTC for phase change transfer processes, the slopes of both curves cannot be infinitely large due to the kinetic limits. Electrochemical kinetics of gas evolution reactions are dictated by the activation energy (grey shadow in Figure 3a), where the resulting activation overpotential can be described by the Butler–Volmer equation,³⁹

$$i = i_0 \left(\exp\left(\frac{\alpha_a z F \eta_{act}}{R_g T}\right) - \exp\left(-\frac{\alpha_c z F \eta_{act}}{R_g T}\right) \right)$$
 (10)

where i_0 , α_a , and α_c are exchange current density, anodic charge transfer coefficient, and cathodic charge transfer coefficient, respectively. z, F, R_g , and T are the number of electrons involved in the electrode reaction, Faraday constant (9.6485×10⁴ C/mol), universal gas constant (8.314 J/mol/K), and absolute temperature, respectively. When $|\eta_{act}| > 0.1$ V, the Butler-Volmer equation can be approximated to the commonly used the Tafel equation,³⁹

$$\eta_{\text{act}} = \eta_0 \log_{10} \frac{i}{i_0} \tag{11}$$

- where η_0 is the Tafel slope, which is related to the activation energy of reaction and can be
- 2 reduced by engineering catalysts. 103–105
- 3 Kinetics of heat transfer across the liquid-vapor interface originates from the non-equilibrium
- 4 Knudsen layer adjacent to the interface from the vapor side (grey shadow in Figure 3b). 106–109
- 5 Heat flux q_S'' due to the presence of Knudsen layer can be analytically modeled by the Schrage
- 6 equation, 110

$$q_{\rm S}^{"} = \frac{2\sigma_{\rm a}}{2 - \sigma_{\rm a}} \frac{h_{\rm lv}}{\sqrt{2\pi R_{\rm g}}} \left(\frac{P_{\rm sat}(T_{\rm l,int})}{\sqrt{T_{\rm l,int}}} - \frac{P_{\rm sat}(T_{\rm v,\infty})}{\sqrt{T_{\rm v,\infty}}} \right)$$
(12)

where σ_a is the accommodation coefficient, which describes the fraction of vapor molecules emitted from the liquid compared to the amount given by the equilibrium distribution. $h_{\rm lv}$ and $P_{\rm sat}$ are vaporization enthalpy and saturation pressure, respectively. $T_{\rm l,int}$ and $T_{\rm v,\infty}$ are the liquid temperature at the interface and vapor temperature at the far field, respectively. Note that a more rigorous theoretical treatment of Knudsen layer kinetics relies on solving the Boltzmann transport equation (BTE). ^{68,111–115} Compared with the BTE solution, the Schrage equation can provide a reasonably good estimation of heat flux for various engineering applications (< 15% discrepancy). ¹¹⁶

The above close connections between polarization curve and boiling curve fundamentally originate from the similar bubble dynamics of electrochemical gas evolution reactions and phase change heat transfer across multiple length scales (Figure 3c).³² In general, bubble nucleation occurs at nanoscale sites for electrochemical gas evolution reactions and microscale sites for boiling, which is followed by the bubble growth due to the mass/heat transfer across the liquid-gas interface. Then, there are bubble coalescence and departure happened at microto-millimeter scale. Finally, stochastic bubble interaction occurs on the entire electrode/heating surface with a length scale typically above a few centimeters, dictating the macroscopic properties (*e.g.*, HTC and MTC) of the boiling and gas evolution processes. Details about the physical origins of bubble dynamics in each length scale will be discussed in Section 3.

From a practical consideration, it is highly desirable to simultaneously enhance MTC and CCD to enable efficient gas evolution with high production rate (light blue curve in Figure 3a). Over the past decade, it has been well demonstrated that both HTC and CHF of boiling can be significantly enhanced by manipulating bubble dynamics through surface engineering (light red curve in Figure 3b). 27,37,38 Although recent studies have shown that both bubble dynamics and overpotentials can be altered by modifying surface structures and wettability of electrodes, 16-18 a rational surface engineering approach of electrodes is not yet developed. Following a similar path that has been established in phase change heat transfer, we will discuss the opportunity to bridge the knowledge gap between surface engineering and optimal electrochemical performance from a perspective of bubble dynamics (Figure 3d). In particular, we will first focus on how to quantify the role of bubbles in overpotentials (Section 3) and then discuss how to control the behaviors of bubbles with surface modifications (Section 4). With an enhanced understanding of bubble dynamics, we expect that the electrochemical gas evolution reactions can be operated with a significantly improved efficiency toward the kinetic limits.

2.3. Physical Origin of Electrochemical Overpotentials

To better understand how bubble dynamics can impact electrochemical gas evolution reactions, in this Section, we lay foundations for the physical origin of various overpotentials in electrochemical processes. Since key concepts of overpotential are widely available in classical electrochemistry textbooks, ^{39,117–120} we would like to only focus on the structure of species concentration near the electrode and its connections with overpotentials. We will first revisit the general physical picture and key assumptions and then comment on a few inconsistencies and missing parts in the theoretical treatments of overpotentials.

We take the cathode reaction of alkaline water electrolysis (eq. 4) as an example to illustrate the basic concepts. To simplify our discussion, we first consider the hydrogen evolution in KOH solution without bubble nucleation. When a potential is applied to the cathode, there is a layered structure of charge density above the cathode due to both electrostatic interaction and mass transfer (Figure 4a). The first layered structure on the electrode surface is known as the

electrical double layer (EDL), which consists of two parallel layers of charges, i.e., the Stern layer and the potential screening layer, surrounding the electrode. One of the most widely accepted physical pictures of the EDL is given by the Gouy-Chapman-Stern model. 122-124 Specifically, solvated cations (K⁺) are adsorbed on the surface of cathode due to the Coulomb force, resulting in a compact monolayer structure known as the Stern layer (Figure 4a). 124 The center position of the Stern layer (λ_s) is called the outer Helmholtz plane (OHP, typically ~ 0.5 nm above the electrode depending on the solvated cation size), which represents the closest distance that a solvated cation can approach the electrode (plane (1) in Figure 4a and 4b). 125 The Stern layer forms the first layer of EDL. The second layer, known as the potential screening layer or diffuse layer, contains more loosely distributed solvated cations to electrically screen the Stern layer (Figure 4a). Since solvated cations in the potential screening layer are not firmly adsorbed on the cathode, they can move within the electrolyte through diffusion, migration, and convection, creating specific concentration profile during the electrochemical process. Within the EDL, solvated cation concentration decays rapidly to the bulk value across a few nanometers (Figure 4b). Therefore, the thickness of the EDL is typically on an order of 1 nm, which can be quantified by the Debye length λ_D . ^{39,126}

1

2

3

4

5

6

7

8

9

10

11

12

13

14

15

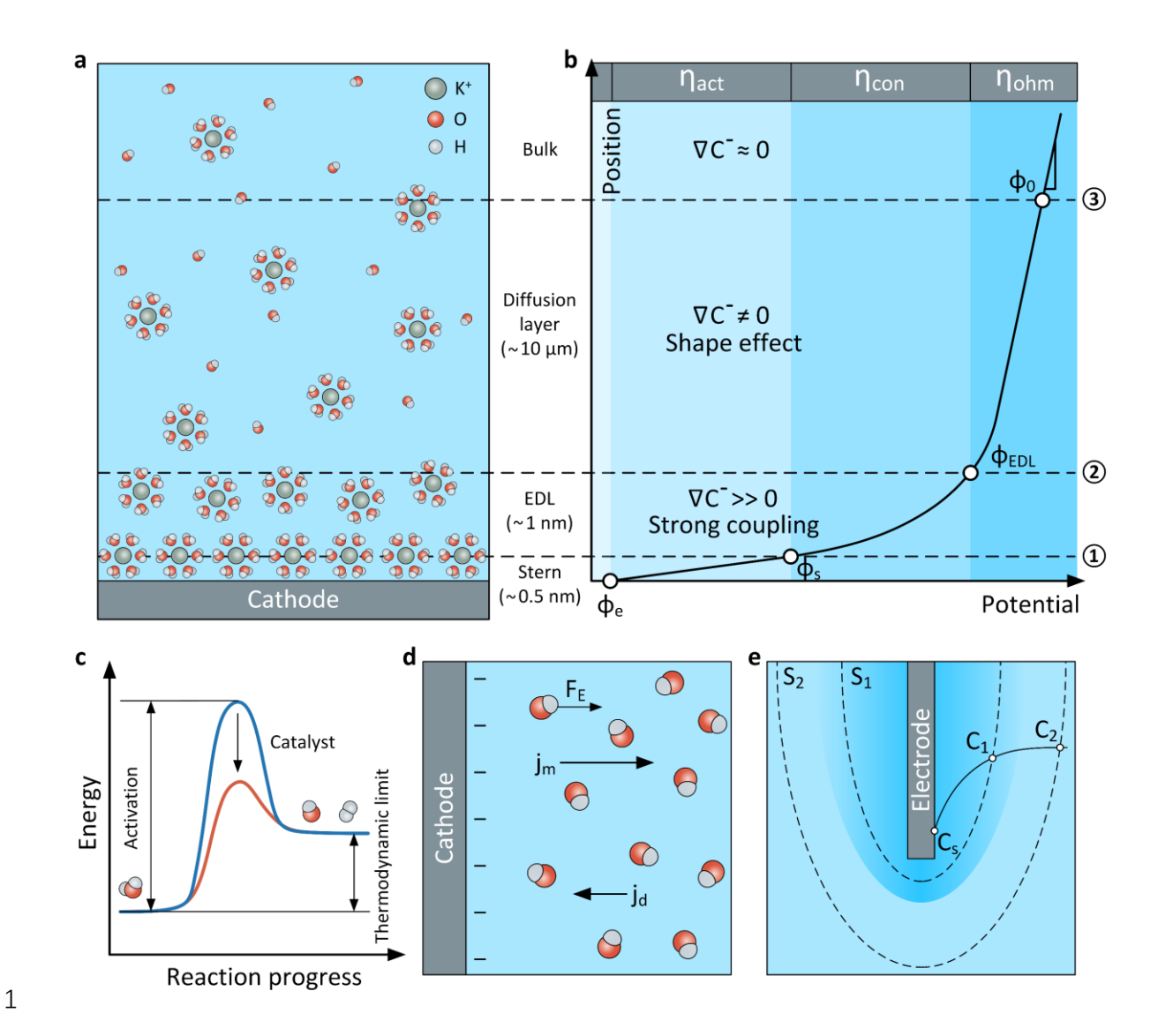


Figure 4. Species concentration profile above gas evolving electrodes and the resulting electrochemical overpotentials. (a) Physical origin and characteristic length scales of the layered structure above gas evolving electrodes. In general, four layers can be found above the electrode, including the Stern layer, potential screening layer (diffuse layer), Nernst diffusion layer, and bulk region. The Stern layer and potential screening layer together form the electrical double layer (EDL). Similar to the thermal diffusion layer in heat transfer, the Nernst diffusion layer is its analogous structure in mass transfer due to the shape effect of electrode. Thickness of the Nernst diffusion layer is scaled with the size of electrode. (b) Potential distribution across the electrolyte due to the layered structure. Potential difference between the electrode surface and outer Helmholtz plane (OHP) corresponds to the activation overpotential. Potential difference across the EDL dictates the concentration overpotential. Potential difference

- 1 required for ion migration across the Nernst diffusion layer and the bulk region contributes to
- 2 the ohmic overpotential. (c) Schematic reaction coordinate diagram of water electrolysis. The
- 3 activation energy barrier can be reduced by applying high-performance catalysts, which is
- 4 reflected in the decrease in Tafel slope. (d) Schematic of solvated ion transport above the
- 5 electrode. Diffusion and migration are two governing transport mechanisms of solvated ions.
- 6 For cathode reaction in alkaline water electrolysis, the migration flux of OH is opposite to the
- 7 diffusion flux. A large migration flux is required to overcome the undesirable diffusion flux
- and ensure the net OH-flux away from the cathode. (e) Schematic of the shape effect in mass
- 9 transfer and the resulting Nernst diffusion layer.
- 10 To further elucidate the layered structure of species concentration profile, we explain the
- fundamental mass transfer associated with alkaline water electrolysis. Mass transfer of both
- 12 solvated ions and dissolved gases during the electrochemical process can be generally
- described by the Nernst-Planck equation, ^{39,40,42,127}

$$\boldsymbol{j}_{n} = \boldsymbol{j}_{d,n} + \boldsymbol{j}_{m,n} + \boldsymbol{j}_{c,n} = -D_{n} \nabla C_{n} - \frac{z_{n} F}{R_{g} T} D_{n} C_{n} \nabla \phi + C_{n} \boldsymbol{v}$$
(13)

- where j_n , D_n , C_n , and z_n are the molar flux, mass diffusivity, molar concentration, and number
- of charges of species n, respectively. Note that for dissolved gases, $z_n = 0$. ϕ is the potential
- field and v is the flow velocity field. The total molar flux j_n is a summation of the diffusion flux
- 17 $j_{d,n}$, migration flux $j_{m,n}$, and convection flux $j_{c,n}$. Species transport is governed by the
- 18 conservation of mass,

$$\frac{\partial \mathcal{C}_n}{\partial t} + \nabla \cdot \boldsymbol{j}_n = 0 \tag{14}$$

- where t is the time. Solving the species concentration profile from eq. 14 requires the potential
- 20 distribution ϕ as the input, which is described by the Poisson–Boltzmann equation, ^{39,40,42,127}

$$\nabla \cdot (\epsilon_0 \epsilon_r \nabla \phi) = -F \sum z_n C_n \tag{15}$$

- where ϵ_0 is the vacuum permittivity and ϵ_r is the relative permittivity of electrolyte. Note that
- eqs. 13 and 15 are fully coupled because the ion migration is driven by the potential gradient
- 23 $\nabla \phi$ (eq. 13) while the potential distribution is determined by the ion concentration profile C_n

(eq. 15). Except for the Stern layer, eqs. 13 to 15 are generally applied to the region from the OHP to the bulk electrolyte. Hydrogen evolution occurs on the Stern layer, which is dictated by the electrochemical kinetics described by the Butler–Volmer equation (eq. 10) or the Tafel equation (eq. 11). Therefore, the activation overpotential η_{act} is given by the potential difference between the cathode (ϕ_e) and the OHP (ϕ_s) (Figure 4b). The Gouy–Chapman-Stern model considers a linear potential profile from the cathode to the OHP, which results in the following relationship on the OHP (plane 1) in Figure 4a and 4b), $^{128-132}$

where n is the surface normal vector of the cathode. Therefore, incorporating the

8

$$\eta_{\text{act}} = \eta_0 \log_{10} \frac{i}{i_0} = \phi_{\text{s}} - \phi_{\text{e}} = -\lambda_{\text{s}} \boldsymbol{n} \cdot \nabla \phi|_{OHP}$$
 (16)

9 electrochemical kinetics of the Stern layer (eq. 16) into Nernst-Planck-Poisson-Boltzmann set of equations (eqs. 13 - 15), the electrochemical process in the entire region above the cathode 10 11 can be fully described (Figure 4a). For example, by varying the Tafel slope η_0 and exchange current density i_0 , the impact of catalysts on the total overpotential can be well quantified by 12 13 the above theoretical framework (Figure 4c). By solving eqs. 13-16, species concentration profile (solvated ions and dissolved gases) and 14 potential distribution across the electrolyte can be well resolved. Within the EDL, transport of 15 solvated ions (K⁺ and OH⁻) is featured by a strong coupling of diffusion and migration (Figure 16 17 4b). Taking the solvated anion (OH⁻) as an example, its concentration (C⁻) increases rapidly from nearly zero on the OHP (plane (1) in Figure 4b) to the bulk value on the boundary of EDL 18 (plane (2) in Figure 4b), which is associated with a rapid build-up of potential across the EDL 19 (Figure 4b). The large potential gradient ($\nabla \phi \gg 0$) within the EDL can be understood from a 20 21 perspective of OH⁻ transport (Figure 4d). The continuous production of OH⁻ from the cathode reaction creates a net flux of OH^- outward the cathode (j > 0). However, the concentration 22 gradient of OH⁻ described above ($\nabla C^- \gg 0$) is undesirable for OH⁻ transport, because it creates 23 a diffusion flux of $OH^{-}(j_d)$ toward the cathode $(j_d < 0)$. According to eq. 13, to ensure the net 24 25 flux j > 0, the migration flux of OH⁻ (j_m) should be large enough $(j_m > 0)$, which requires a large potential gradient to drive OH away from the cathode (Figure 4d). Therefore, the additional 26 potential required to overcome the undesirable OH⁻ concentration profile ($\nabla C^- \gg 0$) across the 27

- EDL is one of a major sources of the concentration overpotential η_{con} (Figure 4b), which can
- 2 be expressed as,

$$\eta_{\rm con} \approx \phi_{\rm EDL} - \phi_{\rm s}$$
(17)

- 3 where ϕ_{EDL} is the potential on the boundary of EDL (plane 2) in Figure 4b).
- 4 The solution to eqs. 13-16 can also capture the second layered structure over the EDL, typically
- 5 known as the Nernst diffusion layer, which is a boundary layer with ion concentration gradient
- 6 covering the electrode (Figure 4a and 4e). Although both the potential screening layer in the
- 7 EDL and the Nernst diffusion layer are featured by ion concentration gradients, we note that
- 8 the corresponding governing mechanisms are different. Instead of the strong coupling of
- 9 diffusion and migration in EDL, the Nernst diffusion layer occurs when the diffusion of
- solvated ions becomes the dominated mode of mass transfer compared to migration, i.e., $|j_d| \gg$
- $|j_s|$. In fact, the Nernst diffusion layer was originally derived from eq. 13 by neglecting the ion
- migration and convection terms, *i.e.*, the diffusion assumption, ^{39,133,134}

$$\boldsymbol{j}_n \approx \boldsymbol{j}_{d,n} = -D_n \nabla C_n. \tag{18}$$

- 13 Substituting eq. 18 into eq. 14 and considering the steady-state condition, we obtain the
- 14 classical Fick's second law to describe the ion concentration profile in the Nernst diffusion
- 15 layer, ^{39,133,134}

$$\nabla^2 C_n = 0. ag{19}$$

- Therefore, the Nernst diffusion layer is a natural result due to the structure of eq. 19, which can
- be understood through a "shape effect" in a two/three-dimension (2D/3D) domain. The term
- 18 "shape effect" is a more familiar concept in heat transfer when dealing with the 2D/3D heat
- conduction. 135 It is not commonly seen in electrochemistry literature despite the same physical
- 20 origin. To better illustrate the physical origin of the Nernst diffusion layer, we provide the
- 21 following additional elaboration. Figure 4e shows the schematic of the shape effect and the
- resulting ion concentration profile surrounding the electrode. We consider the ion diffusion
- 23 across two control surfaces S₁ and S₂ surrounding the electrode. Note that to make eqs. 18 and

- 1 19 valid, both S₁ and S₂ are outside the EDL (Figures 4b and 4e). Conservation of mass requires
- 2 the total ion flow rate J_n through each control surface a constant, which is expressed as,

$$J_n = \int -D_n \nabla C_n \cdot d\mathbf{S} \Big|_{S_1} = \int -D_n \nabla C_n \cdot d\mathbf{S} \Big|_{S_2}.$$
 (20)

- For a 2D/3D domain, the area of S_2 is larger than the area of S_1 (Figure 4e). As a result, the
- 4 magnitude of ion concentration gradient $|\nabla C_n|$ on S_1 should be larger than that on S_2 , leading to
- 5 the concentration boundary layer structure, *i.e.*, the Nernst diffusion layer around the electrode.
- 6 Note that the Nernst diffusion layer cannot exist in the 1D steady-state condition, because the
- 7 ion concentration gradient ∇C_n should always be a constant to conserve mass (eqs. 18-20).
- 8 The solution to eq. 19 typically has a form of,

10

11

12

13

14

15

16

$$J_n = S_f D_n (C_{n,2} - C_{n,b})$$
 (21)

where $C_{n,2}$ is the ion concentration on the boundary of EDL (plane ② in Figure 4b) and $C_{n,b}$ is the bulk concentration. Note that $C_{n,2}$ is typically regarded as the ion concentration on the electrode surface (C_s , on plane ① in Figure 4b). ^{39,44,45} However, it is not an accurate understanding because eq. 19 is not valid in the EDL. S_f is the shape factor of the system (unit in m), which is a function of the geometry of electrode and electrolytic cell. Taking a disk-shape electrode as an example, its shape factor is equal to two times of the disk diameter d_e . ¹³⁵ Based on eq. 21, we can introduce the concept of effective diffusion boundary layer thickness δ_d , ¹³⁵

$$J_n = A_e D_n \frac{\left(C_{n,2} - C_{n,b}\right)}{\delta_d} \tag{22}$$

where A_e is the surface area of the electrode. Comparing eq. 22 with eq. 21, we can obtain,

$$\delta_{\rm d} = \frac{A_{\rm e}}{S_{\rm f}} \tag{23}$$

- which indicates the effective thickness of Nernst diffusion layer is scaled with the characteristic length scale of the electrode. Taking the disk-shape electrode as an example again, we have δ_d
- $=\pi d_e/8$. Therefore, for typically electrodes with the length scale larger than $\sim 10 \,\mu\text{m}$, the Nernst
- 21 diffusion layer should be much thicker than the EDL.

- 1 The original concept of Nernst diffusion layer described in eqs. 18-20 is irrelevant with the
- 2 electric field and hence similar boundary layer structures can be generally seen in any diffusion
- 3 systems (e.g., thermal diffusion process). Despite the much smaller potential gradient across
- 4 the Nernst diffusion layer as compared with that in the EDL, we note that the presence of
- 5 electric field might alter the structure of Nernst diffusion layer, especially in the high
- 6 potential/current density conditions. Therefore, we would suggest a thorough investigation of
- 7 the validity of diffusion assumption (eq. 18) in describing the electrochemical process by
- 8 comparing their results with the solutions of eqs. 13 16.
- 9 The region above the Nernst diffusion layer is the bulk electrolyte solution where the ion
- 10 concentration gradient approaches zero (plane (3) in Figure 4b). Ion transport in this region
- 11 mainly relies on migration,

$$\boldsymbol{j}_{n} \approx \boldsymbol{j}_{\mathrm{m},n} = \frac{z_{n}F}{R_{g}T} D_{n}C_{n,b}\nabla\phi$$
 (24)

- which has a form of the Ohm's law. According to eq. 24, we can define the molar conductivity
- of ions in the electrolyte solution (χ_n , unit in S·m²/mol), ¹³⁶

$$\chi_n = z_n \mu_n F = \frac{z_n^2 F^2 D_n}{R_{\sigma} T} \tag{25}$$

- where μ_n is the ion mobility. Therefore, in addition to the extern circuit, ion migration in the
- bulk electrolyte can be one of the major sources of ohmic overpotential η_{ohm} (Figure 4b).
- Here we provide a brief summary of the key features and the resulting overpotentials in each
- 17 layer of the electrolyte solution,
- 18 (1) Stern layer: the Stern layer is a compact monolayer structure consisting of solvated ions
- which are adsorbed on the electrode via the Coulomb force. The thickness of Stern layer is
- determined by the size of the solvated ion. Electrochemical reactions occur on the Stern layer.
- 21 The potential difference between the OHP and electrode surface $(\phi_s \phi_e)$ represents the
- 22 activation overpotential η_{act} (eq. 16), which is dictated by the electrochemical kinetics
- described by the Butler–Volmer equation (eq. 10) or the Tafel equation (eq. 11).

(2) EDL: the double layer structure comprises the Stern layer and potential screening layer 1 2 (also known as the diffuse layer), which can be described by the Gouy-Chapman-Stern model. 3 The thickness of EDL is typically a few nanometers, scaled with the Debye length λ_D . The EDL is featured by a strong coupling of ion diffusion and migration, which induces significant 4 variations of potential and ion concentration within a few nanometers (i.e., $|\nabla C_n| \gg 0$ and $|\nabla \phi|$ 5 >> 0). Properties of the EDL can be captured by the Nernst-Planck-Poisson-Boltzmann model, 6 7 which includes a set of fully coupled equations describing ion transport (Nernst-Planck 8 equation, eq. 13), potential distribution (Poisson-Boltzmann equation, eq. 15), and 9 electrochemical kinetics (Tafel equation, eq. 16). For the cathode reaction in alkaline solution (eq. 4), diffusion of solvated anion (OH) is opposite to the migration (eq. 13). Therefore, 10 additional potential is required to overcome the undesirable diffusion flux, inducing the 11 12 concentration overpotential η_{con} . Similar situation occurs on the anode reaction in acidic solution (eq. 5). 13 14 (3) Nernst diffusion layer: the Nernst diffusion layer refers to a boundary layer structure with 15 a variation of ion concentration from the boundary of EDL to the bulk electrolyte solution. The thickness of Nernst diffusion layer δ_d is typically larger than tens of micrometers, scaled with 16 the characteristic length scale of the electrode (eq. 23). We note that the original derivation of 17 Nernst diffusion layer is based on a pure diffusion argument (eqs. 18 and 19) by neglecting the 18 19 contribution of ion migration above the EDL. In addition, the Nernst diffusion layer has the 20 same physical origin as the thermal boundary layer in heat conduction, which can only exist in 2D/3D conditions. Therefore, the key results under the diffusion approximation (eq. 18) cannot 21 22 be applied to the EDL, where migration plays a dominant role in ion transport (eq. 13). 23 (4) Bulk region: the bulk region is the position where the ion concentration returns to its bulk 24 value. Since the gradient of ion concentration is approximately zero, ion transport in the bulk

value. Since the gradient of ion concentration is approximately zero, ion transport in the bulk region mainly relies on migration, which induces the ohmic overpotential η_{ohm} (eqs. 24 and 25). Although the above four regions can be completely captured by solving the Nernst-Planck-Poisson-Boltzmann model in the full field of the electrolyte solution, they are more commonly modeled separately in literature by making a few additional assumptions for simplification. In

25

26

27

- this review, we would like to comment on a few inconsistencies of conventional approximate
- 2 approaches and highlight the necessity of rigorous full-field solutions throughout the entire
- 3 electrolyte region for the accurate modeling of overpotentials.
- 4 The conventional approximate approaches decouple the ion transport (eq. 13) and electric field
- 5 (eq. 15) by considering the ion diffusion above the plane (2) in Figure 4b (eq. 19) only and
- 6 estimating the potential difference across the EDL with analytical expressions. 46,47,137,138 In
- 7 particular, two analytical expressions are commonly used to quantify the concentration
- 8 overpotential η_{con} . The first analytical expression describes how the concentration of oxidizing
- 9 and reducing agents can affect the electrochemical kinetics on the Stern layer (plane 1) in
- Figure 4b), which is known as the extended Butler-Volmer equation, ^{39,44}

$$i = i_0 \left(\frac{C_{s,0}}{C_0^*} \exp\left(\frac{\alpha_a z F \eta'_{act}}{R_g T} \right) - \frac{C_{s,R}}{C_R^*} \exp\left(-\frac{\alpha_c z F \eta'_{act}}{R_g T} \right) \right)$$
(26)

- where $C_{s,O}$ and C_0^* are the oxidizing agent concentrations on the Stern layer and in the
- equilibrium condition, respectively. $C_{s,R}$ and C_R^* are the reducing agent concentrations on the
- 13 Stern layer and in the equilibrium condition, respectively. η'_{act} is the total activation potential
- considering the concentration effect. For the cathode reaction in alkaline solution (eq. 4), the
- oxidizing agent is water, and the reducing agents are H₂ and OH⁻. By neglecting the reverse
- reaction component, eq. 26 can be re-expressed as, ^{39,44}

$$\eta_{\text{act}}' = \frac{R_{\text{g}}T}{\alpha_{\text{a}}zF} \ln \frac{i}{i_0} + \frac{R_{\text{g}}T}{\alpha_{\text{a}}zF} \ln \frac{C_0^*}{C_{\text{S},0}} = \eta_{\text{act,BV}} + \eta_{\text{con,BV}}$$
 (27)

- where the first Tafel-type term $\eta_{act,BV}$ is the original activation overpotential and the second
- term $\eta_{\text{con,BV}}$ represents the additional activation overpotential due to the concentration effect.
- Therefore, according to the physical origin of $\eta_{\text{con,BV}}$, it can be treated as a part of either the
- 20 activation overpotential or the concentration overpotential.
- 21 Although eq. 26 itself is rigorous, implementing eq. 26 into the conventional approximate
- 22 approaches can lead to a few inconsistencies. First, to calculate the total activation
- overpotential η'_{act} , concentrations of oxidizing and reducing agents on the Stern layer and in
- 24 the equilibrium (i.e., $C_{s,O}$, C_0^* , $C_{s,R}$, and C_R^*) should be used as the input. The bulk

concentration $(C_{n,b})$ is typically used as the equilibrium concentrations (i.e., C_0^* and C_R^*). However, the concentrations on the Stern layer (i.e., $C_{s,O}$ and $C_{s,R}$) cannot be obtained from the conventional approximate approaches, because only the ion transport above the EDL is solved. To address this challenge, the conventional approximate approaches prescribe $C_{s,O}$ and $C_{s,R}$ as the concentrations on the boundary of the EDL (plane 2) in Figure 4b), instead of their correct values on the Stern layer (plane 1) in Figure 4b). 44,45,137,138 Second, the physical meaning of $C_{s,O}$ and C_0^* in eq. 27 is frequently misunderstood. Taking the cathode reaction in alkaline solution as an example (eq. 4), $C_{s,O}$ and C_{0}^{*} represent the concentration of water and the value of $C_0^*/C_{s,0}$ should be close to one since water is the solvent. However, in some modeling works based on the conventional approximate approaches, OH or H₂ concentration was used to calculate $\eta_{\text{con,BV}}$. These two inconsistencies could make the calculated $\eta_{\text{con,BV}}$ significantly deviate from its intrinsic value.

The second analytical expression describes the concentration overpotential across the EDL, which is derived from the Nernst equation.^{39,43–47} Still considering the cathode reaction in alkaline solution, the Nernst-type concentration overpotential $\eta_{\text{con,Nernst}}$ is given by,³⁹

$$\eta_{\text{con,Nernst}} = \frac{R_{\text{g}}T}{F} \ln \frac{C_{\text{EDL}}}{C_{\text{s}}^{-}}$$
(28)

where $C_{\rm EDL}^-$ and $C_{\rm s}^-$ are the OH⁻ concentration on the boundary of EDL (plane ② in Figure 4b) and Stern layer (plane ① in Figure 4b), respectively. We discuss a few critical concerns when applying eq. 28 to estimate the concentration overpotential. First, the Nernst equation is only valid when the electrochemical equilibrium reaches, *i.e.*, the current density is equal to zero.^{39,43,138} Since the majority of electrochemical gas evolution reactions consider a non-equilibrium state with non-zero current density, the accuracy of eq. 28 in estimating the concentration overpotential, especially for the high-current density conditions, should be carefully examined. In addition, since ion transport across the EDL (below the plane ② in Figure 4b) is not captured by the simple diffusion equation, $C_{\rm EDL}^-$ and $C_{\rm s}^-$ cannot be solved from eq. 19 in the conventional approximate approaches. Instead, OH⁻ concentrations in the bulk electrolyte solution (above the plane ③ in Figure 4b) and the Nernst diffusion layer (above the plane ② in Figure 4b) were commonly substituted into eq. 28 to calculate the

concentration overpotential. 44,45 We therefore raise a significant concern about the accuracy of using the concentration profile across the Nernst diffusion layer (above the plane ② in Figure 4b) to reflect the concentration overpotential across the EDL (below the plane ② in Figure 4b). Considering the above fundamental inconsistencies induced by the conventional approximate approaches (eq. 19, 27, and 28), we suggest a comprehensive assessment of its accuracy under various operating conditions. More importantly, we would highly recommend directly implementing the fully coupled Nernst-Planck-Poisson-Boltzmann model (eqs. 13 – 16) to quantify the overpotential in electrochemical gas evolution reactions. In addition to water electrolysis discussed above, we would note that the multiscale process for species transport commonly occurs in various flow based electrochemical energy conversion devices, such as fuel cells and flow batteries, which were discussed by Modestino *et al.* in detail. 139

3. BUBBLE DYNAMICS: MULTISCALE UNDERSTANDING AND INSIGHTS

FROM PHASE CHANGE HEAT TRANSFER

It has been widely known that bubbles play a significant role in the performance of electrochemical gas evolution reactions. However, a fully quantitative understanding to describe the impact of bubble dynamics on the change of overpotential still remains elusive due to the coupling of multiple physical phenomena (electric field, chemical kinetics, ion transport, gas transport, and liquid electrolyte flow) across multiple length scales (from \sim nm to \sim cm). In this Section, we provide a multiscale perspective of bubble dynamics in electrochemical gas evolution reactions by leveraging insights gained from phase change heat transfer. We aim to highlight a convergent understanding of bubbles in phase change heat transfer and electrochemical gas evolution reactions and review existing and potential opportunities for knowledge translation between two research fields. More importantly, we would like to discuss the knowledge gap between bubble dynamics and electrochemical performance, which requires innovations of both high-precision metrology tools and high-fidelity simulation approaches.

3.1. Bubble Nucleation

3.1.1. Nucleation from a Single Site

1

2

3

4

5

6

7

8

9

10

11

12

13

14

15

16

17

18

19

Nucleation is the initial step of bubble formation, featured by a continuous phase separation from a gas nucleus. In general, nucleation can be classified as homogeneous nucleation and heterogeneous nucleation, which occur in the bulk liquid and on the surface, respectively. In typical boiling and electrochemical gas evolution systems, heterogeneous nucleation is the dominant mode due to the lower energy barrier with the presence of gas-solid interface. Classical nucleation theory describes the thermodynamics of bubble nucleation, which has been systematically summarized in some textbooks. 135,140,141 In this Section, we would like to provide an overview of bubble nucleation from a single site. In general, heterogeneous nucleation from a single site involves the gas trapping (Figure 5a) and the formation of a stable bubble (Figure 5b). Surface inhomogeneity due to the variations of surface chemistry and roughness can serve as a site to trap gas during liquid filling and rewetting. In particular, surface cavity is one of the most representative idealized models to explain the gas trapping process (Figure 5a). $^{64,135,142-144}$ When the cavity angle 2β is smaller than the advancing contact angle of liquid front θ_a , gas is trapped into the cavity during liquid filling and rewetting, and then this gas cavity becomes a preferential site (i.e., a gas nucleus) for bubble nucleation (Figure 5a). However, bubble nucleation cannot occur in a saturation condition because both liquid and gas are in thermodynamic equilibrium with each other. In addition to the gas cavity, a nonequilibrium driving force due to supersaturation is required. 135,142,143,145-149

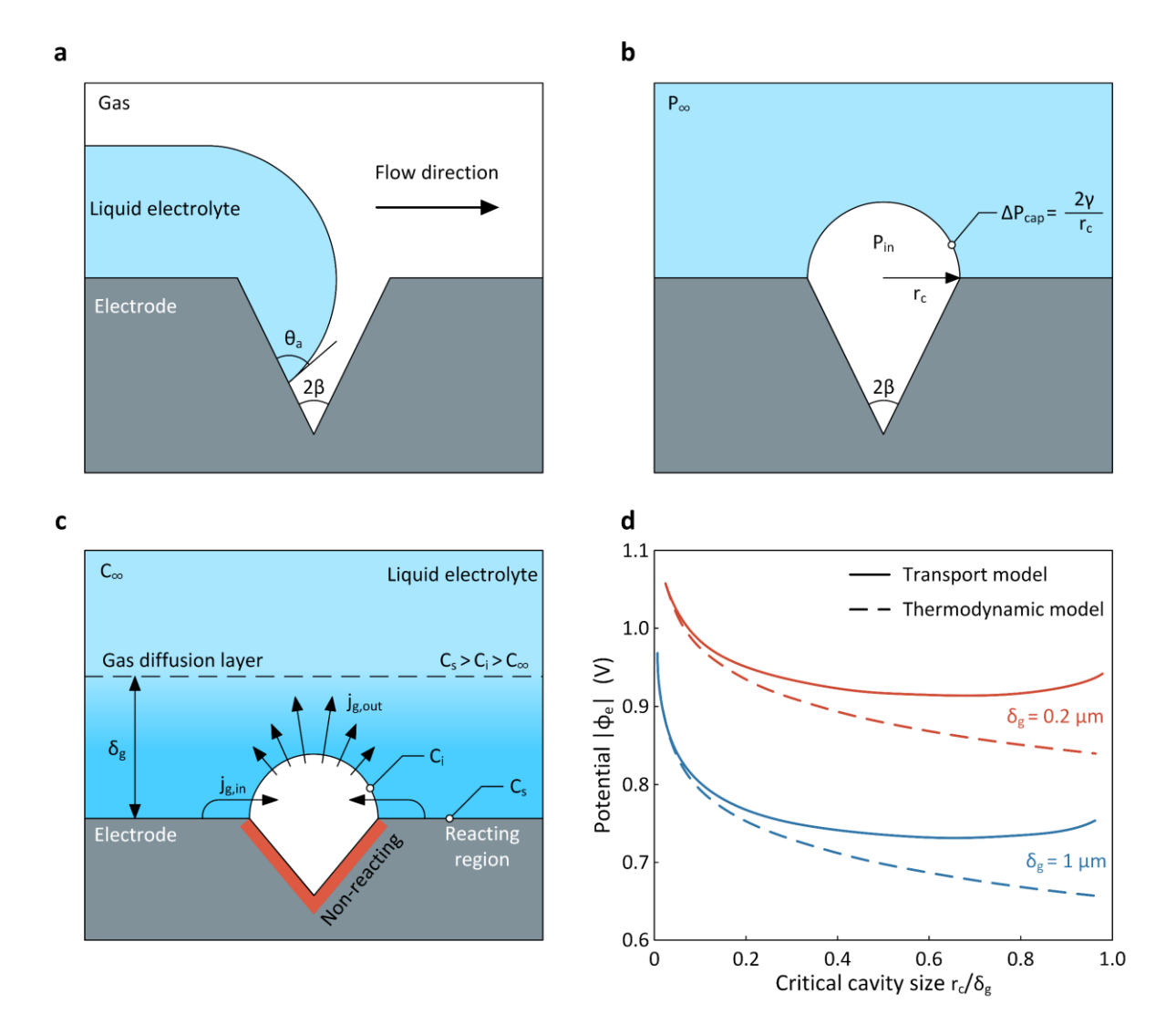


Figure 5. Bubble nucleation from a single gas cavity. (a) Gas trapped into a cavity due to the propagation of liquid front along the surface. The gas cavity can lower the energy barrier and hence serves as a preferential site for heterogeneous nucleation. (b) Thermodynamics-based description of bubble nucleation. To trigger bubble nucleation, pressure inside the gas cavity due to supersaturation should overcome the capillary pressure of liquid-gas interface and the external liquid pressure. (c) Transport-based description of bubble nucleation. Under the transport perspective, bubble nucleation occurs when the inward gas flow across the liquid-gas interface is larger than the outward gas flow, which is dictated by the combined effect of gas cavity and gas diffusion layer. (d) Magnitude of potential applied to cathode as a function of critical cavity size for bubble nucleation predicted by thermodynamics-based and transport-based models. Transport-based model deviates from thermodynamics-based model when the gas cavity size becomes comparable to the gas diffusion layer thickness. The thicker gas

- diffusion layer is, the lower potential is required to activate the gas cavity. Data is reproduced
- 2 from Lu et al.'s numerical simulations with permission from Ref. 152. Copyright 2022
- 3 American Chemical Society.
- 4 Figure 5b shows the pressure balance analysis of a gas bubble pinned by the cavity. To initiate
- bubble nucleation, gas pressure inside the bubble $P_{\rm in}$ should be equal or larger than the
- summation of external liquid pressure P_{∞} and capillary pressure ΔP_{cap} created by the liquid-gas
- 7 interface. Otherwise, the gas bubble is not stable and will collapse back into the cavity. We
- 8 consider the critical condition when ΔP_{cap} reaches its maximum, i.e., the contact angle $\theta = 90^{\circ}$,
- 9 the thermodynamic criterion for bubble nucleation can be expressed as, 135,142–144,147–149

$$P_{\rm in} = P_{\infty} + \Delta P_{\rm cap} = P_{\infty} + \frac{2\gamma}{r_{\rm c}}$$
 (29)

- where ΔP_{cap} is given by the Young-Laplace equation and r_{c} is the critical cavity opening radius.
- 11 The high gas pressure inside the bubble originates from supersaturation. For the boiling process,
- supersaturation is induced by the wall superheat ΔT , ^{135,142,143}

$$P_{\rm in} = P_{\rm sat}(T_{\infty} + \Delta T) \approx P_{\infty} + \frac{dP_{\rm sat}}{dT} \Big|_{T_{\infty}} \Delta T$$
 (30)

- where P_{sat} is the saturation pressure as a function of saturation temperature (i.e., boiling point).
- 14 T_{∞} represents the saturation temperature under P_{∞} . Substituting eq. 30 into eq. 29, the required
- wall superheat to initiate bubble nucleation at the gas cavity is given by, ^{64,135,143}

$$\Delta T = \frac{2\gamma}{r_c \frac{dP_{\text{sat}}}{dT}\Big|_{T_{\infty}}}.$$
(31)

- 16 For the electrochemical gas evolution process, on the other hand, the high pressure inside
- bubble originates from the supersaturation of gas concentration, which can be expressed by the
- 18 Henry's law, 150

$$P_{\rm in} = \frac{C_{\rm s}}{K_{\rm H}} \tag{32}$$

- where C_s is dissolved gas concentration at the electrode-electrolyte interface. K_H is the Henry's
- solubility constant (unit in mol/m³/Pa or mM/atm), which is a function of temperature and types

- of liquid and gas.¹⁵⁰ Taking hydrogen in water at room temperature as an example, its Henry's
- 2 solubility constant is equal to 0.8 mM/atm. 151 Substituting eq. 32 into eq. 29, we can derive the
- 3 required gas concentration to trigger bubble nucleation,

$$C_{\rm s} = C_{\infty} \left(1 + \frac{2\gamma}{r_{\rm c} P_{\infty}} \right) \tag{33}$$

- 4 where $C_{\infty} = K_{\rm H} P_{\infty}$ represents the saturation gas concentration at the far field. According to eqs.
- 5 31 and 33, the smaller cavity radius creates the larger capillary pressure, which requires the
- 6 higher non-equilibrium driving forces (ΔT and C_s) for bubble nucleation. This basic principle
- 7 also explains our physical intuition that it is hard to observe bubble nucleation on very smooth
- 8 surfaces. In addition, rearranging eqs. 31 and 33, we can also calculate the minimum radius of
- 9 gas cavities that can be activated with a given wall superheat ΔT and gas concentration
- 10 $C_{\rm s}$. 135,143,148,149
- 11 Considering a highly smooth electrode with ~ 10 nm roughness, eq. 33 indicates that the
- supersaturation of gas concentration can reach a few hundred to initiate bubble nucleation.
- 13 Meanwhile, there have been a few experimental approaches to quantify the supersaturation
- level during electrochemical gas evolution. 145-149 These approaches directly measured the
- 15 current density during either steady-state or transient operation and then estimated gas
- concentration through analytical expressions with the measured current density as the input. In
- particular, Luo and White developed a nanoelectrode-based approach to enable highly accurate
- and reproducible measurements of steady-state supersaturation levels, which will be discussed
- in Section 3.1.3. 147–149 These measurements typically confirmed that the supersaturation of gas
- 20 concentration during hydrogen evolution is of a few hundred, showing a good consistency with
- 21 the theoretical estimation based on thermodynamics (eq. 33).
- 22 The above thermodynamics-based description (eqs. 29 33) has become one of the most
- 23 widely applied theories to explain nucleation in both phase change heat transfer and
- 24 electrochemical gas evolution reactions. However, in addition to satisfying the pressure balance
- 25 (eq. 29), bubble growth from the cavity also relies on gas transport, which is not involved in
- 26 the thermodynamics-based description (eqs. 29 33). Recently, Lu *et al.* considered the mass
- 27 transfer across the liquid-gas interface and developed a transport-based model for bubble

nucleation in hydrogen evolution. ¹⁵² Figure 5c shows the schematic that describes the mass transfer around a gas cavity during the cathode reaction in alkaline solution. Electrochemical reaction occurs at the electrode-electrolyte interface, which induces high concentration of the dissolved hydrogen C_s on the electrode. C_s is higher than the concentration of the dissolved hydrogen close to the liquid-gas interface C_i , resulting in a dissolved hydrogen flux inward the gas cavity near the three-phase contact line ($j_{g,in}$ in Figure 5c), which promotes bubble nucleation. However, since C_i can be much higher than C_{∞} , on the top surface of the gas cavity, there is also an outward flux of the dissolved hydrogen ($j_{g,out}$ in Figure 5c), which suppresses bubble nucleation. The transport resistance of $j_{g,out}$ is dictated by the gas diffusion layer thickness δ_g , which is a function of electrode geometry and flow field. According to the above gas transport mechanisms, Lu *et al.* provided the transport criterion of bubble nucleation, ¹⁵²

$$J_{\rm g} = \int \boldsymbol{j}_{\rm g} \cdot d\boldsymbol{S} \ge 0 \tag{34}$$

where the integration is along the liquid-gas interface of the gas cavity and the surface normal vector (S) points toward the gas side of the interface. j_g is the gas flux across the liquid-gas interface and J_g is the net gas flow that enters into the gas cavity. $J_g > 0$ indicates gas flowing into the cavity, which leads to bubble nucleation.

Figure 5d shows the required potential to activate a gas cavity predicted by the thermodynamics-based (dashed lines) and transport-based (solid lines) models, where the gas diffusion layer thickness δ_g plays a fundamental role in both models. In general, it is easier to activate a gas cavity with larger δ_g , because C_s increases with δ_g . Specifically, the thermodynamics-based model shows that the larger gas cavity size is, the lower overpotential is required to trigger bubble nucleation, due to the lower capillary pressure across the liquidgas interface (eq. 29). The transport-based model converges with the thermodynamics-based model when the gas cavity is small. However, when r_c becomes comparable with δ_g , the transport-based model starts to deviate from the thermodynamics-based model, leading to the non-monotonic dependence of applied potential with r_c/δ_g (Figure 5d). This is because when the top of the liquid-gas interface approaches the boundary of gas diffusion layer, i.e., r_c/δ_g close to one, the outward flux of the dissolved gas can significantly increase, resulting in the

- increase in overpotential to initiate bubble nucleation. In addition, the transport-based model
- 2 also indicates there is an optimal size ratio of gas cavity to gas diffusion layer, i.e., $r_c/\delta_g \approx 0.7$,
- 3 that corresponds to the minimum overpotential for bubble nucleation (Figure 5d). Practically,
- 4 the optimal size ratio can be achieved not only by engineering the cavity size but also by
- 5 manipulating the gas diffusion layer through electrolyte flow and electrode design.
- 6 In fact, the transport-based model developed by Lu *et al.* provided an example about the huge
- 7 opportunity space of knowledge translation from phase change heat transfer to electrochemical
- 8 gas evolution reactions. 152 This is because if the supersaturation of gas concentration and gas
- 9 diffusion layer are replaced by the wall superheat and thermal diffusion layer, respectively, the
- above transport-based physical picture of bubble nucleation becomes equivalent to the Hsu's
- 11 nucleation model, which has been carefully validated and widely applied in the boiling process
- since 1962. 142 Despite the enhanced theoretical understanding, for electrochemical gas
- evolution reactions, there still lacks experimental evidence to support the physical insights
- given by the transport-based model. To quantify the impact of gas cavity on bubble nucleation,
- it is possible to combine the surface engineering of gas cavity with the advanced metrology
- tools to probe individual nucleation sites, which will be discussed in Section 3.1.3.

18

19

20

21

22

23

24

25

26

27

28

3.1.2. Distribution of Nucleation Sites: Statistical Description and Impacts on Bubble Dynamics

Compared with the understanding of single nucleation sites, behavior of multiple nucleation sites is at least of equal importance while remaining much less well understood. In general, the behavior of multiple nucleation sites can be quantified by nucleation site distributions, including population distribution, spatial distribution, and temporal distribution, which describe how many, how far, and how fast of the nucleation events, respectively. Nucleation site distribution plays a fundamental role in bridging the dynamics of single bubble to the overall behaviors of the electrochemical systems, including the rates of mass (gases and ions) transfer, average current density, and the resulting total overpotential. For example, Figure 6a shows the schematic of multiple nucleation sites of gas bubbles on the electrode. The nearest neighbor distance *s* of a nucleation site is a random variable, which dictates bubble interaction

modes. Specifically, if s is large enough, i.e., much larger than the bubble diameter d, the bubble behaves like an isolated bubble (blue circles in Figure 6a) even though there can be numerous surrounding bubbles. However, if s < d, the bubble can coalesce with its neighbors (red circles in Figure 6a). Different bubble interaction modes can lead to distinct bubble coverage, bubble growth, bubble departure, and flow field, which ultimately impact the mass transfer and overpotential of electrochemical gas evolution reactions. Therefore, with the distribution of s, probability of each bubble interaction mode can be quantified, which makes it possible to predict the performance of the entire electrochemical systems.

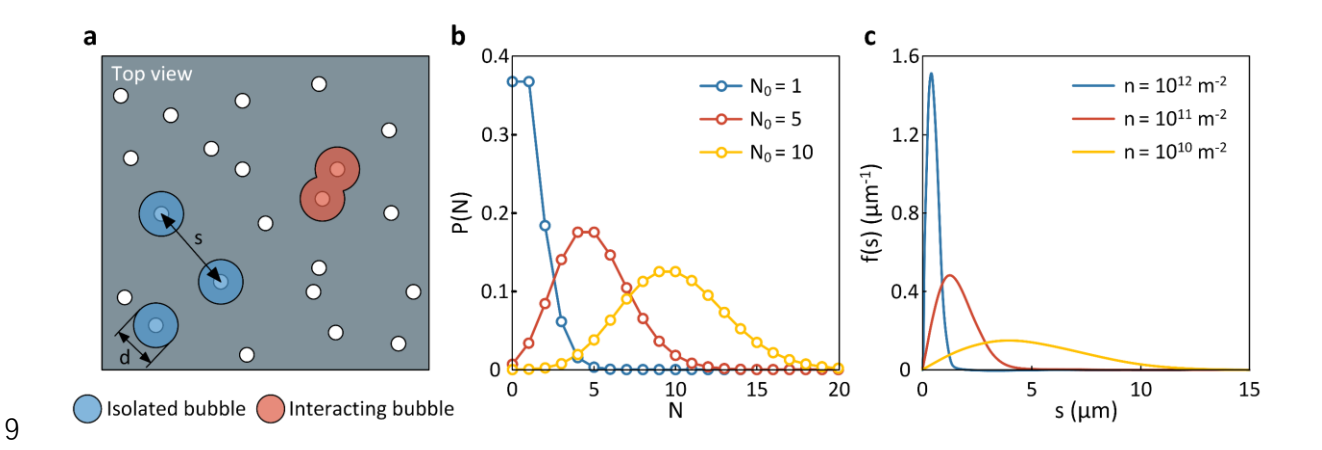


Figure 6. Nucleation site distribution. (a) Schematic of multiple nucleation sites on a surface. Distribution of nucleation sites dictates the population of isolated (blue circles) and interacting bubbles (red circles). (b) Population distribution of nucleation sites given by the Poisson distribution function. (c) Nearest neighbor distance distribution of nucleation sites given by the Rayleigh distribution function.

The statistical behaviors of nucleation sites were first recognized in the boiling process by Gaertner in 1959, where he observed the population of nucleation sites can fit the Poisson distribution function. Sultan and Judd in 1978 as well as Wang and Dhir in 1993 confirmed the Poisson distribution for nucleation site population in flow boiling and pool boiling, respectively. However, they found that the spatial distribution of nucleation sites, which is represented by the distribution of nearest neighbor distance, cannot fit the Poisson distribution. A modified Poisson distribution was then suggested by Wang and Dhir through an empirical fitting to the experimentally measured nearest neighbor distance distribution.

- 1 After these pioneering works, more in-depth understanding of nucleation site distribution has
- become highly limited until 2020. Recently, Zhang et al. provided complete theoretical proofs
- 3 for the nucleation site distributions. 157 They confirmed that the population distribution of
- 4 nucleation sites follows the Poisson distribution P(N),

17

18

19

20

21

22

23

24

25

$$P(N) = \frac{N_0^N}{N!} e^{-N_0} \tag{35}$$

where N and N_0 are the actual and expected nucleation population, respectively. N_0 is the 5 product of surface area A and intrinsic nucleation density n_0 , where n_0 is fundamentally 6 7 determined by the supersaturation condition, surface morphology, and surface wettability as described by the criteria in Section $3.1.1.^{156,158}$ Note that P(N) is a probability function 8 (unitless), which describes the probability of finding N nucleation sites on the surface of area 9 A. Figure 6b shows representative Poisson distributions with different expected nucleation 10 11 populations N_0 . The larger N_0 is, the more probable the actual population of nucleation sites on the surface deviates from its expected value. 12

Meanwhile, Zhang *et al.* rigorously derived the Rayleigh distribution for the nearest neighbor distance, addressing the discrepancies between previous experiments and empirical correlations.¹⁵⁷ The Rayleigh distribution *f*(*s*) is expressed as,

$$f(s) = \frac{s}{\sigma^2} e^{-\frac{s^2}{2\sigma^2}} \tag{36}$$

where $\sigma^2 = A/2\pi N$. Note that f(s) is a probability density function (unit in 1/m), instead of the probability function (unitless) expected by previous empirical fitting approaches. ^{153–156} Figure 6c shows representative Rayleigh distributions with different nucleation density n = N/A. The larger n is, the smaller σ^2 will be, leading to the less spread of the Rayleigh distribution. In addition to the boiling process, recent experiments using the phase-enhanced environmental scanning electron microscopy (p-ESEM) have also shown that the same nucleation site distributions govern the condensation process. ¹⁵⁷ More notably, by analyzing the bubble departure diameter during hydrogen and oxygen evolutions measured by Janssen *et al.*, ¹⁵⁹ Zhang *et al.* suggested that electrochemical gas evolution reactions could also exhibit the same nucleation site distributions, ¹⁵⁷ while more direct experimental evidence is highly required to

- develop a comprehensive understanding of nucleation site distributions in electrochemical gas
- 2 evolution reactions. In the rest of this review, we will assume that the Poisson and Rayleigh
- distributions can well represent the population and nearest neighbor distance distributions of
- 4 gas bubbles in hydrogen evolution. We will provide a few examples in Section 3.3.3 and 3.4.1
- 5 to elucidate how nucleation site distributions can connect the microscopic bubble dynamics
- 6 with the macroscopic transport properties.

12

13

14

15

16

17

18

19

20

21

22

23

- 7 The temporal distribution of nucleation sites originates from the statistical nature of nucleation
- 8 kinetics. 140,141 It can be quantified by the nucleation probability T(t), which represents the
- 9 probability of finding the bubble nucleation by time t. According to the classical nucleation
- theory, T(t) is typically expressed as the following form,

$$T(t) = 1 - e^{-\Gamma At} \tag{37}$$

where Γ is the heterogeneous nucleation rate (unit in $1/(m^2s)$). Γ is determined by the kinetic theory, which exhibits a form of the Arrhenius law. Analytical expressions of Γ are also available in literature. Hotelength 140,141 Note that in some studies of bubble nucleation in electrochemical gas evolution reactions, $\Gamma^* = \Gamma A$ was more commonly regarded as the bubble nucleation rate (unit in 1/s). Hotelength 2. Compared with the tremendous theoretical analysis of nucleation kinetics, Hotelength 2. Compared with the temporal distribution of individual nucleation sites are highly lacking. German *et al.* performed the first experimental characterization of nucleation rate and nucleation probability in hydrogen evolution using the nanoelectrode-based approach. Hotelength 37. More importantly, German *et al.* reported there was a limiting experimental time $t_{lim} \approx 0.4$ ms for their experiments, within which period no bubble nucleation probability expression when $t > t_{lim}$,

$$T(t) = 1 - e^{-\Gamma^*(t - t_{\lim})}. (38)$$

In addition, German *et al.* confirmed that the measured nucleation rate Γ^* is highly consistent with the theoretical expression given by the kinetic theory, ¹⁴⁹

$$\ln\left(\Gamma^*/\Gamma_0^*\right) = B\left(\frac{C_S}{K_H} - P_\infty\right)^{-2} \tag{39}$$

where Γ_0^* is a pre-exponential factor that can be considered as a constant. B is a prefactor 1 related to bubble contact angle. 149,160,161 Eq. 39 indicates that the nucleation rate is highly 2 sensitive to the supersaturation of gas concentration, where four orders of magnitude increase 3 in Γ^* , from 0.3 to 2000 1/s, was observed with only 20% increase in the dissolved hydrogen 4 concentration on the nanoelectrode surface. 149 In addition to the hydrogen bubble, Soto et al. 160 5 and Edwards et al. 161 from the same group of researchers further conducted systematic 6 characterizations for nucleation rates and nucleation probabilities of oxygen and nitrogen 7 8 bubbles using the same nanoelectrode-based approach.

3.1.3. Advances in Metrology Tools for the Probe of Nucleation Sites

9

Fundamental understanding of nucleation sites highly relies on accurate experimental 10 characterizations. However, direct probe of micro-and-nanoscale nucleation sites can be very 11 challenging due to the requirement of high sensitivity, superior resolution, and fast response. 12 In this Section, we review several representative advanced metrology tools that enable the 13 direct probe of nucleation sites, including the (1) nanoelectrode-based approach, 147-149,160-164 14 (2) scanning electrochemical cell microscopy (SECCM), 165-173 (3) conventional optical 15 microscopy, ^{159,174–190} (4) super-resolution optical microscopy, ^{191–210} (5) liquid cell transmission 16 electron microscopy (TEM), ^{211–217} and (6) environmental scanning electron microscopy 17 (ESEM). 157,218–222 Based on the working principles, these techniques can be classified into three 18 categories, i.e., micro-and-nanofabricated probe ((1) and (2)), optical probe ((3) and (4)), and 19 electron probe ((5) and (6)). We will briefly explain the working principles of each metrology 20 21 tool and then discuss potential opportunities and limitations of implementing these tools to understand bubble nucleation in electrochemical gas evolution reactions. 22 The nanoelectrode-based approach was first developed by Luo and White in 2013. 147 In their 23 24 experimental setup, a disk-shape nanoelectrode was fabricated and immersed in the electrolyte solution, where radius of the nanoelectrode Re can range from a few nanometers to a few 25 hundred nanometers (Figure 7a) and platinum (Pt) was commonly used as the electrode 26

material. $^{147-149,160-164}$ Compared with macroelectrodes, the nanoelectrode reduces the number of bubbles and the thickness of gas diffusion layer, enabling the measurement of single nanobubble nucleation at a steady-state condition. The states of the nanobubble nucleation can be precisely reflected from the voltage-current response in a cyclic voltammetry measurement. Specifically, during a cathodic scan, the current response exhibits a smooth increase followed by a sudden decrease to a constant residual current, leading to a peak current I_p . The smooth increase of current is due to the continuous electrochemical reaction on the nanoelectrode without bubble formation (top panel of Figure 7a), whereas the sudden decrease of current corresponds to the formation of single bubble that covers the nanoelectrode (bottom panel of Figure 7a). Therefore, the peak current I_p is an indicator of bubble nucleation, which can be further interpreted to extract the electrochemical environment of bubble nucleation. 147

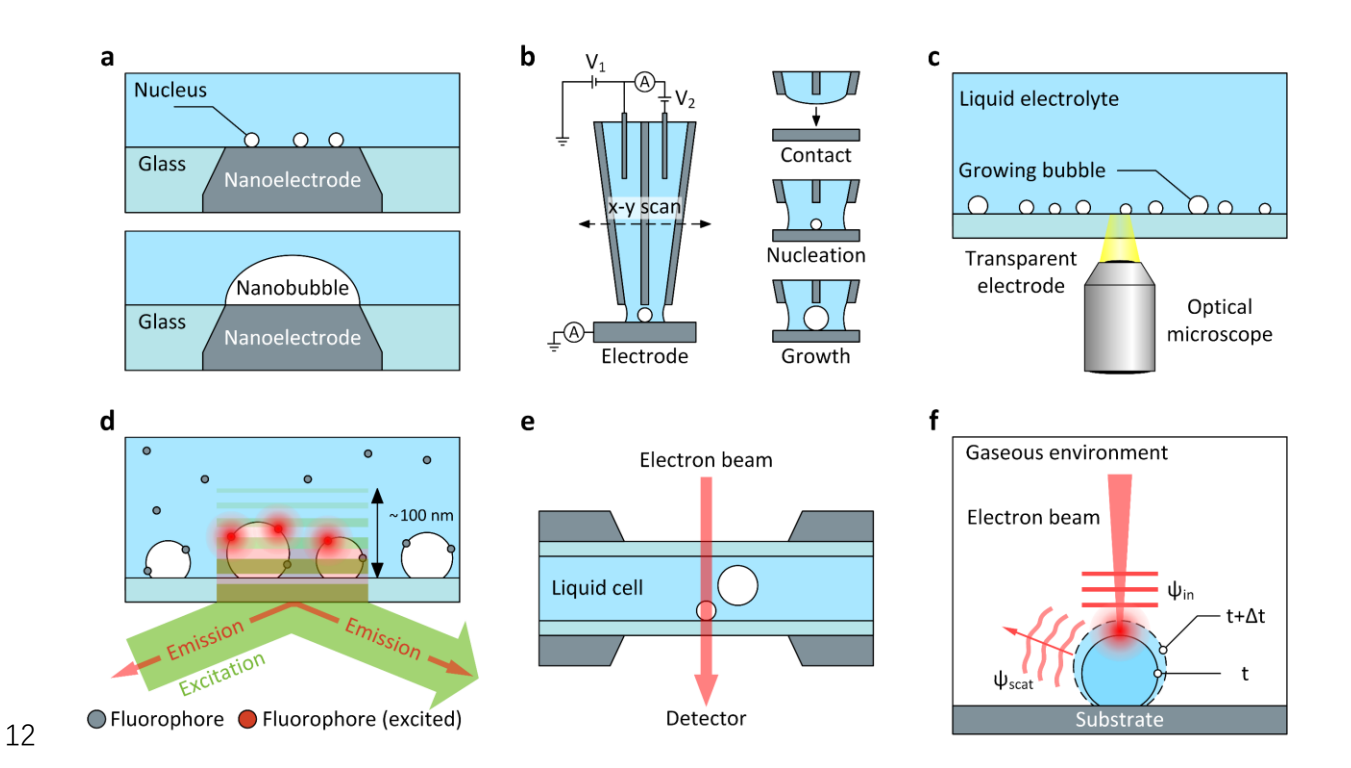


Figure 7. Representative metrology tools for nucleation site detection. (a) Nanoelectrode-based approach for measuring the nucleation of single nanobubbles. Top panel: nanoelectrode immersed into the electrolyte with several bubble nucleus on it. Bottom panel: nanoelectrode surface covered by a nanobubble. Nucleation of the nanobubble blocks the reaction area of the nanoelectrode, leading to a sudden drop of current through the nanoelectrode. (b) Scanning electrochemical cell microscopy (SECCM) for detecting nucleation sites on a surface. Left

panel: double-barreled (theta) pipette as the scanning probe of SECCM. Right panel: states of 1 2 the theta pipette (contact, bubble nucleation, and bubble growth) in a typical SECCM measurement. Variations of liquid meniscus and bubble nucleation can be reflected in the 3 voltage-current response. (c) Bright-field microscopy (BFM) interfaced with a transparent 4 electrode. (d) Super-resolution total internal reflection fluorescence microscopy (TIRFM). 5 Super-resolution imaging is enabled by the localization microscopy. Taking advantage of the 6 7 near-field created by evanescent waves, the TIRFM is sensitive to bubble nucleation at the 8 electrode-electrolyte interface. (e) Liquid cell transmission electron microscopy (TEM). 9 Electrolyte is confined into a liquid cell consisting of two electron transparent membranes. Bubble nucleation inside the liquid cell can be probed by the electron beam with nanoscale 10 resolution. (f) Phase-enhanced environmental scanning electron microscopy (p-ESEM) for 11 detecting nucleation of droplets. Phase of electron wave is very sensitive to the weak scattering 12 13 at liquid-gas interface. By reconstructing the phase of electron wave, the p-ESEM exhibits a largely improved imaging contrast and significantly elevated operating pressure. 14 15 Validity of the nanoelectrode-based approach has been well demonstrated through a series of studies by White and co-workers, where the supersaturation of gas concentration, critical radius 16 of nucleation site, nucleation rate, nucleation probability, nanobubble contact angle, gas 17 pressure, and number of gas molecules inside the nanobubble have been measured during 18 hydrogen, oxygen, and nitrogen evolutions. 147-149,160-164 We would like to briefly illustrate how 19 20 these important properties related to bubble nucleation can be extracted from the nanoelectrode-based measurements. The key assumption of the measurement is that the gas 21 22 diffusion layer is fully developed during nanobubble nucleation. As a result, gas diffusion is always in a steady-state condition (or quasi-steady state more precisely). This assumption is 23 24 valid when the size of electrodes is reduced to nanoscale, where the development of gas diffusion layer becomes much faster than the kinetics of bubble nucleation. This is because the 25

characteristic time of gas diffusion τ_g scales with $R_e^2/D_g \sim$ ns, where D_g is the diffusivity of dissolved gas ($D_g = 4.5 \times 10^{-9}$ m²/s for hydrogen). τ_g is five orders of magnitude smaller than

smallest timescale associated with bubble nucleation (~ 0.1 ms). 149,160,161 The steady-state gas

diffusion leads to the following relationship due to Fick's law,

26

27

28

$$I_{p} = 4R_{e}zFD_{g}(C_{s} - C_{\infty}) \tag{40}$$

where z is the number of electrons transferred per gas molecule (z = 2 for hydrogen). The prefactor $4R_e$ originates from the shape factor of the disk-shape nanoelectrode (eq. 21). With the measured peak current I_p , gas concentration to initiate nanobubble nucleation (C_s) can be calculated. $^{147-149,160-164}$ The gas pressure inside the nanobubble $P_{\rm in}$ and the critical radius of nanobubble r_c are given by Henry's law (eq. 32) and Young-Laplace equation (eq. 29), respectively. 147-149,162,163 The number of gas molecules inside the nanobubble can be estimated using the ideal gas law with $P_{\rm in}$ as the input. 148,161 Nucleation probability and nucleation rate can be determined by performing multiple measurements to record the time of bubble nucleation and fitting the experimental results with the temporal distribution (eq. 38). 149,160,161 Assuming the shape of nanobubble is a spherical cap, the contact angle can be extracted from the prefactor B of eq. 39, which is determined by fitting the measured gas concentration C_s and the corresponding nucleation rate Γ^* to eq. 39. 149,160,161 With the versatile capabilities of measuring multiple physical properties during bubble nucleation, the nanoelectrode-based approach can be a useful tool to quantify the impact of gas cavity and gas diffusion layer on bubble nucleation, if the thickness of gas diffusion layer can be manipulated separately. In addition, it can be of interest to further investigate how to translate the insights gained from the nanoelectrode to guide the design of conventional macroelectrode in future research. SECCM is a recent addition to the scanning electrochemical probe microscope (SEPM) techniques, which was developed by Ebejer, Unwin, and their coworkers in 2010. 168 Details of the SECCM have been systematically summarized in Refs. 166-168. The key component of SECCM is a double-barreled (theta) pipette filled with electrolyte solution (left panel of Figure 7b). In each channel of the theta pipette, there is a quasi-reference counter electrode (QRCE) inserted, which is typically made by chloridized silver wire (Ag/AgCl). 166-168 The spatial resolution of SECCM is determined by the tip diameter of theta pipette and the step of surface scan. With existing fabrication techniques, the tip diameter of theta pipette ranging from a few hundred nanometers to tens of micrometers has been demonstrated. Either the theta pipette or the sample is held by a piezoelectric stage to enable a precise scan along the sample surface (x-

1

2

3

4

5

6

7

8

9

10

11

12

13

14

15

16

17

18

19

20

21

22

23

24

25

26

y scan in Figure 7b). When the theta pipette approaches the sample surface along z-direction, a liquid meniscus forms to connect the pipette with the sample surface, providing a microelectrochemical environment (right panel of Figure 7b). To initiate electrochemical reaction in the liquid meniscus, a voltage V_1 is applied to the theta pipette and the sample substrate acts as the working electrode (left panel of Figure 7b). Meanwhile, additional voltage difference between two QRCEs (V_2) is applied, which is typically maintained as a constant. V_2 induces in an ionic conductance (barrel) current flowing from one QRCE to the other QRCE through the liquid meniscus. Since the ionic conductance between two barrels is highly sensitive to the shape of liquid meniscus, the barrel current serves as an indicator for the zposition of the theta pipette (right panel of Figure 7b). 166,167 When the liquid meniscus contacts the sample surface, there is a sudden increase of the dc component of the barrel current. In addition, there is also an ac component of the barrel current due to the oscillation of meniscus interface during the contact. By keeping a constant barrel current with a feedback control system, the distance between the theta pipette and sample surface can be a constant, enabling a stable meniscus shape during the x-y scan. By altering V_1 and measuring the resulting current through the sample substrate (working electrode), cyclic voltammetry measurement can be carried out at each position on the sample surface. A current map that reflects the surface electrochemical activity can hence be constructed by scanning the entire sample surface. Compared with the conventional SEPM such as the scanning electrochemical microscopy (SECM), 165 the SECCM can work with rougher sample surfaces and does not require to immerse the entire sample into electrolyte solution, providing more flexibilities for a variety of electrochemical measurements. Over the past decade, the SECCM has been widely implemented by electrochemists to understand the dopant and contamination distribution on electrodes, 223,224 heterogeneous electron transfer at nanoscale, 225,226 and electrochemical activities of nanomaterials.^{227,228} Recently, the SECCM has been used to understand bubble nucleation on various substrates during electrochemical gas evolution reactions (right panel of Figure 7b). 169–173 At each position scanned by the SECCM, the corresponding voltage-current response during the cyclic voltammetry measurements showed a similar feature to that of the nanoelectrode-based approach, where a peak current I_p represents the occurrence of bubble

1

2

3

4

5

6

7

8

9

10

11

12

13

14

15

16

17

18

19

20

21

22

23

24

25

26

27

28

nucleation at this position. 166-168 Similar to the nanoelectrode-based approach, the observation of peak current indicates that the SECCM is capable of capturing the nucleation of single bubble. Therefore, the data analyzing approaches for the nanoelectrode (eqs. 29, 32, 38 – 40) can also be used to interpret the SECCM measurements. ^{166,167} More importantly, the magnitude of peak current can well reflect the local electrochemical activity. Therefore, by scanning the entire surface and measuring the I_p of each position, a bubble nucleation map can be constructed where the preferential nucleation sites with lower activation energy barriers are clearly visualized. 169-173 Compared with the nanoelectrode-based approach, the SECCM is more feasible to study macroelectrodes, enabling highly exciting research opportunities to understand how surface micro-and-nanostructures impact bubble nucleation. For example, Mefford et al. investigated the oxygen evolution activity of the microscale single crystalline transition metal (oxy)hydroxide platelet particles (β-Co(OH)₂).¹⁷¹ Leveraging the superior spatial resolution of SECCM (≈ 400 nm), they observed that the sharp edge facets, instead of the large basal plane, of β-Co(OH)₂ particles dominate the electrochemical reaction. More notably, Deng et al. studied the effect surface morphology on bubble nucleation by depositing SiO₂ nanoparticles with different sizes on the electrode. ¹⁷³ Taking advantage of the SECCM, they directly measured the nucleation of single bubble on a single SiO₂ nanoparticle. They showed there is an optimal nanoparticle radius around 10 nm that corresponds to the minimum peak current I_p and the lowest activation energy barrier for bubble nucleation. Considering the unique feature of SECCM that probes the spatial variation of electrochemical activity with high resolution while ensuring the single bubble nucleation at each scanned position, it can be highly rewarding to use the SECCM to quantify the nucleation site distributions in electrochemical gas evolution reactions and validate Zhang et al.'s theory. 157 Moreover, existence of the optimal surface structure size in Deng et al.'s experiments shows a qualitive consistency with the theoretical prediction of Lu et al.'s transport-based model of bubble nucleation. 152,173 It will be of great interest to perform systematic SECCM characterizations on electrodes with different sizes of gas cavities and compare the experiments with the transport-based model. Optical microscopy provides a simple, yet highly effective tool for understanding bubble

1

2

3

4

5

6

7

8

9

10

11

12

13

14

15

16

17

18

19

20

21

22

23

24

25

26

27

28

29

nucleation. Owing to the high resolution and noninvasive feature, optical microscopy is capable

1 of directly detecting bubble dynamics without intervening with the nucleation process. There have been many types of optical microscopy techniques used to understand the behaviors of 2 bubbles, including conventional bright-field microscopy (BFM), 159,174-177,185 dark-field 3 microscopy (DFM), 182-184,186,187,189 fluorescence microscopy, 176 confocal microscopy, 176 4 interferometry, 178-181 and spectroscopy. 190 The BFM is the most basic and common optical 5 microscopy technique consisting of the light source (e.g., halogen lamp, light-emitting diode 6 (LED), and laser), tube lens, objective, camera, and other optical components, which provides 7 8 wide-field images with submicron spatial resolution. The spatial resolution of BFM Δx is 9 governed by the wave nature of light (known as the diffraction limit) and can be estimated as,²²⁹ 10

11

12

13

14

15

16

17

18

19

20

21

22

23

24

25

26

27

$$\Delta x \approx 0.61 \frac{\lambda}{NA} \tag{41}$$

where λ is the wavelength of light scattered by the sample. NA is the numerical aperture of objective (typically ranging from 0.1 to 1.25), which depends on the magnification (typically ranging from 0.5X to 100 X) and immersion media (e.g., air, water, and oil) of the objective. Taking a 100X magnification objective (NA = 0.8) and white-light illumination (average wavelength of 500 nm) as example, $\Delta x \approx 380$ nm, providing a submicron spatial resolution for the conventional optical microscopy. The BFM has been extensively used to study bubble nucleation in both phase change heat transfer and electrochemical gas evolution reactions. 159,175,185 For example, Janssen et al. investigated bubble nucleation density under different current densities during alkaline water electrolysis using the BFM. 159 An inverted BFM was interfaced with the electrolytic cell through an optically transparent nickel electrode. where the evolution of bubble bases from nucleation to departure were clearly imaged (Figure 7c). Although the BFM is capable of detecting small bubbles down to a few hundred nanometers, it becomes less effective to capture bubbles with several tens of nanometers, which can be predominant for the nucleation process during electrochemical gas evolution reactions. 148,149 This is because for the BFM, both the light scattered by bubbles and background illumination are captured by the camera. When the bubble size is below a few hundred nanometers, the

scattered light is too weak as compared with the incident light, leading to undesirable imaging contrast and making it difficult to identify small bubbles from the background illumination and noises. To address this challenge, the DFM has been implemented in electrochemistry. 182-^{184,186,187,189} The key concept of the DFM is to prevent the illumination from entering into the camera, creating a "dark" background in the image, in which condition only the scattered light from the sample is ultimately detected. Owing to the enhanced imaging contrast, the DFM is particularly desirable to study bubble nucleation. For example, Li et al. has demonstrated that the scattered light from individual nanobubbles during hydrogen evolution can be detected by the DFM. 184 By monitoring the variation of scattered light intensity as a function of time, the nanobubble nucleation rate from a single nanoparticle catalyst was precisely quantified. The imaging contrast can be further improved by labeling the nanobubble with strong light emitters such as quantum dots and plasmonic nanoparticles. 182,183,186,187,189 Despite the significantly enhanced imaging contrast, we would like to note that the spatial resolution of the DFM is still diffraction limited, which is governed by eq. 41. In addition to the DFM, fluorescence microscopy and confocal microscopy can also provide improved imaging contrast compared with that of the BFM, making them desirable to image the liquid-gas interface of bubbles. 176 Fluorescence microscopy improves the imaging contrast following the same strategy as that of the DFM, i.e., separating the scattered light from the background illumination. However, fluorescence microscopy achieves this goal leveraging the fluorescence phenomena, i.e., the labeling molecules absorbing shorter wavelength light while emitting longer wavelength light.²³⁰ With a short wavelength light source (e.g., mercury arch lamp, UV light, and blue/green LED/laser) as the excitation and an emission filter between the sample and camera, only the emitted long wavelength light can be recorded by the camera. Therefore, fluorescence microscopy also produces a "dark-field" image where only the regions with fluorescence molecules are visualized. Confocal microscopy is a point-by-point scanning type imaging approach.²³⁰ Instead of using the wide-field illumination, confocal microscopy relies on a focused laser spot to illuminate the sample surface. With the confocal pinholes, scattered light from the out-of-focal plane is filtered whereas only the in-focal plane scattering is recorded by the camera. As a result, confocal microscopy can provide a slightly improved in-plane spatial

1

2

3

4

5

6

7

8

9

10

11

12

13

14

15

16

17

18

19

20

21

22

23

24

25

26

27

28

resolution (≈ 200 nm) and a much enhanced out-of-plane sectioning ability (≈ 500 nm) compared to the BFM. All the above optical microscopy techniques image samples by detecting the intensity variation of light. Since light is an electromagnetic wave, its wave signature such as frequency (wavelength) and phase can also be used for imaging, which can be extracted from spectroscopy and interferometry, respectively. The spectroscopy and interferometry tools have been widely used in phase change heat transfer and electrochemical gas evolution reactions. ^{73,178–181,190} The detailed working principles of spectroscopy and interferometry are out of the scope of this review but can be seen in Refs. ^{231,232}.

1

2

3

4

5

6

7

8

9

10

11

12

13

14

15

16

17

18

19

20

21

22

23

24

25

26

Pushing the spatial resolution of optical microscopy beyond the diffraction limit (eq. 41) is critical to obtain the precise locations of nucleation sites and the detailed profiles of liquid-gas interfaces. Over the past two decades, there has been significant progress in the superresolution optical microscopy, where ~ 20-50 nm or even better spatial resolution has been demonstrated. 191-194 Details regarding different types of super-resolution techniques have been comprehensively summarized by Schermelleh et al. 193 One of the major techniques to realize super-resolution is known as the localization microscopy. ^{191,192} The key concept of localization microscopy relies on the fact that the positions of single point-like emitters or scatters (e.g., fluorescence molecules or nanobubbles) can be precisely determined if the optical signals from the emitters or scatters are not overlapped. To determine the positions of emitters or scatters, their point spread functions (PSFs), i.e., the images of emitters or scatters, are localized multiple times by fitting the PSFs to the 2D Gaussian profiles, where the spatially overlapped PSFs from several emitters or scatters can be separated in the time domain by exploiting their stochastic switch between the active state (e.g., bright state of fluorescence molecules or nucleation of nanobubbles) and inactive state (e.g., dark state of fluorescence molecules or waiting period between nanobubble nucleation). ¹⁹¹ The localization precision σ_{LM} is fundamentally limited by the number of photons $N_{\rm ph}$ collected per switch from the active state to dark state of a single emitter or scatter, 191,194

$$\sigma_{\rm LM} \approx \frac{\sigma_{\rm PSF}}{\sqrt{N_{\rm ph}}}$$
 (42)

- where $\sigma_{PSF} \approx \Delta x$ is the spread of the PSF and the spatial resolution of the localization
- 2 microscopy cannot be better than $2.3\sigma_{LM}$. With the sensitivity of detecting the emission from
- 3 single fluorescence molecules, the single-molecule localization microscopy (SMLM) was
- 4 developed, which has become one of the most predominant localization microscopy techniques.
- 5 Details about the working principles and applications of SMLM have been systematically
- 6 discussed by Lelek *et al.*¹⁹¹
- Recently, several super-resolution techniques have been used to understand bubble nucleation, unlocking unprecedented research opportunities.^{198,203–207} For example, Zhang *et al.* detected
- 9 the scattering of single nanobubbles nucleating from a single nanoparticle catalyst using the
- 10 DFM.²⁰³ Combining with the localization microscopy, they localized the centers of
- 11 nanobubbles with tens of nanometers accuracy and constructed a super-resolution image of
- 12 nanobubble distribution around the nanoparticle catalyst, which reflects the relationship
- between the shape of nanoparticle catalyst and its electrochemical activity. By integrating the
- localization microscopy with the total internal reflection fluorescence microscopy (TIRFM)²⁰⁴
- 15 ²⁰⁷ or surface plasmon resonance microscopy (SPRM)^{198,208}, the probe light can be introduced
- 16 from the backside of the electrode, enabling super-resolution imaging of electrochemical
- processes with the minimum interference with the electrolyte (Figure. 7d). More notably,
- taking advantage of the evanescent waves and surface plasmons excited in the TIRFM and
- 19 SPRM, respectively, these techniques are particularly sensitive to the variations at the
- 20 electrode-electrolyte interface, making them highly desirable to study bubble nucleation. For
- 21 example, using the fluorescence molecule rhodamine 6G (R6G) adsorbed on the liquid-gas
- 22 interface of nanobubbles, Hao et al. obtained super-resolution TIRFM images of hydrogen
- bubble nucleation during water electrolysis (Figure 7d), where they found hydrogen bubble
- nucleation even occurred below the thermodynamic voltage. 204 Chan and Ohl, 205 Su et al., 206
- and Sambur et al.²⁰⁷ further demonstrated that the super-resolution TIRFM is capable of
- 26 quantifying nanobubble dynamics and temporal-and-spatial variations of nanoparticle catalysts
- electrochemical activity in gas evolution reactions. In addition to the localization microscopy,
- 28 we would like to note that the super-resolution imaging of electrochemical processes was also
- 29 achieved using the near-field imaging approaches, such as the near-field infrared (IR)

microscopy²⁰⁹ and the tip-enhanced Raman spectroscopy. ^{196,210} Although there have been quite a few studies aiming to understand the impact of catalysts on bubble nucleation, it is worth exploring the opportunities of using the super-resolution microscopy to further understand the inverse problem, *i.e.*, how the presence of bubbles could ultimately impact the local

5 electrochemical environment and hence the reaction rate.

6

7

8

9

10

11

12

13

14

15

16

17

18

19

20

21

22

23

24

25

26

27

28

29

Compared with optical microscopy, electron microscopy can achieve much improved spatial resolution up to the Angstrom scale.²¹² However, conventional electron microscopy, such as the TEM, has to be operated in a high vacuum condition, which is inaccessible to the liquidstate samples. The liquid cell TEM addresses this challenge by enclosing a liquid thin film, typically tens of nanometers to a few micrometers in thickness, between two electron transparent membranes (Figure 7e), such as the silicon nitride membranes (~ 50 nm thickness) and graphene sheets.^{211–213} By interfacing the liquid cell with the sample holder of TEM, the electron beam can directly probe the liquid film through the transparent membranes, providing high spatial resolution images (Figure 7e). The spatial resolution of liquid cell TEM depends on the electron dose, liquid film thickness, and aberration correction, which ranges from a few Angstroms to tens of nanometers.²¹² The temporal resolution of liquid cell TEM can reach 0.01s or even better.²¹² Details about the working principles of liquid cell TEM have been reviewed by Ross²¹¹ and Jonge et al.²¹² Taking advantage of the superior spatial and temporal resolution, the liquid cell TEM has been used to image bubble nucleation during water electrolysis. 214-217 For example, Grogan et al. observed the nucleation of hydrogen nanobubble in liquid cell due to the radiolysis under high electron dose.²¹⁴ This result indicates that the electron beam can intervene with the electrochemical processes if the electron dose is improperly chosen. By introducing micro-and-nanofabricated electrodes into the liquid cell, Liu and Dillon performed the *in situ* TEM imaging of hydrogen evolution, where they showed that instead of the heterogeneous nucleation, bubbles can nucleate "homogeneously" a few nanometers away from a highly wetting electrode. 215 Similar liquid thin layer between the solid surface and gas bubble was also observed by Wang et al. during the etching of gold nanorods with oxygen bubbles using the liquid cell TEM,²¹⁶ which will be discussed in detail in Section 3.2.2. These liquid cell TEM characterizations have provided experimental evidence that the

presence of gas bubbles can strongly affect the local electrochemical reaction rates, which

2 requires more quantitative understanding in future research.

3

4

5

6

7

8

9

10

11

12

13

14

15

16

17

18

19

20

21

22

23

24

25

26

27

28

29

ESEM is another type of electron microscopy that can deal with liquid and gas-state samples with high spatial resolution. 218,219 Compared with conventional scanning electron microscopy (SEM) that can only image electrically conductive samples in a high vacuum condition, ESEM can be operated in a gaseous environment and image electrical insulators without coating the conductive layer. With the electron beam induced ionization of gas molecules around the samples, charging artifacts due to the electrically insulating samples can be effectively reduced.²¹⁸ Compared with the liquid cell TEM, ESEM does not require complex sample preparations and has simple operation procedures. Details about the working principles and applications of ESEM have been carefully reviewed by Donald²¹⁸ and Zhang et al.²¹⁹ The spatial resolution of ESEM highly depends on the operating pressure. For the high vacuum operation, the spatial resolution of ESEM converges to that of SEM (~ 10 nm). However, the spatial resolution can rapidly degrade with elevated pressure, because the presence of gas molecules can scatter the incident electrons, leading to the spread of electron beam. For this reason, the pressure of ESEM chamber is typically maintained in a low-pressure condition (< 1000 Pa), ensuring submicron spatial resolution.²¹⁸ Recently, Zhang et al. developed new ESEM technique, known as the p-ESEM, which significantly enlarges the allowable operating pressure of ESEM up to 2500 Pa. 220,221 Instead of detecting the intensity of scattered electrons, p-ESEM is capable of reconstructing the phase of electron wave, which reflects how the incident electron wavefront (Ψ_{in}) is deformed to the scattered wavefront (Ψ_{scat}) through the electron-matter interaction (Figure 7f). The phase of electron wave is more sensitive to the weak scattering due to the evolution of liquid-gas interface. Compared with the conventional ESEM, more than six times enhancement of imaging contrast has been demonstrated.^{220,221} Using the p-ESEM, Zhang et al. characterized the nucleation site distributions in the condensation process, validating the Poisson and Rayleigh distributions for the population and spatial distributions of nucleation sites, respectively. 157 Although the ESEM has been widely applied to understand liquid-gas systems, its applications are mainly relevant to phase change heat transfer. It is thus worth understanding the potential of ESEM for electrochemical gas

evolution reactions. Although the main focus of this Review is to discuss the potential path of understanding bubbles in electrochemical gas evolution reactions from the perspective of phase change heat transfer, we would note that substantial innovations of metrology tools in electrochemical systems can bring huge reciprocal benefits to phase change heat transfer. It can be rewarding to explore the opportunity of implementing advanced metrology tools to resolve bubble nucleation during the boiling process.

3.2. Bubble Growth

1

2

3

4

5

6

7

8

9

10

11

12

13

14

15

16

17

18

19

20

21

22

23

24

25

26

27

28

29

After nucleation, bubbles can continuously grow from the nucleation site to a few millimeters large and then depart from the surface of electrode. Bubble growth is one of the most predominant processes that governs the species (ions and dissolved gases) transport in electrochemical gas evolution reactions. On the one hand, the presence of liquid-gas interface creates additional paths for gas transport. Compared to the gas diffusion from the electrodeelectrolyte interface through the bulk electrolyte, gas diffusion across the liquid thin film near the three-phase contact line of bubble exhibits much lower resistance. Meanwhile, evolution of the liquid-gas interface during bubble growth induces fluid flows in the electrolyte, which can accelerate ion transport through convection. On the other hand, during the bubble growth, a large area of the electrode can be covered by bubble bases, which are inaccessible to electrochemical reactions. In addition, bubbles sitting on the electrode and floating in the electrolyte block ion transport, which reduces the ionic conductivity of the bulk electrolyte. Due to the above complex transport mechanisms associated with bubble growth, quantifying the impact of bubble growth on the change of overpotentials has become a highly challenging research question. In this Section, we focus on the growth of single bubbles whereas bubble growth due to coalescence will be discussed in Section 3.3. We will review the general physics that governs single bubble growth. In particular, we will discuss several transport phenomena associated with the liquid-gas interface during bubble growth. These transport phenomena have been well recognized in phase change heat transfer while their counterparts in electrochemical gas evolution reactions are still missing, which highlight the huge opportunity of knowledge translation. Despite the significant promise, we will point out several distinct transport mechanisms for bubble growth in the boiling and gas evolution processes, raising critical

- 1 perspectives when translating knowledge between two research fields. Finally, we will review
- 2 representative approaches and provide critical considerations for estimating the transport
- 3 overpotentials due to bubble growth.

15

16

17

18

19

20

21

22

23

24

25

26

to time,

3.2.1. Regimes of Single Bubble Growth

In general, single bubble growth can be classified into three regimes: inertia-controlled growth, 5 diffusion-controlled growth, and reaction-controlled growth.²³³ These three regimes appear in 6 7 both phase change heat transfer and electrochemical gas evolution reactions. Inertia-controlled growth describes the rapid repulsion of surrounding liquid due to depressurization of gas 8 bubbles, which occurs at the early stage of bubble growth after nucleation. In this regime, 9 pressure inside the gas bubble and inertia of the surrounding liquid are two dominant forces. 10 Due to bubble growth, the surrounding liquid has a velocity profile of $v = \dot{R}(R/r)^2$, where R is 11 bubble radius and r is the spherical coordinate of the flow field (Figure 8a). ^{234,235} By balancing 12 the kinetic energy of the flow field and the total work exerted from the pressure driven bubble 13 expansion, evolution of bubble radius in the inertia-controlled growth regime is linearly related 14

$$R = Gt (43)$$

where *G* is the growth coefficient. eq. 43 can be more rigorously derived from the general Rayleigh–Plesset equation by neglecting the viscous loss and surface tension terms, ²³⁵ which is shown in the theoretical studies of bubble growth in the boiling process by Plesset and Zwick in 1954, ²³⁶ Forster and Zuber in 1954, ²³⁷ and Scriven in 1959. ²³⁸ For the boiling process, they showed that inertia-controlled growth can last for a few hundred microseconds, where the bubble radius is typically smaller than 10 µm. These theoretical predictions were confirmed by multiple experiments and numerical simulations. ^{239,240} On the other hand, Verhaart *et al.*, ²⁴¹ Brandon and Kelsall, ²⁴² and Matsushima *et al.* ²⁴³ demonstrated inertia-controlled growth of bubbles on gas evolving electrodes through theoretical and experimental investigations. In particular, Brandon and Kelsall showed that inertia-controlled growth is dominant in the first a few milliseconds after nucleation when the bubble radius is less than a few micrometers. ²⁴²

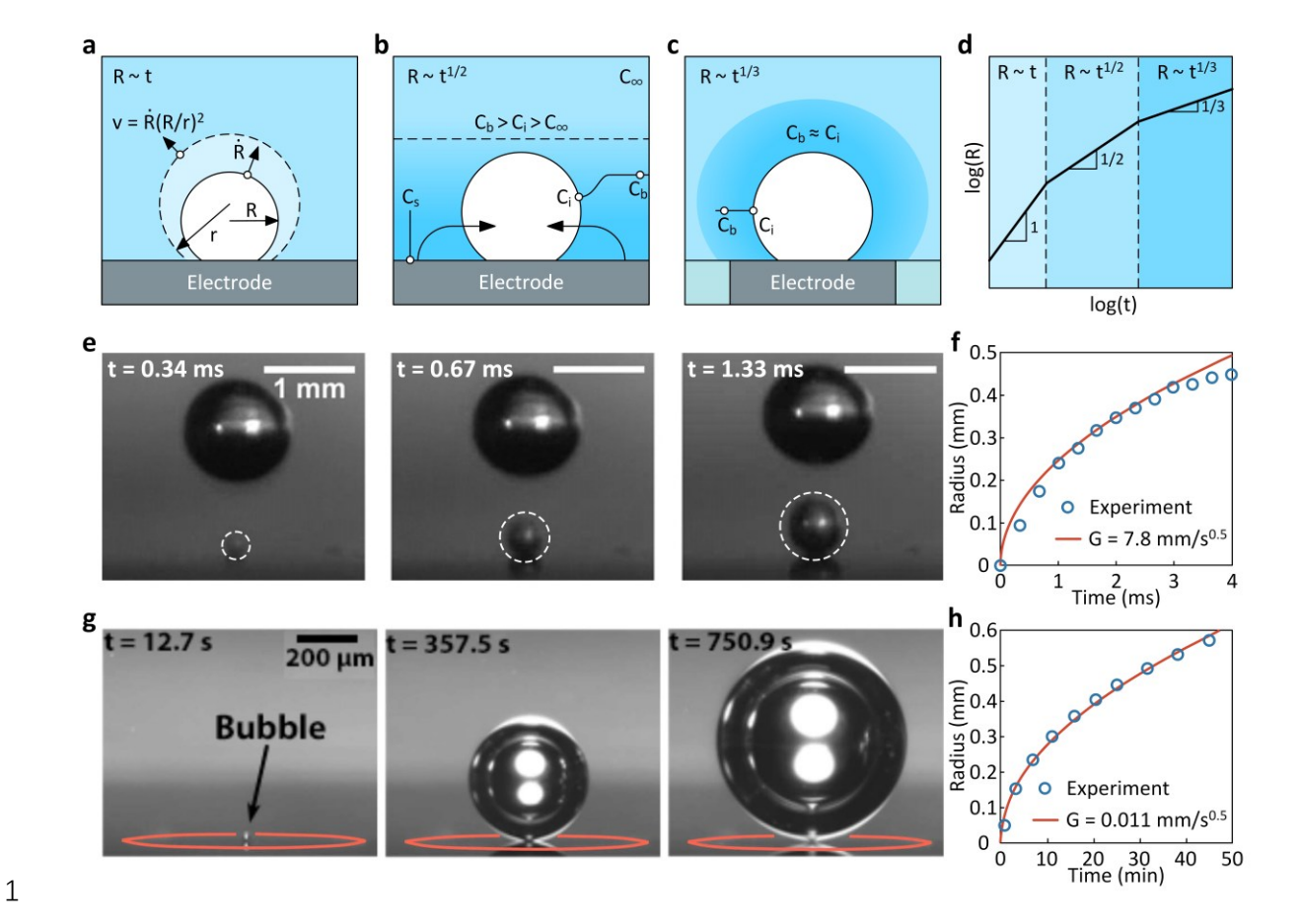


Figure 8. Fundamentals of bubble growth. (a) Inertia-controlled bubble growth. Bubble radius in inertia-controlled regime shows a linear dependence on time. (b) Diffusion-controlled bubble growth. Bubble radius in the diffusion-controlled regime shows a 1/2-power law dependence on time. (c) Reaction-controlled bubble growth. Bubble radius in reaction-controlled regime shows a 1/3-power law dependence on time. (d) Schematic of bubble radius as a function of time across three regimes. (e) Representative time-lapse images of vapor bubble growth from a microfabricated gas cavity during pool boiling of water. The vapor bubble is highlighted by the white-dashed circle. Wall superheat was 5.3 °C. Reproduced with permission from Ref. 264. Copyright 2010 Elsevier. (f) Vapor bubble radius as a function of time during pool boiling of water. Experimental data was obtained from Ref. 264 (blue circles). The growth of vapor bubble falls into the diffusion-controlled regime, which can be fitted to eq. 44 with G = 7.8 mm/s^{0.5} (red curve). (g) Representative time-lapse images of hydrogen bubble growth from a microfabricated gas cavity during water electrolysis. The microfabricated gas cavity was located at the center of a ring-shape microelectrode (red circle).

- 1 Current density applied to the ring-shape microelectrode was 39.3 mA/cm². Reproduced with
- 2 permission from Ref. 258. Copyright 2019 The Electrochemical Society. (h) Hydrogen bubble
- 3 radius as a function of time during water electrolysis. Experimental data was obtained from
- 4 Ref. 258 (blue circles). The growth of hydrogen bubble is also diffusion-controlled, which can
- 5 be fitted to eq. 44 with G = 0.011 mm/s^{0.5} (red curve).
- 6 Diffusion-controlled growth originates from the fact that bubble growth relies on the
- 7 continuous gas transport across the liquid-gas interface (black arrow in Figure 8b). For the
- 8 boiling process, evaporation occurs at the liquid-vapor interface. Due to the large vaporization
- 9 enthalpy, a significant amount of heat is required, which relies on the diffusion from the heating
- 10 surface to the liquid-vapor interface, across the thermal diffusion layer. Similarly, for
- electrochemical gas evolution reactions, bubble growth is dictated by the gas diffusion from
- the electrode surface to the liquid-gas interface, which is driven by the concentration gradient
- across the gas diffusion layer (Figure 8b). Therefore, the capability of transferring heat and
- mass across the thermal and gas diffusion layers leads to another fundamental limit of bubble
- growth rate. Epstein and Plesset performed one of the first theoretical derivations on diffusion-
- 16 controlled bubble growth in supersaturated solution in 1950.²⁴⁴ Then, Plesset and Zwick in
- 17 1954,²³⁶ Forster and Zuber in 1954,²³⁷ and Scriven in 1959²³⁸ conducted pioneering research
- on the theory of diffusion-controlled bubble growth in the boiling process. Taking the thickness
- of thermal diffusion layer into account, they derived the following analytical expression as an
- approximate solution to bubble radius in the diffusion-controlled growth regime,

$$R = Gt^{\frac{1}{2}} \tag{44}$$

- where the growth coefficient G is a function of the supersaturation level, which is quantified
- by a dimensionless number known as the Jakob number Ja, i.e., G = G(Ja). For the boiling
- process, the Jakob number is expressed as, ²⁴⁵

$$Ja = \frac{\rho_{\rm l}c_{\rm p,l}(T_{\rm s} - T_{\infty})}{\rho_{\rm v}h_{\rm lv}} \tag{45}$$

- 24 where $c_{p,l}$ is the specific heat of liquid and ρ_v is the density of vapor. For the electrochemical
- 25 gas evolution reactions, the Jakob number is given by, ²⁴¹

$$Ja = \frac{M_{\rm g}(C_{\rm s} - C_{\infty})}{\rho_{\rm g}} \tag{46}$$

where ρ_g is the gas density and M_g is the gas molar mass. Expressions of G(Ja) through either 1 analytical derivations or empirical correlations have been summarized in Refs. ^{241,245,246}. For 2 typical boiling and gas evolution processes, most of the stage throughout a bubble growth cycle 3 is governed by the diffusion-controlled regime, where the corresponding bubble radius can 4 range from tens of micrometers to a few hundred micrometers. 26,138,246-254 The 1/2-power law 5 dependence of bubble radius on time has been well validated via numerous experiments on the 6 electrodes with flat surfaces. 26,241,242 In addition, taking advantage of micro-and-7 8 nanofabrication technologies, recent experiments also showed that bubble growth on the single microfabricated gas cavity, 252 single pit in micropillar, 255,256 micropillar arrays, 257 ring-shape 9 microelectrode, ²⁵⁸ and nanostructured surfaces ²⁵⁹ follows the diffusion-controlled behaviors. 10 When the size of bubble becomes comparable with the area of reaction surface, the gas 11 concentration gradient from the electrode surface to the liquid-gas interface becomes less 12 significant (Figure 8c), in which condition the reaction-controlled growth occurs. 146,241,242,260-13 ²⁶² The reaction-controlled growth arises from the fact that the rate of bubble volumetric 14 expansion is ultimately proportional to the total electrochemical reaction rate over the entire 15 electrode surface (Figure 8c), which results in the following relationship between bubble radius 16 17 and time,

$$R = Gt^{\frac{1}{3}}. (47)$$

Darby and Haque first reported the above 1/3-power law dependence of bubble radius on time in 1972 when they measured the growth of a hydrogen bubble from 0.5 mm to 2 mm in diameter on the tip of a 1.2 mm diameter platinum-wire electrode. Through a theoretical interpretation to the experimental data, they found that the bubble growth is limited by the reaction rate rather than gas diffusion. Verhaart *et al.* then provided more quantitative theoretical derivations of the reaction-controlled growth and confirmed Darby and Haque's results using a similar experimental apparatus. With the tip of a 100 µm diameter platinum wire as the electrode, they observed that the evolution of bubbles can be well described by eq. 47 when the bubble

18

19

20

21

22

23

24

radius is larger than a few hundred micrometers. More notably, they showed the 1/2-power law dependence of bubble radius on time (eq. 46) when $R < 100 \mu m$, indicating a transition from the diffusion-controlled growth regime to the reaction-controlled growth regime. In general, the observation of reaction-controlled growth requires a bubble size comparable with the reaction area. As shown in the above pioneering studies, one of the most straightforward approaches to achieve this criterion is to ensure the size of electrode smaller than the bubble departure size.^{241,260} With the advances of micro-and-nanofabrication technologies, reactioncontrolled growth has been commonly observed on microelectrodes with diameters from 10 μm to 100 μm. ^{241,242,260} In addition to reducing the size of electrodes, reaction-controlled growth can also be realized by confining the effective reaction area, ^{261,262} enlarging the bubble departure size, ²⁴³ and reducing the space between bubbles. ¹³⁸ For example, Wang et al. studied the growth of hydrogen bubbles during electrolysis and photoelectrolysis on the same TiO₂ nanostructured electrode.²⁶¹ Although the TiO₂ nanostructured electrode has an area of 3 cm². the photoelectrolysis is excited by a laser beam, which confines the effective reaction area to a 1 mm diameter spot. As a result, they observed diffusion-controlled growth during electrolysis and reaction-controlled growth during photoelectrolysis. Later, similar bubble growth mechanisms were confirmed by the same group of researchers in oxygen evolution.²⁶² Matsushima et al. observed the reaction-controlled growth of single hydrogen bubbles on a 200 µm diameter electrode under microgravity, because the bubble departure size becomes larger compared to that under the standard gravity.²⁴³ Higuera theoretically demonstrated the transition from diffusion-controlled growth to reaction-controlled growth in hydrogen evolution when the distance between neighboring bubbles becomes comparable to the bubble size. 138 We note that the reaction-controlled growth in boiling can be more precisely understood as a process dictated by the rate of liquid-vapor phase change since no chemical reactions occur in phase change heat transfer. In addition, we would like to note a few studies also reported that bubble growth can deviate from the above three regimes where the 1/4-power law dependence and 1/5-power law dependence of bubble radius on time have been observed in hydrogen evolution on microelectrode²⁶³ and pool boiling with constant wall superheat,²⁴⁰ respectively.

1

2

3

4

5

6

7

8

9

10

11

12

13

14

15

16

17

18

19

20

21

22

23

24

25

26

27

28

Figure 8d schematically shows the bubble radius as a function of time across all three bubble growth regimes. With the increase in bubble radius, the transition from inertia-controlled growth regime to reaction-controlled growth regime through the diffusion-controlled growth regime has been experimentally observed by Brandon and Kelsall²⁴² as well as Matsushima et al.²⁴³ Specifically, Brandon and Kelsall performed systematic measurements on hydrogen, oxygen, and chlorine bubble growth on microelectrodes with diameters ranging from 10 µm to 500 μm. 242 For the microelectrode diameter smaller than 100 μm, they observed the inertiacontrolled growth when bubble diameter was smaller than 10 µm in the initial stage (< 10 ms), diffusion-controlled growth when bubble diameter was between 10 µm and 100 µm (< 100 ms), and reaction-controlled growth when bubble diameter was larger than 100 µm. However, the reaction-controlled growth was not observed on the 500 µm diameter microelectrode, because the bubble already departed before its size becomes comparable to the size of the microelectrode. We provide representative experimental images showing bubble growth during the boiling and gas evolution processes. Figure 8e shows the growth of a vapor bubble (whitedashed circle) from a 10 µm diameter gas cavity during pool boiling of water when the wall superheat was 5.3 °C. 264 The variation of bubble radius as a function of time can be well described by eq. 44, indicating a diffusion-controlled growth regime (Figure 8f). Figure 8g shows the growth of a hydrogen bubble from a 30 µm diameter gas cavity during water electrolysis.²⁵⁸ The gas cavity was surrounded by a ring-shape microelectrode where a current density of 39.3 mA/cm² was applied. Similar diffusion-controlled bubble growth was observed and the growth coefficient ($G = 0.011 \text{ mm/s}^{0.5}$) was determined by fitting eq. 44 to the experimental data.

1

2

3

4

5

6

7

8

9

10

11

12

13

14

15

16

17

18

19

20

21

22

23

24

25

26

27

28

29

3.2.2. Interfacial Transport Associated with Bubble Growth: Opportunities of Knowledge Translation

Although the general physics associated with bubble growth has been well understood, fundamental understanding of interfacial transport and its impact on the growth coefficient of bubble G is still elusive. In this Section, we aim to provide a comprehensive physical picture of gas transport during bubble growth and discuss several fundamental research questions, which could potentially play a ubiquitous role in bubble growth while not being widely

1 recognized yet. Then, we will discuss a few interfacial transport phenomena observed in recent

2 boiling studies. The critical roles of these phenomena in the boiling process have been

3 identified, whereas their counterparts in electrochemical gas evolution reactions are still

4 unclear, indicating potential opportunities of knowledge translations.

Transport of dissolved gas into the growing bubble is a complicated physical process, because it involves the electrode-electrolyte interface (① in Figure 9a), liquid thin film near the three-phase contact line (② in Figure 9a), and electrolyte-gas interface (③ in Figure 9a), all of which could induce resistance to gas transport. Specifically, as discussed in Section 2.3, gas is generated on the Stern layer and diffuses across the potential screening layer (diffuse layer, Figure 9b). The significant variation of electric field in the EDL (right panel of Figure 9b) induces highly nonuniform ion concentration, which could alter the local fluid properties of the electrolyte. Taking the cathode reaction of alkaline water electrolysis as an example, solutions to the Nernst-Planck-Poisson-Boltzmann model have shown that the concentration of solvated cations in the EDL can be more than one order of magnitude higher than that in the bulk electrolyte. Taking species in the electrolyte. Considering the distinct distributions of solvated with surrounding species in the electrolyte. Considering the distinct distributions of solvated

Transport resistance arising from the gas diffusion across the liquid thin film between electrode-electrolyte and electrolyte-gas interfaces has been widely recognized as the dominant resistance to gas transport (2) in Figure 9a). 46,148,152 Under a simple 1D approximation, the transport resistance due to liquid thin film R_1 can be calculated by,

cations, gas diffusion across the EDL might be fundamentally different from that in the bulk

electrolyte, resulting in an interfacial transport resistance R_{ls} associated with the EDL that has

not been carefully investigated in existing fundamental research of bubble growth.

$$R_{\rm l} = \frac{t_{\rm l}}{D_{\rm g}} \tag{48}$$

where t_1 is the liquid film thickness. Figure 9c shows R_1 as a function of t_1 estimated using eq. 48. Although the liquid film thickness is at microscale, the resulting transport resistance can be very large due to the ultralow gas diffusivity in liquid (blue curve in Figure 9c). For example, when the current density is 0.1 A/cm^2 , transport resistance across a $100 \text{ }\mu\text{m}$ thick liquid film

- can reach $\sim 10^4$ s/m, resulting in ~ 100 supersaturation of dissolved gas at the electrode-
- 2 electrolyte interface (red curve in Figure 9c).

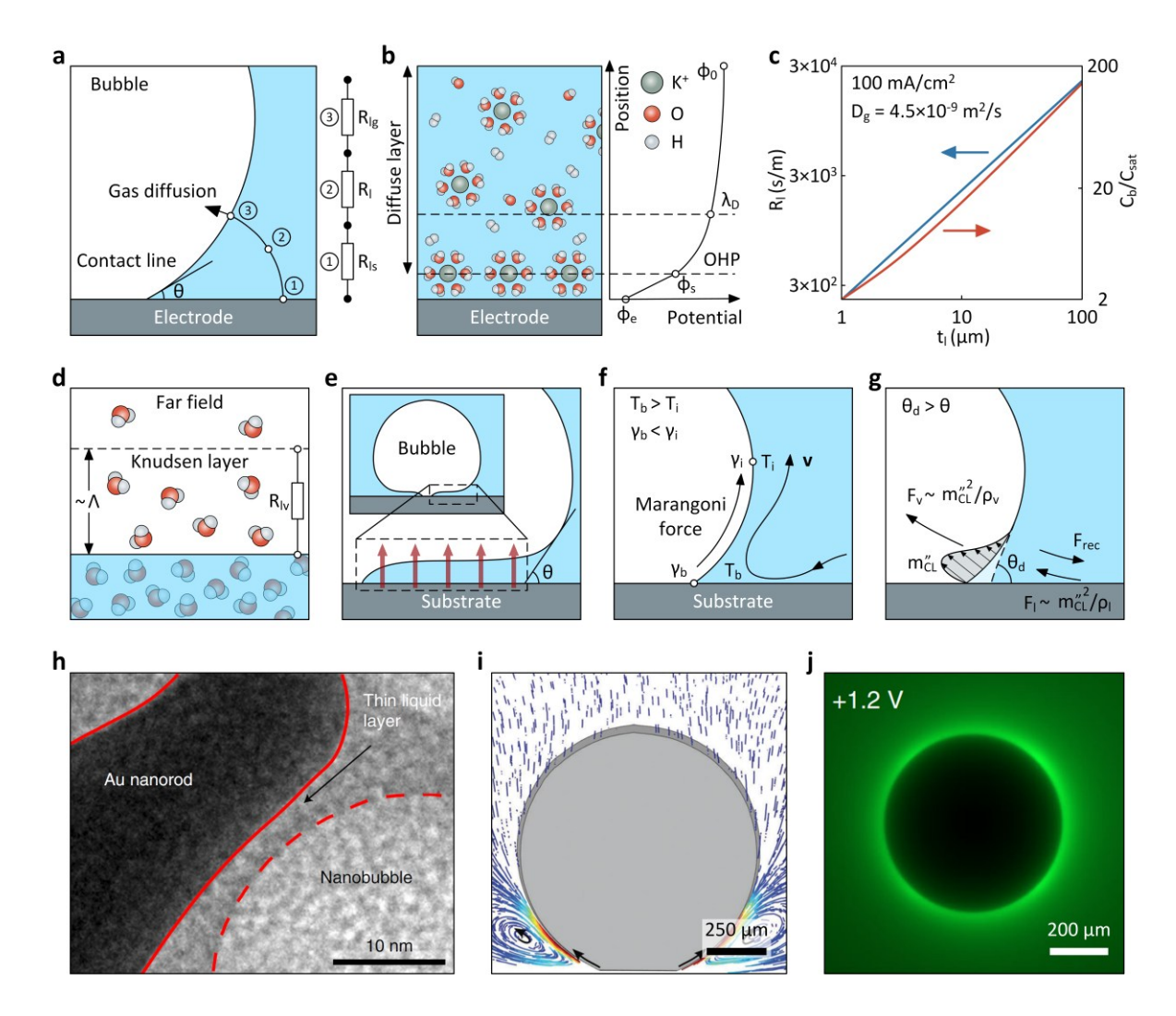


Figure 9. Interfacial transport associated with bubble growth. (a) Gas transport near the three-phase contact line of bubble. Transport resistance can come from the electrode-electrolyte interface (①), liquid thin film between the electrode and bubble (②), and electrolyte-gas interface (③). (b) Structure of the EDL and the resulting potential distribution. The highly non-uniform distribution of solvated cations could induce additional collision mechanisms with dissolved gas and hence create transport resistance across the EDL. (c) Transport resistance across the liquid thin film and the resulting supersaturation of dissolved gas as a function of the liquid film thickness. (d) Transport resistance at the liquid-vapor interface due to the Knudsen layer. Thickness of the Knudsen layer is several mean free paths. (e) Schematic of liquid microlayer beneath the bubble base observed in the boiling process. Microlayer

evaporation plays an important role in the boiling heat transfer. (f) Marangoni flow induced by the temperature gradient along the liquid-vapor interface. Temperature gradient along the liquid-vapor interface creates a gradient of surface tension, which drives the surrounding liquid flowing to the upper part of the bubble. (g) Vapor recoil effect near the three-phase contact line. The distinct momenta carried by vapor and liquid fluxes across the liquid-vapor interface create a vapor recoil force, which increases the bubble contact angle and enlarges the dry area covered by bubble base. (h) Liquid cell TEM image of a liquid thin film between gold nanorod and oxygen nanobubble. Presence of oxygen nanobubbles accelerates the etching rate of gold nanorod through a gas molecule tunnelling-like effect. Reproduced with permission from Ref. 216. Copyright 2022 Springer Nature. (i) Marangoni flow around a hydrogen bubble visualized by particle tracking velocimetry. Reproduced with permission from Ref. 287. Copyright 2018 Royal Society of Chemistry. (j) Epifluorescence image of hydroxyl radicals around a gas bubble. Hydroxyl radicals were produced from the oxidation of hydroxyls at the liquid-gas interface. Reproduced with permission from Ref. 176. Copyright 2022 Springer Nature. In addition to R_1 , gas transport from the liquid phase to the gas phase across the electrolyte-gas interface could also experience resistance R_{lg} (3) in Figure 9a), which arises from the nonequilibrium state of gas molecules within several mean free paths Λ above the liquid interface, in the so-called Knudsen layer (Figure 9d). 107-109 Transition from the non-equilibrium state in the Knudsen layer to the equilibrium state at the far field relies on molecular collisions, which induces transport resistance of gas molecules. 23,68,71,110,116 The Knudsen layer dictates the fundamental limit of gas transport, since it inevitably forms at the liquid-gas interface (Figure 9d). Gas transport with R_{lg} as the dominant resistance is thus known as the kinetically limited transport. 23,68,71,108,116 This interfacial resistance has been extensively studied in liquid-vapor systems and widely recognized in phase change heat transfer. 68 In particular, $R_{\rm lg}$ can be analytically estimated using the Hertz-Knudsen equation 265,266 and the Schrage equation (eq. 12),¹¹⁰ which were derived from the classical kinetic theory. A more accurate theoretical description of R_{lg} is given by the Boltzmann transport equation, which can be analytically approximated with the moment method solution 107,112 or numerically solved using the direct simulation Monte Carlo (DSMC). 106,113-115 On the other hand, the kinetically limited transport

1

2

3

4

5

6

7

8

9

10

11

12

13

14

15

16

17

18

19

20

21

22

23

24

25

26

27

28

has been experimentally confirmed by Lu *et al.* when measuring the evaporation on a nanoporous membrane. Details about recent advances in the kinetically limited transport across liquid-vapor interface have been summarized by Vaartstra *et al.* in Ref. 68. Despite the important role of R_{lg} in gas transport, to the best of our knowledge, it has not been considered into the bubble growth during electrochemical gas evolution reactions. It will be of fundamental interest to understand whether R_{lg} also exists at the electrolyte-gas interface and quantify how large it will be. The above analytical, numerical, and experimental tools developed in phase change heat transfer will be valuable to address this fundamental research question. Comprehensive understanding of R_{ls} , R_{l} , and R_{lg} will ultimately enable a fully quantitative description of how gas molecules migrate from the electrode-electrolyte interface to the electrolyte-gas interface, leading to more accurate predictions and new engineering space of bubble growth from first-principles.

In addition to the above general physical picture of gas transport, we would like to highlight three specific interfacial phenomena, i.e., the liquid microlayer, Marangoni flow, and vapor recoil effect, which have received increasing attentions in phase change heat transfer. More notably, recent studies imply that similar transport phenomena could also exist in electrochemical gas evolution reactions and hence affect the behaviors of bubbles. We will discuss potential connections between two research fields and comment on the opportunity to develop a convergent understanding of bubble dynamics. Conventional description treats the shape of a heterogeneously nucleated bubble as a spherical cap, consisting of a flat electrodegas interface (i.e., the bubble base) and a curved electrolyte-gas interface (Figure 9a). However, recent works on bubbles in the boiling process have shown evidence deviating from this conventional understanding. 94,267-270 Instead of a completely "dry" bubble base covered by gas, there is liquid thin film between the bubble base and heating surface (Figure 9e), resulting in a "wetted" bubble base. 94,268-270 From the center of the bubble base to the three-phase contact line, the liquid thin film transitions from a ~ 10 nm thick adsorbed film to a ~ 1 µm thick evaporating film, and finally to a $\sim 1-10$ µm thick microlayer (Figure 9e). The bubble contact angle θ is hence a more macroscopic quantity to describe the bubble shape, which can be more precisely defined as the apparent contact angle or macroscopic contact angle (Figure 9e). In

general, the variation of liquid thin film is governed by the interplay between the disjoining pressure and capillary pressure. ^{267,269} Specifically, the adsorbed film is a non-evaporating liquid layer where the disjoining pressure due to the long-range fluid-solid molecular interaction plays the dominant role. The evaporating film is featured by a high evaporation flux, where both the disjoining pressure and the capillary pressure are important. The microlayer region, however, is mainly affected by the capillary pressure, which ultimately dictates the apparent contact angle of bubble. Recently, the above physical picture of liquid thin film near the three-phase contact line has been numerically confirmed by Hu and Gong using the lattice Boltzmann method (LBM) simulation.²⁶⁷ Furthermore, using in situ interferometry, Zou et al. experimentally showed that the entire bubble bases can be covered by the liquid thin film on both hydrophilic and hydrophobic surfaces.⁹⁴ With bubble growth, the liquid thin film starts to dry-out from the center of bubble base, leading to a partially wetted bubble base during the boiling process. ^{268,269} Since most of heat transfer mainly occurs in the region close to the threephase contact line, the structure and evolution of adsorbed film, evaporating film, and microlayer can fundamentally affect the thermal resistance between the heating surface and liquid-vapor interface, resulting in distinct bubble growth mechanisms (Figure 9e). 94,268-270 In contrast, when modeling the gas transport during bubble growth in electrochemical gas evolution reactions, it is still commonly believed that the bubble base is completely "dry", i.e., no electrochemical reactions occur (Figure 9a). Inspired by what has been observed in phase change heat transfer as discussed above, it is hence of critical importance to investigate if similar liquid thin film and gas transport process also exist beneath the bubble in electrochemical systems, which could potentially alter the conventional understanding of the role of bubbles in electrochemical gas evolution reactions. The nonuniform temperature distribution, periodic bubble growth and departure, as well as gravitational force can induce complex flow field that contributes to the convective heat transfer. In particular, we would like to provide one example of convection in the boiling process, which is known as the Marangoni flow. Marangoni flow is a type of capillary effect driven by the gradient of surface tension.²⁷¹ Surface tension of fluids increases with the

1

2

3

4

5

6

7

8

9

10

11

12

13

14

15

16

17

18

19

20

21

22

23

24

25

26

27

28

29

decrease of temperature. Since the temperature at liquid-vapor interface (T_i) is lower than that

close to the bubble base (T_b) , surface tension on the upper part of the bubble (y_i) is higher than that at the three-phase contact line (γ_b) , creating a Marangoni force away from the heating surface (Figure 9f). Driven by the Marangoni force along the liquid-vapor interface, there is liquid circulation around the bubble. The flow pattern (v in Figure 9f) indicates that the liquid circulation brings the superheated liquid near the three-phase contact line toward the bulk region and then carries the surrounding cold liquid back to the heating surface, which enhances the heat exchange between the bulk liquid and heating surface. The Marangoni flow in the boiling process was first observed by McGrew et al. in 1966, where they successfully visualized the flow pattern around a bubble on the heating surface using tracer particles.²⁷² With the laser induced plasmonic heating, Namura et al. created a vapor bubble with an equilibrium diameter of approximately 10 µm and visualized the entire flow field induced by the Marangoni effect using tracer particles, where they found the Marangoni flow velocity around the bubble can exceed 1 m/s.²⁷³ Impacts of Marangoni flow on the boiling heat transfer were also investigated on micro-and-nanostructures, 274 under microgravity conditions, 275 and in binary mixtures. 276,277 Although our discussion mainly focuses on the boiling process, the ubiquitous role of Marangoni flow in phase change heat transfer has also been widely recognized in evaporation^{278,279} and condensation.^{280–282}

1

2

3

4

5

6

7

8

9

10

11

12

13

14

15

16

17

18

19

20

21

22

Another interfacial phenomenon occurring near the three-phase contact line is the vapor recoil effect, which originates from the unbalanced momenta carried by the liquid and vapor fluxes across the interface. $^{36,283-286}$ During the boiling process, liquid flows to the liquid-vapor interface and then evaporates to contribute to bubble growth. Momentum of the liquid flux F_1 approaching the liquid-vapor interface is scaled with,

$$F_{\rm l} \sim m_{\rm CL}^{\prime\prime}^2/\rho_{\rm l} \tag{49}$$

23 where m''_{CL} is the mass flux across the liquid-vapor interface. Similarly, momentum of the vapor flux F_v leaving the liquid-vapor interface is scaled with,

$$F_{\rm v} \sim {m_{\rm CL}^{"}}^2/\rho_{\rm v}.$$
 (50)

- 1 As shown in eqs. (49) and (50), the distinct liquid and vapor densities make the vapor
- 2 momentum much higher than the liquid momentum, leading to a vapor recoil force F_{rec} toward
- 3 the liquid side of the interface due to conservation of momentum (Figure 9g), ^{36,283–285}

$$F_{\text{rec}} = F_{\text{v}} - F_{\text{l}}.\tag{51}$$

- According to eqs. (49) (51), a large vapor recoil force can act on the three-phase contact line
- 5 due to the high heat flux in this region (Figure 9g). As a result, the bubble contact angle can
- 6 increase especially in the high heat flux condition (θ_d in Figure 9g), which enlarges the dry area
- 7 covered by bubble base. ^{36,284,285} A few experiments and simulations have provided evidence
- 8 that suggests the vapor recoil force as an important mechanism to trigger the CHF. 36,284-286

10

11

12

13

14

15

16

17

18

19

20

21

22

23

24

25

26

27

Notably, recent works have reported highly similar interfacial phenomena in electrochemical gas evolution reactions. For example, using the *in situ* liquid cell TEM, Liu and Dillon first observed a 6-8 nm thick liquid film between the gold electrode and bubble during hydrogen evolution.²¹⁵ With similar approach, Wang et al. also observed the liquid thin film when etching the gold nanorod using oxygen nanobubbles (Figure 9h).²¹⁶ They described the gas transport across the liquid thin film as a "molecule tunnelling-like effect" and showed that the reaction rate near the liquid thin film region can be enhanced by more than one order of magnitude. It is hence of fundamental interest to understand whether the liquid thin film always forms beneath the bubble base during electrochemical gas evolution reactions and has the same physical origin as the adsorbed film, evaporating film, and microlayer in the boiling process. On the other hand, the Marangoni flow was observed in electrochemical gas evolution reactions, where Yang et al. provided the first characterization in 2018 using the time-resolved particle tracking velocimetry (Figure 9i).²⁸⁷ In addition to the temperature gradient due to joule heating of the electrolyte, surface tension also varies with the gas and ion concentrations, inducing the solutal Marangoni flow.^{287,288} The combined thermal and concentration effects ultimately determine the direction and magnitude of liquid circulation around the bubble. More interestingly, since surface tension can either positively or negatively depend on the ion concentration, the direction of solutal Marangoni flow can vary with electrolyte compositions. Park et al. recently showed highly different bubble dynamics and overpotentials of hydrogen

evolution in H₂SO₄, HCl, HNO₃, and HClO₄ solutions, which were attributed to the distinct solutal Marangoni effects with different electrolyte compositions.²⁸⁸ In addition to the electrode-gas interface and flows in the bulk electrolyte, new insights into the role of electrolyte-gas interface were also obtained in recent study. Specifically, conventional understanding commonly believes that the electrolyte-gas interface is inert to electrochemical reactions. For this reason, the general physical picture of gas transport shown above describes gas generation on the electrode surface and diffusion across the electrolyte-gas interface (Figure 9a). However, Vogel et al. reported experimental evidence deviating from this common understanding. ¹⁷⁶ In the oxidization of hydroxides to hydroxyl radicals, they observed the EDL on the electrolyte-gas interface due to the accumulation of OH (Figure 9j). As a result, the electrochemical reaction also occurs on the electrolyte-gas interface, which extends the reaction area and leads to higher current density compared to the condition without bubbles. These phenomena highlight the necessity to systematically revisit the roles of the electrodeelectrolyte, electrolyte-gas, and electrode-gas interfaces in electrochemical systems. Although we have seen potential connections of interfacial transport between phase change heat transfer and electrochemical gas evolution reactions, there is still no clear path toward a unified understanding, which requires significant efforts in future study.

3.2.3. Bubbles in Phase Change Heat Transfer and Electrochemical Gas Evolution Reactions: Distinctions

We have discussed a number of close connections between phase change heat transfer and electrochemical gas evolution reactions. Although the general principles of heat and mass transfer have the similar physical origin, the coupled gas and ion transport as well as the presence of electric field could also make the transport characteristics of hydrogen evolution distinct from that of the boiling process. This suggests that the knowledge developed in phase change heat transfer are not always directly transformable to electrochemical gas evolution reactions. To enable a clear path of knowledge translation, it is hence necessary to carefully identify the different transport mechanisms between two research fields. In this Section, we provide an example to illustrate the key distinctions in bubble growth and highlight research opportunities for mechanistic understanding.

We discuss the heat and mass transfer associated with single bubble growth during the boiling (Figure 10a) and gas evolution (Figure 10b) processes. We note that our discussion still considers a "dry" bubble base. Figure 10c shows the schematic of representative temperature T_s and heat flux q_s'' distributions along the heating surface. Due to the low thermal resistance, heat flux reaches the maximum near the three-phase contact line of the bubble (red curve in Figure 10c). Since vapor thermal conductivity ($\approx 0.025 \text{ W/m/K}$) is much lower than liquid thermal conductivity ($\approx 0.68 \text{ W/m/K}$), temperature of the bubble base can be higher than that of the solid-liquid interface (blue curve in Figure 10c). In electrochemical systems, the analogous pairs of T_s and q_s'' are twofold: they can be either the potential and current density pair considering electrochemistry or the gas concentration and mass flux pair considering gas evolution, where the current density is proportional to mass flux. Figure 10d shows the schematic of representative dissolved gas concentration C_s , mass flux j_s , and potential ϕ_e distributions along the electrode surface. Since the electrode is a conductor with large electrical conductivity ($\chi_s \sim 10^6 - 10^7$ S/m), the electrode surface is typically an equipotential surface (blue curve in Figure 10d), which results in a highly uniform current density and mass flux distribution along the electrode-electrolyte interface (red curve in Figure 10d) according to the Butler-Volmer equation (eq. 10) or Tafel equation (eq. 11). At the three-phase contact line, the current density and mass flux suddenly drop to zero (red curve in Figure 10d), because it is commonly believed that no electrochemical reactions occur at the electrode-gas interface. As discussed above, the resistance of gas diffusion increases from the three-phase contact line along the electrode-gas interface (Figure 9c). To maintain a uniform mass flux, the dissolved gas concentration also increases from the three-phase contact line accordingly (yellow curve in Figure 10d).

1

2

3

4

5

6

7

8

9

10

11

12

13

14

15

16

17

18

19

20

21

22

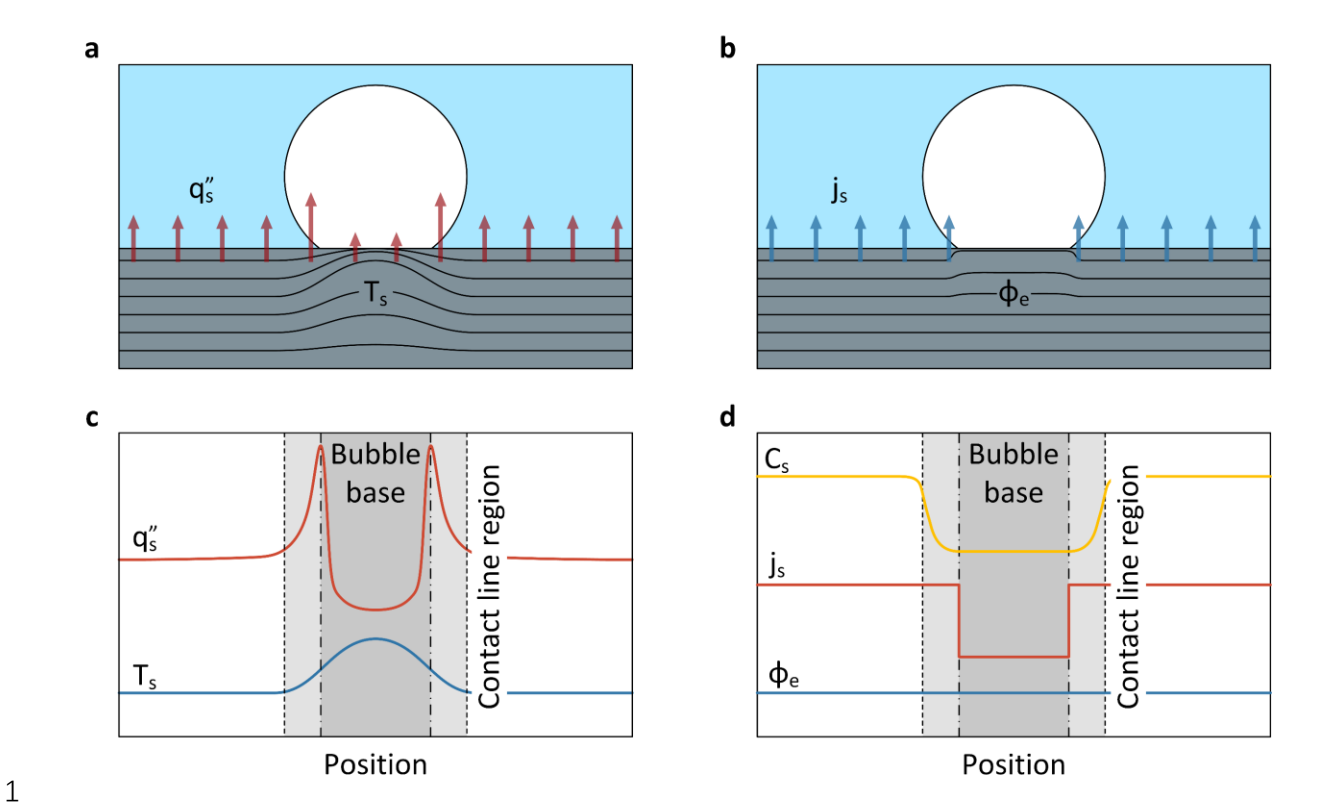


Figure 10. Distinct transport characteristics of the boiling and gas evolution processes near the three-phase contact line. (a) Heat transfer associated with the growth of a vapor bubble during the boiling process. (b) Mass transfer associated with the growth of a gas bubble during the gas evolution process. (c) Schematic of temperature distribution and corresponding heat flux profile along the heating surface. Most of heat transfer occurs near the three-phase contact line of the vapor bubble. Bubble base shows higher temperature and lower heat flux due to the much lower thermal conductivity of vapor as compared with that of solid substrate and surrounding liquid. (d) Schematic of potential distribution and corresponding current density and gas concentration profiles along the electrode surface. Due to the high electrical conductivity, the electrode surface can be treated an equipotential surface, which leads to a uniform current density profile across the electrode-electrolyte interface and high gas concentration far away from the three-phase contact line.

It hence can be seen that heat and mass transfer during the boiling and gas evolution processes

can exhibit distinct behaviors. Comparing the pair (T_s, q_s'') with the pair (ϕ_e, j_s) , the spatial

variation of ϕ_e is much lower than that of T_s (blue curves in Figures 10c and 10d). This is

fundamentally because the range of thermal conductivity from solid to gas is much narrower

than the range of electrical conductivity. 289-291 Although thermal conductivity of the heating 1 surface ($k_s \sim 10^2$ W/m/K) is much higher than that of liquid ($k_l \approx 0.68$ W/m/K) and vapor ($k_v \approx$ 2 0.025 W/m/K), the less than four orders of magnitude difference among them indicates that the 3 heating surface is not an ideal "thermal conductor" and the gas bubble is not an ideal "thermal 4 insulator". 289,290 As a consequence, heat conductions through the heating surface, solid-liquid 5 interface, and liquid-gas interface are highly coupled, leading to non-zero heat flux and 6 7 elevated temperature at the bubble base (dark-grey region in Figure 10c). In contrast, electrical conductivities ranging from solid ($\chi_s \sim 10^6 - 10^7$ S/m) to liquid ($\chi_l \sim 10^{-5} - 1$ S/m) and gas (χ_g 8 $\sim 10^{-15}-10^{-9}$ S/m) can span over 20 orders of magnitude.²⁹¹ Therefore, the electrode can be 9 treated as an ideal "electrical conductor" compared with the electrolyte and gas bubble, 10 exhibiting a highly uniform potential distribution (blue curve in Figure 10d). In addition, the 11 spatial variation of q_s'' also behaves highly different from that of j_s (red curves in Figures 10c 12 and 10d). This is because unlike the relationships between T_s and q_s'' as well as C_s and j_s , 13 which are determined by fundamental transport laws (e.g., Fourier's law and Fick's law), the 14 relationship between ϕ_e and j_s is governed by the electrochemical kinetics (eqs. 10 and 11). 15 16 Therefore, the impact of bubbles on heat and mass transfer during the boiling and gas evolution processes does not always exhibit similar characteristics. We note that we have only discussed 17 one example regarding the distinction between two research fields. More systematic studies to 18 fully understand the connections and distinctions are highly encouraged to facilitate a clear 19 path of knowledge translation. 20

3.2.4. Impact of Bubble Growth on Electrochemical Overpotentials

21

22

23

24

25

26

27

28

29

Although bubble growth during the gas evolution process has been relatively well understood, existing knowledge still cannot fully address the inverse problem, *i.e.*, how bubble growth affects the electrochemical process, which is of even more critical importance from a perspective of high-performance electrolytic cell design. The key challenge to understand the impact of bubble growth on electrochemical overpotentials originates from the complex coupling of multiple overpotential terms with bubble dynamics through gas and ion transport, which has induced significant debates. Therefore, despite numerous experimental evidences showing that bubbles can significantly affect the total overpotential, precisely quantifying how

each specific loss mechanism (i.e., activation, ohmic, and concentration overpotentials) varies with the dynamic behaviors of bubble (e.g., evolution of electrolyte-gas interface, expansion of bubble base, variation of contact angle, and convection of electrolyte, etc.) in different growth regimes (i.e., inertia-controlled growth, diffusion-controlled growth, and reactioncontrolled growth) is fundamentally challenging. In this Section, we aim to critically analyze the role of bubble growth in electrochemical gas evolution reactions by reviewing previous studies. Although it is highly desirable to decouple different loss mechanisms using theoretical approaches, the current analysis will primarily focus on experimental results due to the lack of high-fidelity simulations. Challenges and opportunities for numerical simulation of the gas evolution process will be discussed in Section 3.4. Figure 11a schematically shows a representative temporal response of total overpotential (top panel of Figure 11a) with bubble growth (bottom panel of Figure 11a) under a constant current density, which has been confirmed in many experiments. 258,292-294 From bubble nucleation, the total overpotential (blue curve in Figure 11a) increases with the bubble radius (red curve in Figure 11a) and reaches the maximum when the bubble departs from the electrode surface. After bubble departure, the total overpotential rapidly drops until a new bubble growth cycle starts (Figure 11a). Since the increase of total overpotential is always associated with bubble growth, there can be an impression that bubbles are undesirable for electrolysis, which are commonly believed by the community of electrochemical gas evolution reactions. 13,14,295 However, liquid-vapor phase change through intensive bubble generation is one of the most efficient heat transfer modes as compared with conduction, convection, and radiation. 23,27,38,64,65 This interesting "paradox" between two communities inspires us to carefully re-think the role of bubbles in the gas evolution process.

1

2

3

4

5

6

7

8

9

10

11

12

13

14

15

16

17

18

19

20

21

22

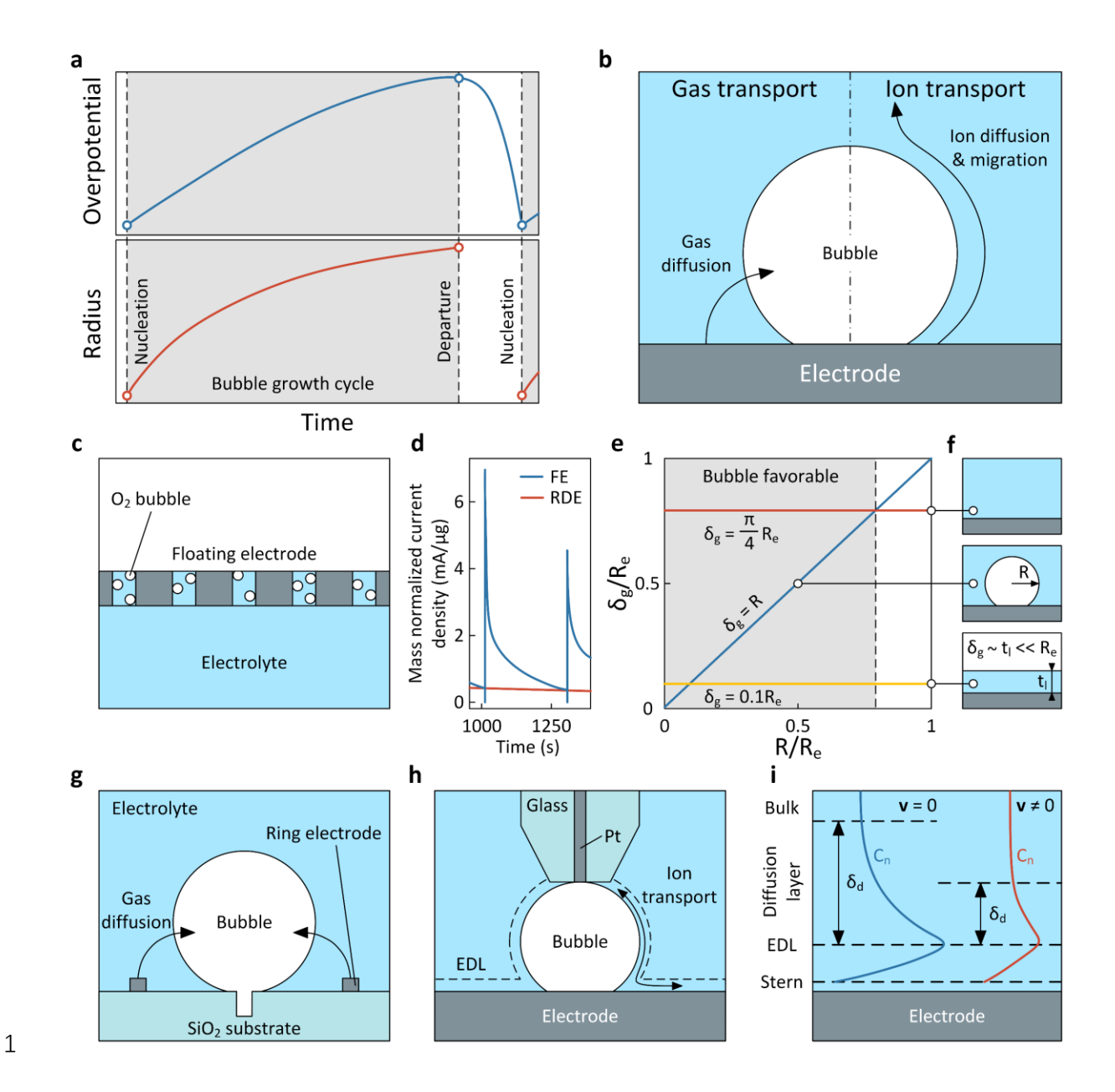


Figure 11. Impact of bubble growth on electrochemical overpotentials. (a) Representative variation of total overpotential during single bubble growth. Total overpotential typically increases with bubble radius and reaches the maximum value at the moment of bubble departure. (b) Schematic of gas and ion transport associated with single bubble growth. Gas and ion transport follows different paths and could bring distinct impacts on each overpotential term. (c) Schematic of a floating electrode (FE) for oxygen evolution. The FE promotes bubble departure and hence reduces overpotentials induced by bubbles. (d) Mass normalized current density as a function of time on the FE and standard rotating disk electrode (RDE). Higher current density was achieved on the FE under the same applied potential. Variations of current

density observed on the FE can be attributed to the periodic bubble departure. Data is reproduced from Jovanovič et al.'s experiments with permission from Ref. 302. Copyright 2019 American Chemical Society. (e) Gas diffusion layer thickness as a function of bubble radius. Both gas diffusion layer thickness and bubble radius are normalized by the electrode radius. (f) Schematics of gas diffusion across the bulk electrolyte (top panel), liquid-gas interface of a bubble (middle panel), and a thin film of electrolyte (bottom panel). For gas diffusion across the bulk electrolyte, the gas diffusion layer thickness is scaled with the electrode radius. For gas diffusion across a thin film of electrolyte, the gas diffusion layer thickness is scaled with the film thickness. For gas diffusion across the liquid-gas interface of a bubble, the gas diffusion layer thickness is scaled with the bubble radius. Compared with the bulk electrolyte, bubbles can be more favorable to reduce the resistance of gas transport unless the electrode size is comparable to the bubble size. (g) Schematic of a ring-shape microelectrode for hydrogen evolution. By spatially separating the locations of bubble growth and electrochemical reaction, impact of bubble coverage on activation overpotential can be decoupled from the measurement. (h) Ion transport through the overlapped EDLs at electrodeelectrolyte and electrolyte-gas interfaces. Bubble induced ohmic resistance for ion transport was characterized by the SECM. (i) Schematic of ion concentration profiles across the electrolyte with and without convention flow. Introducing convection flow into the electrolyte can reduce the Nernst diffusion layer thickness and decrease the ion concentration at the boundary of EDL, which could lower the concentration overpotential across the EDL.

1

2

3

4

5

6

7

8

9

10

11

12

13

14

15

16

17

18

19

20

21

22

23

24

25

26

27

28

We first provide an overview of the potential impacts of bubble growth on each overpotential term. During electrochemical gas evolution reactions, gas and ion transport are highly coupled while following completely different paths, *i.e.*, gas transport is from the electrode to the bubble (left side of Figure 11b) whereas ion transport is around the bubble and between two working electrodes (right side of Figure 11b). This feature naturally makes bubble growth could affect electrochemical overpotential through (1) gas transport and (2) ion transport. In general, gas transport mainly intervenes with the activation overpotential η_{act} by (1) blocking the reaction area via bubble base and (2) altering the gas supersaturation at the electrode-electrolyte

- interface. With a bubble coverage ratio Θ_{bub} , the current density through the reaction area of a
- 2 flat electrode surface can be expressed as,

$$i = \frac{I}{A_{\text{proj}}(1 - \Theta_{\text{bub}})}$$
 (52)

- 3 where I is the total current through the electrolytic cell and A_{proj} is the projected area of
- 4 electrode. In practice, the area-projected effective current density $i_{proj} = I/A_{proj}$ (also known as
- 5 the nominal current density) is commonly used to represent the performance of the electrolytic
- 6 cell, because it reflects the total production rate. Substituting eq. (52) into the Tafel equation
- 7 (eq. (11)), activation overpotential due to bubble coverage can be estimated as,

$$\eta_{\text{act}} = \eta_0 \log_{10} \frac{i_{\text{proj}}}{i_0 (1 - \theta_{\text{bub}})} = \eta_0 \log_{10} \frac{i_{\text{proj}}}{i_0} + \eta_0 \log_{10} \frac{1}{(1 - \theta_{\text{bub}})}.$$
(53)

- 8 As shown in eq. 53, the increase in bubble coverage will lead to the increase in activation
- 9 overpotential with respect to the area-projected effective current density. The bubble coverage
- 10 overpotential can thus be defined as,

11

12

13

14

15

16

17

18

19

20

21

22

23

$$\eta_{\text{bub}} = \eta_0 \log_{10} \frac{1}{(1 - \theta_{\text{bub}})}.$$
(54)

Effects of bubble coverage on overpotential have been shown in several experiments. For example, Darby and Haque studied hydrogen evolution on a 1.2 mm diameter electrode. 260 The small surface area of electrode enables only one bubble on the electrode during most of the time, making it easier to quantify the single bubble impact. They simultaneously measured the electrode surface area exposed to electrolyte and the current density as a function of time. In a bubble growth and departure cycle, the exposed electrode surface area first decreased to approximately 45% of the total electrode surface area and then increased, where the current density exhibited a synchronous dependence. This interesting result provides direct evidence that bubble coverage can create undesirable overpotential to the electrochemical process. We would note that η_{bub} given by eq. 54 only accounts for the effect of bubble coverage on activation overpotential. However, the bubble covered area also blocks ion transport and interferes with the EDL, which could induce additional ohmic and concentration overpotentials and will be discussed later from the perspective of ion transport. Experimental measurements

- typically show the overall effect of bubble coverage on total overpotential, whereas more
- 2 efforts about how to decouple the impact on each overpotential term are expected to be carried
- 3 out in future study.
- 4 Bubble induced gas transport can also impact overpotential by changing the gas supersaturation
- 5 at the electrode-electrolyte interface. When gas transport from the electrode to bubble is
- 6 governed by diffusion, the total mass flow rate can be estimated by,

$$J_{\rm g} = S_{\rm bub} D_{\rm g} (C_{\rm s} - C_{\infty}) \tag{55}$$

- 7 where $S_{\text{bub}} = 4\pi R$ is the shape factor of a spherical bubble. Average mass flux across the liquid-
- 8 gas interface is thus given by,

$$j_{\rm g} = D_{\rm g} \frac{C_{\rm s} - C_{\infty}}{\delta_{\rm g}} \tag{56}$$

where the gas diffusion layer induced by bubble is $\delta_g = 4\pi R^2/S_{bub}$. Under the same current density, eq. 56 shows that the larger bubble will create the thicker gas diffusion layer and the higher gas supersaturation on the electrode surface. According to the extended Butler-Volmer equation (eq. 26), the higher gas concentration on the electrode-electrolyte interface can accelerate the reverse reaction rate, which increases the activation overpotential. We note that the gas concentration induced overpotential is sometimes referred to as the concentration overpotential and estimated using the Nernst equation. However, in Section 2.3, we have demonstrated that this understanding is not accurate, because eq. 26 indicates that the gas concentration induced overpotential is fundamentally related to the activation overpotential. We also note that many studies estimated the activation overpotential using the conventional Butler-Volmer equation (eq. 10) or Tafel equation (eq. 11). Although eqs. 10 and 11 are widely applicable to various electrolysis conditions, the increase of activation overpotential due to gas concentration cannot be captured by these two equations. In addition to directly affecting the activation overpotential, gas supersaturation on the electrode surface can also indirectly change the total overpotential through bubble nucleation. As described by eq. 33, the higher gas

supersaturation will create the more nucleation sites, which then couples with the electrochemical process and alters the total overpotential.

On the other hand, bubbles can impact the electrochemical process by coupling with ion transport, which is typically reflected to the increase in ohmic and concentration overpotentials. Specifically, the bubble induced ohmic loss originates from the fact that gas bubbles are impermeable to ions. As a results, the higher void fraction of gas bubbles floating in the bulk electrolyte, the lower ion conductivities. The bubbly electrolyte can be treated as a porous media for ion transport, where the bubble and electrolyte represent the dispersed and continuum phases, respectively. ^{296–298} According to the effective medium theory, there have been several models developed to estimate the effective ionic conductivity $\chi_{n,\text{bub}}$ due to the presence of dispersed phase, which have been summarized in Ref. 13. As an example, we show the effective ionic conductivity as a function of dispersed phase void fraction (ξ_{dis}) given by the Maxwell-Eucken equation, ¹³

$$\frac{\chi_{n,\text{eff}}}{\chi_n} = \frac{1 - \xi_{\text{dis}}}{1 + \frac{\xi_{\text{dis}}}{2}}.$$
 (57)

Although existing models (*e.g.*, eq. 57) can provide reasonable predictions to the ionic conductivity of electrolytes with glass beads,²⁹⁶ emulsions,²⁹⁷ and foams²⁹⁸ as dispersions, it is still not fully clear if these models can well describe the ohmic overpotential in the gas evolution process due to the lack of direct comparisons with experiments. In particular, we note that multiple dynamic features of bubbles are not considered into the effective medium theory, including the migration and expansion of bubbles, flow field induced by bubbles, bubble size distribution, and spatial distribution of bubble void fraction. For example, since bubble void fraction increases along the liquid channel of PEM-type cell, the resulting ohmic loss cannot be captured by eq. 57, which considers a uniformly distributed dispersed phase. Tobias experimentally showed the variation of bubble void fraction and its impact on the current distribution along the channel of electrolyzer, suggesting a change of ohmic resistance along the flow direction.²⁹⁹ Vogt developed a hydrodynamic model considering the distribution of bubble void fraction as well as the flow rates of liquid and gas.³⁰⁰ He showed that the ionic

1 conductivity increases with the ratio of liquid to gas flow rate, which agrees with Hine and

2 Murakami's experiments well.³⁰¹ In addition to the dynamic features in the bulk region, how

the bubble coverage on the electrode surface affects the total ohmic overpotential also remains

4 elusive, which requires extra considerations in future study.

3

5

6

7

8

9

10

11

12

13

14

15

16

17

18

19

20

21

22

23

24

25

26

27

28

29

The bubble induced resistance to ion transport could create undesirable ion concentration profile near the electrode-electrolyte interface and raise the concentration overpotential. As discussed in Section 2.3, the concentration overpotential corresponds to the potential jump across the EDL that repels ions from the electrode surface to the bulk electrolyte by overcoming the inverse diffusion flux of ions (Figures 4a and 4b). To simplify our discussion, we still take the cathode reaction of alkaline water electrolysis as an example. It can be expected that the higher OH concentration on the boundary of EDL is, the larger OH diffusion flux forms toward the electrode surface and the higher concentration overpotential is required to create an even stronger OH migration flux opposite to the diffusion flux (Figure. 4d). According to this basic principle, bubbles are expected to impact the concentration overpotential through multiple mechanisms. First, the potential distribution and structure of EDL might be affected by the bubble base, which ultimately alter the concentration overpotential. Meanwhile, the presence of bubbles could intervene with ion transport and increase the ion concentration on the boundary of EDL, which potentially increases the concentration overpotential. On the other hand, convection flows due to bubble growth, coalescence, departure, and the Marangoni effect could also promote ion transport and reduce the ion concentration on the boundary of EDL. Due to the challenges of decoupling the above bubble induced effects, it is still unclear which mechanisms dominate the variation of concentration overpotential on gas evolving electrodes. We next review a few representative works that largely advanced the fundamental understanding of how bubbles affect overpotentials through both gas and ion transport. Jovanovič et al. developed a floating electrode (FE) which was placed on the surface of the bulk electrolyte (Figure 11c).³⁰² The floating electrode can significantly reduce the distance between the electrode-electrolyte interface and electrolyte-gas interface, which is highly favorable to promote gas transport and bubble departure (Figure 11c). They measured the mass normalized current density during oxygen evolution and compared the performance of the

floating electrode with that of a standard rotating disk electrode (RDE, Figure 11d). Interestingly, they showed that the current density on the floating electrode exhibits a periodic feature (blue curve in Figure 11d), which is always higher than the current density on the rotating disk electrode (red curve in Figure 11d). In each cycle, there was a sudden increase of the current density on the floating electrode due to bubble departure and formation of new nucleation sites. The current density then gradually decreased with bubble growth and finally converged with the current density on the rotating disk electrode (Figure 11d). We believe the results shown in Jovanovič et al.'s work provide interesting insights into the role of bubbles in electrolysis. Briefly, whether bubble is desirable to electrolysis depends on the references used for comparison. For example, it is commonly seen that the overpotential increases with bubble growth (Figure 11a). We have the impression that bubble is undesirable because the reference used for this comparison is the overpotential at the initial stage of bubble nucleation, which exhibits the lowest resistance approaching to the intrinsic resistance of electrolyte-gas interface. However, if we change the reference to gas transport across the bulk electrolyte via diffusion and convection only, we will see gas transport with bubble growth and departure exhibit a much lower resistance. This is the reason why oxygen evolution across the bulk electrolyte on the rotating disk electrode always has lower current density compared with that on the floating electrode (Figure 11d). In addition, this is also the reason why boiling through massive bubble generation is believed as one of the most efficient modes to transfer heat. As a result, it is not accurate to simply say that bubble is undesirable to electrolysis. In other words, this means eliminating bubble formation is also not always beneficial to the performance of an electrolytic cell. For example, if we eliminate bubbles by raising the nucleation barrier and reducing nucleation sites, gas transport can only rely on diffusion and convection, which will lead to even worse electrolysis performance. However, if we eliminate bubbles by reducing the distance between the electrode-electrolyte and electrolyte-gas interfaces as well as promoting bubble departure at the early stage, there can be a significant improvement of electrolysis performance. Therefore, at least from the perspective of gas transport, bubbles can be favorable for the gas evolution process and smaller bubbles exhibit less transport resistance compared with larger bubbles.

1

2

3

4

5

6

7

8

9

10

11

12

13

14

15

16

17

18

19

20

21

22

23

24

25

26

27

28

We provide more in-depth analysis on gas transport by comparing the resistance induced by bulk electrolyte, gas bubble, and liquid thin film. Figure 11e shows the gas diffusion layer thickness of the bulk electrolyte (red curve), a gas bubble (blue curve), and a thin liquid film (yellow curve), which is proportional to the gas diffusion resistance. The gas diffusion layer thicknesses induced by bulk electrolyte (top panel of Figure 11f) and bubble (middle panel of Figure 11f) are scaled with the electrode size (red curve in Figure 11e) and bubble radius (blue curve in Figure 11e), respectively. As long as the bubble size is much smaller than the electrode size, which is valid for most of gas evolving electrodes, gas transport through bubbles is more efficient than that through the bulk electrolyte (grey shadow in Figure 11e). In addition, since the gas diffusion layer thickness is scaled with bubble radius, reducing bubble size and promoting bubble departure at the early stage can be desirable to decrease gas supersaturation and reduce the total overpotential. For example, Ikeda et al. investigated bubble behaviors during the oxygen evolution process using nickel wire as the electrode.³⁰³ They showed that smaller nickel wire diameter can enhance bubble departure, resulting in lower overpotential. Iwata *et al.* created different bubble departure diameters ranging from $\approx 150 \, \mu \text{m}$ to $\approx 4 \, \text{mm}$ by controlling the wettability of porous electrode, where they observed the transport overpotential induced by large bubbles can be more than three times of that due to small bubbles.³⁰⁴ Compared with reducing bubble diameters, directly decreasing the distance from the electrodeelectrolyte interface to the electrolyte-gas interface seems a more effective approach to further reduce the resistance of gas transport (bottom panel of Figure 11f). We provide an example when the diffusion layer thickness of liquid thin film is equal to 0.1 times of the electrode size (yellow curve in Figure 11e). The improved electrolysis performance demonstrated on the floating electrode³⁰² and the capillary feed-type electrolytic cell²¹ can be attributed to the adoption of liquid thin film. Recently, Peñas decoupled the gas evolution process from the electrochemical process using a ring-shape microelectrode with a gas cavity located at the center of the substrate (Figure 11g).²⁵⁸ Since bubble nucleation occurs in the gas cavity instead of the ring microelectrode (Figure 11g), the impact of bubble coverage on the activation overpotential was decoupled from the measurements. Combining the experiments with simulations, they showed that the presence of electrolyte-gas interface due to bubble growth

1

2

3

4

5

6

7

8

9

10

11

12

13

14

15

16

17

18

19

20

21

22

23

24

25

26

27

28

- can significantly reduce the supersaturation on the electrode surface and enhance gas transport.
- 2 The same group of researchers further identified the competing effect of bubbles on reducing
- 3 the gas supersaturation while increasing the ohmic loss using a similar experimental
- 4 apparatus.³⁰⁵
- 5 On the other hand, the impact of bubble growth on ion transport and relevant overpotentials
- 6 (i.e., ohmic overpotential and concentration overpotential) has also been carefully
- 7 characterized in recent studies. For example, Haziri reported a new path for ion transport due
- 8 to the overlap of EDLs created by the electrode and the gas bubble (Figure 11h).³⁰⁶ Depending
- on the sign of voltages applied to the electrode, ion transport through the path can be either
- enhanced or suppressed. By switching the applied voltage from -1 V to +1 V, the bubble
- induced ohmic resistance increased from 133 M Ω to 302 M Ω , as compared with the ohmic
- resistance of 160 M Ω without bias. In addition, Angulo *et al.* investigated the impact of bubbles
- on the concentration overpotential in a microfluidic electrolyzer.³⁰⁷ With pH sensitive dyes,
- 14 they imaged the H⁺ concentration profile during acidic water electrolysis using fluorescence
- microscopy. In particular, they observed a significant increase of H⁺ concentration in an
- approximately 20 µm region surrounding to a single oxygen bubble (≈ 25 µm radius), which
- agrees well with the length scale of the bubble induced Nernst diffusion layer (eqs. 21-23 and
- eqs. 55-56). By introducing convection flow into the electrolyzer, they showed that the H⁺
- 19 concentration and Nernst diffusion layer thickness around the bubble can be significantly
- 20 reduced, which could potentially decrease the concentration overpotential on the gas evolving
- 21 electrode (Figure 11i). Considering the critical role of convection flow in reducing the
- 22 undesirable ion concentration, it is essential to further quantify whether the bubble induced
- 23 convection flows could bring similar impact on concentration overpotential. To make the above
- 24 discussion clear, we summarized the potential impacts of bubble growth on electrochemical
- overpotentials in Table 1.

- Table 1. Summary of potential impacts due to bubble growth induced gas and ion transport on
- 27 electrochemical overpotentials

Overpotentials	$\eta_{ m act}$	η ohm	$\eta_{ m con}$	
----------------	-----------------	------------	-----------------	--

	ı	I	I
Gas transport	1. Blocking the	1. Dictating the gas	1. Dictating the gas
	reaction area (η_{bub} in	supersaturation and	supersaturation and
	eq. 54) ^{258,260,305}	affecting bubble	affecting bubble
	2. Altering the reverse	nucleation	nucleation
	reaction rate (eq. 26)		
	3. Dictating the gas		
	supersaturation and		
	affecting bubble		
	nucleation		
Ion transport	1. Altering the reverse	1. Blocking ion	1. Interfering with the
	reaction rate (eq. 26)	transport on the	EDL due to bubble
		electrode surface and	coverage
		bulk electrolyte (eq. 57) ^{258,305}	2. Creating the Nernst
			diffusion layer
		2. Creating new path	thickness around
		for ion transport due to	bubbles ³⁰⁷
		the overlap of EDLs ³⁰⁶	3. Accelerating ion
			transport via bubble
			induced convection
			flow ³⁰⁷

1 3.3. Bubble Interaction and Departure

- 2 Bubble departure is the final step of gas evolution that carries the electrochemically generated
- 3 gas products away from the electrode surfaces. In this Section, we discuss mechanisms of
- 4 bubble departure and review recent advances in theoretical understanding and experimental
- 5 measurements. We first discuss two general regimes, i.e., the buoyancy-driven departure and
- 6 the coalescence-induced departure, that govern the departure of an isolated bubble and multiple
- 7 interacting bubbles, respectively (Section 3.3.1). Combining with the nucleation site

distributions shown in Section 3.1.2, we then establish a statistical description of bubble interaction and explain the distribution of bubble departure diameter observed in recent experiments (Section 3.3.2). We aim to show the fundamental consistency among nucleation site distributions, bubble interaction, and distribution of bubble departure diameter, which are typically treated as three separate physical phenomena. With a unified understanding, we finally discuss how the bubble interaction and departure affect the transport overpotential in electrochemical gas evolution reactions (Section 3.3.3).

3.3.1. Regimes of Bubble Departure

Behaviors of bubble departure can be primarily understood through the force balance on an isolated bubble. $^{264,308-312}$ Buoyancy and surface tension are two predominant forces that exhibit the opposite effects on the bubble. Buoyancy F_B is a body force that tends to drive the bubble departing from the surface, whereas surface tension F_h acts on the three-phase contact line and holds the bubble onto the surface (Figure 12a). When the bubble becomes sufficiently large, buoyancy is stronger than surface tension and bubble departure occurs. Taking these two predominant forces into account, Fritz established an empirical correlation to describe the buoyancy-driven bubble departure in $1935,^{308}$

$$d_{\rm dep} = 0.0208\theta \sqrt{\frac{\gamma}{g(\rho_{\rm l} - \rho_{\rm g})}}$$
 (58)

where $d_{\rm dep}$ is the bubble departure diameter and the contact angle in eq. 58 has the unit of degree. The Fritz's correlation has been widely used to describe the departure of an isolated bubble in both boiling and gas evolution processes and shows reasonable agreements with various experiments. $^{264,308-311}$ In addition to buoyancy and surface tension, hydrodynamic forces such as lift and drag forces as well as electrostatic force can also play an important role in bubble departure, which has been discussed by Zhang and Zeng³¹³ and Taqieddin *et al.* 314,315 . It has been shown that the bubble departure diameter depends on current density, nucleation density, species concentration, and electrolyte viscosity, which cannot be fully captured by the Fritz's correlation. 288,292,316,317 For example, Fernández *et al.* showed a sudden transition from periodic departure of a single large bubble (> 500 µm diameter) to aperiodic departure of multiple small

bubbles (< 100 μm diameter) due to the slight decrease of electrolyte surface tension from 70 mN/m to 65 mN/m.²⁹² Bashkatov *et al.* observed the similar bubble departure behavior on a platinum microelectrode.³¹⁷ More notably, they observed that the large hydrogen bubble was sitting on a carpet of microbubbles (~ 10 μm thickness) covering the electrode surface. The carpet of microbubbles started to oscillate at the final stage of bubble growth before the large bubble departure. Combining numerical simulation, they attributed this unusual bubble departure phenomenon to the competition between buoyancy and electrostatic force. Recently, Park *et al.* revisited this problem by considering the effect of electrolyte composition and pointed out that the solutal Marangoni effect is the dominant mechanism to the transition from the periodic to aperiodic departures.²⁸⁸

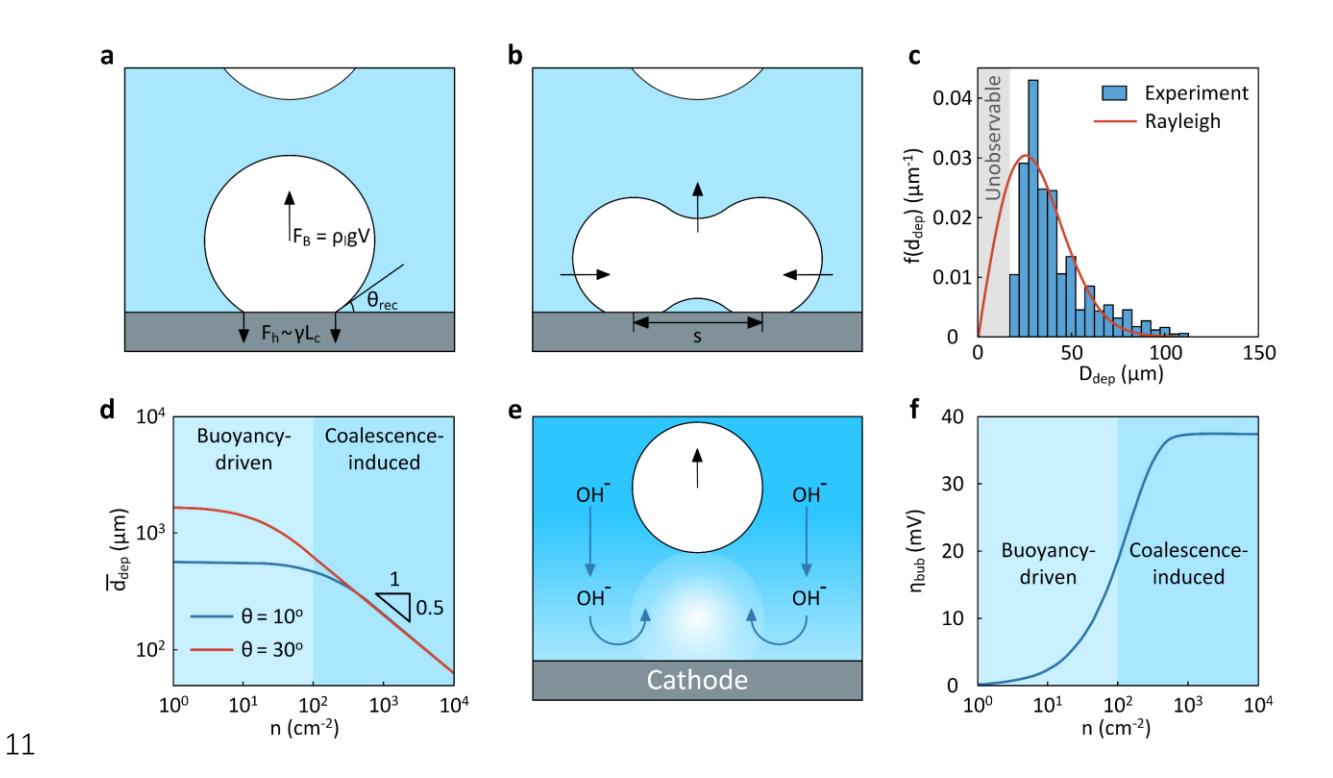


Figure 12. Physics of bubble departure and its impact on electrochemical overpotentials. (a) Buoyancy-driven bubble departure. Buoyancy-driven departure is the dominant mode for an isolated bubble, which occurs when the buoyancy is larger than the holding force at the three-phase contact line. (b) Coalescence-induced bubble departure. Bubble departure can also occur due to the spontaneous coalescence of two small bubbles. (c) Distribution of bubble departure diameter when the coalescence-induced departure is the dominant mode. The distribution of bubble departure diameter originates from the nucleation site distribution. Theoretical

prediction is compared with Rox *et al.*'s measurements.³²¹ (d) Average bubble departure diameter as a function of nucleation density. Buoyancy-driven departure is the dominant mode at low nucleation density whereas coalescence-induced departure becomes more important at high nucleation density. (e) Schematic of convection flow induced by bubble departure. (f) Bubble coverage overpotential as a function of nucleation density based on the statistical description of bubble interaction. The bubble coverage overpotential first increases with nucleation density and then reaches a plateau when the coalescence-induced departure becomes dominant.

When the bubble diameter becomes comparable with the nearest neighbor distance, it will coalesce with their neighbors before departure. Bubble coalescence can be significant in the high nucleation density condition, which not only leads to the rapid increase of bubble size but also creates new bubble departure mechanisms deviating from the buoyancy-driven process described by the Fritz's correlation (eq. 58). In a specific electrolytic environment, eq. 58 indicates that the bubble departure diameter is a constant. However, several recent experiments using the high-resolution microscopy showed that the bubble departure diameter can span a wide range and follow a certain distribution. For example, Chandran et al. studied the distribution of hydrogen bubble departure diameter during water electrolysis and showed that the departure diameter can range from less than 10 µm to more than 100 µm under the same current density.³¹⁸ Similar distributions of bubble departure diameter were also observed by Abdelghani-Idrissi et al., 319 Krause et al., 320 and Rox et al. 321 In addition, Janssen et al. showed that the bubble departure diameter monotonically decreased with the increase of nucleation density. 159 In the high nucleation density condition, bubble departure diameter shown in Janssen et al.'s experiment can be much smaller than that determined by the Fritz's correlation (eq. 58). All of these bubble departure behaviors are closely related to bubble coalescence and cannot be simply explained by the force balance on an isolated bubble.

Discovery of the coalescence-induced bubble departure provides a new perspective for understanding the small bubble departure diameter and its distribution (Figure 12b). Soto *et al.*³²² and Zhou *et al.*³²³ first observed the departure of two adjacent microbubbles (\approx 300 µm diameter) upon the spontaneous coalescence in the gas evolution and boiling processes. Then,

Ly et al. performed systematic characterization of the coalescence-induced departure of oxygen bubbles during the catalytic decomposition of hydrogen peroxide (H₂O₂) on a microhole patterned surface. 324 They observed that the coalescence-induced departure can occur within a broad range of bubble size ratios when the bubble radius was larger than $\approx 10 \mu m$ (i.e., the critical bubble radius). To understand the underlying physics of the coalescence-induced departure, Iwata et al. numerically simulated the coalescence of two identical microbubbles using computational fluid dynamics (CFD).³²⁵ They successfully recovered Soto et al.'s experimental results and identified a critical contact angle ($\approx 30^{\circ}$) above which the coalescenceinduced departure cannot occur. Combining the numerical simulation with scaling analysis, they attributed the coalescence-induced departure to the dynamics of three-phase contact line during bubble interaction, which is dictated by the competition between bubble necking and contact line depinning (Figure 12b). With LBM simulation, Zhao et al. further extended Iwata et al.'s work by considering the effects of contact angle hysteresis. 326 With a constant static contact angle, they showed that reducing the advancing and receding contact angles can significantly promote the coalescence-induced bubble departure and enlarge the critical contact angle up to $\approx 70^{\circ}$. Park et al. performed systematic investigation on the interaction of two bubbles in the boiling process, where four modes of bubble coalescence were identified.³²⁷ Insights gained from Lv et al., 324 Iwata et al., 325 Zhao et al. 326, and Park et al. 327 studies have constructed a completed regime for the coalescence-induced departure, which is bounded by the critical bubble radii, bubble size ratios, and contact angles. Recently, coalescence-induced bubble departure has attracted increasing attentions in more practical electrolytic systems. For example. Wu et al. performed alkaline water electrolysis on porous electrodes. 328 They showed that coalescence-induced departure can be the dominant bubble departure mode, especially for the porous electrode with high tortuosity. For two identical bubbles with contact angle below the critical contact angle, Iwata et al. suggested the following criterion to determine whether the bubble departure is driven by buoyancy or coalescence, ³²⁵

1

2

3

4

5

6

7

8

9

10

11

12

13

14

15

16

17

18

19

20

21

22

23

24

25

$$d_{\text{dep}}(s) = \begin{cases} 0.0208\theta \sqrt{\frac{\gamma}{g(\rho_{\text{l}} - \rho_{\text{g}})}}, & s \ge s_{\text{buo}} \\ \left(\frac{2 + 3\cos\theta - \cos^3\theta}{2}\right)^{\frac{1}{3}} s, & s < s_{\text{buo}} \end{cases}$$
(59)

where s_{buo} is defined as the buoyancy limited distance between two neighboring bubbles,

$$s_{\text{buo}} = 0.0208\theta \sqrt{\frac{\gamma}{g(\rho_{\text{l}} - \rho_{\text{g}})}} \left(\frac{2 + 3\cos\theta - \cos^3\theta}{4}\right)^{-\frac{1}{3}}.$$
 (60)

- s_{buo} is an indicator of bubble coalescence. When the distance between two neighboring bubbles
- 3 is larger than s_{buo} , these two bubbles can be regarded as isolated bubbles because the buoyancy-
- 4 driven departure will occur before the bubble coalescence. However, if the distance between
- 5 two neighboring bubbles is smaller than s_{buo} , these two bubbles are interacting with each other
- 6 and bubble departure occurs after the spontaneous coalescence.

3.3.2. Statistical Description of Bubble Interaction

- 8 In this Section, we introduce a statistical description of stochastic bubble interaction by
- 9 combining the fundamental understanding of bubble departure (Section 3.3.1) with the
- distributions of nucleation sites (Section 3.1.2). We will show this statistical description not
- only quantitatively explains the distribution of bubble departure diameter and its dependence
- on nucleation density observed in experiments, but also lays a foundation for quantifying the
- impact of bubble interaction on transport overpotential in electrochemical gas evolution
- reactions (Section 3.3.3).

- Distinct from the buoyancy-driven departure, which exhibits a constant bubble departure
- diameter, the coalescence-induced departure indicates that the bubble departure diameter is a
- function of the nearest neighbor distance (eq. 59). As shown in Section 3.1.2, the nearest
- 18 neighbor distance of nucleation sites is the random variable that follows the Rayleigh
- distribution (eq. 36).¹⁵⁷ The statistical nature of the nearest neighbor distance results in the
- distribution of bubble departure diameter. Substituting eq. 59 into eq. 36, we can obtain the
- 21 probability distribution function of bubble departure diameter, which explains the wide-spread

bubble departure diameter observed in Chandran et al., 318 Abdelghani-Idrissi et al., 319 Krause

2 et al., 320 and Rox et al.'s experiments. 321 For example, Figure 12c shows our theoretical

3 predictions of bubble departure diameter (red curve) as compared with Rox et al.'s experiment

4 (blue histogram).³²¹ The consistency between the theory and experiment except for the

unobservable region (grey shadow in Figure 12c) confirms the statistical nature of bubble

6 departure diameter.

5

9

10

13

15

16

17

20

21

7 Iwata et al. further developed a unified relationship of bubble departure and explained the

8 dependence of bubble departure diameter on nucleation density.³²⁵ The average bubble

departure diameter through multiple measurements among a large number of bubbles can be

of more interest in practical applications. Taking the distribution of bubble departure diameter

11 into account (eqs. 36 and 59), the average bubble departure diameter $\bar{d}_{\rm dep}$ is given by,

$$\bar{d}_{\rm dep} = \int d_{\rm dep}(s)f(s)ds. \tag{61}$$

Figure 12d shows the average bubble departure diameter as a function of nucleation density

given by eq. 61. In general, there are two distinct regimes of the average bubble departure

diameter, which are dictated by the buoyancy-driven (light blue region in Figure 12d) and

coalescence-induced departures (dark blue region in Figure 12d), respectively. When the

nucleation density is low (< 10² cm⁻²), the average bubble departure diameter approaches a

constant dictated by the Fritz's correlation. In the high nucleation density condition (> 10³ cm⁻

18 ²), however, eq. 61 can be reduced to, ^{157,325}

$$\bar{d}_{\rm dep} \approx 0.5 n^{-0.5} \tag{62}$$

19 which describes a -1/2-power law dependence with the nucleation density. Iwata et al.

demonstrated that eq. (62) can quantitatively explain the average bubble departure diameter as

a function of nucleation density observed in Janssen et al.'s experiment. 159,325

The above discussion mainly focuses on the interaction of bubbles on the electrode surface.

However, bubble interaction could also occur in the vertical direction, which receives much

less attention. Recently, Bashkatov et al. observed the interaction between two vertically

aligned bubbles, where the first bubble was attached to the electrode surface while the second bubble just departed from the electrode.³²⁹ With proper control of the bubble growth cycle, they showed that instead of moving away from the first bubble, the second bubble can be "attracted" by the first bubble, exhibiting a sudden reversal in motion, and then coalesce with the first bubble. Meanwhile, the coalescence of these two vertically aligned bubbles leads to a rapid increase of current density. Using the Toepler's schlieren technique, they attributed this phenomenon to the competition between buoyancy and Marangoni effect. It is interesting to further investigate whether the vertical interaction of bubbles commonly occurs in conventional electrolytic cells and how to extend the existing statistical description to quantify its impact on the electrolysis performance.

3.3.3. Impact of Bubble Interaction on Electrochemical Overpotentials

Bubble coalescence and departure can induce convection flow and alter bubble coverage, which affect the transport overpotential of water electrolysis. Phenomenologically, bubble departure is associated with the lowest overpotential induced by a single bubble as depicted in Figure 11a. This is because bubble departure drives the rewetting of surrounding electrolyte, which brings reactants to the electrode surface and elevates the local supersaturation level to trigger bubble nucleation (Figure 12e). Meanwhile, bubble departure ensures the full access of electrolyte to the electrode surface, eliminating the undesirable overpotential due to bubble coverage (eq. 54). According to the above qualitative understanding, it is widely agreed that promoting bubble departure is highly desirable to reduce the bubble induced overpotentials. However, a fully quantitative description of how bubble departure enhances the mass transfer of electrochemical gas evolution reactions is still lacking.³³⁰

In contrast, the critical role of bubble departure in the boiling process has been extensively

In contrast, the critical role of bubble departure in the boiling process has been extensively investigated. The first theoretical description of heat transfer during bubble departure, known as the transient conduction theory, was developed by Rohsenow in 1952.⁸⁹ The transient conduction theory describes that bubble departure induces the spontaneous detachment of superheated thermal diffusion layer around the vapor bubble from the heating surface. As a result, the surrounding liquid with saturation temperature replaces the superheated thermal

diffusion layer and comes into contact with the heating surface, creating a "step change" in temperature difference between the heating surface and the liquid on it. With such a physical picture, Rohsenow and co-workers estimated the heat conduction due to the "step change" in temperature at the heating surface. 89,331 They showed that heat transfer due to bubble departure plays a dominant role in the boiling process and established an analytical expression, known as the Rohsenow correlation, that relates the heat transfer data of nucleate pool boiling to the properties of working fluids. 89

Since the first theory from Rohsenow and co-workers, a number of theoretical and experimental investigations have been carried out, which have constructed a completed physical picture for the bubble departure induced heat transfer during the boiling process. 332-336 Specifically, in each bubble growth and departure cycle, the heating surface temperature at the bubble base first decreases rapidly due to the microlayer evaporation during bubble growth and the "quenching effect" associated with the detachment of thermal diffusion layer. After the bubble departure, the heating surface temperature increases gradually due to the rewetting of surrounding superheated liquid and heat conduction through the solid substrate. 251 Recently, Zhang *et al.* theoretically showed that the rewetting of superheated liquid originates from the buoyancy of vapor bubble, exhibiting similar behaviors to natural convection. 337 As a result, heat transfer during the rewetting of superheated liquid can be described as,

$$Nu = C_{\rm w} Ra^{0.25} \tag{63}$$

where $Nu = hd_{\rm dep}/k_{\rm l}$ is the Nusselt number. h is the convection heat transfer coefficient of the rewetting flow. $C_{\rm w}$ is a universal proportionality constant and Zhang *et al.* suggested $C_{\rm w} \approx$ 4.5.³³⁷ Ra is the Rayleigh number that describes the buoyancy of the departed bubble,

$$R\alpha = \frac{g(\rho_{\rm l} - \rho_{\rm v})d_{\rm dep}^3}{\mu_{\rm l}\alpha_{\rm l}} \tag{64}$$

where α_1 is the thermal diffusivity of the liquid. Interestingly, similar phenomenon was observed by Enriquez *et al.* during the gas evolution process.³³⁸ They showed that the growth of a CO₂ bubble in the supersaturated liquid can be affected by the buoyancy driven natural convection, where the Sherwood number, *i.e.*, the analogous dimensionless number to the

Nusselt number in mass transfer, also exhibits a similar 1/4-power law dependence with the Rayleigh number (eq. 63). Soto et al. further investigated the development of natural convection around single CO₂ in both unconfined and confined conditions.^{339,340} It is hence essential to investigate whether the knowledge developed in the boiling process can be extended to the electrochemical process and understand how much mass transfer enhancement and overpotential reduction can be attributed to the bubble departure induced convection flow. In addition to the convection flow, departure of multiple bubbles on the electrode surface changes the bubble coverage, which can affect the total overpotential through multiple mechanisms as discussed in Section 3.2.4. Although there still lacks quantitative understanding to describe how the bubble coverage affects the ohmic and concentration overpotentials, its impact on the increase of activation overpotential is relatively straightforward (eqs. 53 and 54). Here, we would like to provide an example to illustrate how to use the statistical description of bubble interaction to estimate the bubble coverage overpotential (η_{bub}). According to the distribution of bubble departure diameter, the upper bound of bubble coverage ratio (Θ_{bub}) is given by,

$$\Theta_{\text{bub}} = n \int \frac{\pi}{4} d_{\text{dep}}(s)^2 f(s) ds. \tag{65}$$

Substituting eq. 65 into eq. 54, the resulting bubble coverage overpotential (η_{bub}) due to stochastic bubble interaction can be estimated. Figure 12f shows the bubble coverage overpotential as a function of nucleation density given by eqs. 54 and 65. When the bubble departure is governed by buoyancy (light blue region in Figure 12f), the bubble coverage overpotential monotonically increases with nucleation density. However, when the coalescence-induced bubble departure becomes dominant (dark blue region in Figure 12f), the bubble coverage overpotential gradually converges to a constant value, because in this regime the bubble departure diameter decreases with nucleation density (Figure 12d). More importantly, this example demonstrates that the impact of numerous bubbles on the entire electrochemical system can be obtained from the dynamics of single bubble through the statistical description of stochastic bubble interaction. If the impact of single bubble on ohmic and concentration overpotentials can be well understood (Table 1), similar statistical

approaches (eqs. 54 and 65) can be carried out to further quantify the overpotentials of the

2 entire electrochemical systems due to the stochastic interaction among multiple bubbles.

3.4. Bridging the Microscopic Bubble Dynamics to the Macroscopic Transport Properties

We have discussed the fundamentals of bubble dynamics from nucleation to departure and their impacts on transport overpotential across multiple length scales. One of the key challenges to fully understand the role of bubbles in electrochemical gas evolution reactions is how to translate the knowledge gained from one or a few bubbles (*i.e.*, microscopic bubble dynamics) to the overall mass transfer and electrochemical characteristics (*i.e.*, macroscopic transport properties) of the electrolytic cell that contains a large number of bubbles. In this Section, we will introduce a few approaches to bridge the knowledge gap between microscopic bubble dynamics and macroscopic transport properties, which have been demonstrated in phase change heat transfer. Then, we will discuss opportunities and challenges of leveraging these approaches to unlock the full-field understanding of electrochemical gas evolution reactions.

3.4.1. Multiscale Understanding of Phase Change Heat Transfer through a Statistical Description

One approach to bridge the distinct length scales is to describe the stochastic bubble interaction using statistics. In Sections 3.3.2 and 3.3.3, we have introduced the basic concept of statistical treatment and provided two examples about the calculations of average bubble departure diameter and bubble coverage overpotential. The key principle of statistical treatment is that if the behavior of single entities (*e.g.*, bubbles and droplets) is known, the collective behavior reflected in a large ensemble of entities can be obtained through the probability distribution of each entity. In history, such statistical treatment has gained great success in explaining the macroscopic properties of various "many-body" systems, ^{341–344} such as pressure and temperature of gases (*i.e.*, ensemble of molecules), electrical conductivity and optical reflectivity of metals (*i.e.*, ensemble of electrons), heat capacity and thermal conductivity of crystals (*i.e.*, ensemble of lattice vibrations), and spectrum of thermal radiation (*i.e.*, ensemble of electromagnetic waves). Recently, similar statistical treatments were implemented to

1 understand the phase change phenomena, which successfully described the stochastic bubble

2 and droplet interactions and provided a new perspective on explaining the heat transfer during

3 the boiling and condensation processes. 32,345-349 In this Section, we aim to elucidate how to

leverage the statistical description to achieve a multiscale understanding of phase change heat

5 transfer and discuss potential opportunities for electrochemical gas evolution reactions.

4

6

7

8

9

10

11

12

13

14

15

16

17

18

19

20

21

22

23

24

25

26

27

28

To understand heat transfer characteristics in the boiling process, especially the mechanism of CHF, tremendous efforts have been made during the past century. 90,91,350-352 Several pioneering theories primarily focused on the hydrodynamics of single vapor entities, which either attributed the CHF to the flow instability of vapor columns ^{90,350,351} or the force balance of vapor bubbles.⁹¹ These theories have achieved reasonable agreement with early-stage experiments, especially the CHF values on flat heating surfaces. However, they did not provide a very clear physical picture for the stochastic bubble interaction and cannot well explain the effect of surface wettability and structure on the CHF. 32,353 Owing to recent advances in metrology tools, there has been increasing experimental evidence that shows the CHF is not only dictated by the single bubble dynamics, but more importantly, governed by the collective behaviors of multiple bubbles (Figure 13a). 31,354 For example, Lloveras et al. measured the acoustic emission during the boiling process.³⁵⁴ Using statistical analysis, they identified a power-law energy distribution of the acoustic emission signals during the CHF, which disappeared during the nucleate boiling and film boiling regimes. They attributed this phenomenon to the competition between dry and wetting areas on the heating surface. More interestingly, to explain the experimental observations, they developed a lattice spin model, which is a simple statistical model to describe phase transition. They showed that despite significant simplification of the hydrodynamics during the boiling process, the simple lattice spin model can well describe the key features of their experiment. This indicates that the stochastic bubble interaction might be a dominant mechanism of the CHF instead of the hydrodynamics. In addition, using high-speed IR imaging of bubble bases, Zhang et al. further confirmed that the CHF is associated with the stochastic bubble interaction, where the CHF always occurred when the second largest cluster of interconnected dry bubble bases reached the maximum.³¹

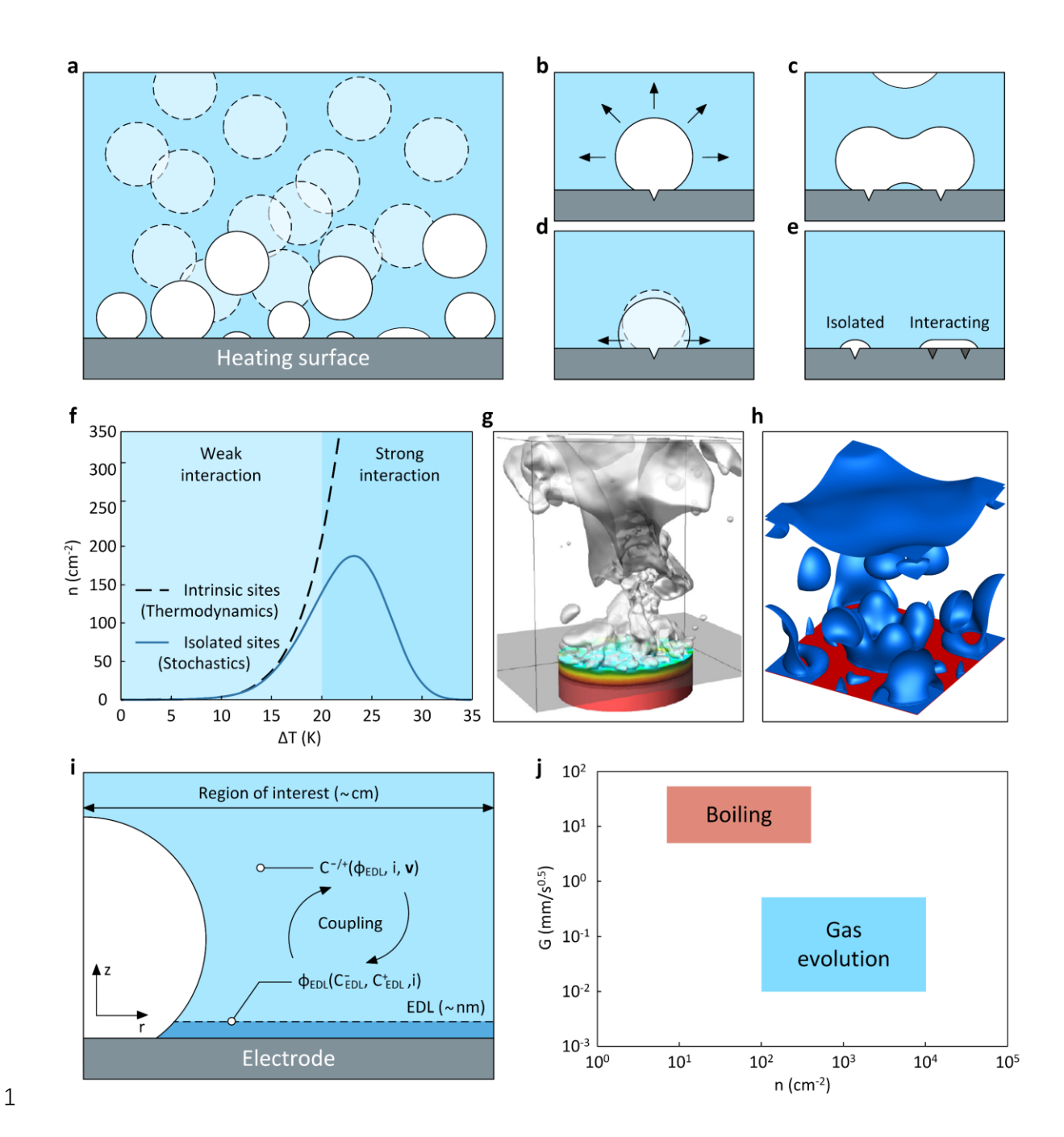


Figure 13. Advances in modeling approaches for the boiling and gas evolution processes. (a) Stochastic interaction of multiple bubbles on a heating surface during the boiling process. (b) Diffusion-controlled growth of single vapor bubble. (c) Coalescence-induced bubble departure. (d) Increase of bubble contact angle due to vapor recoil effect. (e) Interaction of nucleation sites dictated by their distributions. Statistical treatment considers the impact of stochastic bubble interaction on the overall heat transfer, which bridges the microscopic bubble dynamics (b – e) to the macroscopic transport properties of the boiling process. (f) Isolated nucleation site density as a function of wall superheat given by the statistical treatment. The number of

isolated nucleation sites first increases and then decreases with wall superheat due to the stochastic bubble interaction. The peak of isolated nucleation site density corresponds to the CHF of the boiling process. (g) High-fidelity numerical simulation of the pool boiling process by solving conservation equations. Reproduced with permission from Ref. 35. Copyright 2018 Elsevier. (h) High-fidelity numerical simulation of the pool boiling process using the lattice Boltzmann method (LBM). Reproduced with permission from Ref. 32. Copyright 2022 Elsevier. (i) Schematic of the simulation domain for representative electrochemical gas evolution systems. To enable the full-field analysis throughout the entire electrolyte region, the sub-nanometer scale EDL and microscale gas bubbles in a centimeter-scale electrolytic cell should be simultaneously resolved. (j) Regime map of bubble growth coefficient and nucleation density for the boiling and gas evolution processes. Bubbles in the gas evolution process typically exhibit much higher nucleation density but much lower growth rate as compared with bubbles in the boiling process.

Inspired by the above experimental observations, Zhang *et al.* developed a new theory that

combines the dynamics of single bubbles with the stochastic bubble interaction using a statistical treatment (Figure 13a).³² Zhang *et al.*'s theory first accounted for several thermalfluid features at the single bubble level, including the diffusion-controlled bubble growth (Figure 13b), coalescence-induced bubble departure (Figure 13c), and increase in bubble contact angle due to the vapor recoil effect (Figure 13d), which have been recognized as critical phenomena in the high heat flux condition.^{36,64,233,236,237,284,286,323} With these thermal-fluid features, behaviors of single bubble, including bubble departure diameter, bubble frequency, and heat transfer of single bubble, can be well described. Owing to the vapor recoil effect, nucleation sites are always covered by vapor even after the bubble departure (Figure 13e).³⁶ As a result, interaction of neighboring nucleation sites can create a large "dry area" covering multiple nucleation sites (Figure 13e). Zhang *et al.* believed that such nucleation site interaction is the major mechanism that enlarges the dry area on the heating surface and deactivates nucleation sites. Based on the above analysis, they postulated that only the isolated nucleation sites carry the most of boiling heat transfer and the CHF occurs when the number of isolated nucleation sites reaches the maximum. With the population and spatial distributions of

nucleation sites (eqs. 35 and 36), Zhang *et al*. derived the average number of isolated nucleation sites,³²

3

4

5

6

7

8

9

10

11

12

13

14

15

16

17

18

19

20

21

22

23

24

25

26

$$N_{\rm iso} = \sum_{N=1}^{\infty} \frac{N_0^N}{(N-1)!} e^{-\left(N_0 + \frac{\pi N d_{\rm b}^2}{A}\right)}$$
 (66)

where d_b is the bubble base diameter that can be calculated from the bubble departure diameter and contact angle. Figure 13f shows the theoretically calculated nucleation site densities as a function of wall superheat. The intrinsic nucleation site density (black dashed curve) monotonically increases with wall superheat, because the higher temperature, the more gas cavities become thermodynamically favorable to nucleate (eq. 31). The isolated nucleation site density given by eq. 66 ($n_{iso} = N_{iso}/A$, blue curve) follows the same trend as the intrinsic nucleation site density at low wall superheat (light blue region in Figure 13f). This suggests that the majority of intrinsic nucleation sites are isolated and contribute to the overall heat transfer. However, at high wall superheat, the isolated nucleation site density can significantly deviate from the intrinsic nucleation density due to the strong interaction among nucleation sites (dark blue region in Figure 13f). When the wall superheat is sufficiently high, the isolated nucleation site density even decreases with the wall superheat, leading to a peak value that represents the CHF point. Combining the heat transfer of single bubble with the number of isolated nucleation sites, Zhang et al. demonstrated simultaneous predictions of the CHF value and the corresponding wall superheat, which shows good agreement with existing experiments.³² More importantly, with the statistical treatment, they extracted a dimensionless number $\Pi = n_{\rm iso} \times d_b^2$ that can be universally related to the CHF. When the CHF occurs, Π is always equal to $1/(\pi e)$. This dimensionless constant indicates that at the CHF point, only 9.2% area of the total heating surface contributes to the boiling heat transfer and less than 25% area of the total heating surface is covered by the dry bubble bases. Zhang et al.'s theory demonstrates that the CHF is dictated by both the thermal-fluid characteristics of single bubbles and the stochastic bubble interaction on the entire heating surface.³² Their approach provides an example of how to establish a multiscale understanding of the boiling process through the lens of single bubble dynamics and probability distributions.

Although our discussion mainly focuses on the boiling process, we would like to note that similar statistical treatments have already been implemented in the droplet condensation and gained great success in predicting the overall heat transfer of dropwise and jumping-droplet condensation processes.^{345–349} Considering the similar statistical features exhibited in the gas evolution process and the promising results obtained from the preliminary statistical treatments (Sections 3.3.2 and 3.3.3), it is highly rewarding to further assess whether the same statistical treatment to phase change heat transfer is also effective to the electrochemical gas evolution reactions. In addition, more in-depth understanding of single bubble dynamics, especially the mass transfer resistance and overpotentials induced by single bubbles (Sections 3.2.2 and 3.2.4), is highly required to fill the critical knowledge gap of the multiscale framework.

3.4.2. Full-field Analysis of Phase Change Heat Transfer with High-fidelity Simulations

Although the statistical treatment provides an effective approach to bridge bubble dynamics across distinct length scales, it requires an accurate understanding at the single bubble level as the input, which relies on additional numerical simulations or experimental characterizations. In addition, outputs of the statistical treatment are the macroscopic properties through ensemble average, such as the average bubble departure diameter and heat transfer coefficient, whereas the detailed temporal-and-spatial variations of key physical quantities, such as the temperature profile, local heat flux, and morphology of liquid-vapor interface, cannot be resolved. In contrast, high-fidelity numerical simulations provide a promising means to capture detailed thermal-fluid characteristics of phase change heat transfer, bringing unique values to understand bubble dynamics and guide the heat transfer enhancement design. Owing to recent advances in numerical approaches, there has been significant progress that enables the fullfield analysis of boiling, evaporation, and condensation processes. In this Section, taking the boiling process as an example, we will discuss the basic principles, representative applications, and fundamental limitations of state-of-the-art high-fidelity simulations. Knowledge developed in numerical approaches to phase change heat transfer could shed light on the full-field analysis of electrochemical gas evolution reactions.

Full-field analysis of the pool boiling process requires the temporal-and-spatial resolved simulation from the bottom solid substrate to the top free surface of liquid pool, which contains numerous interacting bubbles. This is fundamentally challenging due to the complex interactions among multiple phases, physical phenomena, and length scales. Specifically, a representative boiling system includes solid (heating surface), liquid, and gas (vapor bubbles) phases. Distinct from conventional multiphase systems with a constant volume fraction of each phase in an isothermal condition, the boiling process is featured by the continuous evolution of liquid-vapor interface through the exchange of mass, momentum, and energy with surrounding solid and liquid phases. Meanwhile, the behaviors of bubbles are dictated by the strong coupling among heat transfer, mass transfer, and fluid flow. In addition to conventional heat transfer modes such as conduction and convection, most of heat is carried by the liquid-vapor phase change, which is associated with the mass transfer across the liquid-vapor interface. Bubble growth, coalescence, and departure induce a highly transient fluid flow, which in turn, couples with heat and mass transfer through convection. Moreover, these complex interactions occur at each individual length scale from sub-micrometer to centimeter. High-fidelity numerical simulation needs to simultaneously resolve bubble nucleation and microlayer evaporation at microscale and capture stochastic bubble interaction at macroscale, spanning more than four orders of magnitude in length scales. From a practical consideration, numerical approaches such as the finite difference, finite volume, and finite element methods rely on a mesh to discretize the simulation domain. To fully capture the multiscale features with sufficient mesh quality, high-fidelity simulation of the boiling process requires significant computational resources. To address the above challenges, tremendous breakthroughs in numerical approaches have been made during the past two decades. 93,355-357 One of the most predominant numerical

1

2

3

4

5

6

7

8

9

10

11

12

13

14

15

16

17

18

19

20

21

22

23

24

25

26

27

To address the above challenges, tremendous breakthroughs in numerical approaches have been made during the past two decades. 93,355–357 One of the most predominant numerical approaches to simulate the boiling process is enabled by solving the conservation equations of mass (eq. 67), momentum (eq. 68), and energy (eq. 69) in both liquid and vapor regions within the framework of CFD,

$$\frac{\partial \rho}{\partial t} + \nabla \cdot (\rho \mathbf{v}) = 0 \tag{67}$$

$$\frac{\partial \rho \mathbf{v}}{\partial t} + \nabla \cdot (\rho \mathbf{v} \mathbf{v}) = -\nabla p + \nabla \cdot [\mu (\nabla \mathbf{v} + (\nabla \mathbf{v})^{\mathrm{T}})] + \mathbf{b}$$
(68)

$$\rho c_{\rm p} \left(\frac{\partial T}{\partial t} + \boldsymbol{v} \cdot \nabla T \right) = \nabla \cdot (k \nabla T) \tag{69}$$

where ρ , μ , c_p , and k are the fluid (i.e., liquid or vapor) density, dynamic viscosity, specific heat, 1 and thermal conductivity, respectively. b is an effective body force term (unit in N/m³) that 2 accounts for both surface tension and gravity. Since the above conservation equations are 3 derived by treating the fluid as a continuum, for the convenience of our discussion, we will 4 5 refer to the relevant numerical approaches as the "continuum approximation method (CAM)". In this review, we highlight a few representative achievements in the CAM-based high-fidelity 6 7 simulations, whereas more numerical studies of the boiling process were summarized by relevant reviews. 93,355–357 8 Dhir and co-workers conducted several pioneering works on high-fidelity simulations of the 9 boiling process using the CAM. 92,93,358-364 These works provide an effective solution to dealing 10 with the coupled heat transfer, mass transfer, and fluid flow between liquid and vapor phases. 11 12 For example, Son et al. simulated the growth and departure of a single bubble on a horizontal surface with a constant wall superheat in 1999.92 They implemented the level set method to 13 track the moving liquid-vapor interface of the bubble. 92,359 By introducing a smooth step 14 function, known as the "level set function" to represent the liquid and vapor phases, the level 15 16 set method is capable of describing moving interfaces in a fixed mesh. They further modified the level set method by incorporating the phase change phenomenon at the liquid-vapor 17 interface. As a result, their simulation successfully captured the flow patterns, temperature 18 fields, and evolution of liquid-vapor interface throughout a bubble growth cycle, which showed 19 20 quantitative agreement with experiments. Later, Dhir and co-workers further extended the level set method-based approach to numerically investigate bubble coalescence during the pool 21 boiling, ^{360,361} single bubble dynamics during the flow boiling, ³⁶² and nucleate boiling in the 22 high heat flux condition. 363,364 These works have demonstrated the level set method as an 23 24 effective numerical approach to deal with the liquid-vapor interaction and the coupled heat and 25 mass transfer associated with the boiling process. Despite the significant promise, Dhir and co-26 workers' studies mainly focused on the boiling process with only one or a few bubbles due to

the limitations of mesh technique and computational power. Recently, Jungho and co-workers further advanced the level set method with adaptive mesh refinement and parallel computation technique, where high-fidelity simulations of pool boiling with hundreds of nucleation sites were demonstrated. 365,366 In addition to the level set method, phase field method is a similar numerical approach to simulate liquid-vapor interface in a fixed mesh, where both methods are already accessible in several commercial software. We would like to note that although level set and phase field methods have become mature numerical approaches to track liquid-vapor interface, both methods cannot guarantee the mass conservation of liquid and vapor phases, which might induce numerical errors when simulating liquid-vapor phase change heat transfer. Another significant advance in high-fidelity simulations of the boiling process was achieved by Sato and Niceno. 35,270,367-370 Their works demonstrated how to effectively resolve the multiscale bubble dynamics with the presence of solid, liquid, and vapor phases. As discussed above, to completely capture the microlayer evaporation in a centimeter-scale liquid pool, direct simulation approach requires an ultrafine mesh to discretize the simulation domain, which induces significant computational expenses. ^{371,372} For example, Urbano et al. performed direct simulation to compute the evolution of microlayer during bubble growth.³⁷² They showed that the microlayer thickness can be as small as 2 µm. As a result, a mesh size of 0.25 μm was used to resolve the dynamics of microlayer, leading to more than 6.7×10^7 computational cells to discretize a 2 mm 2D-axisymmetric simulation domain. Although only one bubble was simulated, parallel computation on 256 processors was required. Despite the superior numerical accuracy, it is practically challenging to implement the direct simulation approach to a more realistic boiling system that contains a large number of bubbles. To improve the computational efficiency of high-fidelity simulations, Sato and Niceno developed a depletable microlayer model that can be integrated into the CFD framework.³⁶⁸ In their approach, the microlayer was not necessarily resolved by the mesh. Instead, the microlayer thickness was treated as a variable stored in each fluid computational cell adjacent to the solid substrate. Considering the coupled heat conduction through the solid substrate and microlayer, they described the microlayer thickness using an ordinary differential equation, which can be solved with the temperature in solid computational cells as the input. As a result, the actual

1

2

3

4

5

6

7

8

9

10

11

12

13

14

15

16

17

18

19

20

21

22

23

24

25

26

27

28

mesh size can be much larger than the microlayer thickness, while the evolution of microlayer in the sub-computational cell scale can still be captured. Using this approach, the multiscale features dictated by microlayer, millimeter-scale bubbles, and centimeter-scale liquid pool in a boiling system can be simultaneously resolved with an improved computational efficiency. Meanwhile, Sato and Niceno developed a new interface tracking method based on the volume of fluid approach.³⁶⁷ Compared with level set and phase field methods, their approach conserves the mass of liquid and vapor phases and captures a sharp liquid-vapor interface. This is achieved by introducing a "color function" which represents the liquid volume fraction in each computational cell. The governing equation of the color function was directly derived from the mass conservation equation (eq. 67). With additional numerical sharpening, the liquidvapor interface was determined as the position when the value of color function is equal to 0.5 and liquid-vapor phase change only occurred within the computational cells that contain the interface. Combining the depletable microlayer model and mass-conservative interface tracking method, Sato and Niceno demonstrated a 3D full-field simulation of the boiling process with high-fidelity (Figure 13g). 35,370 Notably, taking the experimentally characterized nucleation density as the input, their simulation simultaneously captured the evolution of microlayer beneath each bubble, the stochastic interaction among multiple bubbles, and their coalescence into a large vapor mushroom in a 3D liquid pool with 4 cm in size. In addition, by incorporating heat conduction within the solid substrate into the simulation domain, both heat flux and temperature can be applied from the bottom of the solid substrate, which is closer to the realistic operation of boiling apparatuses. As a result, they successfully simulated the transition from the nucleate boiling regime to the film boiling regime through the CHF point, with wall superheat increasing from 10 °C to 50 °C and heat flux rising from 5 W/cm² to 150 W/cm².³⁵ The boiling curve was recovered from the high-fidelity simulation, which shows good agreement with experiments. As discussed above, the CAM-based approaches have gained great success in addressing multiple challenges associated with high-fidelity simulations of the boiling process. However, we would like to comment on a few limitations of existing approaches, which might also occur when simulating the gas evolution process. State-of-the-art CAM-based approaches cannot

1

2

3

4

5

6

7

8

9

10

11

12

13

14

15

16

17

18

19

20

21

22

23

24

25

26

27

28

capture bubble nucleation, because the thermodynamics associated with the liquid-vapor phase change was not included into the conservation equations (eqs. 67 - 69). To simulate bubble growth, most of current CAM-based approaches rely on pre-assigning multiple nucleation sites on the heating surface or setting a nucleation activation temperature. 35,365,366,370,373,374 Considering nucleation density can vary a lot with surface properties (e.g., surface chemistry and roughness), it can be challenging to perform high-fidelity simulations if the nucleation density on a heating surface is not experimentally characterized before. In addition, owing to the significant computational expenses, most of simulations of the boiling process were performed on a flat heating surface. Efficient numerical approaches to resolve various surface structures and quantify their impacts on the boiling process are highly required.³⁷⁵ Compared to the CAM-based approaches, microscale and mesoscale approaches provide an alternative solution to realize high-fidelity simulations of the boiling process. Microscale and mesoscale approaches, including molecular dynamics (MD), direct simulation Monte Carlo (DSMC), and lattice Boltzmann method (LBM), are available to understand phase change heat transfer. With a more mechanistic description of liquid and vapor phases, some limitations encountered by the CAM-based approaches can be overcome. For example, these approaches focus on describing either the dynamics of individual molecules (e.g., MD) or the statistical characteristics of molecule clusters (e.g., DSMC and LBM), which fundamentally break the continuum approximation. MD tracks the motion of each molecule under a pre-defined intermolecular force field. However, due to the high computational expenses to resolve the trajectories of all molecules in the simulation, the size of simulation domain for state-of-theart MD is typically only a few nanometers. As a result, instead of enabling the full-field analysis, MD is mainly used to understand the impacts of surface chemistry and structures on the boiling process at nanoscale^{376–380} and extract the fundamental transport properties of liquid-vapor

1

2

3

4

5

6

7

8

9

10

11

12

13

14

15

16

17

18

19

20

21

22

23

24

25

26

27

28

29

molecules using a probabilistic algorithm. By quantifying the non-equilibrium distribution of molecules within the Knudsen layer, DSMC is commonly used to understand the transport

interface, such as the accommodation coefficient. 381-385 DSMC solves the distribution of

resistance at the liquid-vapor interface during evaporation and condensation, where the size of

simulation domain for DSMC is a few mean free paths.^{386–390} Compared with MD and DSMC,

1 LBM has shown huge potential to enable the full-field simulation of the boiling process with

high fidelity. Therefore, we will briefly explain the basic principles of LBM and review recent

3 advances in simulations.

LBM is a mesoscopic simulation approach that solves the distribution of fluid particles. The theoretical foundation of the LBM originates from the Boltzmann transport equation (BTE), which describes the distribution of microscopic particles (*e.g.*, molecules, electrons, and phonons) due to diffusion, collision, and external force field. ⁶⁸ By discretizing the velocity space with a "lattice", the fluid particles are constrained to move only along certain discrete directions defined by the lattice structures. With such discretization approach, the lattice Boltzmann equation (LBE) was derived from the BTE. ³⁹¹ By solving the LBE, the fluid density, velocity, and temperature can be recovered from the distribution of molecules. The LBM was developed in the 1990s. ^{391–394} With the rapid progress during the past two decades, the LBM has become one of the most popular approaches in CFD. More importantly, owing to the unique structure of LBE, the LBM is particularly desirable for multiphase flows and naturally amenable to parallel computation. ^{395–399} Under the Bhatnagar–Gross–Krook (BGK) approximation, also known as the single-relaxation time approximation, the LBE can be expressed as, ^{391–393,395,400}

$$f_i(\mathbf{x} + \mathbf{c}_i \delta_t, t + \delta_t) - f_i(\mathbf{x}, t) = -\frac{1}{\tau} \Big(f_i(\mathbf{x}, t) - f_i^{\text{eq}}(\mathbf{x}, t) \Big)$$
(70)

where f_i is the single-particle distribution function in discrete direction i and f_i^{eq} is the equilibrium distribution function. For gas molecules, f_i^{eq} is given by the Maxwell-Boltzmann distribution function. c_i is the moving velocity in discrete direction i per time step and δ_t is the discrete time step. τ is the relaxation time that represents the characteristic timescale of fluid particles to reach equilibrium through collision. It has been shown that eq. 70 is closely related to the governing equations under the continuum approximation. Chen et al. have demonstrated that both conservation equations of mass (eq. 67) and momentum (eq. 68) can be recovered from eq. 70 using the Chapman-Enskog multiscale expansion. By introducing another LBE describing the evolution of temperature distribution function, the conservation equation of

1 energy (eq. 69) can also be recovered. 401 By solving two LBEs simultaneously, density,

2 velocity, and temperature of the flow field can be obtained.

3

4

5

6

7

8

9

10

11

12

13

14

15

16

17

18

19

20

21

22

23

24

25

26

27

28

29

Owing to the superior computational efficiency in dealing with the multiphase systems, LBM has been extensively used to study phase change heat transfer. 398,399 In particular, Gong and Cheng conducted several pioneering works to enable full-field simulations of the boiling process with high fidelity. 34,36,401-404 The key breakthrough demonstrated in Gong and Cheng's approach is to make the separation of liquid and vapor phases and the associated heat transfer a natural physical process that occurs automatically in the simulation. ⁴⁰¹ As a result, there is no need of implementing additional numerical approaches to track the liquid-vapor interface. To enable the liquid-vapor phase separation, they developed a modified pseudo-potential model to describe the interaction among fluid particles. 401,402 By incorporating the equation of state for real fluids into the modified pseudo-potential model, the thermodynamic driving force responsible to liquid-vapor phase change and phase separation was included into the LBM. They also introduced the interaction between solid wall and fluid particles, which determines the surface wettability. In addition, they derived a source term based on the thermodynamic relation of entropy and equation of state, which describes the amount of heat released during liquid-vapor phase change. 401 This source term was incorporated into the LBE for the temperature distribution function. Since the thermodynamic relations that govern the liquidvapor phase change have been incorporated into Gong and Cheng's approach, bubble nucleation can naturally occur without the need to pre-assign nucleation sites on the heating surface. For example, they investigated bubble nucleation during pool boiling by creating multiple cavities on the heating surface. 403,404 At the beginning of simulation, the entire fluid domain was filled by liquid. However, with the increase of wall superheat, they successfully captured bubble nucleation and growth from cavities, which agrees with the physical picture described in Section 3.1.1. By solving the LBE for temperature distribution function in the solid substrate, they further coupled heat conduction through the solid substrate with the liquid and vapor phases. 403,404 With all above efforts, in 2017, Gong and Cheng demonstrated the direct simulation of the entire boiling curve from the natural convection regime to the film boiling regime, with the onsite of nucleate boiling, nucleate boiling regime, CHF point,

transition boiling regime, and Leidenfrost point well captured.³⁴ Figure 13h shows an example
of the 3D full-field simulation of pool boiling using the LBM, where the interaction among
multiple bubbles was well resolved.³² Owing to the effectiveness to deal with multiphase
interaction and superior computational efficiency, over the past five years, Gong and Cheng's
approach has been widely used to understand multiple fundamental problems in the boiling
process, including the vapor recoil effect,³⁶ microlayer evaporation,³⁶ stochastic bubble
interaction,³² and impacts of surface structures on boiling heat transfer.⁴⁰⁵

3.4.3. Opportunities and Challenges for High-fidelity Simulations of Electrochemical

Gas Evolution Reactions

The critical roles of high-fidelity simulations in understanding the fundamental bubble dynamics and guiding the enhanced device design have been widely recognized in electrochemical gas evolution reactions. However, full-field analysis that simultaneously captures the electrochemical kinetics, gas and ion transport, electric field distribution, as well as bubble dynamics is highly lacking. From a perspective of numerical simulation, phase change heat transfer and electrochemical gas evolution reactions exhibit similar features in terms of governing equations, boundary conditions, simulation domain, and discretization methods. Therefore, we envision advances in high-fidelity simulations of the boiling process shown in Section 3.4.2 could bring transformative impact on the gas evolution process. In this Section, we aim to discuss several key challenges when simulating the gas evolution process and comment on the opportunity space of multiple numerical approaches demonstrated in the boiling process. In addition, we will discuss a few distinct features of the gas evolution process, which require additional innovations in numerical approaches.

Similar to the boiling process, the gas evolution process is also featured by the complex interactions among multiple phases, physical phenomena, and length scales, which have posed significant challenges to enable high-fidelity simulations. To deal with the continuous evolution of liquid-vapor interface due to mass transfer and fluid flow, effective interface tracking method needs to be developed. However, conventional approaches typically modeled the liquid-gas interface as "a rigid sphere", which is either a stationary surface under the quasi-

static approximation⁴⁶ or a moving surface with a pre-defined velocity determined by the overall mass transfer. 406,407 Although gas and ion transport due to the presence of liquid-gas interface can be captured to some extent, impacts of hydrodynamic forces, surface tension, and nonuniform mass flux on the deformation, coalescence, and departure of bubbles cannot be resolved. In comparison, with proper modifications to incorporate the mass transfer through the liquid-gas interface, the level set, phase field, and volume of fluid methods introduced in Section 3.4.2 can be more desirable solutions to address the interaction between liquid and gas phases. However, these interface tracking methods are not commonly applied to existing simulations of the gas evolution process yet and only a few representative examples can be seen in recently studies. Vachaparambil et al. simulated the evolution of single and two hydrogen bubbles during the alkaline water electrolysis. 408 Similar to Sato and Niceno's work as discussed above (Section 3.4.2),³⁶⁷ the volume of fluid method was used to track the liquidgas interface, where the deformation of liquid-gas interface due to bubble growth, coalescence, and departure was captured. Zhan et al. simulated the growth of single hydrogen bubble on a microelectrode using the volume of fluid method. 409 They compared the numerical results with experimental measurements and good agreement was demonstrated. Raman et al. simulated the growth and departure of single hydrogen bubble from the center of a ring-shape microelectrode. 410 A sharp liquid-gas interface was described by a moving mesh with the arbitrary Lagrangian-Eulerian formulation, where mass and momentum conservation equations at the liquid-gas interface were solved. Although the gas evolution process is also featured by the interaction among solid, liquid, and gas phases, compared to the boiling process, the coupling of the current transport through the electrode with liquid and gas phases might be less significant. As discussed in Section 3.2.3, due to the high electrical conductivity of electrode, the electrode-electrolyte interface is typically treated as an equipotential surface with uniform current density (Figure 10d). This distinction could reduce the complexity when dealing with the multiphase interaction in electrochemical gas evolution systems.

1

2

3

4

5

6

7

8

9

10

11

12

13

14

15

16

17

18

19

20

21

22

23

24

25

26

27

28

29

Compared to the boiling process, addressing the multiscale transport under the coupling among multiple physical phenomena in the electrochemical gas evolution system can be even more challenging. To enable high-fidelity simulations, dynamic behaviors within three characteristic

length scales ranging from sub-nanometer to a few centimeters should be well resolved, across eight orders of magnitude. The first length scale is dictated by the thickness of EDL, which can be estimated by the Debye length ($\lambda_D \sim \text{nm}$). Bohra et al. performed 1D numerical simulation of the EDL during the electrochemical reduction of carbon dioxide. 132 They showed that the variation of potential across the EDL can contribute to more than 80% of the total potential difference across the entire electrolyte domain, leading to more than two orders of magnitude change of ion concentration. Therefore, to precisely model the overpotential and ion concentration within the electrolytic cell, the Nernst-Planck-Poisson-Boltzmann set of equations (eqs. 13 - 16) should be solved with sub-nanometer spatial resolution. Meanwhile, the second length scale is associated with the size of bubble, which ranges from a few nanometers during bubble nucleation to a few millimeters before bubble departure. To understand the mass transfer and fluid flow induced by individual bubbles, numerical approaches capable of resolving the details of liquid-gas interface and surrounding flow field are required (Figure 13i). Furthermore, conventional electrolytic cells have a size larger than a few centimeters. To capture the stochastic bubble interaction within the entire region of interest, an ideal simulation domain should be at least at the centimeter scale, which includes both the EDL and multiple gas bubbles (Figure 13i). As a result, an ultrafine mesh with sub-nanometer computational cells is required to discretize a 3D centimeter-scale simulation domain containing liquid and gas phases, which creates an impractical computational expense. On the other hand, the Nernst-Planck-Poisson-Boltzmann set of equations (eqs. 13 - 16) coupled with the conservation equations of mass and momentum (eqs. 67 and 68) should be rigorously solved in the entire simulation domain. Compared with solving the governing equations (eqs. 67-69) for the boiling process, solving eqs. 13-16, 67, and 68 for the gas evolution process can be even more challenging. This is because in addition to the nonlinear coupling between gas transport (eq. 13) and flow field (eq. 68), ion transport (eq. 13) is also nonlinearly coupled with both flow field (eq. 68) and electric field (eq. 15), leading to intensive numerical iterations among multiple equations to reach convergence.

1

2

3

4

5

6

7

8

9

10

11

12

13

14

15

16

17

18

19

20

21

22

23

24

25

26

27

28

29

The above challenges can be partly overcome through two approaches, *i.e.*, direct simulation and decoupled method. The direct simulation rigorously solves the governing equations (eqs.

13 – 16, 67, and 68) in the entire region of interest including the EDL. This approach enables high-fidelity simulation of the gas evolution process but requires considerable computational expenses. As a result, it is challenging to apply direct simulation to centimeter-scale gas evolution systems. For example, Lu et al. modeled the nucleation of hydrogen bubble in a gas cavity using direct simulation. 152 Ion concentration and potential distribution across the EDL as well as mass flux through the liquid-gas interface were well resolved in their work. However, to enable such simulation with sufficient numerical accuracy, approximately 4×10⁵ computational cells were used to discretize a 30 nm × 20 nm 2D-axisymmetric simulation domain. Compared to direct simulation, the decoupled method is more commonly used to deal with larger simulation domain containing macroscopic bubbles. To reduce the computational expense, the decoupled method neglects the EDL while only solving the governing equations in the region above the EDL (Figure 13i). For example, Torii et al. performed 3D simulation on the alkaline water electrolysis in a millimeter-scale electrolytic cell using the decoupled method.¹³⁷ Gas and ion transport in the region above the EDL was captured. Overpotential across the EDL was then estimated from analytical expressions (eq. 27) with numerical solutions to current density and ion concentration as the input. Despite the superior computational efficiency, there can be critical concerns regarding to the accuracy of the decoupled method. As discussed in Section 2, in principle, overpotential across the EDL is given by the solution to a set of fully coupled partial differential equation (eqs. 13 - 16), i.e., the Nernst-Planck-Poisson-Boltzmann model, which cannot be simply expressed by analytical expressions such as eq. 27. In addition, to solve the governing equations in the region above the EDL, potential distribution and strength of electric field on the boundary of EDL are required as the boundary conditions, which remain unknown without solving the EDL first (Figure 13i). However, to solve the EDL, ion concentration on the boundary of EDL should be used as the boundary condition, which cannot be obtained without solving the region above the EDL (Figure 13i). As a result, the EDL and the region above are fully coupled, which is constrained by the continuity of potential, electric field, species concentration, and mass flux at their shared boundary (dashed line in Figure 13i). To make the decoupled method work, additional inconsistences might be introduced into the simulation, which have been discussed

1

2

3

4

5

6

7

8

9

10

11

12

13

14

15

16

17

18

19

20

21

22

23

24

25

26

27

28

in Section 2 in details. Therefore, we would like to highlight the necessity of performing comprehensive assessments to better understand the accuracy of decoupled method under various conditions (e.g., current density, simulation domain size, and bubble size, etc.). Nonetheless, we would note that the decoupled method is still a highly promising strategy, because it is one of the only practical numerical approaches to enable full-field simulations of electrolytic cells. However, it is critical to identify the regime to implement the decoupled method with satisfactory accuracy. More importantly, new numerical approaches in addition to direct simulation and decoupled methods are urgently needed to enable full-field simulations of the gas evolution process with high-fidelity. Finally, we discuss a few distinctions between the boiling and gas evolution processes in terms of bubble dynamics, which might lead to additional considerations for high-fidelity simulations. Figure 13j shows the bubble growth coefficient (G) and nucleation density (n) of representative boiling and gas evolution processes. The ranges of bubble growth coefficient were estimated based on both analytical expressions and experimental data in the diffusion-controlled growth regime, ^{238,239,241,245,304} whereas the ranges of nucleation density were determined from Wang and Dhir's boiling experiments and Janssen et al.'s water electrolysis experiments. 156,159 In general, bubble growth rate during the gas evolution process can be more than one order of magnitude lower than that during the boiling process, which is partly attributed to the much lower gas diffusivity ($D_g \sim 10^{-9} \text{ m}^2/\text{s}$) in electrolyte as compared to thermal diffusivity of water $(\alpha_1 \sim 4.5 \times 10^{-7} \text{ m}^2/\text{s})$. In contrast, the gas evolution process exhibits much higher nucleation density $(n \sim 10^2 - 10^4 \text{ 1/cm}^2)$ than the boiling process $(n \sim 10 - 10^2 \text{ 1/cm}^2)$, which can be explained by the large gas supersaturation at the electrode-electrolyte interface. Insights gained from bubble dynamics could provide practical guide for numerical simulation. For example, considering the relatively low bubble growth rate, the temporal resolution required for the numerical simulation of gas evolution process might be less significant. However, it is expected that high spatial resolution along the in-plane direction can be more critical to capture numerous nucleation sites on the electrode surfaces. With these distinctions, additional investigations are needed when translating the numerical approaches developed in phase change heat transfer to electrochemical gas evolution reactions.

1

2

3

4

5

6

7

8

9

10

11

12

13

14

15

16

17

18

19

20

21

22

23

24

25

26

27

28

4. PATHWAY TOWARD A BETTER DESIGN OF GAS EVOLUTION SYSTEMS BY

2 MANIPULATING BUBBLES

1

3

4

5

6

7

8

9

10

11

12

13

14

15

16

17

18

19

20

21

22

23

24

25

26

27

28

29

With the mechanistic understanding discussed in Sections 2 and 3, it is possible to find the optimal bubble dynamics that induce the minimum overpotential in the electrolytical cell. To enable real-world device design, however, developing effective approaches to manipulate bubble dynamics toward the optimal configuration is of equal importance. In general, bubble manipulation approaches can be classified as the active and passive methods. 14 The active method leverages external forces, such as shear flows, 40,84-88 magnetic fields, 293,294,409 and ultrasound irradiations⁴¹¹⁻⁴¹³ to control the dynamic behaviors of bubbles. Details of representative active methods have been systematically reviewed by Angulo et al.¹⁴ On the other hand, recent advances in material synthesis and micro-and-nanofabrication have facilitated a well-controlled approach to manipulate bubbles passively through the engineered surfaces with micro-and-nanoscale features. In particular, over the past two decades, microand-nanoengineered surfaces have been extensively used to improve liquid-vapor phase change heat transfer performance, where the critical roles of surface structures in manipulating liquidvapor interface at each length scale have been systematically investigated. Recently, there has been increasing interest in reducing the bubble induced overpotential by introducing microand-nanoscale features to the electrode surface. Therefore, we envision tremendous opportunities in translating the knowledge developed in phase change heat transfer to unlock the full design space of micro-and-nanoengineered surfaces for electrochemical gas evolution reactions. In this Section, we first provide a brief review to elucidate the fundamentals of how surface structures alter bubble dynamics by manipulating the three-phase contact line (Section 4.1). Then, we discuss a few design trade-offs and their physical origins when introducing surface structures to engineer transport properties of liquid-gas systems (Section 4.2). Finally, we comment on a potential path to overcome these design-offs and approach the fundamental limits of liquid-gas transport with hierarchical structures, i.e., a mix of micro-and-nanoscale features (Section 4.3). We will review recent advances in hierarchical structured surfaces to enhance liquid-vapor phase change heat transfer and discuss a few critical questions to be addressed in electrochemical gas evolution reactions.

4.1. Role of Surface Structures in Manipulating Bubbles: Insights from Phase Change

1

2

28

Heat Transfer

Surface modifications with micro-and-nanoscale features have been broadly used to enhance 3 heat transfer performance in boiling, evaporation, and condensation. 27,37,38,414 Taking 4 advantage of the unique capability of manipulating liquid-vapor interface and transport at 5 6 microscale, structured surfaces provide an effective means to engineer the dynamics of bubbles 7 and droplets in a highly tunable and well-controlled manner. With tremendous efforts made over the past two decades, role of surface structures in improving liquid-vapor phase change 8 heat transfer has become relatively well understood, which has been systematically 9 summarized by Attinger et al.,³⁷ Cho et al.,²⁷ and Upot et al.³⁸ In this Section, taking the boiling 10 process as an example, we aim to elucidate the key principles of how to engineer bubble 11 dynamics by introducing surface structures, which will lay a foundation for the knowledge 12 13 translation to electrochemical gas evolution systems. In general, surface modifications refer to (1) altering surface chemistry (e.g., oxidization, 14 15 deposition, and coating) and (2) introducing physical textures (e.g., random roughness, micropillar, microcavity, microparticle, nanoblade, and nanowire). These surface 16 modifications can affect bubble dynamics via two major mechanisms: (1) wettability and (2) 17 wickability, which are reflected in the change of bubble contact angle and the formation of 18 capillary flow through surface structures, respectively. By tuning the liquid wetting and 19 wicking behaviors on the surface, bubble nucleation, growth, coalescence, and departure can 20 be largely engineered, which ultimately impacts the overall heat transfer of the boiling process. 21 22 Figure 14a – 14d show four representative approaches to control bubble nucleation with surface 23 modifications. As discussed in Section 3.1.1, gas cavities created by surface roughness can be the preferential sites for bubble nucleation. By introducing micro-fabricated cavities on the 24 heating surface with proper size and spacing (Figure 14a), nucleation density, onset of nucleate 25 26 boiling, and bubble interaction can be well controlled. For example, Sadaghiani et al. created 27 an array of micro-fabricated cavities on a heating surface made by silicon wafer, where the

diameter of the cavity varied from 50 µm to 200 µm and the pitch of the array was between

500 μm and 2000 μm. ⁴¹⁵ They showed that bubble nucleation preferentially occurred on the micro-fabricated cavities and bubble dynamics significantly varied by changing the cavity diameter and pitch. Guzman *et al.* fabricated microcavity arrays with a diameter of 30 μm and pitches varying from 100 μm to 2000 μm on silicon wafer. ⁴¹⁶ Effective control of bubble nucleation through micro-fabricated cavities was demonstrated using fluorocarbon as the working fluid. Song *et al.* fabricated similar microcavity arrays on silicon wafer. ⁴¹⁷ They showed that by increasing the cavity diameter from 5 μm to 12 μm, the onset of nucleate boiling temperature decreased accordingly, which agrees with the classical nucleation theory (eq. 31). In fact, the micro-fabricated cavity has already been utilized in the gas evolution process to precisely define the location of bubble nucleation. ^{255,256,258} For example, Linde *et al.* fabricated an electrode surface with a single micropillar and created a microcavity within the micropillar. ²⁵⁶ They performed hydrogen evolution on this surface and observed bubble nucleation exactly at the pre-defined microcavity under a low supersaturation condition.

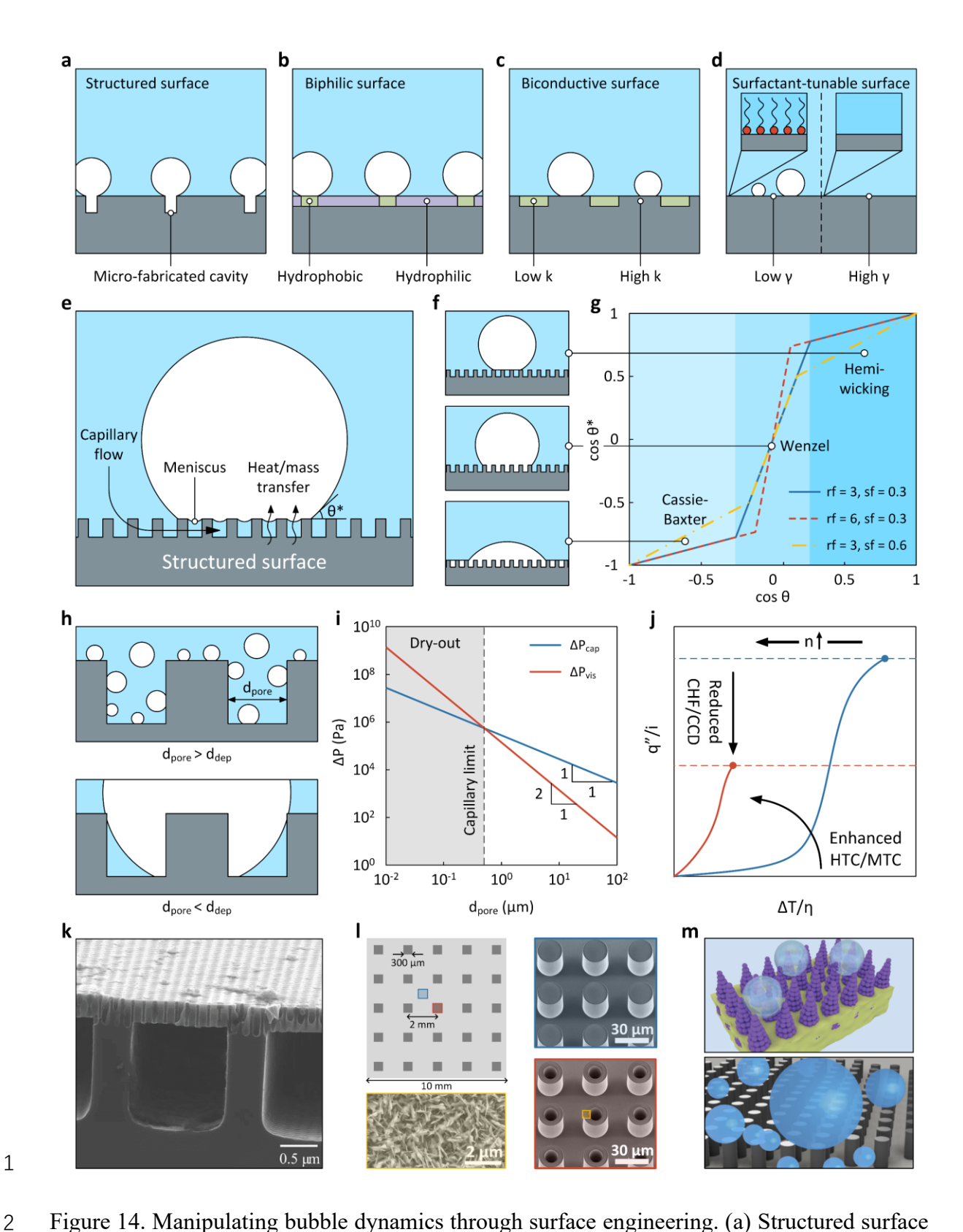


Figure 14. Manipulating bubble dynamics through surface engineering. (a) Structured surface with micro-fabricated cavities. The micro-fabricated cavity is a preferential site for bubble nucleation. (b) Biphilic surface with periodic variation of wettability. Bubble nucleation preferentially occurs in the hydrophobic region whereas the hydrophilic region serves as the

path for liquid rewetting. (c) Biconductive surface with spatially alternating thermal conductivities. Bubble nucleation first occurs in the high thermal conductivity region whereas the low thermal conductivity region is designed for liquid rewetting. (d) Surfactant-tunable surface. Adsorption and desorption of surfactants are tuned by an external electric field. Adsorption of surfactants reduces the surface energy and promotes bubble nucleation. (e) Heat transfer enhancement mechanisms of structured surfaces. Surface structures alter bubble behaviors by changing the apparent contact angle (wetting phenomenon) and inducing capillary flow (wicking phenomenon). (f) Bubble wetting states on structured surfaces. Top panel: hemiwicking bubble. The hemi-wicking bubble is residing on the tips of surface structures. Middle panel: Wenzel bubble. The Wenzel bubble penetrates into surface structures. Bottom panel: Cassie-Baxter bubble. Liquid phase is suspending on the tips of surface structures. (g) Apparent contact angle as a function of intrinsic contact angle with different roughness factors and solid fractions. Apparent contact angle in hemi-wicking, Wenzel, and Cassie-Baxter states can be predicted with intrinsic contact angle, roughness factor, and solid faction as input. (h) Interaction between pore and bubble in a porous electrode. Top panel: schematic of bubble behaviors when bubble departure diameter is smaller than pore diameter. Bottom panel: schematic of bubble behaviors when bubble departure diameter is larger than pore diameter. (i) Competition between capillarity and viscous loss in the design of structured surfaces for thin film evaporation and boiling processes. Smaller pores create larger capillary pressure but also induces higher viscous loss, leading to a design trade-off for structured surfaces. When the capillary pressure cannot overcome the pressure drop due to viscous loss, surface dry-out occurs, which is known as the capillary limit. (i) Effect of nucleation density on the transport characteristics of the boiling and gas evolution processes. Increasing nucleation density typically improves the HTC of the boiling process but can be detrimental for the CHF enhancement. Similar design trade-off is expected in the gas evolution process. (k) SEM image of a hierarchical thin film evaporator with nanoporous membrane supported on microchannels. The nanoporous membrane creates large capillary pressure and the microchannels reduce viscous loss for liquid transport. Reproduced with permission from Ref. 458. Copyright 2020 American Chemical Society. (1) Three-tier hierarchical structured surface for simultaneous

1

2

3

4

5

6

7

8

9

10

11

12

13

14

15

16

17

18

19

20

21

22

23

24

25

26

27

28

1 enhancement of HTC and CHF. Left-top panel: schematic of the boiling surface consisting of 2 three-tier hierarchical structures. Micropillar arrays and microtube clusters are represented by the light-grey and dark-grey regions, respectively. Blue shadow: SEM image of micropillar 3 arrays. Red shadow: SEM image of microtube clusters. Yellow shadow: SEM image of 4 5 nanoblades around microtubes. Reproduced with permission from Ref. 101. Copyright 2022 Wiley-VCH GmbH. (m) Representative designs of surface structures on gas evolving 6 7 electrodes. Top panel: schematic of porous catalyst layer with ordered cone-shape microspikes 8 for alkaline water electrolysis. Cone-shape microspikes promote bubble departure and hence 9 reduce the total overpotential. Reproduced with permission from Ref. 460. Copyright 2022 Royal Society of Chemistry. Bottom panel: schematic of micropillar structured electrode for 10 hydrogen evolution. Reproduced with permission from Ref. 461. Copyright 2022 American 11 12 Chemical Society. In addition to the gas cavity, surface wettability is another critical factor that governs bubble 13 14 nucleation. In general, the energy barrier of bubble nucleation increases with the increase of wettability. Therefore, hydrophobic surfaces with large bubble contact angle typically exhibits 15 low onset of boiling temperature and high nucleation density.^{23,27} Taking advantage of this 16 fundamental principle, biphilic surfaces with well-patterned hydrophobic and hydrophilic 17 regions provide an effective means to control bubble nucleation (Figure 14b). During the 18 boiling process, bubble nucleation preferentially occurs in the hydrophobic region whereas 19 20 liquid wetting occurs in the hydrophilic region. With bubble growth, the three-phase contact line can be pinned at the boundary of the hydrophobic and hydrophilic regions, which prevents 21 22 the formation of continuous vapor film due to intensive bubble coalescence. In practical situations, hydrophilicity can be achieved by introducing oxidation, such as silicon dioxide and 23 metal oxide, 418,419 whereas hydrophobic surfaces can be functionalized through self-assembled 24 monolayers^{420,421} and polymer coating.⁴²² Betz et al. fabricated a biphilic surface to enhance 25

boiling heat transfer in 2010, where hexagonal hydrophobic islands with 40 µm in size and 100

μm in pitch were patterned on a hydrophilic surface. 98 Silicon wafer with oxidized layer on the

top was selected as the heating surface. By further treating the surface with a diluted solution

of buffered hydrofluoric acid, the hydrophilic region exhibits a contact angle of 7°. The

26

27

28

hydrophobic islands were coated with Teflon using photolithography, leading to 110° contact angle. By performing boiling tests at low wall superheat, they observed bubble nucleation primarily occurred on the hydrophobic islands with large bubbles pinned at the boundary of the hydrophobic and hydrophilic regions. With the effective manipulation of bubble nucleation and interaction, they demonstrated 65% and 100% enhancements of the CHF and HTC as compared with the boiling heat transfer performance on a flat hydrophilic surface. Then, Betz et al. developed a superbiphilic surface to further increase the wettability contrast between the hydrophilic and hydrophobic regions. 423 By introducing random nanostructures onto the surface, the hydrophilic and hydrophobic regions became superhydrophilic and superhydrophobic with 0° and $150 - 165^{\circ}$ contact angles, respectively. As a result, bubble nucleation can be significantly promoted on the superhydrophobic patterns. Meanwhile, bubble bases were well confined within the superhydrophobic islands due to the extreme contrast of wettability. At low wall superheat $(5 - 10 \, ^{\circ}\text{C})$, they showed that the HTC of the superbiphilic surface can be more than one order of magnitude higher than that of the flat hydrophilic surface. Notably, the concept of biphilic surface has been implemented by a recent study to improve the performance of hydrogen evolution. Zhang et al. patterned superhydrophobic stripes on a hydrophilic platinum electrode. 424 Each superhydrophobic strip is a porous structure consisting of silicon dioxide nanoparticles. Hydrogen bubble nucleation first occurred on the platinum surface. When the hydrogen bubble contacted the superhydrophobic strip, it was absorbed into the superhydrophobic strip due to capillary pressure. As a result, the superhydrophobic strip was rapidly covered by gas and served as a channel for efficient gas transport. They further increased hydrophilicity of the platinum surface by creating nanoblade structures. With these combined efforts, they demonstrated a high current density of 0.8 A/cm² under 0.5 V overpotential, compared to 0.1 A/cm² on the flat platinum electrode. Similar to the biphilic surface, bubble nucleation can also be manipulated by introducing a contrast of thermal conductivity to the heating surface, which is known as the biconductive surface (Figure 14c). For example, Rahman et al. created periodic in-plane variation of thermal conductivity by embedding epoxy arrays (k < 1 W/m/K) into a copper substrate ($k \approx 400$ W/m/K). 425 Owing to the distinct thermal conductivities between epoxy and copper, the heating

1

2

3

4

5

6

7

8

9

10

11

12

13

14

15

16

17

18

19

20

21

22

23

24

25

26

27

28

surface exhibited a spatially periodic temperature variation when a heat flux was applied from the bottom of the substrate. With high-speed imaging, they showed that bubble nucleation primarily occurred on the copper surface due to the higher surface temperature, whereas the low-temperature epoxy surface suppressed bubble nucleation and served as a liquid path that avoids the formation of continuous vapor film. Compared to the boiling heat transfer performance on a bare copper surface, they showed that the CHF and HTC on a well-designed biconductivity surface can be improved by two and five times, respectively. Considering the analogy between thermal and electrical conductivities, it is interesting to explore if an electrode surface with spatially alternating electrical conductivities can effectively control bubble nucleation and hence improve the performance of water electrolysis.

1

2

3

4

5

6

7

8

9

10

11

12

13

14

15

16

17

18

19

20

21

22

23

24

25

26

27

28

29

Another approach to control bubble nucleation is adding surfactants to the bulk liquid. Surfactants are a type of chemical compound consisting of a hydrophilic "head" and a hydrophobic "tail", which can be absorbed at the liquid-vapor and solid-liquid interfaces to lower their surface energy (Figure 14d). Surfactants absorbed on the solid surface reduce the wettability and hence enhance bubble nucleation. In addition, reducing surface tension is also desirable to promote bubble departure (eq. 58). Altering the boiling heat transfer performance by adding surfactants has been well investigated, 426-428 where details relevant to this approach was reviewed by Cheng et al. 429 In particular, active control of bubble nucleation was demonstrated by Cho et al. using ionic surfactants and electric field. 430 Two ionic surfactants, sodium dodecyl sulfate (SDS) and dodecyl trimethylammonium bromide (DTAB), were used, which were negatively and positively charged when dissolving into water. By applying an electric field, ionic surfactants can be attracted to or repelled from the heating surface due to the electrostatic interaction, realizing an active control of surfactant adsorption and desorption (Figure 14d). When applying a more negative potential from -0.1 V to -0.2V to the SDS solution, they observed a fourfold reduction of HTC because of the desorption of SDS from the solid-liquid interface. In contrast, the HTC was enhanced by twofold due to the adsorption of DTAB. More interestingly, they demonstrated a spatial control of bubble nucleation using an array of electrodes. When applying potential to a specific electrode, bubble nucleation can be activated on this electrode whereas liquid on the rest of electrodes stayed in a quiescent state.

By varying the potential of different electrodes, the boiling process can be actively turned on and off at different positions of the heat surface. In addition to ionic surfactants and electric field, Zhao *et al.* developed another approach to control bubble behaviors using light and photoresponsive surfactants.⁴³¹ By introducing illumination with proper wavelengths, the molecular conformation of photo-responsive surfactants can be reversibly switched, leading to distinct surface energies of liquid-gas interface and bubble departure behaviors.

7

8

9

10

11

12

13

14

15

16

17

18

19

20

21

22

23

24

25

Figure 14e shows the wetting and wicking phenomena induced by surface structures. In addition to the intrinsic surface chemistry discussed above, surface wettability can be further modified by creating physical textures, which makes the apparent contact angle (θ^*) deviate from the intrinsic contact angle. In general, the hydrophilicity or hydrophobicity of a surface can be magnified by introducing surface structures. For this reason, in practical applications, superhydrophilicity ($\theta^* \approx 0^\circ$) and superhydrophobicity ($\theta^* > 150^\circ$) are typically achieved by adding micro-and-nanoscale features to hydrophilic (e.g., silicon dioxide and metal oxide) and hydrophobic (e.g., self-assembled monolayers and polymer coating) surfaces. 27,37,38 The combined effect of surface chemistry and surface structure leads to three wetting states of bubble, i.e., (1) Cassie-Baxter state, (2) Wenzel state, and (3) hemi-wicking state (Figure 14f). Formation of these three wetting states is attributed to the global minimization of surface energy. The Cassie-Baxter state describes the condition when the liquid phase is suspending on the tips of surface structures with the gas phase trapped inside (bottom panel of Figure 14f), which was first theoretically derived by Cassie and Baxter in 1944. 432,433 The Cassie-Baxter state was more commonly used to describe the wetting state of droplet on superhydrophobic surfaces. 27,37,38,348,421 However, we would note that the wetting state of bubble has the same physical origin and can be described by the same governing equations. ³¹² The apparent contact angle of a Cassie-Baxter bubble can be determined from the intrinsic contact angle (θ) and solid fraction of the structured surface (sf),

$$\cos\theta^* = sf \cdot \cos\theta - (1 - sf) \tag{71}$$

- where the solid fraction sf is defined as the ratio of the structure area in contact with liquid to
- 2 the projected area. We note that eq. 71 is valid when $\theta > \theta_{c1}$, where θ_{c1} is a critical contact angle
- 3 given by the surface structure,

$$\cos\theta_{c1} = (sf - 1)/(rf - sf) \tag{72}$$

- 4 where rf is the roughness factor defined as the ratio of the actual structure area to the projected
- 5 area.
- 6 The Wenzel state shows that the gas phase completely penetrates into surface structures, in
- 7 which condition the bubble is pinned by surface structures (middle panel of Figure 14f). The
- 8 Wenzel state was first experimentally observed and theoretically analyzed by Wenzel in
- 9 1936. 434 For a Wenzel bubble, its apparent contact angle can be expressed as,

$$\cos\theta^* = rf \cdot \cos\theta \tag{73}$$

- which is valid when $\theta_{c2} < \theta < \theta_{c1}$. θ_{c2} is another critical contact angle determined by the surface
- 11 structure,

$$\cos\theta_{\rm c2} = (1 - sf)/(rf - sf). \tag{74}$$

- 12 The Wenzel equation (eq. 73) indicates that surface roughness can enhance the wettability of
- surface. This is because when introducing physical textures onto the surface, the roughness
- 14 factor becomes larger than one. According to eq. 73, the surface will be more wetting if it is
- 15 intrinsically hydrophilic.
- 16 The hemi-wicking state describes the condition when surface structures are completely wetted
- by liquid and the gas bubble rests on the tips of surface structures (top panel of Figure 14f).
- 18 The apparent contact angle of a hemi-wicking bubble is given by,

$$\cos\theta^* = sf \cdot \cos\theta + (1 - sf) \tag{75}$$

- which is valid when $\theta < \theta_{c2}$. Figure 14g shows the apparent contact angle as a function of the
- 20 intrinsic contact angle with representative solid fractions and roughness factors given by eqs.
- 71 75. It can be seen that the surface wettability can be largely tailored by engineering surface
- structures. For example, the hemi-wicking bubble can be created on a surface with even

moderate intrinsic wettability ($\theta \le 90^{\circ}$) by increasing the solid fraction and roughness factor 1 2 (red-dashed and yellow-dashed curves in Figure 14g). Considering a structured surface 3 comprising micropillar arrays, raising the height of micropillar while remaining the diameter unchanged can increase the roughness factor separately without changing the solid fraction. 4 When rf = 6 and sf = 0.3 (red-dashed curve in Figure 14g), gas bubble can transition to the 5 hemi-wicking state with an apparent contact angle of 43° when the intrinsic contact angle is 6 7 83°. On the other hand, the solid fraction can be enlarged by increasing the micropillar diameter 8 or reducing the micropillar pitch. With the increase of solid fraction, gas bubble can stay in the 9 hemi-wicking state with a relatively large apparent contact angle. For example, when increasing the solid fraction from 0.3 to 0.6 with the roughness factor unchanged (rf = 3), gas 10 bubble on the surface with moderate intrinsic wettability ($\theta = 80^{\circ}$) can still transition to the 11 12 hemi-wicking state with a large apparent contact angle of 60° (yellow-dashed curve in Figure 14g). Effectiveness of eqs. 71 - 75 in guiding the design of structured surfaces has been 13 demonstrated in numerous studies. 435 The Cassie-Baxter and Wenzel equations have also been 14 further modified to account for various surface conditions. 436-443 15 Creating hemi-wicking bubbles is highly desirable to enhance the heat transfer performance of 16 boiling process due to multiple mechanisms. On the one hand, the hemi-wicking state is 17 typically associated with superhydrophilicity. The extremely small apparent contact angle on 18 19 the superhydrophilic surface not only largely reduces the thermal resistance near the three-20 phase contact line but also significantly promotes bubble departure. On the other hand, the liquid layer confined by surface structures beneath the hemi-wicking bubble provides 21 22 additional liquid-vapor interface for heat transfer and enables effective liquid rewetting (Figure 14e). Specifically, a number of micro-and-nanoscale liquid-vapor menisci are pinned at the tips 23 24 of surface structures due to the capillary effect (Figure 14e). The liquid film thickness near the three-phase contact line of the meniscus can be less than a few micrometers, exhibiting small 25 thermal resistance. As a result, thin film evaporation occurs at the bubble base region, where 26 heat preferentially first flows through the solid structure with high thermal conductivity and 27 then crosses the liquid thin film near the three-phase contact line to drive liquid-vapor phase 28 change. ^{68,69,71,73,444} Due to the continuous evaporation, the meniscus can recede to create a

- larger capillary pressure (eq. 7), which induces a capillary flow through surface structures (eq.
- 8) to rewet the bubble base (Figure 14e). This liquid wicking process effectively avoids the
- 3 formation of dry area beneath the bubble base, which has been recognized as one of the major
- 4 mechanisms to explain the significantly enhanced CHF on structured surfaces.

5

6

7

8

9

10

11

12

13

14

15

16

17

18

19

20

21

22

23

24

25

26

27

28

29

The critical role of surface structures in enhancing boiling heat transfer has been extensively investigated over the past decade. For example, Chu et al. demonstrated a twofold enhancement of CHF using the micropillar structured surfaces.⁹⁹ Since the maximum CHF of 208 W/cm² was observed on the surface with highest roughness factor (rf = 6), they attributed the enhanced boiling performance to the surface structure-magnified wettability. Rahman et al. showed that in addition to the roughness factor, wickability of the structured surface is another fundamental mechanism to enhance the CHF. 100 They fabricated similar micropillar structured surfaces as well as hierarchical structured surfaces and characterized the wickability of these structured surfaces by measuring the volumetric wicking flow rate using a capillary tube. By comparing the wickability and CHF, they observed that structured surfaces with the larger wickability had the higher CHF, exhibiting a linear dependence. With high-speed optical and IR imaging, Dhillon et al. further confirmed that the rewetting of dry bubble base due to the wicking effect can be the major mechanism of the enhanced CHF on structured surfaces, where the CHF occurred when the surface heating timescale is equal to the rewetting time scale of dry bubble base. 447 More notably, Yu et al. introduced synchrotron x-ray into the boiling apparatus to visualize the dynamics of liquid-vapor interface on micropillar structured surfaces.⁹⁶ Taking advantage of the high spatial resolution enabled by x-ray, they directly imaged the liquid-vapor meniscus pinned by micropillars, dry-out process of the bubble base, and rewetting process driven by the capillary flow. More importantly, they observed the partially dry-out and fully dry-out of the micropillar structured surfaces when the applied heat flux approached the CHF. These fundamental characterizations provide direct experimental evidence that the capillaryinduced rewetting is a key mechanism responsible to the CHF enhancement on structured surfaces. Recently, Song et al. re-examined existing experimental data of the CHF on micropillar structured surfaces.³⁵³ They found that neither the roughness factors nor the surface wickability can solely describe the CHF enhancement on structured surfaces. With a scaling

- analysis, they derived a unified descriptor representing the combined effects of surface
- 2 roughness magnified thin film density and surface structure induced capillary flow, which
- 3 shows a reasonable linear correlation with the CHF. Their results demonstrated that surface
- 4 structures have separate effects on the boiling process by creating more thin film regions for
- 5 liquid-vapor phase change and delaying the formation of dry bubble base through wicking.

4.2. Design Trade-off by Engineering Surface Structures

6

9

10

11

12

13

14

15

16

17

18

19

20

21

22

23

24

25

26

27

28

7 Although introducing surface structures is an effective means to manipulate bubbles and

8 enhance heat transfer performance, it does not necessarily mean surface modifications with

complex features and extreme length scales are always desirable. In this Section, we discuss

multiple design trade-offs and underlying competing mechanisms associated with surface

modifications. These design trade-offs have been well implemented to guide the optimization

of structured surfaces in phase change heat transfer. By reviewing several recent studies in

electrochemical gas evolution reactions, we will discuss how these design trade-offs could

impact the optimal design of gas evolving electrodes.

Creating surface structures can increase the specific surface area for heat and mass transfer. In particular, porous electrodes are highly desirable for the high current density applications due to the largely extended surface area for electrochemical reactions. Intuitively, under the same porosity, the smaller pore diameter, the larger reaction area will be created. That is one of the reasons that nanoscale porosity is commonly introduced into various electrochemical systems, such as batteries 448–450 and supercapacitors. However, for electrochemical gas evolution reactions, in addition to pore diameter, another characteristic length scale, *i.e.*, the bubble diameter, is also involved into the porous electrode. The interaction between pore and bubble leads to a design trade-off when optimizing the porous electrode performance (Figure 14h). For example, Iwata *et al.* showed that the ratio of bubble diameter (d_{dep}) to pore diameter (d_{pore}) ζ is a critical design parameter dictating the performance of gas evolving electrodes. By carefully controlling the area coverage ratio of polytetrafluoroethylene (PTFE) coating on a nickel porous electrode with a few hundred micrometers pore diameter, the electrode transitioned from the superhydrophilic state to superhydrophobic state, leading to a dramatic

increase of bubble departure diameter from less than 80 µm to more than 4 mm. As a result, a wide range of ζ was created. They performed alkaline water electrolysis on the porous electrodes and observed distinct bubble dynamics and transport overpotentials with different ζ . Specifically, when $\zeta < 1$, bubble nucleation, growth, and departure occurred both on the top surface and inside the porous electrode (top panel of Figure 14h). A sharp transition occurred when the bubble size becomes comparable to the pore size (i.e., $\zeta \approx 1$). Although the electrode was still wetted by electrolyte and bubble can still grow inside the pore, the interference between bubble and porous structure impeded efficient bubble departure (bottom panel of Figure 14h) and hence resulted in a twofold increase in the transport overpotential. When ζ became much larger than one, the electrode was gradually filled by gas because of the intensive bubble coalescence and inefficient bubble departure. As a result, bubble growth and departure only occurred on the top surface. In such gas filled state, the benefits of utilizing porous structure to enlarge reaction surface area are diminished. According to the above experimental observations, Iwata et al. suggested $\zeta < 1$ as a design criterion to exploit the full potential of porous structures for the gas evolution process, which can be achieved by engineering the wettability and pore size of the electrode. Similar design trade-off was also reported by Jin et al. on a microgrid electrode during hydrogen evolution, where the highest current density was achieved on the electrode with a moderate microgrid size ($\approx 40 \mu m$). ⁴⁵⁴ Another design trade-off arises from the competition between capillarity and viscous loss. As discussed in Section 4.1, one of the major heat transfer enhancement mechanisms induced by surface structures is the wicking effect where the capillary flow overcomes the viscous loss to rewet the heating surface. As described by eq. 7, the capillary pressure (ΔP_{cap}) is inversely proportional to the length scale of surface structures ($\Delta P_{\rm cap} \sim 1/d_{\rm pore}$). This indicates that introducing smaller features to the surface is favorable to create larger driving force for liquid rewetting. However, smaller features also make the surface less permeable, inducing larger viscous loss to liquid rewetting as the same time. ^{69,71,444,445} The pressure drop due to viscous loss (ΔP_{vis}) is scaled with 1/ d^2_{pore} (eq. 8). Figure 14i shows an example of the competition between capillarity and viscous loss across a 1 mm thick porous structure when maintaining a wicking flow velocity of 1 cm/s. Viscous loss can be extremely large by reducing the pore size

1

2

3

4

5

6

7

8

9

10

11

12

13

14

15

16

17

18

19

20

21

22

23

24

25

26

27

28

to nanoscale. When ΔP_{vis} becomes larger than the maximum of ΔP_{cap} , the surface cannot be rewetted by the capillary flow and dry-out occurs (grey shadow in Figure 14i). Therefore, the intersection of ΔP_{cap} and ΔP_{vis} dictates the capillary limit of the porous structure. ^{69,444,445} The above design trade-off has been widely recognized in thin film evaporation and pool boiling processes on structured surfaces. For example, Zhu et al. modeled the dry-out heat flux of micropillar structured surfaces. 445 They showed that the dry-out heat flux first increased with the micropillar pitch due to the increase of permeability and then decreased because of the reduction of capillary pressure, leading to a maximum dry-out heat flux for thin film evaporation. Adera et al. experimentally confirmed the design trade-off by performing thin film evaporation on micropillar structured surfaces with different geometries.⁶⁹ Similar behaviors of heat flux were also observed during the boiling process. For example, Dhillon et al. showed that the CHF on micropillar structured surfaces followed a similar dependence to the dry-out heat flux, where an optimal micropillar pitch ($\sim 10 \, \mu m$) exists corresponding to the highest CHF ($\approx 200 \text{ W/cm}^2$). And Pham et al. measured the boiling heat transfer on microporous structures consisting of well-ordered spherical pores. 455 The optimal pore diameter to minimize the viscous loss was experimentally characterized. Considering the increasing interest in both capillary feed-type electrolytic cell²¹ and wicking-based porous electrode, ^{304,454} it is necessary to examine whether the same design trade-off is also a limiting factor for the gas evolution process. The ultimate goal of manipulating bubbles and introducing surface structures is to enable the boiling and gas evolution systems to be operated in the high flux conditions (i.e., high CHF and CCD, respectively) with high energy efficiencies (i.e., high HTC and MTC, respectively). However, research on the boiling process has shown that it is challenging to achieve the simultaneously enhanced HTC and CHF due to the inherent limitation of bubble nucleation.²⁷ In general, promoting bubble nucleation can increase the HTC and left-shift the boiling curve (Figure 14m). However, the more bubbles are generated, the more intensive bubble interaction will occur and the easier large dry area will form on the heating surface. As a result, high nucleation density is typically associated with high HTC but low CHF (Figure 14m). The design trade-off between the HTC and CHF has been experimentally confirmed through

1

2

3

4

5

6

7

8

9

10

11

12

13

14

15

16

17

18

19

20

21

22

23

24

25

26

27

28

numerous studies. 27,101,417-419,426-430,456 For example, reducing the surface wettability (e.g., hydrophobic coating and surfactants) can decrease the energy barrier of bubble nucleation. As a result, non-wetting surfaces are useful to improve the HTC but limited by relatively low CHF (< 100 W/m²). 426-430 Similar constraint also occurred when creating micro-fabricated cavities to enhance bubble nucleation. Song et al. showed that the HTC can be enhanced by more than three times with microcavity arrays while the CHF remaining almost unchanged compared to that on a flat surface (≈ 110 W/cm²).⁴¹⁷ On the other hand, it has been well known that micropillar structured surfaces can significantly enhance the CHF. 96,99,100,353,447 However, the HTC demonstrated on the micropillar structured surfaces can be comparable to or even lower than that on the flat surface. 99 Since bubbles play similar roles in dictating the mass transfer of the gas evolution process, it is essential to understand whether there is a design trade-off between the MTC and CCD when manipulating bubble nucleation on gas evolving electrodes with surface modifications.

4.3. Approaching the Fundamental Limits by Manipulating Transport across Multiple

Length Scales

Although the design trade-offs discussed in Section 4.2 originate from multiple fundamental competing effects, they can be largely mitigated by introducing hierarchical structures at different length scales. In this Section, we aim to discuss how to effectively decouple the competing effects associated with several design trade-offs and hence approach the kinetic limits through hierarchical structures. We will first introduce a few representative hierarchical structure design strategies demonstrated in phase change heat transfer. Then, we will review recent advances in creating surface structures into gas evolving electrodes and comment on a few critical problems to be addressed to further improve the performance of electrochemical gas evolution reactions.

The competition between capillarity and viscous loss can be largely decoupled by introducing surface structures at two hierarchy where structures with smaller length scale are responsible for creating high capillary pressure while larger structures with higher permeability are desirable to reduce the viscous loss during liquid transport. For example, Ćoso *et al.* fabricated

a bi-porous structured surface for thin film evaporation, where large clusters of micropillar arrays $(3 - 30 \mu m \text{ diameter and pitch})$ were periodically separated by microchannels $(30 - 60 \mu m \text{ diameter})$ μm width). 457 The high density of micropillars provided large capillary pressure and created substantial thin film regions for evaporation. The large microchannels reduced the pressure drop for liquid supply and hence extended the capillary limit of thin film evaporation. A dryout heat flux of 120 W/cm² was demonstrated on the bi-porous structured surface, which is much higher than the dry-out heat flux on typical micropillar structured surfaces (< 50 W/cm²).^{69,73} Hanks et al. developed a hierarchical thin film evaporator by supporting a nanoporous membrane on multiple parallel microchannels (Figure 14k). 458,459 Pore diameter of the nanoporous membrane was less than 140 nm, which created large capillary pressure. Meanwhile, the thickness of the nanoporous membrane was only 600 nm, which can reduce the pressure drop across the device to a minimal level. In addition, the design of straight microchannels with 2 μ m \times 2 μ m cross section area further reduced the viscous loss for liquid transport from the reservoir to the nanoporous membrane. With a careful design at both nanoscale and microscale, a high evaporation heat flux of 144 W/cm² was demonstrated for water and an ultrahigh evaporation heat flux of 550 W/cm² was obtained with pentane as the working fluid. Taking into account the fact that bubble nucleation occurs at the microscale while bubble interaction becomes more significant at the millimeter scale, the design trade-off associated with nucleation density can also be largely overcome by manipulating bubble dynamics at different length scales. As a result, it is possible to simultaneously enhance the HTC and CHF of the boiling process. For example, Song et al. developed a three-tier hierarchical structured surface consisting of micropillars, microtubes, and nanoblades (Figure 141). 101 Specifically, the entire 10 mm × 10 mm heating surface was covered by micropillar arrays (blue shadow in the left-top panel of Figure 14l) and microtube clusters (red shadow in the left-top panel of Figure 141). Micropillars with 22 µm diameter, 30 µm height, and 40 µm pitch were designed to induce strong capillary flow and enhance the CHF (right-top panel of Figure 141). Microtubes with 5 μm and 12 μm diameters were fabricated inside the micropillars (right-bottom panel of Figure 141) and patterned into 300 μ m \times 300 μ m clusters (dark-grey patterns in the left-top panel of

1

2

3

4

5

6

7

8

9

10

11

12

13

14

15

16

17

18

19

20

21

22

23

24

25

26

27

28

Figure 14l). The spacing between two microtube clusters was 2 mm, which was determined by the capillary length scale and comparable to the bubble departure diameter. These microtubes served as gas cavities to promote bubble nucleation and enhance the HTC. During the boiling process, bubbles were preferentially generated on microtube clusters. The presence of micropillars surrounding microtube clusters not only enabled sufficient liquid rewetting but effectively separated millimeter-scale bubbles from intensive coalescence, which avoids the formation of large dry area on the heating surface. Furthermore, nanoblades were created around microtubes, which further extended the three-phase contact line and improved local thin film evaporation (left-bottom panel of Figure 14l). With a careful control of liquid-vapor interface at submicron scale, bubble nucleation and capillary flow at microscale, and bubble coalescence at millimeter scale, the three-tier hierarchical structured surface can simultaneously enhance the HTC and CHF up to 389% and 138%, respectively, as compared to a flat surface.

In fact, we note that surface structures have also been implemented to manipulate bubble behaviors on gas evolving electrodes in recent studies and highly promising results were reported. ¹⁶ In particular, the structure-magnified wettability has been identified as an important mechanism to promote bubble departure and hence improve the performance of electrochemical gas evolution reactions. For example, Kempler et al. fabricated micropillar structured electrode for hydrogen evolution in H₂SO₄ electrolyte.²⁵⁷ Micropillar arrays with 3 $-6 \mu m$ diameters and $11-28 \mu m$ pitches were fabricated from a silicon wafer and metallized with titanium and platinum. Hydrogen evolution was performed by placing the micropillar structured electrode under different orientations with respect to the gravity direction. They showed that even in a nearly inverted operating configuration with only 15° tilt angle, the micropillar structured electrode exhibited an ultralow overpotential approaching the electrochemical kinetic limits dictated by the Tafel equation. When the current density was 0.07 A/cm², the transport overpotential on the electrode with 3 µm micropillar diameter and 11 um micropillar pitch was more than ten times lower than that on a planar electrode with the same orientation. They measured bubble departure diameter on both micropillar structured and planar electrodes. Compared to the planar counterpart, bubble departure diameters on the

micropillar structured electrode ($\approx 300-400~\mu m$) were much smaller and less sensitive to the electrode orientations. As a result, they attributed the enhanced electrochemical performance to the hemi-wicking state of bubbles on the micropillar arrays, in which condition, the adhesion force between bubble and electrode was minimized and hence bubbles can be easily removed from the electrode surface even in a nearly inverted operating configuration. Wan *et al.* designed a compact membrane electrode assembly for alkaline water electrolysis. 460 A highly porous catalyst layer with ordered cone-shape microspikes was fabricated using electrodeposition and directly coated on the anion exchange membrane (top panel of Figure 14m). They showed that the porous catalyst layer was superhydrophilic, which is desirable to create hemi-wicking bubbles and promote bubble departure (top panel of Figure 14m). As a result, an ultrahigh current density over 8 A/cm² was achieved with less than 1 V total overpotential. Under 2 A/cm² current density, they showed that the transport overpotential (\approx 0.15 V) of their membrane electrode assembly can be more than five times lower than that of a conventional assembly with catalyst coated gas diffusion layer electrodes.

Despite a rewarding direction in general, there has also been experimental evidence that the electrochemical performance is not necessarily improved by adding surface structures to the electrode. Specifically, Lake *et al.* fabricated a structured electrode by depositing platinum on silicon micropillar arrays (bottom panel of Figure 14m).⁴⁶¹ They fixed the micropillar diameter and height to 10 µm and varied the micropillar pitch from 5 µm to 50 µm to create different specific surface areas for electrochemical reactions. Hydrogen evolution was performed on the micropillar structured electrode in H₂SO₄ electrolyte. Similar to Kempler *et al.*'s results, they observed that bubble departure diameter on the micropillar structured electrode decreased by almost a factor of two as compared with that on the planar electrode, resulting in a more stable current density as a function of time. However, deviating from our expectation, under the same applied potential, they showed that area-projected effective current densities on multiple micropillar structured electrodes with distinct geometries were always similar to that on the planar electrode, even though the specific surface area of the micropillar structured electrode can be more than four times larger than the planar counterpart. This indicates that the electrode with the densest micropillar arrays actually had the lowest electrochemical performance in

terms of the current density defined by the actual electrode surface area. With high-speed imaging, they attributed the limited electrochemical performance to bubble growth within the micropillar arrays, which deactivated the additional electrode surface area created by micropillars. This work implies that our understanding about the role of surface structures in electrochemical systems is still highly lacking. In particular, it is necessary to elucidate the relationship among surface structures, bubble dynamics, and electrochemical performance. More fundamental studies need to be carried out to provide a rationale guide of designing the optimal surface structures for gas evolving electrodes. The knowledge of how surface structures enhance phase change heat transfer might suggest a few meaningful angles to access this challenging problem.

5. CONCLUSIONS AND OUTLOOK

Our mission to realize energy sustainability highlights the critical role of electrochemical gas evolution reactions. To develop electrolytic cells that can be operated under high current density with high energy efficiency, new insights into key physical phenomena associated with electrochemistry, gas and ion transport, and liquid-gas interface are urgently needed. With a primary focus on bubble, the unique entity that makes the gas evolution process distinct from the rest of electrochemical processes, this review aims to elucidate the challenges and opportunities for the design of next-generation electrochemical gas evolution systems. In particular, we discussed two important knowledge gaps to be filled: (1) how bubbles affect electrochemical performance and (2) how surface engineering alters bubble dynamics (Figure 3d). Taking into account numerous similarities between electrochemical gas evolution reactions and liquid-vapor phase change heat transfer, from fundamental transport characteristics to practical device configurations, exciting developments in boiling, evaporation, and condensation over the past two decades have unlocked unprecedented opportunity space for understanding and engineering bubble dynamics on gas evolving electrodes via a knowledge translation. Through the lens of phase change heat transfer, we encourage a synergetic effort across multiple disciplines by combining fundamental transport

- phenomena, advanced metrology tools, high-fidelity simulations, and surface modifications,
- 2 which ultimately enables a convergent understanding of bubbles in heat and mass transfer.
- 3 We provided a fundamental background for both electrochemical gas evolution reactions and
- 4 phase change heat transfer in Section 2. Close connections between electrolytic cells and
- 5 boiling devices as well as similar behaviors of polarization curve and boiling curve due to
- 6 bubbles were systematically discussed, which laid a foundation for the concept of knowledge
- 7 translation between two research fields. In Section 3, we delivered a multiscale perspective of
- 8 bubble dynamics that governs both gas evolution and boiling processes. We discussed the key
- 9 physical phenomena and the associated governing mechanisms at each individual length scale.
- 10 In addition to the general bubble dynamics that have been well understood, this review
- particularly focuses on the transport phenomena across electrode-electrolyte-gas interfaces,
- distinctions between gas and ion transport, connections with bubble dynamics in the boiling
- process, and full-field understanding beyond a single bubble. In summary, we would highlight
- the following five directions for further research.
- 15 (1) Developing a fully quantitative understanding of bubble dynamics in electrochemical gas
- 16 evolution reactions.
- 17 Compared to understanding bubble behaviors during the gas evolution process, addressing the
- inverse problem, i.e., how bubble dynamics impact electrochemical overpotentials, is even
- more challenging but also more important from a perspective of performance improvement. To
- 20 define the problem clearly, we first systematically discussed the physical origins of all
- 21 overpotential terms (i.e., activation overpotential, ohmic overpotential, concentration
- 22 overpotential, and bubble coverage overpotential) with rigorous derivations based on the
- 23 Nernst-Planck-Poisson-Boltzmann description of electrochemical processes. Several
- 24 inconsistencies due to the misunderstanding of gas and ion transport and improper utilizations
- of governing equations were carefully clarified. Then, we re-structured the problem by
- 26 considering the impacts of bubble induced gas transport and ion transport separately on each
- overpotential term (Table 1), where substantial efforts are required to precisely quantify the
- 28 concentration overpotential across the EDL and the ohmic overpotential across the bubbly

- electrolyte. Inspired by recent advances in phase change heat transfer, we discussed multiple
- 2 opportunities ground in interfaces, including the transport resistance at liquid-gas interface, gas
- 3 diffusion across electrode-electrolyte interface, and microlayer around the electrode-gas
- 4 interface.
- 5 (2) Advancing both metrology and modeling tools to precisely quantify the impact of bubbles
- 6 on electrochemical overpotentials.
- 7 Developing new tools is highly desirable to further advance the knowledge of bubble dynamics.
- 8 Advanced experimental characterization apparatus leveraging micro-and-nanofabrication
- 9 technologies, optical imaging and spectroscopy, and electron beam probes has achieved high
- spatial resolution and excellent sensitivity to detect various electrochemical environments with
- the presence of bubbles. These metrology tools are expected to be further extended to resolve
- multiple interfaces at extreme length and time scales. Compared to experimental techniques,
- 13 effective modeling approaches with the full-field analysis capability of simultaneously
- capturing sub-nanometer scale EDL and centimeter-scale electrolytic cell are more urgently
- needed. Statistical treatment is an emerging approach to bridge the dynamics of single bubble
- to the overall heat transfer of the boiling process through the statistical distributions of
- 17 nucleation sites and bubble interaction. Despite the success gained in phase change heat
- transfer, the effectiveness of statistical treatment in the gas evolution process remains for
- further exploration. In addition, high-fidelity simulations by solving the conservation equations
- or lattice Boltzmann equations have been demonstrated as a promising means to understand
- bubble dynamics in phase change heat transfer. Numerical techniques developed to deal with
- 22 the complex interactions among multiple phases, physical phenomena, and length scales
- 23 associated with liquid-vapor phase change can be valuable to address similar challenges
- 24 encountered in realizing high-fidelity simulations of electrochemical gas evolution reactions.
- 25 (3) Establishing a rational design strategy of surface engineering for the next-generation gas
- 26 evolving electrodes.
- 27 Engineering electrode surfaces by modifying surface chemistry and introducing physical
- 28 textures can largely manipulate the behaviors of bubbles, holding significant promise for

- 1 mitigating the undesirable overpotentials induced by bubbles (Section 4). With continuous
- 2 efforts throughout the past two decades, surface engineering has become the major driving
- 3 force that facilitates an unprecedented improvement of phase change heat transfer performance.
- 4 Therefore, we envision that the knowledge of manipulating bubbles through surface structures
- 5 attained in phase change heat transfer is now available to guide the design of gas evolving
- 6 electrodes. In particular, wetting and wicking phenomena have been recognized as two major
- 7 heat transfer enhancement mechanisms induced by surface structures. Design trade-offs due to
- 8 multiple competing mechanisms can be largely mitigated through a careful design of
- 9 hierarchical structures. Questions to be addressed in the future are how to mechanistically
- understand the role of the wettability and wickability in the gas evolution process and how to
- fully harness surface structures across multiple length scales to approach the extreme limits of
- 12 electrochemical overpotential and critical current density.
- 13 (4) Identifying the key distinctions of bubble dynamics and transport phenomena between
- phase change heat transfer and electrochemical gas evolution reactions.
- We believe that translating the knowledge from phase change heat transfer will enable better
- designs of electrochemical gas evolution reactions. Meanwhile, we also noted a few key
- distinctions that require sufficient attentions in future exploration. For example, in addition to
- gas transport, electrochemical processes are also featured by the ion transport strongly coupled
- with electric field, which is absent from liquid-vapor phase change systems. The distinct
- 20 variations of electrical and thermal transport properties from solid to gas could lead to dramatic
- 21 difference in heat and mass transfer near the three-phase contact line. More nanoscale features,
- 22 including nucleation sites and the EDL, are involved in the gas evolution process. All above
- 23 fundamental phenomena could ultimately make the electrochemical gas evolution systems
- being operated in a regime with distinct bubble growth rate and nucleation density as compared
- 25 with the phase change systems.
- 26 (5) Assessing the safety and technoeconomic performance toward a real-world application.
- 27 Although this Review mainly focuses on a more fundamental aspect of bubbles in the boiling
- 28 and gas evolution processes, we would like to note that safety and technoeconomic

- 1 considerations can be equally important, especially from a perspective of large-scale adoption.
- 2 Some connections between phase change heat transfer and electrochemical gas evolution
- 3 reactions shown in this Review can be useful to facilitate relevant discussions. For example,
- 4 the CHF point has been recognized an important indicator for the safe operation of boiler. It
- 5 can be interesting to explore if the CCD point plays a similar role in the safe operation of
- 6 electrolytic cells in high current density conditions. In addition, from a perspective of reducing
- 7 the operational expenditure (OPEX), it is always desirable to optimize bubble dynamics and
- 8 improve the energy efficiency of gas evolution systems. However, manipulating bubbles
- 9 through surface engineering might induce additional capital expenditure (CAPEX) and OPEX
- at the same time, which should be carefully incorporated into the technoeconomic analysis of
- the entire system. 462,463 We highlight the needs of a comprehensive safety and technoeconomic
- analysis in future studies. Considering the ever-growing applications of electrochemical gas
- evolution reactions, we expect that the successful knowledge translation from phase change
- 14 heat transfer could bridge multiple critical knowledge gaps and hence bring huge impact to
- numerous industrial processes for chemical production and energy conversion.

AUTHOR INFORMATION

Corresponding Author

- 19 Lenan Zhang Sibley School of Mechanical and Aerospace Engineering, Cornell University,
- 20 Ithaca, New York 14853, United States;
- 21 Department of Mechanical Engineering, Massachusetts Institute of Technology, Cambridge,
- 22 Massachusetts 02139, United States; https://orcid.org/0000-0002-8740-2736;
- 23 Email: lzhang@cornell.edu
- 24 Email: lzhang2@mit.edu

25 Authors

16

17

- 1 Ryuichi Iwata Toyota Central R&D Labs., Inc, Nagakute City, 480-1192, Japan;
- 2 https://orcid.org/0000-0001-7723-3302;
- 3 Zhengmao Lu Institute of Mechanical Engineering, EPFL, 1015 Lausanne, Switzerland;
- 4 https://orcid.org/0000-0002-5938-717X;
- 5 Xuanjie Wang Department of Mechanical Engineering, Massachusetts Institute of
- 6 Technology, Cambridge, Massachusetts 02139, United States; https://orcid.org/0000-0003-
- 7 2756-8889;
- 8 Carlos D. Díaz-Marín Department of Mechanical Engineering, Massachusetts Institute of
- 9 Technology, Cambridge, Massachusetts 02139, United States; https://orcid.org/0000-0002-
- 10 1890-4863;
- 11 Yang Zhong Department of Mechanical Engineering, Massachusetts Institute of Technology,
- 12 Cambridge, Massachusetts 02139, United States; https://orcid.org/0000-0001-6748-903X;

13 Author Contributions

- L.Z. and R.I. conceived the topic and proposed the structure of this review. L.Z. produced the
- 15 figures and wrote the manuscript with input from all coauthors.
- 16 Notes
- 17 The authors declare no competing financial interest.

18 Biographies

- 19 Lenan Zhang is an Assistant Professor in the Sibley School of Mechanical and Aerospace
- 20 Engineering at Cornell University. His research program combines the fundamental
- 21 understanding of transport phenomena with the development of advanced metrology tools to
- create innovative solutions to energy sustainability. He received his B.S. degree in Mechanical
- Engineering from Shanghai Jiao Tong University and Purdue University in 2016; and his M.S.
- 24 and Ph.D. degrees in Mechanical Engineering from Massachusetts Institute of Technology
- 25 (MIT) in 2018 and 2022, respectively. Prior to joining the faculty, he was a Research Scientist
- 26 in the Department of Mechanical Engineering at MIT. His work was recognized by several

- awards and honors including the Best Inventions of 2023 (TIME Magazine), Wunsch
- 2 Foundation Silent Hoist and Crane Award, Best Presentation Award in Materials Research
- 3 Society, Top 10 MIT Research Stories of 2023 and 2020, and Martin Family Fellowship for
- 4 Sustainability. His works have also been highlighted in TIME Magazine, Scientific American,
- 5 MIT Technology Review, The Economist, Nature, among others.
- 6 Ryuichi Iwata is a researcher at Toyota Central R&D Labs., Inc. He received his Ph.D. degree
- 7 from Osaka university in 2010. His research interests include thermal energy storage systems,
- 8 artificial photosynthesis, and water electrolysis.
- 9 Zhengmao Lu is an Assistant Professor of Mechanical Engineering at EPFL. Previously,
- 20 Zhengmao was a postdoctoral scholar in the Department of Materials Science and Engineering
- at Massachusetts Institute of Technology (MIT) and received his Ph.D. and M.S. in Mechanical
- 12 Engineering also at MIT. At EPFL, Zhengmao leads the Energy Transport Advances
- 13 Laboratory (ETA-Lab), focusing on interfacial transport research for energy and water
- 14 applications. Zhengmao is a recipient of the Keck Travel Award in Thermal Sciences and the
- Outstanding Graduate Research Award from MIT Mechanical Engineering.
- 16 Xuanjie Wang is a postdoctoral associate in the Department of Mechanical Engineering at
- 17 Massachusetts Institute of Technology (MIT). He received his Ph.D. in Mechanical
- 18 Engineering from Rensselaer Polytechnic Institute (RPI) in 2022. His research specializes in
- 19 thermal science and nano-engineering, with a focus on fundamental principles and their
- 20 practical applications in the areas of thermal management, renewable energy, and water
- 21 desalination.
- 22 Carlos D. Díaz-Marín received his M.S. in Mechanical Engineering under the supervision of
- 23 Prof. Evelyn Wang from the Massachusetts Institute of Technology (MIT) in 2021. His current
- research interests lie at the intersection of phase change processes, transport phenomena, and
- 25 soft materials for sustainability applications.
- 26 Yang Zhong is a Ph.D. candidate in the Department of Mechanical Engineering at the
- 27 Massachusetts Institute of Technology (MIT). He received his dual M.S. in Mechanical
- 28 Engineering and Electrical Engineering and Computer Science from MIT along with dual B.S.

- in Mechanical Engineering from Shanghai Jiao Tong University and Purdue University. Under
- 2 the supervision of Prof. Evelyn Wang and Prof. Gang Chen, his research centers on
- 3 fundamental water and energy sciences, with applications in atmospheric water harvesting,
- 4 desalination, and thermal management of miniaturized electronic devices. Yang has been
- 5 recognized as an Activate Fellow, Evergreen Graduate Innovation Fellow, and MathWorks
- 6 Engineering Fellow.

7

8

ACKNOWLEDGEMENTS

- 9 This work is supported by Toyota Central R&D Laboratories. L.Z., X.W., C.D., and Y.Z. thank
- 10 their advisor, Dr. Evelyn N. Wang, for her guidance on this work, until the date of her
- confirmation (December 22, 2022) by the U.S. Senate to serve as Director of the Advanced
- Research Projects Agency-Energy (ARPA-E). The authors thank Dr. Hidemasa Kosaka and Dr.
- 13 Tsuyoshi Hamaguchi from Toyota Central R&D Laboratories for their critical review of the
- 14 manuscript.

15

16

REFERENCES

- 17 (1) Botte, G. G. Electrochemical Manufacturing in the Chemical Industry. *Electrochem. Soc.*18 *Interface* **2014**, *23*, 49–55.
- 19 (2) Haupin, W. E. Electrochemistry of the Hall-Heroult Process for Aluminum Smelting. *J. Chem. Educ.* **1983**, *60*, 279.
- Viswanathan, K.; Tilak, B. V. Chemical, Electrochemical, and Technological Aspects of Sodium Chlorate Manufacture. *J. Electrochem. Soc.* **1984**, *131*, 1551–1559.
- 23 (4) Karlsson, R. K. B.; Cornell, A. Selectivity between Oxygen and Chlorine Evolution in 24 the Chlor-Alkali and Chlorate Processes. *Chem. Rev.* **2016**, *116*, 2982–3028.
- 25 (5) Shih, A. J.; Monteiro, M. C. O.; Dattila, F.; Pavesi, D.; Philips, M.; da Silva, A. H. M.; 26 Vos, R. E.; Ojha, K.; Park, S.; van der Heijden, O.; et al. Water Electrolysis. *Nat. Rev.*
- 27 *Methods Primers* **2022**, *2*, 84.
- 28 (6) Rees, N. V.; Compton, R. G. Carbon-Free Energy: A Review of Ammonia- and 29 Hydrazine-Based Electrochemical Fuel Cells. *Energy Environ. Sci.* **2011**, *4*, 1255.

- 1 (7) Morris, A. J.; Meyer, G. J.; Fujita, E. Molecular Approaches to the Photocatalytic Reduction of Carbon Dioxide for Solar Fuels. *Acc. Chem. Res.* **2009**, *42*, 1983–1994.
- 3 (8) Zhao, T. S.; Xu, C.; Chen, R.; Yang, W. W. Mass Transport Phenomena in Direct 4 Methanol Fuel Cells. *Prog. Energy Combust. Sci.* **2009**, *35*, 275–292.
- 5 (9) Velazquez Abad, A.; Dodds, P. E. Green Hydrogen Characterisation Initiatives:
- Definitions, Standards, Guarantees of Origin, and Challenges. *Energy Policy* **2020**, *138*, 111300.
- 8 (10) Oliveira, A. M.; Beswick, R. R.; Yan, Y. A Green Hydrogen Economy for a Renewable Energy Society. *Curr. Opin. Chem. Eng.* **2021**, *33*, 100701.
- (11) Ishaq, H.; Dincer, I.; Crawford, C. A Review on Hydrogen Production and Utilization:
 Challenges and Opportunities. *Int. J. Hydrogen Energy* 2022, 47, 26238–26264.
- 12 (12) Ardo, S.; Fernandez Rivas, D.; Modestino, M. A.; Schulze Greiving, V.; Abdi, F. F.;
- Alarcon Llado, E.; Artero, V.; Ayers, K.; Battaglia, C.; Becker, J.-P.; et al. Pathways to
- Electrochemical Solar-Hydrogen Technologies. Energy Environ. Sci. 2018, 11, 2768–
- 15 2783.
- 16 (13) Zhao, X.; Ren, H.; Luo, L. Gas Bubbles in Electrochemical Gas Evolution Reactions.
 17 Langmuir 2019, 35, 5392–5408.
- 18 (14) Angulo, A.; van der Linde, P.; Gardeniers, H.; Modestino, M.; Fernández Rivas, D.
- 19 Influence of Bubbles on the Energy Conversion Efficiency of Electrochemical Reactors.
- 20 *Joule* **2020**, *4*, 555–579.
- 21 (15) Yuan, S.; Zhao, C.; Cai, X.; An, L.; Shen, S.; Yan, X.; Zhang, J. Bubble Evolution and
- Transport in PEM Water Electrolysis: Mechanism, Impact, and Management. Prog.
- 23 Energy Combust. Sci. **2023**, 96, 101075.
- 24 (16) Li, M.; Xie, P.; Yu, L.; Luo, L.; Sun, X. Bubble Engineering on Micro-/Nanostructured Electrodes for Water Splitting. *ACS Nano* **2023**, *17*, 23299–23316.
- Cheng, X.; Du, Z.; Ding, Y.; Li, F.; Hua, Z.; Liu, H. Bubble Management for Electrolytic
 Water Splitting by Surface Engineering: A Review. *Langmuir* 2023, *39*, 16994–17008.
- 28 (18) Xu, W.; Lu, Z.; Sun, X.; Jiang, L.; Duan, X. Superwetting Electrodes for Gas-Involving Electrocatalysis. *Acc. Chem. Res.* **2018**, *51*, 1590–1598.
- 30 (19) Whitney, G. M.; Tobias, C. W. Mass-transfer Effects of Bubble Streams Rising near Vertical Electrodes. *AIChE Journal* **1988**, *34*, 1981–1995.
- 32 (20) Koynov, A.; Khinast, J. G.; Tryggvason, G. Mass Transfer and Chemical Reactions in 33 Bubble Swarms with Dynamic Interfaces. *AIChE Journal* **2005**, *51*, 2786–2800.

- 1 (21) Hodges, A.; Hoang, A. L.; Tsekouras, G.; Wagner, K.; Lee, C.-Y.; Swiegers, G. F.;
- Wallace, G. G. A High-Performance Capillary-Fed Electrolysis Cell Promises More
- 3 Cost-Competitive Renewable Hydrogen. *Nat. Commun.* **2022**, *13*, 1304.
- 4 (22) International Renewable Energy Agency. *Green Hydrogen Cost Reduction: Scaling up Electrolysers to Meet the 1.5 ^oC Climate Goal;* Abu Dhabi, 2020.
- 6 (23) Carey, V. P. Liquid-Vapor Phase-Change Phenomena; CRC Press, 2020.
- 7 (24) Mazza, B.; Pedeferri, P.; Re, G. Hydrodynamic Instabilities in Electrolytic Gas Evolution. *Electrochim. Acta* **1978**, *23*, 87–93.
- 9 (25) Stephan, K.; Vogt, H. A Model for Correlating Mass Transfer Data at Gas Evolving Electrodes. *Electrochim. Acta* **1979**, *24*, 11–18.
- 11 (26) Sillen, C.; Barendrecht, E.; Janssen, L.; van Stralen, S. Gas Bubble Behaviour during 12 Water Electrolysis. *Int. J. Hydrogen Energy* **1982**, *7*, 577–587.
- 13 (27) Cho, H. J.; Preston, D. J.; Zhu, Y.; Wang, E. N. Nanoengineered Materials for Liquid– 14 Vapour Phase-Change Heat Transfer. *Nat. Rev. Mater.* **2016**, *2*, 16092.
- 15 (28) Vogt, H.; Aras, Ö.; Balzer, R. J. The Limits of the Analogy between Boiling and Gas 16 Evolution at Electrodes. *Int. J. Heat Mass Transf.* **2004**, *47*, 787–795.
- 17 (29) Vogt, H. Heat Transfer in Boiling and Mass Transfer in Gas Evolution at Electrodes-18 The Analogy and Its Limits. *Int. J. Heat Mass Transf.* **2013**, *59*, 191–197.
- 19 (30) Yeager, E., Bockris, J. O., Conway, B. E., Sarangapani, S., Eds.; *Comprehensive Treatise of Electrochemistry*; Springer US: Boston, MA, 1983.
- Zhang, L.; Seong, J. H.; Bucci, M. Percolative Scale-Free Behavior in the Boiling Crisis.
 Phys. Rev. Lett. 2019, *122*, 134501.
- Zhang, L.; Gong, S.; Lu, Z.; Cheng, P.; Wang, E. N. Boiling Crisis Due to Bubble
 Interactions. Int. J. Heat Mass Transf. 2022, 182, 121904.
- 25 (33) Zhang, L.; Wang, C.; Su, G.; Kossolapov, A.; Matana Aguiar, G.; Seong, J. H.;
- Chavagnat, F.; Phillips, B.; Rahman, M. M.; Bucci, M. A Unifying Criterion of the
- 27 Boiling Crisis. *Nat. Commun.* **2023**, *14*, 2321.
- 28 (34) Gong, S.; Cheng, P. Direct Numerical Simulations of Pool Boiling Curves Including
- Heater's Thermal Responses and the Effect of Vapor Phase's Thermal Conductivity. *Int.*
- 30 *Commun. Heat Mass Transf.* **2017**, *87*, 61–71.
- 31 (35) Sato, Y.; Niceno, B. Pool Boiling Simulation Using an Interface Tracking Method: From
- Nucleate Boiling to Film Boiling Regime through Critical Heat Flux. *Int. J. Heat Mass*
- 33 *Transf.* **2018**, *125*, 876–890.

- 1 (36) Gong, S.; Zhang, L.; Cheng, P.; Wang, E. N. Understanding Triggering Mechanisms for
- 2 Critical Heat Flux in Pool Boiling Based on Direct Numerical Simulations. Int. J. Heat
- 3 *Mass Transf.* **2020**, *163*, 120546.
- 4 (37) Attinger, D.; Frankiewicz, C.; Betz, A. R.; Schutzius, T. M.; Ganguly, R.; Das, A.; Kim,
- 5 C.-J.; Megaridis, C. M. Surface Engineering for Phase Change Heat Transfer: A Review.
- 6 MRS Energy & Sustainability **2014**, 1, 4.
- 7 (38) Upot, N. V.; Fazle Rabbi, K.; Khodakarami, S.; Ho, J. Y.; Kohler Mendizabal, J.;
- 8 Miljkovic, N. Advances in Micro and Nanoengineered Surfaces for Enhancing Boiling
- and Condensation Heat Transfer: A Review. *Nanoscale Adv.* **2023**, *5*, 1232–1270.
- 10 (39) Bard, A. J.; Faulkner, L. R. Electrochemical Methods: Fundamentals and Applications,
- 2nd ed.; John Wiley: New York, 2001.
- 12 (40) Ibrahim, O. A.; Navarro-Segarra, M.; Sadeghi, P.; Sabaté, N.; Esquivel, J. P.; Kjeang,
- E. Microfluidics for Electrochemical Energy Conversion. *Chem. Rev.* **2022**, *122*, 7236–
- 14 *7266*.
- 15 (41) Zhao, T. S.; Kreuer, K.-D.; Nguyễn, T. V. Advances in Fuel Cells; Elsevier: Amsterdam,
- 16 2007.
- 17 (42) Bui, J. C.; Lees, E. W.; Pant, L. M.; Zenyuk, I. V.; Bell, A. T.; Weber, A. Z. Continuum
- Modeling of Porous Electrodes for Electrochemical Synthesis. Chem. Rev. 2022, 122,
- 19 11022-11084.
- 20 (43) Enyo, M.; Yokoyama, T. Theory of Concentration Overpotential and Applicability of
- 21 the Rotating Disk Electrode to the Analysis of Electrode Kinetics. *Electrochim. Acta*
- 22 **1970**, *15*, 183–191.
- 23 (44) Murthy, S. K.; Sharma, A. K.; Choo, C.; Birgersson, E. Analysis of Concentration
- Overpotential in an All-Vanadium Redox Flow Battery. J. Electrochem. Soc. 2018, 165,
- 25 A1746–A1752.
- 26 (45) Popat, S. C.; Ki, D.; Young, M. N.; Rittmann, B. E.; Torres, C. I. Buffer PKa and
- 27 Transport Govern the Concentration Overpotential in Electrochemical Oxygen
- Reduction at Neutral PH. ChemElectroChem **2014**, *1*, 1909–1915.
- 29 (46) Dukovic, J.; Tobias, C. W. The Influence of Attached Bubbles on Potential Drop and
- 30 Current Distribution at Gas-Evolving Electrodes. J. Electrochem. Soc. 1987, 134, 331–
- 31 343.
- 32 (47) Vogt, H. The Concentration Overpotential of Gas Evolving Electrodes as a Multiple
- 33 Problem of Mass Transfer. *J. Electrochem. Soc.* **1990**, *137*, 1179–1184.
- 34 (48) de Levie, R. The Electrolysis of Water. J. Electroanal. Chem. 1999, 476, 92–93.

- 1 (49) Rosa, V. New Materials for Water Electrolysis Diaphragms. *Int. J. Hydrogen Energy* 2 **1995**, *20*, 697–700.
- 3 (50) Kerres, J.; Eigenberger, G.; Reichle, S.; Schramm, V.; Hetzel, K.; Schnurnberger, W.;
- 4 Seybold, I. Advanced Alkaline Electrolysis with Porous Polymeric Diaphragms.
- 5 *Desalination* **1996**, *104*, 47–57.
- 6 (51) Thurston, R. H.; Barnard, W. N. (William N. *A History of the Growth of the Steam- Engine.*, Centennial ed.; Cornell university press: Ithaca, N.Y, 1939.
- 8 (52) Breeze, P. Power Generation Technologies, 2nd ed.; Newnes: Oxford, 2014.
- 9 (53) Mehta, V.; Cooper, J. S. Review and Analysis of PEM Fuel Cell Design and Manufacturing. *J. Power Sources* **2003**, *114*, 32–53.
- 11 (54) Carmo, M.; Fritz, D. L.; Mergel, J.; Stolten, D. A Comprehensive Review on PEM Water 12 Electrolysis. *Int. J. Hydrogen Energy* **2013**, *38*, 4901–4934.
- 13 (55) Wu, H.-W. A Review of Recent Development: Transport and Performance Modeling of PEM Fuel Cells. *Appl. Energy* **2016**, *165*, 81–106.
- 15 (56) Shiva Kumar, S.; Himabindu, V. Hydrogen Production by PEM Water Electrolysis A
 Review. *Mater. Sci. Energy Technol.* 2019, 2, 442–454.
- 17 (57) Wang, Y.; Ruiz Diaz, D. F.; Chen, K. S.; Wang, Z.; Adroher, X. C. Materials, 18 Technological Status, and Fundamentals of PEM Fuel Cells – A Review. *Materials* 19 *Today* **2020**, *32*, 178–203.
- 20 (58) Ji, M.; Wei, Z. A Review of Water Management in Polymer Electrolyte Membrane Fuel Cells. *Energies* **2009**, *2*, 1057–1106.
- (59) Sangtam, B. T.; Park, H. Review on Bubble Dynamics in Proton Exchange Membrane
 Water Electrolysis: Towards Optimal Green Hydrogen Yield. *Micromachines* 2023, *14*,
 2234.
- 25 (60) Hussaini, I. S.; Wang, C.-Y. Visualization and Quantification of Cathode Channel 26 Flooding in PEM Fuel Cells. *J. Power Sources* **2009**, *187*, 444–451.
- 27 (61) Majasan, J. O.; Cho, J. I. S.; Dedigama, I.; Tsaoulidis, D.; Shearing, P.; Brett, D. J. L. 28 Two-Phase Flow Behaviour and Performance of Polymer Electrolyte Membrane
- 29 Electrolysers: Electrochemical and Optical Characterisation. Int. J. Hydrogen Energy
- **2018**, *43*, 15659–15672.
- 31 (62) Maier, M.; Meyer, Q.; Majasan, J.; Owen, R. E.; Robinson, J. B.; Dodwell, J.; Wu, Y.;
- Castanheira, L.; Hinds, G.; Shearing, P. R.; et al. Diagnosing Stagnant Gas Bubbles in a
- Polymer Electrolyte Membrane Water Electrolyser Using Acoustic Emission. *Front.*
- 34 Energy Res. **2020**, 8, 582919.

- 1 (63) Xin, S.; LiJun, X.; Di, Z.; Bing, H.; LuXiang, M. Electrochemical Performance Study
- of Proton Exchange Membrane Electrolyzer Considering the Effect of Bubble Coverage.
- 3 *Int. J. Hydrogen Energy* **2023**, *48*, 27079–27094.
- 4 (64) Dhir, V. K. Boiling Heat Transfer. Annu. Rev. Fluid Mech. 1998, 30, 365–401.
- 5 (65) Kandlikar, S. G. History, Advances, and Challenges in Liquid Flow and Flow Boiling
- 6 Heat Transfer in Microchannels: A Critical Review. *J. Heat Transfer.* **2012**, *134*, 034001.
- 7 (66) Cheng, L.; Xia, G. Fundamental Issues, Mechanisms and Models of Flow Boiling Heat
- 8 Transfer in Microscale Channels. *Int. J. Heat Mass Transf.* **2017**, *108*, 97–127.
- 9 (67) Plawsky, J. L.; Fedorov, A. G.; Garimella, S. V.; Ma, H. B.; Maroo, S. C.; Chen, L.;
- Nam, Y. Nano- and Microstructures for Thin-Film Evaporation—A Review. *Nanoscale*
- 11 *Microscale Thermophys. Eng.* **2014**, *18*, 251–269.
- 12 (68) Vaartstra, G.; Zhang, L.; Lu, Z.; Díaz-Marín, C. D.; Grossman, J. C.; Wang, E. N.
- Capillary-Fed, Thin Film Evaporation Devices. J. Appl. Phys. **2020**, 128, 130901.
- 14 (69) Adera, S.; Antao, D.; Raj, R.; Wang, E. N. Design of Micropillar Wicks for Thin-Film
- 15 Evaporation. Int. J. Heat Mass Transf. 2016, 101, 280–294.
- 16 (70) Lu, Z.; Wilke, K. L.; Preston, D. J.; Kinefuchi, I.; Chang-Davidson, E.; Wang, E. N. An
- Ultrathin Nanoporous Membrane Evaporator. *Nano Lett.* **2017**, *17*, 6217–6220.
- 18 (71) Lu, Z.; Kinefuchi, I.; Wilke, K. L.; Vaartstra, G.; Wang, E. N. A Unified Relationship
- for Evaporation Kinetics at Low Mach Numbers. *Nat. Commun.* **2019**, *10*, 2368.
- 20 (72) Antao, D. S.; Adera, S.; Zhu, Y.; Farias, E.; Raj, R.; Wang, E. N. Dynamic Evolution of
- 21 the Evaporating Liquid-Vapor Interface in Micropillar Arrays. *Langmuir* **2016**, *32*, 519–
- 22 526.
- 23 (73) Zhang, L.; Zhu, Y.; Lu, Z.; Zhao, L.; Bagnall, K. R.; Rao, S. R.; Wang, E. N.
- 24 Characterization of Thin Film Evaporation in Micropillar Wicks Using Micro-Raman
- 25 Spectroscopy. *Appl. Phys. Lett.* **2018**, *113*, 163701.
- 26 (74) Vincent, I.; Bessarabov, D. Low Cost Hydrogen Production by Anion Exchange
- Membrane Electrolysis: A Review. Renew. Sustain. Energy Rev. 2018, 81, 1690–1704.
- 28 (75) Park, J. E.; Kang, S. Y.; Oh, S.-H.; Kim, J. K.; Lim, M. S.; Ahn, C.-Y.; Cho, Y.-H.;
- Sung, Y.-E. High-Performance Anion-Exchange Membrane Water Electrolysis.
- 30 *Electrochim. Acta* **2019**, *295*, 99–106.
- 31 (76) Miller, H. A.; Bouzek, K.; Hnat, J.; Loos, S.; Bernäcker, C. I.; Weißgärber, T.; Röntzsch,
- 32 L.; Meier-Haack, J. Green Hydrogen from Anion Exchange Membrane Water
- 33 Electrolysis: A Review of Recent Developments in Critical Materials and Operating
- 34 Conditions. *Sustain. Energy Fuels* **2020**, *4*, 2114–2133.

- 1 (77) Henkensmeier, D.; Najibah, M.; Harms, C.; Žitka, J.; Hnát, J.; Bouzek, K. Overview:
- 2 State-of-the Art Commercial Membranes for Anion Exchange Membrane Water
- 3 Electrolysis. J. Electrochem. En. Conv. Stor. 2021, 18, 024001.
- 4 (78) Mardle, P.; Chen, B.; Holdcroft, S. Opportunities of Ionomer Development for Anion-5 Exchange Membrane Water Electrolysis. *ACS Energy Lett.* **2023**, *8*, 3330–3342.
- 6 (79) Ni, M.; Leung, M.; Leung, D. Technological Development of Hydrogen Production by Solid Oxide Electrolyzer Cell (SOEC). *Int. J. Hydrogen Energy* **2008**, *33*, 2337–2354.
- 8 (80) AlZahrani, A. A.; Dincer, I. Thermodynamic and Electrochemical Analyses of a Solid 9 Oxide Electrolyzer for Hydrogen Production. *Int. J. Hydrogen Energy* **2017**, *42*, 21404—
- 10 21413.
- 11 (81) Wang, L.; Chen, M.; Küngas, R.; Lin, T.-E.; Diethelm, S.; Maréchal, F.; Van herle, J.
- Power-to-Fuels via Solid-Oxide Electrolyzer: Operating Window and Techno-
- 13 Economics. Renew. Sustain. Energy Rev. **2019**, 110, 174–187.
- 14 (82) Hauch, A.; Küngas, R.; Blennow, P.; Hansen, A. B.; Hansen, J. B.; Mathiesen, B. V.;
- Mogensen, M. B. Recent Advances in Solid Oxide Cell Technology for Electrolysis.
- 16 *Science* **2020**, *370*, eaba6118.
- 17 (83) Xu, Y.; Cai, S.; Chi, B.; Tu, Z. Technological Limitations and Recent Developments in
- a Solid Oxide Electrolyzer Cell: A Review. *Int. J. Hydrogen Energy* **2024**, *50*, 548–591.
- 19 (84) H. Hashemi, S. M.; Modestino, M. A.; Psaltis, D. A Membrane-Less Electrolyzer for
- 20 Hydrogen Production across the PH Scale. *Energy Environ. Sci.* **2015**, *8*, 2003–2009.
- 21 (85) H. Hashemi, S. M.; Karnakov, P.; Hadikhani, P.; Chinello, E.; Litvinov, S.; Moser, C.;
- 22 Koumoutsakos, P.; Psaltis, D. A Versatile and Membrane-Less Electrochemical Reactor
- for the Electrolysis of Water and Brine. Energy Environ. Sci. 2019, 12, 1592–1604.
- 24 (86) Esposito, D. V. Membraneless Electrolyzers for Low-Cost Hydrogen Production in a
- 25 Renewable Energy Future. *Joule* **2017**, *1*, 651–658.
- 26 (87) Swiegers, G. F.; Hoang, A. L.; Hodges, A.; Tsekouras, G.; Lee, C.-Y.; Wagner, K.;
- Wallace, G. Current Status of Membraneless Water Electrolysis Cells. Curr. Opin.
- 28 *Electrochem.* **2022**, *32*, 100881.
- 29 (88) Manzotti, A.; Robson, M. J.; Ciucci, F. Recent Developments in Membraneless
- 30 Electrolysis. Curr. Opin. Green Sustain. Chem. 2023, 40, 100765.
- 31 (89) Rohsenow, W. M. A Method of Correlating Heat-Transfer Data for Surface Boiling of
- 32 Liquids. J. Fluids Eng. 1952, 74, 969–975.
- 33 (90) Zuber, N. On the Stability of Boiling Heat Transfer. J. Fluids Eng. 1958, 80, 711–714.

- 1 (91) Kandlikar, S. G. A Theoretical Model to Predict Pool Boiling CHF Incorporating Effects of Contact Angle and Orientation. *J. Heat Transfer* **2001**, *123*, 1071–1079.
- 3 (92) Son, G.; Dhir, V. K.; Ramanujapu, N. Dynamics and Heat Transfer Associated with a Single Bubble During Nucleate Boiling on a Horizontal Surface. *J. Heat Transfer* **1999**, 121, 623–631.
- 6 (93) Dhir, V. K.; Warrier, G. R.; Aktinol, E. Numerical Simulation of Pool Boiling: A Review. *J. Heat Transfer* **2013**, *135*, 061502.
- 8 (94) Zou, A.; Chanana, A.; Agrawal, A.; Wayner, P. C.; Maroo, S. C. Steady State Vapor 9 Bubble in Pool Boiling. *Sci. Rep.* **2016**, *6*, 20240.
- 10 (95) Richenderfer, A.; Kossolapov, A.; Seong, J. H.; Saccone, G.; Demarly, E.; Kommajosyula, R.; Baglietto, E.; Buongiorno, J.; Bucci, M. Investigation of Subcooled Flow Boiling and CHF Using High-Resolution Diagnostics. *Exp. Therm. Fluid Sci.* **2018**, 99, 35–58.
- 14 (96) Yu, D. I.; Kwak, H. J.; Noh, H.; Park, H. S.; Fezzaa, K.; Kim, M. H. Synchrotron X-Ray 15 Imaging Visualization Study of Capillary-Induced Flow and Critical Heat Flux on 16 Surfaces with Engineered Micropillars. *Sci. Adv.* **2018**, *4*, e1701571.
- 17 (97) Li, J.; Zhu, G.; Kang, D.; Fu, W.; Zhao, Y.; Miljkovic, N. Endoscopic Visualization of 18 Contact Line Dynamics during Pool Boiling on Capillary-Activated Copper 19 Microchannels. *Adv. Funct. Mater.* **2021**, *31*, 2006249.
- 20 (98) Betz, A. R.; Xu, J.; Qiu, H.; Attinger, D. Do Surfaces with Mixed Hydrophilic and 21 Hydrophobic Areas Enhance Pool Boiling? *Appl. Phys. Lett.* **2010**, *97*, 141909.
- 22 (99) Chu, K.-H.; Enright, R.; Wang, E. N. Structured Surfaces for Enhanced Pool Boiling 23 Heat Transfer. *Appl. Phys. Lett.* **2012**, *100*, 241603.
- 24 (100) Rahman, M. M.; Ölçeroğlu, E.; McCarthy, M. Role of Wickability on the Critical Heat 25 Flux of Structured Superhydrophilic Surfaces. *Langmuir* **2014**, *30*, 11225–11234.
- (101) Song, Y.; Díaz-Marín, C. D.; Zhang, L.; Cha, H.; Zhao, Y.; Wang, E. N. Three-Tier
 Hierarchical Structures for Extreme Pool Boiling Heat Transfer Performance. *Adv. Mat.* 2022, 34, 2200899.
- (102) Lee, J. K.; Lee, C.; Fahy, K. F.; Zhao, B.; LaManna, J. M.; Baltic, E.; Jacobson, D. L.;
 Hussey, D. S.; Bazylak, A. Critical Current Density as a Performance Indicator for Gas Evolving Electrochemical Devices. *Cell Rep. Phys. Sci.* 2020, *1*, 100147.
- 32 (103) Zou, X.; Zhang, Y. Noble Metal-Free Hydrogen Evolution Catalysts for Water Splitting.
 33 *Chem. Soc. Rev.* 2015, *44*, 5148–5180.
- 34 (104) Blakemore, J. D.; Crabtree, R. H.; Brudvig, G. W. Molecular Catalysts for Water Oxidation. *Chem. Rev.* **2015**, *115*, 12974–13005.

- 1 (105) Voiry, D.; Shin, H. S.; Loh, K. P.; Chhowalla, M. Low-Dimensional Catalysts for 2 Hydrogen Evolution and CO₂ Reduction. *Nat. Rev. Chem.* **2018**, *2*, 0105.
- 3 (106) Bird, G. A. *Molecular Gas Dynamics*; Oxford engineering science series; Clarendon Press: Oxford, 1976.
- 5 (107) Ytrehus, T. Molecular-Flow Effects in Evaporation and Condensation at Interfaces.
 6 *Multiphase Science and Technology* **1997**, *9*, 205–327.
- 7 (108) Sone, Y. Kinetic Theoretical Studies of the Half-Space Problem of Evaporation and Condensation. *Transp. Theory Stat. Phys.* **2000**, *29*, 227–260.
- 9 (109) Sone, Y. *Molecular Gas Dynamics: Theory, Techniques, and Applications*, 1st ed.; 10 Modeling and simulation in science, engineering and technology; Birkhäuser: Boston, 11 2007.
- 12 (110) Schrage, R. W. A Theoretical Study of Interphase Mass Transfer, New York, 1953.
- (111) Pao, Y. Application of Kinetic Theory to the Problem of Evaporation and Condensation.
 Phys. Fluids 1971, 14, 306–312.
- (112) Labuntsov, D. A.; Kryukov, A. P. Analysis of Intensive Evaporation and Condensation.
 Int. J. Heat Mass Transf. 1979, 22, 989–1002.
- 17 (113) Meland, R.; Ytrehus, T. Evaporation and Condensation Knudsen Layers for Nonunity 18 Condensation Coefficient. *Phys. Fluids* **2003**, *15*, 1348–1350.
- 19 (114) Frezzotti, A. Boundary Conditions at the Vapor-Liquid Interface. *Phys. Fluids* **2011**, *23*, 030609.
- 21 (115) Jafari, P.; Amritkar, A.; Ghasemi, H. Temperature Discontinuity at an Evaporating Water Interface. *J. Phys. Chem. C* **2020**, *124*, 1554–1559.
- (116) Vaartstra, G.; Lu, Z.; Lienhard, J. H.; Wang, E. N. Revisiting the Schrage Equation for
 Kinetically Limited Evaporation and Condensation. *J. Heat Transfer* 2022, *144*, 080802.
- 25 (117) Bockris, J. O.; Reddy, A. K. N. *Volume 2 Modern Electrochemistry*, 1st ed. 1970.; 26 Springer US: Boston, MA, 1973.
- (118) Sawyer, D. T.; Sobkowiak, Andrzej.; Roberts, J. L.; Sawyer, D. T. *Electrochemistry for Chemists*, 2nd ed.; Wiley: New York, 1995.
- 29 (119) Bagotskii, V. S. (Vladimir S. *Fundamentals of Electrochemistry*, 2nd ed.; The 30 Electrochemical Society series; Wiley-Interscience: Hoboken, N.J, 2006.
- 31 (120) Gileadi, E. *Physical Electrochemistry: Fundamentals, Techniques and Applications*; 32 Wiley-VCH: Weinheim, 2011.

- (121) Wu, J. Understanding the Electric Double-Layer Structure, Capacitance, and Charging 1 2 Dynamics. Chem. Rev. 2022, 122, 10821–10859.
- (122) Gouy, M. On the Constitution of the Electric Charge at the Surface of an Electrolyte. C. 3 4 R. Acad. Sci. 1909, 149, 654-657.
- (123) Chapman, D. L. LI. A Contribution to the Theory of Electrocapillarity. *Philos. Mag.* 5 **1913**, *25*, 475–481. 6
- 7 (124) Stern, O. Zur Theorie Der Elektrolytischen Doppelschicht. Z Elektrochem. Angew Phys. *Chem.* **1924**, *30*, 508–516. 8
- 9 (125) Helmholtz, H. Ueber Einige Gesetze Der Vertheilung Elektrischer Ströme in Körperlichen Leitern Mit Anwendung Auf Die Thierisch-elektrischen Versuche. Ann. 10 11 Phys. 1853, 165, 211–233.
- (126) Debye, P.; Hückel, E. Zur Theorie Der Elektrolyte. I. Gefrierpunktserniedrigung Und 12 13 Verwandte Erscheinungen. Physik. Z. 1923, 24, 185–206.
- (127) Zheng, Q.; Wei, G.-W. Poisson–Boltzmann–Nernst–Planck Model. J. Chem. Phys. 2011, 14 *134*, 194101. 15
- (128) Wang, H.; Pilon, L. Accurate Simulations of Electric Double Layer Capacitance of 16 Ultramicroelectrodes. J. Phys. Chem. C 2011, 115, 16711–16719. 17
- 18 (129) Singh, M. B.; Kant, R. Debye-Falkenhagen Dynamics of Electric Double Layer in Presence of Electrode Heterogeneities. J. Electroanal. Chem. 2013, 704, 197–207. 19
- 20 (130) Singh, M. B.; Kant, R. Theory for Anomalous Electric Double-Layer Dynamics in Ionic 21 Liquids. J. Phys. Chem. C 2014, 118, 8766–8774.
- (131) Singh, M. B.; Kant, R. Theory of Anomalous Dynamics of Electric Double Layer at 22 Heterogeneous and Rough Electrodes. J. Phys. Chem. C 2014, 118, 5122–5133. 23
- 24 (132) Bohra, D.; Chaudhry, J. H.; Burdyny, T.; Pidko, E. A.; Smith, W. A. Modeling the Electrical Double Layer to Understand the Reaction Environment in a CO2 25 Electrocatalytic System. Energy Environ. Sci. 2019, 12, 3380–3389. 26
- 27 (133) Amatore, C.; Szunerits, S.; Thouin, L.; Warkocz, J.-S. The Real Meaning of Nernst's Steady Diffusion Layer Concept under Non-Forced Hydrodynamic Conditions. A 28 29 Simple Model Based on Levich's Seminal View of Convection. J. Electroanal. Chem.
- **2001**, *500*, 62–70. 30
- (134) Molina, A.; González, J.; Laborda, E.; Compton, R. G. On the Meaning of the Diffusion 31 Layer Thickness for Slow Electrode Reactions. Phys. Chem. Chem. Phys. 2013, 15, 2381. 32
- (135) Mills, Anthony. Heat and Mass Transfer; Irwin heat transfer series; Routledge: 33 Blacklick, 2018. 34

- 1 (136) Atkins, P. W.; De Paula, J.; Keeler, J. *Atkins' Physical Chemistry*, Eleventh edition.; Oxford University Press: Oxford, United Kingdom, 2018.
- (137) Torii, K.; Kodama, M.; Hirai, S. Three-Dimensional Coupling Numerical Simulation of
 Two-Phase Flow and Electrochemical Phenomena in Alkaline Water Electrolysis. *Int. J. Hydrogen Energy* 2021, *46*, 35088–35101.
- 6 (138) Higuera, F. J. A Model of the Growth of Hydrogen Bubbles in the Electrolysis of Water.
 7 *J. Fluid Mech.* **2021**, *927*, A33.
- 8 (139) Modestino, M. A.; Fernandez Rivas, D.; Hashemi, S. M. H.; Gardeniers, J. G. E.; Psaltis, D. The Potential for Microfluidics in Electrochemical Energy Systems. *Energy Environ Sci* **2016**, *9*, 3381–3391.
- 11 (140) Schmelzer, J. (Jürn). *Nucleation Theory and Applications*; Wiley-VCH: Weinheim, 2005.
- 13 (141) Vehkamäki, Hanna. *Classical Nucleation Theory in Multicomponent Systems*; Springer, 2006.
- 15 (142) Hsu, Y. Y. On the Size Range of Active Nucleation Cavities on a Heating Surface. J.
 16 Heat Transfer 1962, 84, 207–213.
- 17 (143) Wang, C. H.; Dhir, V. K. On the Gas Entrapment and Nucleation Site Density During 18 Pool Boiling of Saturated Water. *J. Heat Transfer* **1993**, *115*, 670–679.
- 19 (144) Solymosi, T.; Geißelbrecht, M.; Mayer, S.; Auer, M.; Leicht, P.; Terlinden, M.; 20 Malgaretti, P.; Bösmann, A.; Preuster, P.; Harting, J.; et al. Nucleation as a Rate-21 Determining Step in Catalytic Gas Generation Reactions from Liquid Phase Systems. 22 Sci. Adv. 2022, 8, eade3262.
- 23 (145) Shibata, S. The Concentration of Molecular Hydrogen on the Platinum Cathode. *Bull.* 24 *Chem. Soc. Jpn.* **1963**, *36*, 53–57.
- Yang, X.; Karnbach, F.; Uhlemann, M.; Odenbach, S.; Eckert, K. Dynamics of Single
 Hydrogen Bubbles at a Platinum Microelectrode. *Langmuir* 2015, 31, 8184–8193.
- 27 (147) Luo, L.; White, H. S. Electrogeneration of Single Nanobubbles at Sub-50-nm-Radius 28 Platinum Nanodisk Electrodes. *Langmuir* **2013**, *29*, 11169–11175.
- 29 (148) German, S. R.; Edwards, M. A.; Chen, Q.; Liu, Y.; Luo, L.; White, H. S. Electrochemistry of Single Nanobubbles. Estimating the Critical Size of Bubble-31 Forming Nuclei for Gas-Evolving Electrode Reactions. *Faraday Discuss.* **2016**, *193*, 223–240.
- 33 (149) German, S. R.; Edwards, M. A.; Ren, H.; White, H. S. Critical Nuclei Size, Rate, and Activation Energy of H₂ Gas Nucleation. *J. Am. Chem. Soc.* **2018**, *140*, 4047–4053.

- (150) Henry, W. III. Experiments on the Quantity of Gases Absorbed by Water, at Different 1
- 2 Temperatures, and under Different Pressures. Philos. Trans. R. Soc. Lond. 1803, 93, 29–
- 3 274.
- (151) Sander, R. Compilation of Henry's Law Constants (Version 4.0) for Water as Solvent. 4
- Atmos. Chem. Phys. 2015, 15, 4399-4981. 5
- (152) Lu, Z.; Zhang, L.; Iwata, R.; Wang, E. N.; Grossman, J. C. Transport-Based Modeling 6 of Bubble Nucleation on Gas Evolving Electrodes. Langmuir 2020, 36, 15112–15118. 7
- (153) Gaertner, R. F. Population of Active Sites in Nucleate Boiling Heat Transfer, University 8 of Illinois at Urbana-Champaign, Urbana, 1959. 9
- (154) Gaertner, R.; Westwater, J. Population of Active Sites in Nucleate Boiling Heat Transfer. 10 11 Chem. eng. prog. symp. ser. 1960, 56, 39–48.
- (155) Sultan, M.; Judd, R. L. Spatial Distribution of Active Sites and Bubble Flux Density. J. 12 13 Heat Transfer 1978, 100, 56-62.
- (156) Wang, C. H.; Dhir, V. K. Effect of Surface Wettability on Active Nucleation Site 14 Density During Pool Boiling of Water on a Vertical Surface. J. Heat Transfer 1993, 115, 15 659-669. 16
- (157) Zhang, L.; Iwata, R.; Zhao, L.; Gong, S.; Lu, Z.; Xu, Z.; Zhong, Y.; Zhu, J.; Cruz, S.; 17 Wilke, K. L.; et al. Nucleation Site Distribution Probed by Phase-Enhanced 18 Environmental Scanning Electron Microscopy. Cell Rep. Phys. Sci. 2020, 1, 100262. 19
- (158) Hibiki, T.; Ishii, M. Active Nucleation Site Density in Boiling Systems. Int. J. Heat 20 Mass Transf. 2003, 46, 2587-2601. 21
- (159) Janssen, L. J. J.; Sillen, C. W. M. P.; Barendrecht, E.; van Stralen, S. J. D. Bubble 22 Behaviour during Oxygen and Hydrogen Evolution at Transparent Electrodes in KOH 23 24 Solution. Electrochim. Acta 1984, 29, 633-642.
- (160) Soto, A. M.; German, S. R.; Ren, H.; van der Meer, D.; Lohse, D.; Edwards, M. A.; 25 White, H. S. The Nucleation Rate of Single O₂ Nanobubbles at Pt Nanoelectrodes. 26 Langmuir 2018, 34, 7309-7318. 27
- (161) Edwards, M. A.; White, H. S.; Ren, H. Voltammetric Determination of the Stochastic 28 Formation Rate and Geometry of Individual H2, N2, and O2 Bubble Nuclei. ACS Nano 29 **2019**, *13*, 6330–6340. 30
- 31 (162) Chen, Q.; Luo, L.; Faraji, H.; Feldberg, S. W.; White, H. S. Electrochemical Measurements of Single H₂ Nanobubble Nucleation and Stability at Pt Nanoelectrodes. 32 33
- J. Phys. Chem. Lett. 2014, 5, 3539-3544.

- 1 (163) German, S. R.; Edwards, M. A.; Chen, Q.; White, H. S. Laplace Pressure of Individual 2 H₂ Nanobubbles from Pressure–Addition Electrochemistry. *Nano Lett.* **2016**, *16*, 6691–
- 3 6694.
- 4 (164) Chen, Q.; Wiedenroth, H. S.; German, S. R.; White, H. S. Electrochemical Nucleation of Stable N₂ Nanobubbles at Pt Nanoelectrodes. *J. Am. Chem. Soc.* **2015**, *137*, 12064–12069.
- 7 (165) Bard, A. J.; Fan, F. R. F.; Kwak, Juhyoun.; Lev, Ovadia. Scanning Electrochemical Microscopy. Introduction and Principles. *Anal. Chem.* **1989**, *61*, 132–138.
- 9 (166) Ebejer, N.; Güell, A. G.; Lai, S. C. S.; McKelvey, K.; Snowden, M. E.; Unwin, P. R. Scanning Electrochemical Cell Microscopy: A Versatile Technique for Nanoscale Electrochemistry and Functional Imaging. *Annu. Rev. Anal. Chem.* **2013**, *6*, 329–351.
- 12 (167) Snowden, M. E.; Güell, A. G.; Lai, S. C. S.; McKelvey, K.; Ebejer, N.; O'Connell, M. A.; Colburn, A. W.; Unwin, P. R. Scanning Electrochemical Cell Microscopy: Theory and Experiment for Quantitative High Resolution Spatially-Resolved Voltammetry and Simultaneous Ion-Conductance Measurements. *Anal. Chem.* **2012**, *84*, 2483–2491.
- (168) Ebejer, N.; Schnippering, M.; Colburn, A. W.; Edwards, M. A.; Unwin, P. R. Localized
 High Resolution Electrochemistry and Multifunctional Imaging: Scanning
 Electrochemical Cell Microscopy. *Anal. Chem.* 2010, 82, 9141–9145.
- 19 (169) Wang, Y.; Gordon, E.; Ren, H. Mapping the Nucleation of H₂ Bubbles on 20 Polycrystalline Pt via Scanning Electrochemical Cell Microscopy. *J. Phys. Chem. Lett.* 21 **2019**, 10, 3887–3892.
- 22 (170) Liu, Y.; Jin, C.; Liu, Y.; Ruiz, K. H.; Ren, H.; Fan, Y.; White, H. S.; Chen, Q. Visualization and Quantification of Electrochemical H₂ Bubble Nucleation at Pt, Au, and MoS₂ Substrates. *ACS Sens* **2021**, *6*, 355–363.
- (171) Mefford, J. T.; Akbashev, A. R.; Kang, M.; Bentley, C. L.; Gent, W. E.; Deng, H. D.;
 Alsem, D. H.; Yu, Y.-S.; Salmon, N. J.; Shapiro, D. A.; et al. Correlative Operando
 Microscopy of Oxygen Evolution Electrocatalysts. *Nature* 2021, *593*, 67–73.
- 28 (172) Liu, Y.; Lu, X.; Peng, Y.; Chen, Q. Electrochemical Visualization of Gas Bubbles on
 29 Superaerophobic Electrodes Using Scanning Electrochemical Cell Microscopy. *Anal.* 30 *Chem.* 2021, 93, 12337–12345.
- 31 (173) Deng, X.; Shan, Y.; Meng, X.; Yu, Z.; Lu, X.; Ma, Y.; Zhao, J.; Qiu, D.; Zhang, X.; Liu, Y.; et al. Direct Measuring of Single–Heterogeneous Bubble Nucleation Mediated by Surface Topology. *Proc. Natl. Acad. Sci.* **2022**, *119*, e2205827119.
- 34 (174) Yount, D. E.; Gillary, E. W.; Hoffman, D. C. A Microscopic Investigation of Bubble Formation Nuclei. *J. Acoust. Soc. Am.* **1984**, *76*, 1511–1521.

- 1 (175) Strenge, P. H.; Orell, A.; Westwater, J. W. Microscopic Study of Bubble Growth during Nucleate Boiling. *AIChE Journal* **1961**, *7*, 578–583.
- 3 (176) Vogel, Y. B.; Evans, C. W.; Belotti, M.; Xu, L.; Russell, I. C.; Yu, L.-J.; Fung, A. K. K.; 4 Hill, N. S.; Darwish, N.; Gonçales, V. R.; et al. The Corona of a Surface Bubble 5 Promotes Electrochemical Reactions. *Nat. Commun.* **2020**, *11*, 6323.
- 6 (177) Aliabouzar, M.; Kripfgans, O. D.; Brian Fowlkes, J.; Fabiilli, M. L. Bubble Nucleation 7 and Dynamics in Acoustic Droplet Vaporization: A Review of Concepts, Applications, 8 and New Directions. *Z. Med. Phys.* **2023**, *33*, 387–406.
- 9 (178) Giustini, G.; Kim, I.; Kim, H. Comparison between Modelled and Measured Heat 10 Transfer Rates during the Departure of a Steam Bubble from a Solid Surface. *Int. J. Heat* 11 *Mass Transf.* **2020**, *148*, 119092.
- 12 (179) Vakarelski, I. U.; Langley, K. R.; Yang, F.; Thoroddsen, S. T. Interferometry and Simulation of the Thin Liquid Film between a Free-Rising Bubble and a Glass Substrate.

 14 Langmuir 2022, 38, 2363–2371.
- 15 (180) Vadlamudi, S. R. G.; Moiz, M.; Srivastava, A. Microlayer Dynamics of 16 Hydrodynamically Interacting Vapour Bubbles in Flow Boiling. *J. Fluid Mech.* **2023**, 17 *958*, A44.
- 18 (181) Jung, S.; Kim, H. An Experimental Study on Heat Transfer Mechanisms in the 19 Microlayer Using Integrated Total Reflection, Laser Interferometry and Infrared 20 Thermometry Technique. *Heat Transf. Eng.* **2015**, *36*, 1002–1012.
- 21 (182) Ma, Y.; Highsmith, A. L.; Hill, C. M.; Pan, S. Dark-Field Scattering 22 Spectroelectrochemistry Analysis of Hydrazine Oxidation at Au Nanoparticle-Modified 23 Transparent Electrodes. J. Phys. Chem. C 2018, 122, 18603–18614.
- 24 (183) Xu, S.; Yu, X.; Chen, Z.; Zeng, Y.; Guo, L.; Li, L.; Luo, F.; Wang, J.; Qiu, B.; Lin, Z. 25 Real-Time Visualization of the Single-Nanoparticle Electrocatalytic Hydrogen 26 Generation Process and Activity under Dark Field Microscopy. *Anal. Chem.* **2020**, *92*, 27 9016–9023.
- (184) Li, S.; Du, Y.; He, T.; Shen, Y.; Bai, C.; Ning, F.; Hu, X.; Wang, W.; Xi, S.; Zhou, X.
 Nanobubbles: An Effective Way to Study Gas-Generating Catalysis on a Single
 Nanoparticle. J. Am. Chem. Soc. 2017, 139, 14277–14284.
- 31 (185) Leenheer, A. J.; Atwater, H. A. Water-Splitting Photoelectrolysis Reaction Rate via 32 Microscopic Imaging of Evolved Oxygen Bubbles. *J. Electrochem. Soc.* **2010**, *157*, 33 B1290.
- 34 (186) Seo, D.; Park, G.; Song, H. Plasmonic Monitoring of Catalytic Hydrogen Generation by a Single Nanoparticle Probe. *J. Am. Chem. Soc.* **2012**, *134*, 1221–1227.

- 1 (187) Hwang, H.; Song, H. Nanoscale Reaction Monitoring Using Localized Surface Plasmon 2 Resonance Scatterometry. *Chem. Phys. Rev.* **2022**, *3*, 031301.
- 3 (188) Yu, J.; Hu, K.; Zhang, Z.; Luo, L.; Liu, Y.; Zhou, D.; Wang, F.; Kuang, Y.; Xu, H.; Li, H.; et al. Interfacial Nanobubbles' Growth at the Initial Stage of Electrocatalytic Hydrogen Evolution. *Energy Environ. Sci.* **2023**, *16*, 2068–2079.
- 6 (189) Novo, C.; Funston, A. M.; Mulvaney, P. Direct Observation of Chemical Reactions on 7 Single Gold Nanocrystals Using Surface Plasmon Spectroscopy. *Nat. Nanotechnol.* 8 **2008**, *3*, 598–602.
- 9 (190) Chang, X.; Vijay, S.; Zhao, Y.; Oliveira, N. J.; Chan, K.; Xu, B. Understanding the 10 Complementarities of Surface-Enhanced Infrared and Raman Spectroscopies in CO 11 Adsorption and Electrochemical Reduction. *Nat. Commun.* **2022**, *13*, 2656.
- (191) Lelek, M.; Gyparaki, M. T.; Beliu, G.; Schueder, F.; Griffié, J.; Manley, S.; Jungmann,
 R.; Sauer, M.; Lakadamyali, M.; Zimmer, C. Single-Molecule Localization Microscopy.
 Nat. Rev. Methods Primers 2021, 1, 39.
- (192) Sauer, M.; Heilemann, M. Single-Molecule Localization Microscopy in Eukaryotes.
 Chem. Rev. 2017, 117, 7478-7509.
- 17 (193) Schermelleh, L.; Ferrand, A.; Huser, T.; Eggeling, C.; Sauer, M.; Biehlmaier, O.; 18 Drummen, G. P. C. Super-Resolution Microscopy Demystified. *Nat. Cell Biol.* **2019**, *21*, 19 72–84.
- (194) Reinhardt, S. C. M.; Masullo, L. A.; Baudrexel, I.; Steen, P. R.; Kowalewski, R.; Eklund,
 A. S.; Strauss, S.; Unterauer, E. M.; Schlichthaerle, T.; Strauss, M. T.; et al. Ångström Resolution Fluorescence Microscopy. *Nature* 2023, 617, 711–716.
- 23 (195) Dong, J.; Lu, Y.; Xu, Y.; Chen, F.; Yang, J.; Chen, Y.; Feng, J. Direct Imaging of Single-24 Molecule Electrochemical Reactions in Solution. *Nature* **2021**, *596*, 244–249.
- 25 (196) Zhong, J.-H.; Jin, X.; Meng, L.; Wang, X.; Su, H.-S.; Yang, Z.-L.; Williams, C. T.; Ren,
 B. Probing the Electronic and Catalytic Properties of a Bimetallic Surface with 3 nm
 Resolution. *Nat. Nanotechnol.* 2017, *12*, 132–136.
- 28 (197) Wilson, A. J.; Willets, K. A. Visualizing Site-Specific Redox Potentials on the Surface 29 of Plasmonic Nanoparticle Aggregates with Superlocalization SERS Microscopy. *Nano* 30 *Lett.* **2014**, *14*, 939–945.
- 31 (198) Wang, Y.; Yuan, T.; Su, H.; Zhou, K.; Yin, L.; Wang, W. A Bubble-STORM Approach 32 for Super-Resolved Imaging of Nucleation Sites in Hydrogen Evolution Reactions. *ACS* 33 *Sens.* **2021**, *6*, 380–386.

- 1 (199) Tachikawa, T.; Wang, N.; Yamashita, S.; Cui, S.; Majima, T. Design of a Highly
- 2 Sensitive Fluorescent Probe for Interfacial Electron Transfer on a TiO₂ Surface. *Angew*.
- 3 *Chem. Int. Ed.* **2010**, *49*, 8593–8597.
- 4 (200) Roeffaers, M. B. J.; De Cremer, G.; Libeert, J.; Ameloot, R.; Dedecker, P.; Bons, A.;
- Bückins, M.; Martens, J. A.; Sels, B. F.; De Vos, D. E.; et al. Super-Resolution
- Reactivity Mapping of Nanostructured Catalyst Particles. *Angew. Chem. Int. Ed.* **2009**,
- 7 48, 9285–9289.
- 8 (201) Zhou, X.; Andoy, N. M.; Liu, G.; Choudhary, E.; Han, K.-S.; Shen, H.; Chen, P.
- 9 Quantitative Super-Resolution Imaging Uncovers Reactivity Patterns on Single
- Nanocatalysts. *Nat. Nanotechnol.* **2012**, 7, 237–241.
- 11 (202) Xu, W.; Kong, J. S.; Yeh, Y.-T. E.; Chen, P. Single-Molecule Nanocatalysis Reveals
- Heterogeneous Reaction Pathways and Catalytic Dynamics. *Nat. Mater.* **2008**, 7, 992–
- 13 996.
- 14 (203) Zhang, T.; Li, S.; Du, Y.; He, T.; Shen, Y.; Bai, C.; Huang, Y.; Zhou, X. Revealing the
- Activity Distribution of a Single Nanocatalyst by Locating Single Nanobubbles with
- Super-Resolution Microscopy. J. Phys. Chem. Lett. 2018, 9, 5630–5635.
- 17 (204) Hao, R.; Fan, Y.; Howard, M. D.; Vaughan, J. C.; Zhang, B. Imaging Nanobubble
- Nucleation and Hydrogen Spillover during Electrocatalytic Water Splitting. *Proc. Natl.*
- 19 *Acad. Sci.* **2018**, *115*, 5878–5883.
- 20 (205) Chan, C. U.; Ohl, C.-D. Total-Internal-Reflection-Fluorescence Microscopy for the
- Study of Nanobubble Dynamics. Phys. Rev. Lett. 2012, 109, 174501.
- 22 (206) Su, H.; Fang, Y.; Chen, F.; Wang, W. Monitoring the Dynamic Photocatalytic Activity
- of Single CdS Nanoparticles by Lighting up H₂ Nanobubbles with Fluorescent Dyes.
- 24 *Chem. Sci.* **2018**, *9*, 1448–1453.
- 25 (207) Sambur, J. B.; Chen, T.-Y.; Choudhary, E.; Chen, G.; Nissen, E. J.; Thomas, E. M.; Zou,
- N.; Chen, P. Sub-Particle Reaction and Photocurrent Mapping to Optimize Catalyst-
- 27 Modified Photoanodes. *Nature* **2016**, *530*, 77–80.
- 28 (208) Chen, J.; Zhou, K.; Wang, Y.; Gao, J.; Yuan, T.; Pang, J.; Tang, S.; Chen, H.-Y.; Wang,
- W. Measuring the Activation Energy Barrier for the Nucleation of Single Nanosized
- 30 Vapor Bubbles. *Proc. Natl. Acad. Sci.* **2019**, *116*, 12678–12683.
- 31 (209) Wu, C.-Y.; Wolf, W. J.; Levartovsky, Y.; Bechtel, H. A.; Martin, M. C.; Toste, F. D.;
- Gross, E. High-Spatial-Resolution Mapping of Catalytic Reactions on Single Particles.
- 33 *Nature* **2017**, *541*, 511–515.
- 34 (210) van Schrojenstein Lantman, E. M.; Deckert-Gaudig, T.; Mank, A. J. G.; Deckert, V.;
- Weckhuysen, B. M. Catalytic Processes Monitored at the Nanoscale with Tip-Enhanced
- Raman Spectroscopy. *Nat. Nanotechnol.* **2012**, 7, 583–586.

- 1 (211) Ross, F. M. Opportunities and Challenges in Liquid Cell Electron Microscopy. *Science* 2 **2015**, *350*, aaa9886.
- 3 (212) de Jonge, N.; Houben, L.; Dunin-Borkowski, R. E.; Ross, F. M. Resolution and Aberration Correction in Liquid Cell Transmission Electron Microscopy. *Nat. Rev. Mater.* **2018**, *4*, 61–78.
- 6 (213) Pu, S.; Gong, C.; Robertson, A. W. Liquid Cell Transmission Electron Microscopy and Its Applications. *R. Soc. Open. Sci.* **2020**, *7*, 191204.
- 8 (214) Grogan, J. M.; Schneider, N. M.; Ross, F. M.; Bau, H. H. Bubble and Pattern Formation in Liquid Induced by an Electron Beam. *Nano Lett.* **2014**, *14*, 359–364.
- 10 (215) Liu, Y.; Dillon, S. J. In Situ Observation of Electrolytic H₂ Evolution Adjacent to Gold Cathodes. *Chem. Commun.* **2014**, *50*, 1761–1763.
- 12 (216) Wang, W.; Xu, T.; Chen, J.; Shangguan, J.; Dong, H.; Ma, H.; Zhang, Q.; Yang, J.; Bai, T.; Guo, Z.; et al. Solid–Liquid–Gas Reaction Accelerated by Gas Molecule Tunnelling-like Effect. *Nat. Mater.* **2022**, *21*, 859–863.
- Yin, Z.-W.; Betzler, S. B.; Sheng, T.; Zhang, Q.; Peng, X.; Shangguan, J.; Bustillo, K.
 C.; Li, J.-T.; Sun, S.-G.; Zheng, H. Visualization of Facet-Dependent Pseudo Photocatalytic Behavior of TiO₂ Nanorods for Water Splitting Using In Situ Liquid Cell
 TEM. Nano Energy 2019, 62, 507–512.
- 19 (218) Donald, A. M. The Use of Environmental Scanning Electron Microscopy for Imaging 20 Wet and Insulating Materials. *Nat. Mater.* **2003**, *2*, 511–516.
- 21 (219) Zhang, Z.; Zhou, Y.; Zhu, X.; Fei, L.; Huang, H.; Wang, Y. Applications of ESEM on 22 Materials Science: Recent Updates and a Look Forward. *Small Methods* **2020**, *4*, 23 1900588.
- 24 (220) Zhang, L.; Zhu, J.; Wilke, K. L.; Xu, Z.; Zhao, L.; Lu, Z.; Goddard, L. L.; Wang, E. N.
 25 Enhanced Environmental Scanning Electron Microscopy Using Phase Reconstruction
 26 and Its Application in Condensation. ACS Nano 2019, 13, 1953–1960.
- 27 (221) Zhu, J.; Zhang, L.; Li, X.; Wilke, K. L.; Wang, E. N.; Goddard, L. L. Quasi-Newtonian 28 Environmental Scanning Electron Microscopy (QN-ESEM) for Monitoring Material 29 Dynamics in High-Pressure Gaseous Environments. *Adv. Sci.* **2020**, *7*, 2001268.
- 30 (222) Rossi, M. P.; Ye, H.; Gogotsi, Y.; Babu, S.; Ndungu, P.; Bradley, J.-C. Environmental 31 Scanning Electron Microscopy Study of Water in Carbon Nanopipes. *Nano Lett.* **2004**, 32 *4*, 989–993.
- 33 (223) Wilson, N. R.; Clewes, S. L.; Newton, M. E.; Unwin, P. R.; Macpherson, J. V. Impact 34 of Grain-Dependent Boron Uptake on the Electrochemical and Electrical Properties of

- Polycrystalline Boron Doped Diamond Electrodes. *J. Phys. Chem. B* **2006**, *110*, 5639–5646.
- 3 (224) Patten, H. V.; Meadows, K. E.; Hutton, L. A.; Iacobini, J. G.; Battistel, D.; McKelvey,
- 4 K.; Colburn, A. W.; Newton, M. E.; Macpherson, J. V.; Unwin, P. R. Electrochemical
- 5 Mapping Reveals Direct Correlation between Heterogeneous Electron-Transfer Kinetics
- and Local Density of States in Diamond Electrodes. Angew. Chem. Int. Ed. 2012, 51,
- 7 7002–7006.
- 8 (225) Lai, S. C. S.; Patel, A. N.; McKelvey, K.; Unwin, P. R. Definitive Evidence for Fast
- 9 Electron Transfer at Pristine Basal Plane Graphite from High-Resolution
- Electrochemical Imaging. Angew. Chem. Int. Ed. 2012, 51, 5405–5408.
- 11 (226) Güell, A. G.; Ebejer, N.; Snowden, M. E.; McKelvey, K.; Macpherson, J. V.; Unwin, P.
- R. Quantitative Nanoscale Visualization of Heterogeneous Electron Transfer Rates in
- 2D Carbon Nanotube Networks. *Proc. Natl. Acad. Sci.* **2012**, *109*, 11487–11492.
- 14 (227) Lai, S. C. S.; Dudin, P. V.; Macpherson, J. V.; Unwin, P. R. Visualizing Zeptomole
- (Electro)Catalysis at Single Nanoparticles within an Ensemble. J. Am. Chem. Soc. 2011,
- 16 *133*, 10744–10747.
- 17 (228) Kleijn, S. E. F.; Lai, S. C. S.; Miller, T. S.; Yanson, A. I.; Koper, M. T. M.; Unwin, P.
- 18 R. Landing and Catalytic Characterization of Individual Nanoparticles on Electrode
- 19 Surfaces. J. Am. Chem. Soc. **2012**, 134, 18558–18561.
- 20 (229) Hecht, E. Optics, 5 ed.; Pearson Education, Inc.: Boston, 2017.
- 21 (230) Sanderson, J. B. *Understanding Light Microscopy*; Royal Microscopical Society/John
- Wiley Series; Wiley: Hoboken, NJ, 2019.
- 23 (231) Gupta, P.; Das, S. S.; Singh, N. B. Spectroscopy; Jenny Stanford Publishing Pte. Ltd.:
- Singapore, 2023.
- 25 (232) Steel, W. H. Interferometry, 2nd ed.; Cambridge monographs on physics; Cambridge
- University Press: Cambridge, 1983.
- 27 (233) Prosperetti, A. Vapor Bubbles. *Annu. Rev. Fluid Mech.* **2017**, *49*, 221–248.
- 28 (234) Rayleigh, Lord. On the Pressure Developed in a Liquid during the Collapse of a
- 29 Spherical Cavity. *Philos. Mag.* **1917**, *34*, 94–98.
- 30 (235) Brennen, C. E. Fundamentals of Multiphase Flow; Cambridge University Press: West
- 31 Nyack, 2005.
- 32 (236) Plesset, M. S.; Zwick, S. A. The Growth of Vapor Bubbles in Superheated Liquids. J.
- 33 *Appl. Phys.* **1954**, *25*, 493–500.

- 1 (237) Forster, H. K.; Zuber, N. Growth of a Vapor Bubble in a Superheated Liquid. *J. Appl. Phys.* **1954**, *25*, 474–478.
- 3 (238) Scriven, L. E. On the Dynamics of Phase Growth. Chem. Eng. Sci. 1959, 10, 1–13.
- 4 (239) Robinson, A. J.; Judd, R. L. The Dynamics of Spherical Bubble Growth. *Int. J. Heat Mass Transf.* **2004**, *47*, 5101–5113.
- 6 (240) Lee, H. C.; Oh, B. Do; Bae, S. W.; Kim, M. H. Single Bubble Growth in Saturated Pool Boiling on a Constant Wall Temperature Surface. *Int. J. Multiph. Flow.* **2003**, *29*, 1857–1874.
- 9 (241) Verhaart, H. F. A.; de Jonge, R. M.; van Stralen, S. J. D. Growth Rate of a Gas Bubble during Electrolysis in Supersaturated Liquid. *Int. J. Heat Mass Transf.* **1980**, *23*, 293–11 299.
- 12 (242) Brandon, N. P.; Kelsall, G. H. Growth Kinetics of Bubbles Electrogenerated at Microelectrodes. *J. Appl. Electrochem.* **1985**, *15*, 475–484.
- 14 (243) Matsushima, H.; Kiuchi, D.; Fukunaka, Y.; Kuribayashi, K. Single Bubble Growth 15 during Water Electrolysis under Microgravity. *Electrochem. commun.* **2009**, *11*, 1721– 16 1723.
- 17 (244) Epstein, P. S.; Plesset, M. S. On the Stability of Gas Bubbles in Liquid-Gas Solutions.
 18 *J. Chem. Phys.* **1950**, *18*, 1505–1509.
- (245) Ghazivini, M.; Hafez, M.; Ratanpara, A.; Kim, M. A Review on Correlations of Bubble
 Growth Mechanisms and Bubble Dynamics Parameters in Nucleate Boiling. *J. Therm.* Anal. Calorim. 2022, 147, 6035–6071.
- (246) Du, J.; Zhao, C.; Bo, H. A Modified Model for Bubble Growth Rate and Bubble
 Departure Diameter in Nucleate Pool Boiling Covering a Wide Range of Pressures. *Appl. Therm. Eng.* 2018, *145*, 407–415.
- 25 (247) Stephan, P.; Hammer, J. A New Model for Nucleate Boiling Heat Transfer; Springer Verlag, 1994; Vol. 30.
- 27 (248) Glas, J. P.; Wrstwatrr, J. W. *Measurements of the Growth of Electrolytic Bubbles*; 28 Pergamon Press, 1964; Vol. 7.
- 29 (249) Chi-Yeh, H.; Griffith, P. The Mechanism of Heat Transfer in Nucleate Pool Boiling— 30 Part I. *Int. J. Heat Mass Transf.* **1965**, *8*, 887–904.
- 31 (250) Mikic, B. B.; Rohsenow, W. M.; Griffith, P. On Bubble Growth Rates. *Int. J. Heat Mass* 32 *Transf.* **1970**, *13*, 657–666.

- (251) Gerardi, C.; Buongiorno, J.; Hu, L.; McKrell, T. Study of Bubble Growth in Water Pool 1 2 Boiling through Synchronized, Infrared Thermometry and High-Speed Video. Int. J.
- 3 Heat Mass Transf. 2010, 53, 4185-4192.
- 4 (252) Moreno Soto, Á.; Prosperetti, A.; Lohse, D.; Van Der Meer, D. Gas Depletion through Single Gas Bubble Diffusive Growth and Its Effect on Subsequent Bubbles. J. Fluid 5 Mech. 2017, 831, 474-490. 6
- 7 (253) Lv, P.; Le The, H.; Eijkel, J.; Van den Berg, A.; Zhang, X.; Lohse, D. Growth and Detachment of Oxygen Bubbles Induced by Gold-Catalyzed Decomposition of 8 Hydrogen Peroxide. J. Phys. Chem. C 2017, 121, 20769–20776. 9
- 10 (254) Thorncroft, G. E.; Klausnera, J. F.; Mei, R. An Experimental Investigation of Bubble Growth and Detachment in Vertical Upflow and Downflow Boiling. Int. J. Heat Mass 11 Transf. 1998, 41, 3857–3871. 12
- (255) van der Linde, P.; Moreno Soto, Á.; Peñas-López, P.; Rodríguez-Rodríguez, J.; Lohse, 13 D.; Gardeniers, H.; van der Meer, D.; Fernández Rivas, D. Electrolysis-Driven and 14 Pressure-Controlled Diffusive Growth of Successive Bubbles on Microstructured 15 16 Surfaces. *Langmuir* **2017**, *33*, 12873–12886.
- (256) van der Linde, P.; Peñas-López, P.; Moreno Soto, Á.; van der Meer, D.; Lohse, D.; 17 Gardeniers, H.; Fernández Rivas, D. Gas Bubble Evolution on Microstructured Silicon 18 19 Substrates. Energy Environ. Sci. 2018, 11, 3452–3462.
- (257) Kempler, P. A.; Coridan, R. H.; Lewis, N. S. Effects of Bubbles on the Electrochemical 20 21 Behavior of Hydrogen-Evolving Si Microwire Arrays Oriented against Gravity. *Energy* 22 Environ. Sci. 2020, 13, 1808–1817.
- 23 (258) Peñas, P.; van der Linde, P.; Vijselaar, W.; van der Meer, D.; Lohse, D.; Huskens, J.; 24 Gardeniers, H.; Modestino, M. A.; Rivas, D. F. Decoupling Gas Evolution from Water-Splitting Electrodes. J. Electrochem. Soc. 2019, 166, H769–H776. 25
- (259) Qin, J.; Xie, T.; Zhou, D.; Luo, L.; Zhang, Z.; Shang, Z.; Li, J.; Mohapatra, L.; Yu, J.; 26 Xu, H.; et al. Kinetic Study of Electrochemically Produced Hydrogen Bubbles on Pt 27 Electrodes with Tailored Geometries. Nano Res. 2021, 14, 2154–2159. 28
- 29 (260) Darby, R.; Haque, M. S. The Dynamics of Electrolytic Hydrogen Bubble Evolution. 30 Chem. Eng. Sci. 1973, 28, 1129–1138.
- (261) Wang, Y.; Hu, X.; Cao, Z.; Guo, L. Investigations on Bubble Growth Mechanism during 31 32 Photoelectrochemical and Electrochemical Conversions. Colloids Surf. A: Physicochem. Eng. Asp. 2016, 505, 86-92. 33
- 34 (262) She, Y.; Xu, Q.; Nie, T.; Luo, X.; Wang, M.; Tao, L.; Guo, L. In Situ Investigation of Oxygen Bubble Evolution at Photoanode Surface Affected by Reaction Temperature. J. 35 Phys. Chem. C 2023, 127, 14197–14210. 36

- 1 (263) Bashkatov, A.; Hossain, S. S.; Mutschke, G.; Yang, X.; Rox, H.; Weidinger, I. M.;
- Eckert, K. On the Growth Regimes of Hydrogen Bubbles at Microelectrodes. *Phys.*
- 3 Chem. Chem. Phys. **2022**, 24, 26738–26752.
- 4 (264) Nam, Y.; Aktinol, E.; Dhir, V. K.; Ju, Y. S. Single Bubble Dynamics on a
- 5 Superhydrophilic Surface with Artificial Nucleation Sites. *Int. J. Heat Mass Transf.*
- 6 **2011**, *54*, 1572–1577.
- 7 (265) Hertz, H. Ueber Die Verdunstung Der Flüssigkeiten, Insbesondere Des Quecksilbers,
- 8 Im Luftleeren Raume. *Ann. Phys.* **1882**, *253*, 177–193.
- 9 (266) Knudsen, M. Die Maximale Verdampfungsgeschwindigkeit Des Quecksilbers. Ann.
- 10 *Phys.* **1915**, *352*, 697–708.
- 11 (267) Hu, Z.; Gong, S. Mesoscopic Model for Disjoining Pressure Effects in Nanoscale Thin
- Liquid Films and Evaporating Extended Meniscuses. *Langmuir* **2023**, *39*, 13359–13370.
- 13 (268) Zou, A.; Singh, D. P.; Maroo, S. C. Early Evaporation of Microlayer for Boiling Heat
- 14 Transfer Enhancement. *Langmuir* **2016**, *32*, 10808–10814.
- 15 (269) Zou, A.; Gupta, M.; Maroo, S. C. Origin, Evolution, and Movement of Microlayer in
- 16 Pool Boiling. J. Phys. Chem. Lett. 2018, 9, 3863–3869.
- 17 (270) Bureš, L.; Sato, Y. Comprehensive Simulations of Boiling with a Resolved Microlayer:
- Validation and Sensitivity Study. *J. Fluid Mech.* **2022**, *933*, A54.
- 19 (271) Brutin, D. Droplet Wetting and Evaporation From Pure to Complex Fluids, 1st ed.;
- Elsevier: San Diego, 2015.
- 21 (272) McGrew, J. L.; Bamford, F. L.; Rehm, T. R. Marangoni Flow: An Additional
- Mechanism in Boiling Heat Transfer. Science 1966, 153, 1106–1107.
- 23 (273) Namura, K.; Nakajima, K.; Suzuki, M. Quasi-Stokeslet Induced by Thermoplasmonic
- Marangoni Effect around a Water Vapor Microbubble. Sci. Rep. 2017, 7, 45776.
- 25 (274) Kim, B. S.; Choi, G.; Shin, S.; Gemming, T.; Cho, H. H. Nano-Inspired Fluidic
- Interactivity for Boiling Heat Transfer: Impact and Criteria. Sci. Rep. 2016, 6, 34348.
- 27 (275) Zhang, N.; Chao, D. F. Models for Enhanced Boiling Heat Transfer by Unusual
- Marangoni Effects under Microgravity Conditions. Int. Commun. Heat Mass Transf.
- 29 **1999**, *26*, 1081–1090.
- 30 (276) Sun, C.; Carey, V. P. Marangoni Effects on the Boiling of 2-Propanol/Water Mixtures
- 31 in a Confined Space. *Int. J. Heat Mass Transf.* **2004**, *47*, 5417–5426.
- 32 (277) Hu, Y.; Chen, S.; Huang, J.; Song, M. Marangoni Effect on Pool Boiling Heat Transfer
- Enhancement of Self-Rewetting Fluid. *Int. J. Heat Mass Transf.* **2018**, *127*, 1263–1270.

- 1 (278) Karpitschka, S.; Liebig, F.; Riegler, H. Marangoni Contraction of Evaporating Sessile 2 Droplets of Binary Mixtures. *Langmuir* **2017**, *33*, 4682–4687.
- 3 (279) Diddens, C.; Li, Y.; Lohse, D. Competing Marangoni and Rayleigh Convection in Evaporating Binary Droplets. *J. Fluid Mech.* **2021**, *914*, A23.
- 5 (280) Phadnis, A.; Rykaczewski, K. The Effect of Marangoni Convection on Heat Transfer during Dropwise Condensation on Hydrophobic and Omniphobic Surfaces. *Int. J. Heat Mass Transf.* **2017**, *115*, 148–158.
- 8 (281) Xu, Z.; Zhang, L.; Wilke, K.; Wang, E. N. Multiscale Dynamic Growth and Energy Transport of Droplets during Condensation. *Langmuir* **2018**, *34*, 9085–9095.
- (282) Zheng, S. F.; Wu, Z. Y.; Gao, Y. Y.; Yang, Y. R.; Sundén, B.; Wang, X. D. Transient
 Multiphysics Coupled Model for Multiscale Droplet Condensation out of Moist Air.
 Numeri. Heat Transf. A: Appl. 2023, 84, 16–34.
- 13 (283) Palmer, H. J. The Hydrodynamic Stability of Rapidly Evaporating Liquids at Reduced 14 Pressure. *J. Fluid Mech.* **1976**, *75*, 487.
- (284) Sefiane, K.; Benielli, D.; Steinchen, A. A New Mechanism for Pool Boiling Crisis,
 Recoil Instability and Contact Angle Influence. *Colloids Surf. A: Physicochem. Eng.* Asp. 1998, 142, 361–373.
- 18 (285) Nikolayev, V. S.; Beysens, D. A. Boiling Crisis and Non-Equilibrium Drying Transition.
 19 *Europhys. Lett.* **1999**, *47*, 345–351.
- 20 (286) Nikolayev, V. S.; Chatain, D.; Garrabos, Y.; Beysens, D. Experimental Evidence of the Vapor Recoil Mechanism in the Boiling Crisis. *Phys. Rev. Lett.* **2006**, *97*, 184503.
- 22 (287) Yang, X.; Baczyzmalski, D.; Cierpka, C.; Mutschke, G.; Eckert, K. Marangoni 23 Convection at Electrogenerated Hydrogen Bubbles. *Phys. Chem. Chem. Phys.* **2018**, *20*, 24 11542–11548.
- (288) Park, S.; Liu, L.; Demirkır, Ç.; van der Heijden, O.; Lohse, D.; Krug, D.; Koper, M. T.
 M. Solutal Marangoni Effect Determines Bubble Dynamics during Electrocatalytic
 Hydrogen Evolution. *Nat. Chem.* 2023, *15*, 1532–1540.
- 28 (289) Vargaftik, N. B.; Gorshkov, Yu. A. *Handbook of Thermal Conductivity of Liquids and* 29 *Gases*; CRC Press: Boca Raton, 1994.
- 30 (290) Yaws, C. L. *Handbook of Thermal Conductivity*; Library of physico-chemical property data; Gulf Pub. Co.: Houston, 1995.
- 32 (291) Dyos, G. T.; Farrell, T. *Electrical Resistivity Handbook*; IEE materials & devices series; 33 10; Peter Peregrinus on behalf of the Institution of Electrical Engineers: London, U.K, 1992.

- 1 (292) Fernández, D.; Maurer, P.; Martine, M.; Coey, J. M. D.; Möbius, M. E. Bubble 2 Formation at a Gas-Evolving Microelectrode. *Langmuir* **2014**, *30*, 13065–13074.
- 3 (293) Liu, H.; Pan, L.; Huang, H.; Qin, Q.; Li, P.; Wen, J. Hydrogen Bubble Growth at Micro-4 Electrode under Magnetic Field. *J. Electroanal. Chem.* **2015**, *754*, 22–29.
- 5 (294) Zhan, S.; Huang, Y.; Zhang, W.; Li, B.; Jiang, M.; Wang, Z.; Wang, J. Experimental
- 6 Investigation on Bubble Growth and Detachment Characteristics on Vertical
- 7 Microelectrode Surface under Electrode-Normal Magnetic Field in Water Electrolysis.
- 8 *Int. J. Hydrogen Energy* **2021**, *46*, 36640–36651.
- 9 (295) Lee, J. K.; Bazylak, A. Bubbles: The Good, the Bad, and the Ugly. *Joule* **2021**, *5*, 19–10 21.
- 11 (296) Rue, R. E. D. La; Tobias, C. W. On the Conductivity of Dispersions. *J. Electrochem.*12 *Soc.* **1959**, *106*, 827.
- 13 (297) Meredith, R. E.; Tobias, C. W. Conductivities in Emulsions. *J. Electrochem. Soc.* **1961**, 108, 286.
- 15 (298) Clark, N. O. The Electrical Conductivity of Foam. *Trans. Faraday Soc.* **1948**, *44*, 13.
- 16 (299) Tobias, C. W. Effect of Gas Evolution on Current Distribution and Ohmic Resistance in 17 Electrolyzers. *J. Electrochem. Soc.* **1959**, *106*, 833.
- 18 (300) Vogt, H. A Hydrodynamic Model for the Ohmic Interelectrode Resistance of Cells with Vertical Gas Evolving Electrodes. *Electrochim. Acta* **1981**, *26*, 1311–1317.
- 20 (301) Hine, F.; Murakami, K. Bubble Effects on the Solution IR Drop in a Vertical Electrolyzer Under Free and Forced Convection. *J. Electrochem. Soc.* **1980**, *127*, 292–22 297.
- (302) Jovanovič, P.; Stojanovski, K.; Bele, M.; Dražić, G.; Koderman Podboršek, G.;
 Suhadolnik, L.; Gaberšček, M.; Hodnik, N. Methodology for Investigating
 Electrochemical Gas Evolution Reactions: Floating Electrode as a Means for Effective
 Gas Bubble Removal. Anal. Chem. 2019, 91, 10353–10356.
- (303) Ikeda, H.; Misumi, R.; Kojima, Y.; Haleem, A. A.; Kuroda, Y.; Mitsushima, S.
 Microscopic High-Speed Video Observation of Oxygen Bubble Generation Behavior
 and Effects of Anode Electrode Shape on OER Performance in Alkaline Water
 Electrolysis. Int. J. Hydrogen Energy 2022, 47, 11116–11127.
- 31 (304) Iwata, R.; Zhang, L.; Wilke, K. L.; Gong, S.; He, M.; Gallant, B. M.; Wang, E. N. Bubble 32 Growth and Departure Modes on Wettable/Non-Wettable Porous Foams in Alkaline 33 Water Splitting. *Joule* **2021**, *5*, 887–900.
- (305) Raman, A.; Peñas, P.; van der Meer, D.; Lohse, D.; Gardeniers, H.; Fernández Rivas, D.
 Potential Response of Single Successive Constant-Current-Driven Electrolytic

- Hydrogen Bubbles Spatially Separated from the Electrode. *Electrochim. Acta* 2022, 425,
 140691.
- 3 (306) Haziri, V.; Nha, T. P. T.; Berisha, A.; Boily, J.-F. A Gateway for Ion Transport on Gas 4 Bubbles Pinned onto Solids. *Commun. Chem.* **2021**, *4*, 43.
- 5 (307) Angulo, A. E.; Frey, D.; Modestino, M. A. Understanding Bubble-Induced 6 Overpotential Losses in Multiphase Flow Electrochemical Reactors. *Energy & Fuels* 7 **2022**, *36*, 7908–7914.
- 8 (308) Fritz, W. Maximum Volume of Vapour Bubbles. *Physik. Zeitschr.* **1935**, *36*, 379–384.
- 9 (309) Cole, R. Bubble Frequencies and Departure Volumes at Subatmospheric Pressures. 10 *AIChE Journal* **1967**, *13*, 779–783.
- (310) Vogt, H. The Problem of the Departure Diameter of Bubbles at Gas-Evolving Electrodes.
 Electrochim. Acta 1989, *34*, 1429–1432.
- 13 (311) Wang, X.; Wu, Z.; Wei, J.; Sundén, B. Correlations for Prediction of the Bubble 14 Departure Radius on Smooth Flat Surface during Nucleate Pool Boiling. *Int. J. Heat* 15 *Mass Transf.* **2019**, *132*, 699–714.
- 16 (312) Li, J.; Gong, S.; Zhang, L.; Cheng, P.; Ma, X.; Hong, F. Wetting States and Departure 17 Diameters of Bubbles on Micro-/Nanostructured Surfaces. *Langmuir* **2022**, *38*, 3180– 18 3188.
- 19 (313) Zhang, D.; Zeng, K. Evaluating the Behavior of Electrolytic Gas Bubbles and Their 20 Effect on the Cell Voltage in Alkaline Water Electrolysis. *Ind. Eng. Chem. Res.* **2012**, 21 51, 13825–13832.
- (314) Taqieddin, A.; Nazari, R.; Rajic, L.; Alshawabkeh, A. Review—Physicochemical
 Hydrodynamics of Gas Bubbles in Two Phase Electrochemical Systems. *J. Electrochem.* Soc. 2017, 164, E448–E459.
- 25 (315) Taqieddin, A.; Allshouse, M. R.; Alshawabkeh, A. N. Editors' Choice—Critical
 Review—Mathematical Formulations of Electrochemically Gas-Evolving Systems. J.
 27 Electrochem. Soc. 2018, 165, E694–E711.
- 28 (316) Qiu, H.; Obata, K.; Yuan, Z.; Nishimoto, T.; Lee, Y.; Nagato, K.; Kinefuchi, I.; Shiomi, J.; Takanabe, K. Quantitative Description of Bubble Formation in Response to Electrolyte Engineering. *Langmuir* **2023**, *39*, 4993–5001.
- 31 (317) Bashkatov, A.; Hossain, S. S.; Yang, X.; Mutschke, G.; Eckert, K. Oscillating Hydrogen 32 Bubbles at Pt Microelectrodes. *Phys. Rev. Lett.* **2019**, *123*, 214503.
- 33 (318) Chandran, P.; Bakshi, S.; Chatterjee, D. Study on the Characteristics of Hydrogen 34 Bubble Formation and Its Transport during Electrolysis of Water. *Chem. Eng. Sci.* **2015**, 35 *138*, 99–109.

- 1 (319) Abdelghani-Idrissi, S.; Dubouis, N.; Grimaud, A.; Stevens, P.; Toussaint, G.; Colin, A. 2 Effect of Electrolyte Flow on a Gas Evolution Electrode. *Sci. Rep.* **2021**, *11*, 4677.
- 3 (320) Krause, L.; Skibińska, K.; Rox, H.; Baumann, R.; Marzec, M. M.; Yang, X.; Mutschke,
- 4 G.; Żabiński, P.; Lasagni, A. F.; Eckert, K. Hydrogen Bubble Size Distribution on
- 5 Nanostructured Ni Surfaces: Electrochemically Active Surface Area Versus Wettability.
- 6 ACS Appl. Mater. Interfaces **2023**, 15, 18290–18299.
- 7 (321) Rox, H.; Bashkatov, A.; Yang, X.; Loos, S.; Mutschke, G.; Gerbeth, G.; Eckert, K.
- 8 Bubble Size Distribution and Electrode Coverage at Porous Nickel Electrodes in a Novel
- 9 3-Electrode Flow-through Cell. *Int. J. Hydrogen Energy* **2023**, *48*, 2892–2905.
- 10 (322) Moreno Soto, A.; Maddalena, T.; Fraters, A.; van der Meer, D.; Lohse, D. Coalescence of Diffusively Growing Gas Bubbles. *J. Fluid Mech.* **2018**, *846*, 143–165.
- 12 (323) Zhou, J.; Qi, B.; Zhang, Y.; Wei, J.; Yang, Y.; Cao, Q. Experimental and Theoretical
- 13 Study of Bubble Coalescence and Departure Behaviors during Nucleate Pool Boiling on
- 14 Uniform Smooth and Micro-Pin-Finned Surfaces under Different Subcoolings and Heat
- 15 Fluxes. Exp. Therm. Fluid Sci. 2020, 112, 109996.
- 16 (324) Lv, P.; Peñas, P.; Le The, H.; Eijkel, J.; van den Berg, A.; Zhang, X.; Lohse, D. Self-
- Propelled Detachment upon Coalescence of Surface Bubbles. *Phys. Rev. Lett.* **2021**, *127*,
- 18 235501.
- 19 (325) Iwata, R.; Zhang, L.; Lu, Z.; Gong, S.; Du, J.; Wang, E. N. How Coalescing Bubbles 20 Depart from a Wall. *Langmuir* **2022**, *38*, 4371–4377.
- 21 (326) Zhao, P.; Hu, Z.; Cheng, P.; Huang, R.; Gong, S. Coalescence-Induced Bubble
- Departure: Effects of Dynamic Contact Angles. *Langmuir* **2022**, *38*, 10558–10567.
- 23 (327) Park, H.; Ahmadi, S. F.; Foulkes, T. P.; Boreyko, J. B. Coalescence-Induced Jumping
- Bubbles during Pool Boiling. Adv. Funct. Mater. 2023, 34, 2312088.
- 25 (328) Wu, R.; Hu, Z.; Zhang, H.; Wang, J.; Qin, C.; Zhou, Y. Bubbles in Porous Electrodes
- for Alkaline Water Electrolysis. *Langmuir* **2024**, *40*, 721–733.
- 27 (329) Bashkatov, A.; Babich, A.; Hossain, S. S.; Yang, X.; Mutschke, G.; Eckert, K. H₂ Bubble
- Motion Reversals during Water Electrolysis. *J. Fluid Mech.* **2023**, *958*, A43.
- 29 (330) Vogt, H.; Stephan, K. Local Microprocesses at Gas-Evolving Electrodes and Their
- Influence on Mass Transfer. *Electrochim. Acta* **2015**, *155*, 348–356.
- 31 (331) Mikic, B. B.; Rohsenow, W. M. A New Correlation of Pool-Boiling Data Including the
- 32 Effect of Heating Surface Characteristics. *J. Heat Transfer* **1969**, *91*, 245–250.
- 33 (332) Vachon, R. I.; Nix, G. H.; Tanger, G. E. Evaluation of Constants for the Rohsenow Pool-
- Boiling Correlation. J. Heat Transfer 1968, 90, 239–246.

- 1 (333) Pioro, I. l. Experimental Evaluation of Constants for the Rohsenow Pool Boiling Correlation. *Int. J. Heat Mass Transf.* **1999**, *42*, 2003–2013.
- 3 (334) Pioro, I. L.; Rohsenow, W.; Doerffer, S. S. Nucleate Pool-Boiling Heat Transfer. I: 4 Review of Parametric Effects of Boiling Surface. *Int. J. Heat Mass Transf.* **2004**, *47*,
- 5 5033–5044.
- 6 (335) Mehrvand, M.; Putnam, S. A. Transient and Local Two-Phase Heat Transport at Macro-Scales to Nano-Scales. *Commun. Phys.* **2018**, *1*, 21.
- 8 (336) Mahmoud, M. M.; Karayiannis, T. G. Pool Boiling Review: Part I Fundamentals of Boiling and Relation to Surface Design. *Therm. Sci. Eng. Prog.* **2021**, *25*, 101024.
- 10 (337) Zhang, L.; Gong, S.; Lu, Z.; Cheng, P.; Wang, E. N. A Unified Relationship between 11 Bubble Departure Frequency and Diameter during Saturated Nucleate Pool Boiling. *Int.*
- 12 J. Heat Mass Transf. 2021, 165, 120640.
- 13 (338) Enríquez, O. R.; Sun, C.; Lohse, D.; Prosperetti, A.; van der Meer, D. The Quasi-Static 14 Growth of CO₂ Bubbles. *J. Fluid Mech.* **2014**, *741*, R1.
- (339) Moreno Soto, A.; Enríquez, O. R.; Prosperetti, A.; Lohse, D.; van der Meer, D.
 Transition to Convection in Single Bubble Diffusive Growth. *J. Fluid Mech.* 2019, 871,
 332–349.
- 18 (340) Moreno Soto, Á.; Lohse, D.; van der Meer, D. Diffusive Growth of Successive Bubbles 19 in Confinement. *J. Fluid Mech.* **2020**, *882*, A6.
- 20 (341) Sheffield, Scott.; Spencer, T. Statistical Mechanics; IAS/Park City mathematics series;
 v. 16; American Mathematical Society: Providence, R.I, 2009.
- 22 (342) Pathria, R. K.; Beale, P. D. *Statistical Mechanics*; Butterworth-Heinemann: Boston, 2011.
- 24 (343) Kittel, Charles. *Introduction to Solid State Physics*, 8th ed.; Wiley: Hoboken, NJ, 2005.
- (344) Ashcroft, N. W.; Mermin, N. David. *Solid State Physics*; Saunders College: Philadelphia,
 1976.
- 27 (345) Wen, H. W.; Jer, R. M. On the Heat Transfer in Dropwise Condensation. *J. Chem. Eng.* 28 1976, 12, 225–231.
- 29 (346) Rose, J. W.; Glicksman, L. R. Dropwise Condensation—The Distribution of Drop Sizes.
 30 *Int. J. Heat Mass Transf.* 1973, 16, 411–425.
- 31 (347) Kim, S.; Kim, K. J. Dropwise Condensation Modeling Suitable for Superhydrophobic 32 Surfaces. *J. Heat Transfer* **2011**, *133*, 081502.
- 33 (348) Miljkovic, N.; Enright, R.; Wang, E. N. Modeling and Optimization of Superhydrophobic Condensation. *J. Heat Transfer* **2013**, *135*, 111004.

- 1 (349) Zhang, L.; Xu, Z.; Lu, Z.; Du, J.; Wang, E. N. Size Distribution Theory for Jumping-2 Droplet Condensation. *Appl. Phys. Lett.* **2019**, *114*, 163701.
- (350) Zuber, N. Hydrodynamic Aspects of Boiling Heat Transfer, University of California,
 Los Angeles, Los Angeles, 1959.
- 5 (351) Haramura, Y.; Katto, Y. A New Hydrodynamic Model of Critical Heat Flux, Applicable 6 Widely to Both Pool and Forced Convection Boiling on Submerged Bodies in Saturated 7 Liquids. *Int. J. Heat Mass Transf.* **1983**, *26*, 389–399.
- 8 (352) Yagov, V. V. Is a Crisis in Pool Boiling Actually a Hydrodynamic Phenomenon? *Int. J. Heat Mass Transf.* **2014**, *73*, 265–273.
- 10 (353) Song, Y.; Zhang, L.; Díaz-Marín, C. D.; Cruz, S. S.; Wang, E. N. Unified Descriptor for 11 Enhanced Critical Heat Flux during Pool Boiling of Hemi-Wicking Surfaces. *Int. J. Heat* 12 *Mass Transf.* **2022**, *183*, 122189.
- 13 (354) Lloveras, P.; Salvat-Pujol, F.; Truskinovsky, L.; Vives, E. Boiling Crisis as a Critical Phenomenon. *Phys. Rev. Lett.* **2012**, *108*, 215701.
- 15 (355) Cheng, P.; Quan, X.; Gong, S.; Liu, X.; Yang, L. Recent Analytical and Numerical 16 Studies on Phase-Change Heat Transfer. *Adv. Heat Transf.* **2014**, *46*, 187–248.
- 17 (356) Kharangate, C. R.; Mudawar, I. Review of Computational Studies on Boiling and Condensation. *Int. J. Heat Mass Transf.* **2017**, *108*, 1164–1196.
- 19 (357) Jiang, H.; Liu, Y.; Chu, H. A Review of Numerical Investigation on Pool Boiling. J.
 20 Therm. Anal. Calorim. 2023, 148, 8697–8745.
- 21 (358) Lay, J. H.; Dhir, V. K. Shape of a Vapor Stem During Nucleate Boiling of Saturated 22 Liquids. *J. Heat Transfer* **1995**, *117*, 394–401.
- 23 (359) Son, G.; Dhir, V. K. Numerical Simulation of Film Boiling Near Critical Pressures with a Level Set Method. *J. Heat Transfer* **1998**, *120*, 183–192.
- (360) Son, G.; Ramanujapu, N.; Dhir, V. K. Numerical Simulation of Bubble Merger Process
 on a Single Nucleation Site During Pool Nucleate Boiling. *J. Heat Transfer* 2002, *124*,
 51–62.
- 28 (361) Mukherjee, A.; Dhir, V. K. Study of Lateral Merger of Vapor Bubbles During Nucleate 29 Pool Boiling. *J. Heat Transfer* **2004**, *126*, 1023–1039.
- (362) Li, D.; Dhir, V. K. Numerical Study of Single Bubble Dynamics During Flow Boiling.
 J. Heat Transfer 2007, *129*, 864–876.
- 32 (363) Wu, J.; Dhir, V. K.; Qian, J. Numerical Simulation of Subcooled Nucleate Boiling by 33 Coupling Level-Set Method with Moving-Mesh Method. *Numer. Heat Tr. B: Fund.* 34 **2007**, *51*, 535–563.

- 1 (364) Son, G.; Dhir, V. K. Numerical Simulation of Nucleate Boiling on a Horizontal Surface 2 at High Heat Fluxes. *Int. J. Heat Mass Transf.* **2008**, *51*, 2566–2582.
- 3 (365) Dhruv, A.; Balaras, E.; Riaz, A.; Kim, J. A Formulation for High-Fidelity Simulations of Pool Boiling in Low Gravity. *Int. J. Multiph. Flow* **2019**, *120*, 103099.
- (366) Dhruv, A.; Balaras, E.; Riaz, A.; Kim, J. An Investigation of the Gravity Effects on Pool
 Boiling Heat Transfer via High-Fidelity Simulations. *Int. J. Heat Mass Transf.* 2021,
 180, 121826.
- 8 (367) Sato, Y.; Ničeno, B. A Sharp-Interface Phase Change Model for a Mass-Conservative 9 Interface Tracking Method. *J. Comput. Phys.* **2013**, *249*, 127–161.
- 10 (368) Sato, Y.; Niceno, B. A Depletable Micro-Layer Model for Nucleate Pool Boiling. *J. Comput. Phys.* **2015**, *300*, 20–52.
- 12 (369) Lal, S.; Sato, Y.; Niceno, B. Direct Numerical Simulation of Bubble Dynamics in Subcooled and Near-Saturated Convective Nucleate Boiling. *Int. J. Heat Fluid Flow* **2015**, *51*, 16–28.
- (370) Sato, Y.; Niceno, B. Nucleate Pool Boiling Simulations Using the Interface Tracking
 Method: Boiling Regime from Discrete Bubble to Vapor Mushroom Region. *Int. J. Heat* Mass Transf. 2017, 105, 505–524.
- 18 (371) Lee, R. C.; Nydahl, J. E. Numerical Calculation of Bubble Growth in Nucleate Boiling 19 from Inception Through Departure. *J. Heat Transfer* **1989**, *111*, 474–479.
- 20 (372) Urbano, A.; Tanguy, S.; Huber, G.; Colin, C. Direct Numerical Simulation of Nucleate 21 Boiling in Micro-Layer Regime. *Int. J. Heat Mass Transf.* **2018**, *123*, 1128–1137.
- (373) Li, J.; Yang, Z.; Duan, Y. Numerical Simulation of Single Bubble Growth and Heat
 Transfer Considering Multi-Parameter Influence during Nucleate Pool Boiling of Water.
 AIP Adv. 2021, 11, 125207.
- 25 (374) Huber, G.; Tanguy, S.; Sagan, M.; Colin, C. Direct Numerical Simulation of Nucleate
 Pool Boiling at Large Microscopic Contact Angle and Moderate Jakob Number. *Int. J. Heat Mass Transf.* 2017, 113, 662–682.
- 28 (375) Guo, Y.; Zhu, C.-Y.; Gong, L.; Zhang, Z.-B. Numerical Simulation of Flow Boiling 29 Heat Transfer in Microchannel with Surface Roughness. *Int. J. Heat Mass Transf.* **2023**, 30 *204*, 123830.
- 31 (376) Ranathunga, D. T. S.; Shamir, A.; Dai, X.; Nielsen, S. O. Molecular Dynamics 32 Simulations of Water Condensation on Surfaces with Tunable Wettability. *Langmuir* 33 **2020**, *36*, 7383–7391.

- 1 (377) Karalis, K.; Zahn, D.; Prasianakis, N. I.; Niceno, B.; Churakov, S. V. Deciphering the
- 2 Molecular Mechanism of Water Boiling at Heterogeneous Interfaces. Sci. Rep. 2021, 11,
- 3 19858.
- 4 (378) Lavino, A. D.; Smith, E.; Magnini, M.; Matar, O. K. Surface Topography Effects on
- 5 Pool Boiling via Non-Equilibrium Molecular Dynamics Simulations. *Langmuir* **2021**,
- 6 37, 5731–5744.
- 7 (379) Zhou, W.; Han, D.; Ma, H.; Hu, Y.; Xia, G. Molecular Dynamics Study on Enhanced
- Nucleate Boiling Heat Transfer on Nanostructured Surfaces with Rectangular Cavities.
- 9 *Int. J. Heat Mass Transf.* **2022**, *191*, 122814.
- 10 (380) Gao, S.; Qu, J.; Liu, Z.; Liu, W. Nanoscale Thin-Film Boiling Processes on
- Heterogeneous Surfaces. *Langmuir* **2022**, *38*, 6352–6362.
- 12 (381) Tsuruta, T.; Tanaka, H.; Masuoka, T. Condensation/Evaporation Coefficient and
- Velocity Distributions at Liquid-Vapor Interface. Int. J. Heat Mass Transf. 1999, 42,
- 14 4107–4116.
- 15 (382) Nagayama, G.; Tsuruta, T. A General Expression for the Condensation Coefficient
- Based on Transition State Theory and Molecular Dynamics Simulation. J. Chem. Phys.
- **2003**, *118*, 1392–1399.
- 18 (383) Tsuruta, T.; Nagayama, G. Molecular Dynamics Studies on the Condensation
- 19 Coefficient of Water. J. Phys. Chem. B 2004, 108, 1736–1743.
- 20 (384) Julin, J.; Shiraiwa, M.; Miles, R. E. H.; Reid, J. P.; Pöschl, U.; Riipinen, I. Mass
- Accommodation of Water: Bridging the Gap Between Molecular Dynamics Simulations
- and Kinetic Condensation Models. J. Phys. Chem. A 2013, 117, 410–420.
- 23 (385) Liang, Z.; Biben, T.; Keblinski, P. Molecular Simulation of Steady-State Evaporation
- and Condensation: Validity of the Schrage Relationships. *Int. J. Heat Mass Transf.* **2017**,
- 25 *114*, 105–114.
- 26 (386) Li, R.; Wang, J.; Xia, G. Theoretical and Numerical Study of Nanoporous Evaporation
- with Receded Liquid Surface: Effect of Knudsen Number. J. Fluid Mech. 2021, 928, A9.
- 28 (387) Li, R.; Wang, J.; Xia, G. New Model for Liquid Evaporation and Vapor Transport in
- Nanopores Covering the Entire Knudsen Regime and Arbitrary Pore Length. *Langmuir*
- **2021**, *37*, 2227–2235.
- 31 (388) Li, R.; Xia, G.; Wang, J. Two-Dimensional Kinetic Evaporation by Direct Simulation
- Monte Carlo (DSMC) with Independently Controlled Downstream Boundary
- 33 Conditions. Int. J. Heat Mass Transf. **2022**, 194, 123075.

- 1 (389) John, B.; Enright, R.; Sprittles, J. E.; Gibelli, L.; Emerson, D. R.; Lockerby, D. A.
- Numerical Investigation of Nanoporous Evaporation Using Direct Simulation Monte
- 3 Carlo. Phys. Rev. Fluids **2019**, 4, 113401.
- 4 (390) John, B.; Gibelli, L.; Enright, R.; Sprittles, J. E.; Lockerby, D. A.; Emerson, D. R.
- 5 Evaporation from Arbitrary Nanoporous Membrane Configurations: An Effective
- 6 Evaporation Coefficient Approach. *Phys. Fluids* **2021**, *33*, 032022.
- 7 (391) Chen, S.; Doolen, G. D. Lattice Boltzmann Method for Fluid Flows. *Annu. Rev. Fluid Mech.* **1998**, *30*, 329–364.
- 9 (392) Chen, H.; Chen, S.; Matthaeus, W. H. Recovery of the Navier-Stokes Equations Using a Lattice-Gas Boltzmann Method. *Phys. Rev. A* **1992**, *45*, R5339–R5342.
- 11 (393) Qian, Y. H.; D'Humières, D.; Lallemand, P. Lattice BGK Models for Navier-Stokes 12 Equation. *Europhys. Lett.* **1992**, *17*, 479–484.
- 13 (394) Qian, Y. H. Simulating Thermohydrodynamics with Lattice BGK Models. *J. Sci.* 14 *Comput.* **1993**, *8*, 231–242.
- (395) Aidun, C. K.; Clausen, J. R. Lattice-Boltzmann Method for Complex Flows. *Annu. Rev. Fluid Mech.* 2010, 42, 439–472.
- 17 (396) Grunau, D.; Chen, S.; Eggert, K. A Lattice Boltzmann Model for Multiphase Fluid 18 Flows. *Phys. Fluids* **1993**, *5*, 2557–2562.
- 19 (397) Zhang, L.; Jebakumar, A. S.; Abraham, J. Lattice Boltzmann Method Simulations of 20 Stokes Number Effects on Particle Motion in a Channel Flow. *Phys. Fluids* **2016**, *28*, 21 063306.
- 22 (398) Chen, L.; Kang, Q.; Mu, Y.; He, Y.-L.; Tao, W.-Q. A Critical Review of the 23 Pseudopotential Multiphase Lattice Boltzmann Model: Methods and Applications. *Int.* 24 *J. Heat Mass Transf.* **2014**, *76*, 210–236.
- (399) Li, Q.; Luo, K. H.; Kang, Q. J.; He, Y. L.; Chen, Q.; Liu, Q. Lattice Boltzmann Methods
 for Multiphase Flow and Phase-Change Heat Transfer. *Prog. Energy Combust. Sci.* 2016,
 52, 62–105.
- (400) Bhatnagar, P. L.; Gross, E. P.; Krook, M. A Model for Collision Processes in Gases. I.
 Small Amplitude Processes in Charged and Neutral One-Component Systems. *Phys. Rev.* 1954, 94, 511–525.
- 31 (401) Gong, S.; Cheng, P. A Lattice Boltzmann Method for Simulation of Liquid–Vapor 32 Phase-Change Heat Transfer. *Int. J. Heat Mass Transf.* **2012**, *55*, 4923–4927.
- 33 (402) Gong, S.; Cheng, P. Numerical Investigation of Droplet Motion and Coalescence by an
- 34 Improved Lattice Boltzmann Model for Phase Transitions and Multiphase Flows.
- 35 *Comput. Fluids* **2012**, *53*, 93–104.

- 1 (403) Gong, S.; Cheng, P.; Quan, X. Two-Dimensional Mesoscale Simulations of Saturated 2 Pool Boiling from Rough Surfaces. Part I: Bubble Nucleation in a Single Cavity at Low
- 3 Superheats. Int. J. Heat Mass Transf. 2016, 100, 927–937.
- 4 (404) Gong, S.; Cheng, P. Two-Dimensional Mesoscale Simulations of Saturated Pool Boiling 5 from Rough Surfaces. Part II: Bubble Interactions above Multi-Cavities. *Int. J. Heat* 6 *Mass Transf.* **2016**, *100*, 938–948.
- 7 (405) Zhou, P.; Liu, W.; Liu, Z. Lattice Boltzmann Simulation of Nucleate Boiling in Micro-8 Pillar Structured Surface. *Int. J. Heat Mass Transf.* **2019**, *131*, 1–10.
- 9 (406) Meulenbroek, A. M.; Bernts, B. W. J.; Deen, N. G.; Vreman, A. W. Numerical 10 Simulation of Marangoni Flow around a Growing Hydrogen Bubble on a 11 Microelectrode. *Electrochim. Acta* **2023**, *472*, 143457.
- 12 (407) Khalighi, F.; Deen, N. G.; Tang, Y.; Vreman, A. W. Hydrogen Bubble Growth in 13 Alkaline Water Electrolysis: An Immersed Boundary Simulation Study. *Chem. Eng. Sci.* 14 **2023**, *267*, 118280.
- 15 (408) Vachaparambil, K. J.; Einarsrud, K. E. Numerical Simulation of Continuum Scale 16 Electrochemical Hydrogen Bubble Evolution. *Appl. Math. Model.* **2021**, *98*, 343–377.
- 17 (409) Zhan, S.; Yuan, R.; Huang, Y.; Zhang, W.; Li, B.; Wang, Z.; Wang, J. Numerical
 18 Simulation of Hydrogen Bubble Growth and Mass Transfer on Horizontal
 19 Microelectrode Surface under Electrode-Normal Magnetic Field. *Phys. Fluids* **2022**, *34*,
 20 112120.
- (410) Raman, A.; Porto, C. C. dos S.; Gardeniers, H.; Soares, C.; Fernández Rivas, D.; Padoin,
 N. Investigating Mass Transfer around Spatially-Decoupled Electrolytic Bubbles. *Chem. Eng. J.* 2023, 477, 147012.
- 24 (411) Li, S.-D.; Wang, C.-C.; Chen, C.-Y. Water Electrolysis in the Presence of an Ultrasonic Field. *Electrochim. Acta* **2009**, *54*, 3877–3883.
- 26 (412) Li, J.; Xue, J.; Tan, Z.; Zheng, Y.; Zhang, L. Ultrasound-Assisted Electrolysis in NaOH 27 Solution for Hydrogen Generation. In *EPD Congress 2011*; Wiley, 2011; pp 919–926.
- 28 (413) Islam, M. H.; Burheim, O. S.; Pollet, B. G. Sonochemical and Sonoelectrochemical 29 Production of Hydrogen. *Ultrason. Sonochem.* **2019**, *51*, 533–555.
- 30 (414) Liang, X.; Kumar, V.; Ahmadi, F.; Zhu, Y. Manipulation of Droplets and Bubbles for Thermal Applications. *Droplet* **2022**, *1*, 80–91.
- 32 (415) Sadaghiani, A. K.; Altay, R.; Noh, H.; Kwak, H. J.; Şendur, K.; Mısırlıoğlu, B.; Park, H.
- 33 S.; Koşar, A. Effects of Bubble Coalescence on Pool Boiling Heat Transfer and Critical
- 34 Heat Flux A Parametric Study Based on Artificial Cavity Geometry and Surface
- 35 Wettability. Int. J. Heat Mass Transf. 2020, 147, 118952.

- 1 (416) Narezo Guzman, D.; Xie, Y.; Chen, S.; Fernandez Rivas, D.; Sun, C.; Lohse, D.; Ahlers,
- G. Heat-Flux Enhancement by Vapour-Bubble Nucleation in Rayleigh-Bénard
- 3 Turbulence. *J. Fluid Mech.* **2016**, 787, 331–366.
- 4 (417) Song, Y.; Gong, S.; Vaartstra, G.; Wang, E. N. Microtube Surfaces for the Simultaneous
- 5 Enhancement of Efficiency and Critical Heat Flux during Pool Boiling. ACS Appl. Mater.
- 6 *Interfaces* **2021**, *13*, 12629–12635.
- 7 (418) Song, Y.; Zhang, L.; Liu, Z.; Preston, D. J.; Wang, E. N. Effects of Airborne
- 8 Hydrocarbon Adsorption on Pool Boiling Heat Transfer. Appl. Phys. Lett. 2020, 116,
- 9 253702.
- 10 (419) Song, Y.; Cha, H.; Liu, Z.; Seong, J. H.; Zhang, L.; Preston, D. J.; Wang, E. N. Alteration
- of Pool Boiling Heat Transfer on Metallic Surfaces by in Situ Oxidation. Int. J. Heat
- 12 Mass Transf. 2022, 185, 122320.
- 13 (420) Torresin, D.; Tiwari, M. K.; Del Col, D.; Poulikakos, D. Flow Condensation on Copper-
- Based Nanotextured Superhydrophobic Surfaces. *Langmuir* **2013**, *29*, 840–848.
- 15 (421) Miljkovic, N.; Enright, R.; Nam, Y.; Lopez, K.; Dou, N.; Sack, J.; Wang, E. N. Jumping-
- Droplet-Enhanced Condensation on Scalable Superhydrophobic Nanostructured
- 17 Surfaces. *Nano Lett.* **2013**, *13*, 179–187.
- 18 (422) Paxson, A. T.; Yagüe, J. L.; Gleason, K. K.; Varanasi, K. K. Stable Dropwise
- 19 Condensation for Enhancing Heat Transfer via the Initiated Chemical Vapor Deposition
- 20 (ICVD) of Grafted Polymer Films. *Adv. Mat.* **2014**, *26*, 418–423.
- 21 (423) Betz, A. R.; Jenkins, J.; Kim, C.-J. "CJ"; Attinger, D. Boiling Heat Transfer on
- 22 Superhydrophilic, Superhydrophobic, and Superbiphilic Surfaces. Int. J. Heat Mass
- 23 *Transf.* **2013**, *57*, 733–741.
- 24 (424) Zhang, C.; Xu, Z.; Han, N.; Tian, Y.; Kallio, T.; Yu, C.; Jiang, L.
- Superaerophilic/Superaerophobic Cooperative Electrode for Efficient Hydrogen
- Evolution Reaction via Enhanced Mass Transfer. Sci. Adv. 2023, 9, eadd6978.
- 27 (425) Rahman, M. M.; Pollack, J.; McCarthy, M. Increasing Boiling Heat Transfer Using Low
- 28 Conductivity Materials. Sci. Rep. 2015, 5, 13145.
- 29 (426) Hetsroni, G.; Zakin, J. L.; Lin, Z.; Mosyak, A.; Pancallo, E. A.; Rozenblit, R. The Effect
- of Surfactants on Bubble Growth, Wall Thermal Patterns and Heat Transfer in Pool
- 31 Boiling. Int. J. Heat Mass Transf. **2001**, 44, 485–497.
- 32 (427) Zhang, J.; Manglik, R. M. Effect of Ethoxylation and Molecular Weight of Cationic
- Surfactants on Nucleate Boiling in Aqueous Solutions. J. Heat Transfer 2004, 126, 34—
- 34 42.

- 1 (428) Mata, M. R.; Ortiz, B.; Luhar, D.; Evereux, V.; Cho, H. J. How Dynamic Adsorption 2 Controls Surfactant-Enhanced Boiling. *Sci. Rep.* **2022**, *12*, 18170.
- 3 (429) Cheng, L.; Mewes, D.; Luke, A. Boiling Phenomena with Surfactants and Polymeric Additives: A State-of-the-Art Review. *Int. J. Heat Mass Transf.* **2007**, *50*, 2744–2771.
- 5 (430) Cho, H. J.; Mizerak, J. P.; Wang, E. N. Turning Bubbles on and off during Boiling Using Charged Surfactants. *Nat. Commun.* **2015**, *6*, 8599.
- 7 (431) Zhao, L.; Seshadri, S.; Liang, X.; Bailey, S. J.; Haggmark, M.; Gordon, M.; Helgeson, M. E.; Read de Alaniz, J.; Luzzatto-Fegiz, P.; Zhu, Y. Depinning of Multiphase Fluid Using Light and Photo-Responsive Surfactants. *ACS Cent. Sci.* **2022**, *8*, 235–245.
- 10 (432) Cassie, A. B. D.; Baxter, S. Wettability of Porous Surfaces. *Trans. Faraday Soc.* **1944**, 11 40, 546.
- 12 (433) Cassie, A. B. D.; Baxter, S. Large Contact Angles of Plant and Animal Surfaces. *Nature* 13 **1945**, *155*, 21–22.
- 14 (434) Wenzel, R. N. Resistance of Solid Surfaces to Wetting by Water. *Ind. Eng. Chem.* **1936**, 28, 988–994.
- (435) Wang, F.; Wu, Y.; Nestler, B. Wetting Effect on Patterned Substrates. *Adv. Mat.* 2023,
 35, 2210745.
- 18 (436) Kwon, H.-M.; Paxson, A. T.; Varanasi, K. K.; Patankar, N. A. Rapid Deceleration-19 Driven Wetting Transition during Pendant Drop Deposition on Superhydrophobic 20 Surfaces. *Phys. Rev. Lett.* **2011**, *106*, 036102.
- 21 (437) Lee, J.-H.; Loya, P. E.; Lou, J.; Thomas, E. L. Dynamic Mechanical Behavior of 22 Multilayer Graphene via Supersonic Projectile Penetration. *Science* **2014**, *346*, 1092– 23 1096.
- 24 (438) Kreder, M. J.; Alvarenga, J.; Kim, P.; Aizenberg, J. Design of Anti-Icing Surfaces: Smooth, Textured or Slippery? *Nat. Rev. Mater.* **2016**, *1*, 15003.
- (439) Domingues, E. M.; Arunachalam, S.; Nauruzbayeva, J.; Mishra, H. Biomimetic
 Coating-Free Surfaces for Long-Term Entrapment of Air under Wetting Liquids. *Nat. Commun.* 2018, 9, 3606.
- 29 (440) Wang, D.; Sun, Q.; Hokkanen, M. J.; Zhang, C.; Lin, F.-Y.; Liu, Q.; Zhu, S.-P.; Zhou, 30 T.; Chang, Q.; He, B.; et al. Design of Robust Superhydrophobic Surfaces. *Nature* **2020**, 31 582, 55–59.
- 32 (441) Feng, S.; Zhu, P.; Zheng, H.; Zhan, H.; Chen, C.; Li, J.; Wang, L.; Yao, X.; Liu, Y.; Wang, Z. Three-Dimensional Capillary Ratchet-Induced Liquid Directional Steering. *Science* **2021**, *373*, 1344–1348.

- (442) Wilke, K. L.; Lu, Z.; Song, Y.; Wang, E. N. Turning Traditionally Nonwetting Surfaces 1 2 Wetting for Even Ultra-High Surface Energy Liquids. Proc. Natl. Acad. Sci. 2022, 119,
- 3 e2109052119.
- 4 (443) Vu, H. H.; Nguyen, N.; Kashaninejad, N. Re-Entrant Microstructures for Robust Liquid 5 Repellent Surfaces. Adv. Mater. Technol. 2023, 8, 2201836.
- 6 (444) Vaartstra, G.; Lu, Z.; Wang, E. N. Simultaneous Prediction of Dryout Heat Flux and 7 Local Temperature for Thin Film Evaporation in Micropillar Wicks. Int. J. Heat Mass 8 Transf. 2019, 136, 170-177.
- 9 (445) Zhu, Y.; Antao, D. S.; Lu, Z.; Somasundaram, S.; Zhang, T.; Wang, E. N. Prediction 10 and Characterization of Dry-out Heat Flux in Micropillar Wick Structures. Langmuir **2016**, *32*, 1920–1927. 11
- (446) Zhu, Y.; Antao, D. S.; Chu, K.-H.; Chen, S.; Hendricks, T. J.; Zhang, T.; Wang, E. N. 12 Surface Structure Enhanced Microchannel Flow Boiling. J. Heat Transfer 2016, 138. 13
- 14 (447) Dhillon, N. S.; Buongiorno, J.; Varanasi, K. K. Critical Heat Flux Maxima during Boiling Crisis on Textured Surfaces. Nat. Commun. 2015, 6, 8247. 15
- (448) Lin, D.; Liu, Y.; Liang, Z.; Lee, H.-W.; Sun, J.; Wang, H.; Yan, K.; Xie, J.; Cui, Y. 16 17 Layered Reduced Graphene Oxide with Nanoscale Interlayer Gaps as a Stable Host for Lithium Metal Anodes. Nat. Nanotechnol. 2016, 11, 626–632. 18
- (449) Lin, D.; Liu, Y.; Cui, Y. Reviving the Lithium Metal Anode for High-Energy Batteries. 19 20 Nat. Nanotechnol. 2017, 12, 194-206.
- (450) Pikul, J. H.; Gang Zhang, H.; Cho, J.; Braun, P. V.; King, W. P. High-Power Lithium 21 Ion Microbatteries from Interdigitated Three-Dimensional Bicontinuous Nanoporous 22 Electrodes. Nat. Commun. 2013, 4, 1732. 23
- 24 (451) Salanne, M.; Rotenberg, B.; Naoi, K.; Kaneko, K.; Taberna, P.-L.; Grey, C. P.; Dunn, B.; Simon, P. Efficient Storage Mechanisms for Building Better Supercapacitors. Nat. 25 26 Energy **2016**, *1*, 16070.
- (452) Li, X.; Shao, J.; Kim, S.-K.; Yao, C.; Wang, J.; Miao, Y.-R.; Zheng, Q.; Sun, P.; Zhang, 27 R.; Braun, P. V. High Energy Flexible Supercapacitors Formed via Bottom-up Infilling 28 of Gel Electrolytes into Thick Porous Electrodes. Nat. Commun. 2018, 9, 2578. 29
- (453) Qin, H.; Liu, P.; Chen, C.; Cong, H.-P.; Yu, S.-H. A Multi-Responsive Healable 30 Supercapacitor. Nat. Commun. 2021, 12, 4297. 31
- (454) Jin, J.; Xiao, T.; Luo, R.; Nie, X.; Wang, Y.; Liu, Z. Superaerophobic Platinum 32 Nanosheets Arrays on Conductive Microgrids: A Highly Efficient Electrocatalytic 33 Electrode for Hydrogen Evolution Reaction. ChemCatChem 2020, 12, 5062–5066. 34

- (455) Pham, Q. N.; Zhang, S.; Hao, S.; Montazeri, K.; Lin, C.-H.; Lee, J.; Mohraz, A.; Won,
 Y. Boiling Heat Transfer with a Well-Ordered Microporous Architecture. ACS Appl.
 Mater. Interfaces 2020, 12, 19174–19183.
- 4 (456) Zhao, H.; Dash, S.; Dhillon, N. S.; Kim, S.; Lettiere, B.; Varanasi, K. K.; Hart, A. J. Microstructured Ceramic-Coated Carbon Nanotube Surfaces for High Heat Flux Pool Boiling. *ACS Appl. Nano Mater.* **2019**, *2*, 5538–5545.
- 7 (457) Ćoso, D.; Srinivasan, V.; Lu, M.-C.; Chang, J.-Y.; Majumdar, A. Enhanced Heat 8 Transfer in Biporous Wicks in the Thin Liquid Film Evaporation and Boiling Regimes. 9 *J. Heat Transfer* **2012**, *134*.
- (458) Hanks, D. F.; Lu, Z.; Sircar, J.; Salamon, T. R.; Antao, D. S.; Bagnall, K. R.; Barabadi,
 B.; Wang, E. N. Nanoporous Membrane Device for Ultra High Heat Flux Thermal
 Management. *Microsyst. Nanoeng.* 2018, 4, 1.
- (459) Hanks, D. F.; Lu, Z.; Sircar, J.; Kinefuchi, I.; Bagnall, K. R.; Salamon, T. R.; Antao, D.
 S.; Barabadi, B.; Wang, E. N. High Heat Flux Evaporation of Low Surface Tension
 Liquids from Nanoporous Membranes. ACS Appl. Mater. Interfaces 2020, 12, 7232–7238.
- (460) Wan, L.; Xu, Z.; Xu, Q.; Wang, P.; Wang, B. Overall Design of Novel 3D-Ordered MEA
 with Drastically Enhanced Mass Transport for Alkaline Electrolyzers. *Energy Environ*.
 Sci. 2022, 15, 1882–1892.
- 20 (461) Lake, J. R.; Soto, Á. M.; Varanasi, K. K. Impact of Bubbles on Electrochemically Active 21 Surface Area of Microtextured Gas-Evolving Electrodes. *Langmuir* **2022**, *38*, 3276– 22 3283.
- (462) Nami, H.; Rizvandi, O. B.; Chatzichristodoulou, C.; Hendriksen, P. V.; Frandsen, H. L.
 Techno-Economic Analysis of Current and Emerging Electrolysis Technologies for
 Green Hydrogen Production. *Energy Convers. Manag.* 2022, 269, 116162.
- (463) Nemitallah, M. A.; Alnazha, A. A.; Ahmed, U.; El-Adawy, M.; Habib, M. A. Review
 on Techno-Economics of Hydrogen Production Using Current and Emerging Processes:
 Status and Perspectives. *Results Eng.* 2024, 21, 101890.

29

30